PhD Thesis

Designing Nanoscale Metal Particles for Higher Order Assembly

A Thesis Submitted by

Anushree Dutta

Roll No. 11612245

to

Indian Institute of Technology Guwahati

for the award of the degree of

DOCTOR OF PHILOSOPHY

Department of Chemistry

Indian Institute of Technology Guwahati
Guwahati- 781039
Assam, India
November 2017

Designing Nanoscale Metal Particles for Higher Order Assembly

A thesis submitted by ***Anushree Dutta***
to ***Indian Institute of Technology Guwahati***
under the supervision of ***Prof. Arun Chattopadhyay***
for the award of the degree of
Doctor of Philosophy

Department of Chemistry
Indian Institute of Technology Guwahati
Guwahati, Assam-781039
India

DECLARATION

I hereby declare that the results and discussions embodied in the thesis titled "***Designing Nanoscale Metal Particles for Higher Order Assembly"*** is the outcome of research work carried out by me under the supervision of ***Prof. Arun Chattopadhyay***, **Department of Chemistry**, **Indian Institute of Technology Guwahati**, **Guwahati**, **Assam**, **India** for the award of the degree of Doctor of Philosophy. To the best of my knowledge, the present thesis has not been submitted for any degree, diploma, associateship etc. of any Institute or University elsewhere.

Anushree Dutta
Department of Chemistry
IIT Guwahati, Guwahati-781039
Assam, India
Date:

भारतीय प्रौद्योगिकी संस्थान गुवाहाटी
INDIAN INSTITUTE OF TECHNOLOGY GUWAHATI

CERTIFICATE

This is to certify that the thesis entitled *"Designing Nanoscale Metal Particles for Higher Order Assembly"* being submitted to the **Indian Institute of Technology Guwahati** by ***Anushree Dutta*** (Roll No. **11612245**) for the award of the degree of **Doctor of Philosophy** in **Chemistry** is a bonafide record of research work carried by her. The data reported and the conclusion drawn herein is the results of the original findings of her work. This work has not been submitted elsewhere for any degree or diploma.

Prof. Arun Chattopadhyay
Thesis Supervisor
Department of Chemistry
IIT Guwahati, Guwahati-781039
Assam, India.
Date:

Dedicated to my parents

and

all my beloved

ACKNOWLEDGEMENTS

Penning down through this space not only gives me immense pleasure but also helps me recollect my innumerable memories made at IIT Guwahati. Firstly, a big heartfelt thank you to all the kind hearted people who had cheered me up at the odd and even times during my stay at IIT Guwahati. I am happy to be a part of this coveted IIT fraternity and can't thank IIT Guwahati enough for giving me a chance to carry out my doctoral studies in this beautiful green campus where the stay was indeed very pleasant.

First, I would like convey my sincere gratitude and thanks to my supervisor, Prof. Arun Chattopadhyay for qualifying me as a member of his group. His constant support towards carrying out my research work, positive motivation and constructive criticism have been fundamental in helping me gain ground as a researcher and as an individual with positive personality. Thank you Sir for all the timely discussions, indispensable advices and constant support during my tough days that kept me going. I also thank you for specially providing me with a splendid research environment endowed with all instrumental facilities and freedom to work. It has been my privilege to work with a generous person like him and share knowledge both scientifically and non-scientifically. Hope the virtues and enlightenment earned through the various knowledgeable discussions with him resides in me forever.

I also extend my thanks to Prof. Anumita Paul for her support and help not just as a collaborator but as a keen advisor as well. I am grateful to Madam for conveniently making out time for our long discussions and for her cooperation and interest for solving any of my problems. I have learned a lot during the days I had worked with her and sincerely acknowledge her contribution in my research work.

Next, I express my sincere thanks to my doctoral committee chairman Dr. Chandan Mukherjee and to the other committee members Dr. A. S. Achalkumar and Dr. Biplab Bose for their timely assessment of my thesis work in addition to their valuable suggestions and corrections made for the same. I am grateful to Prof. Siddhartha Sankar Ghosh for allowing me to use equipment's and other facilities in his lab.

I acknowledge Central Instrumental Facility and Centre for Nanotechnology, IIT Guwahati for providing me with the much needed instrumental facilities. I thank IIT Guwahati for providing me with the PhD scholarship and fundings for attending national and international conferences.

Next, I take this opportunity to convey my thanks and gratitude to all my collaborators – Dr. Pallab Sanpui, Dr. Subhojit Das, Upashi Goswami, Deepanjali Dutta, *Kasturi Gogoi and Srimanta Pal. You all have been pretty pleasing in your own way to work with and hearty thanks to you all for your kind cooperation in getting my work done at the earliest. Many thanks to Upashi for her endless efforts to get the best confocal images for my work in addition to her support and helpful insights. I also thank Deepanjali for giving her best to get my work done at the earliest. Working and discussions with Kasturi was pretty nice. Lastly, I would like to mention how good it feels to work with Srimanta – the cheerful and inquisitive person, who tries to enjoy his work amongst all odds. You all have helped me learn so much in your own little ways.*

I am grateful to Srestha Basu for carrying out the TEM measurements for my work. Thank you for all your efforts and help whenever I needed the same.

I am thankful to Dr. Jasmini Deka and Dr. Rama Ghosh for helping me with my research work during my initial days at IITG.

I extend my sincere thanks to all the staff members of Department of Chemistry, Centre for Nanotechnology and Central Instruments Facility for their kind cooperation and timely help. I specially thank Indrajit Sir, Chandan Sir and Madhurjya Sir for their cooperation and generosity.

My stay at IITG with my seniors: Dr. Sadhucharan Mallick, Dr. Amaresh Sahoo, Dr. Aditi Banerjee, Dr. Raihana Begum, Dr. Amit Jaiswal, Dr. Rumi Khandelia, Dr. Palashuddin Sheikh, Dr. Madhulekha Gogoi and Dr. Satyapriya Bhandari and labmates: Dr. Sunil Sailapu, Shilaj, Uday, Kafeel, Sabyasachi, Ayan, Mihir, Chirantan, Manideepa, Komal, Bandhan, Anitha and Deboshree have been pleasant and their kind help is acknowledged.

My heartfelt and special thanks to B. Ravi, Dr. Nayan Mani Das, Arunangshu, Akhtar, M. Gopi, Dilip, Nithi, Dr. Manas Mandal, Tanmay, Nilanjan, Shaad, Namami, Asif, Sunny, Nivedita, Soumi, Deboleena, Jitender and Somorjit for their selfless help and immense support throughout the stint of my research and for being around whenever I needed them.

Also, I cherish the time spent with our hostel pet dog Poltu.

Lastly, I extend my thanks and well wishes to all of my other friends at IITG.

Last but not the least, I convey my thanks and gratitude to my parents, my brother and relatives for their well wishes, encouragement and support in all my endeavours.

Many thanks and cheers to all.

Anushree

TABLE OF CONTENTS

THESIS ABSTRACT

Engineering matter at the nanoscale to fine tune the properties associated with miniaturization has been a major challenge and opportunity for the physicists, material scientists, chemists and biologists across the globe. For example, fabrication of higher order ensemble nanostructures of zero-dimensional plasmonic and luminescent nanoscale particles via various chemical and physical means is likely to generate newer physicochemical properties, which could be of potential interest for various applications. In principle, solution state chemistry may offer us with a large repertoire of options for the attainment of such systematic design of plasmonic and luminescent nanoparticles and their higher order nanostructures. Furthermore, understanding and studying the reaction pathway towards the emergence of such ensembles is equally important.

The present thesis, therefore, adopts a two-step approach which exploits the synthetic advantage of plasmonic and luminescent nanoparticles employing rationally designed molecules, external stimuli *via* physical means and chemical reaction strategy to generate assembled nanostructures and further understand their reaction kinetic pathway for their potential utility in spectroscopy and biology. In this regard, **CHAPTER 1** gives a general overview of nanoscale metal particles and current state of the art development of higher order nano architectures of metal nanoscale particles and their future potential application. **CHAPTER 2** demonstrates a new way to study reaction of citrate stabilised gold nanoparticles (cit-Au NPs) in liquid medium *via* ligand (stabilizer) desorption method following a method of dialysis, to drive the assembly of AuNPs and further delineate the kinetic pathway of the reaction. Based on the reaction among the NPs and their aggregates, a model was further proposed to account for the observed kinetics. Taking a step further, **CHAPTER 3** further illustrates the effect of temperature on the reaction kinetics of the partially bare cit-Au NPs in aqueous medium in order to determine activation energy of the reaction and underlying reason towards barrier to activation based on a proposed model.

However, control over the reaction of nanoparticles in the due course of assembly is necessary to achieve desired optical properties. Therefore, **CHAPTER 4** presents a new way to synthesize dimers of Cit-AuNPs employing a rationally designed metal complex of europium, which acted as a ligating unit to generate discrete dimers along with some population of trimers and oligomers in liquid medium. Importantly, the as-synthesized Au dimers served as potent SERS substrate showing enhanced Raman scattering signal of the Eu-complex trapped in the hot-junction of the nanodimer. Further, **Chapter 5** and **Chapter 6** deal with fluorescent probe of gold (Au) and copper (Cu) nanoclusters (NCs) and cover the engineering technique to fine tune their properties for the advantage of the same in bio-imaging and detection. Therefore, in **CHAPTER 5**, pH stimulus responsive CuNCs with aggregation induced emission (AIE) characteristics have been fabricated that upon internalisation into living cells (MCF-7) exhibited orange-red emission at pH_i 4.5 whereas green emission was observed with time at pH_i 7 and above *via* its AIE attribute. Further, the rate constant derived from the AIE kinetics followed inside living cells indicated 3-fold higher value for MCF-7 cells than that observed in HEK-293 cells thereby opening up a new strategy to study different cell lines. Next, in **CHAPTER 6**, a new strategy to develop a superior luminescent probe for cellular imaging have been demonstrated through biomimetic crystallization of zinc phosphate in peptide stabilised gold nanocluster (Au NC) assembly. The as-developed organic-inorganic hybrid nanostructures of zinc phosphate (AuNC-$Zn_3(PO4)_2$), allowed the clustering of peptide stabilised AuNCs in one platform leading to efficient internalization into the mammalian cells for convenient and enhanced fluorescence imaging than that with discrete as synthesized AuNCs only. In addition, it qualified as better imaging agent being resistant to protease and for its stability in human blood serum.

CHAPTER 1

Introduction and Literature Review

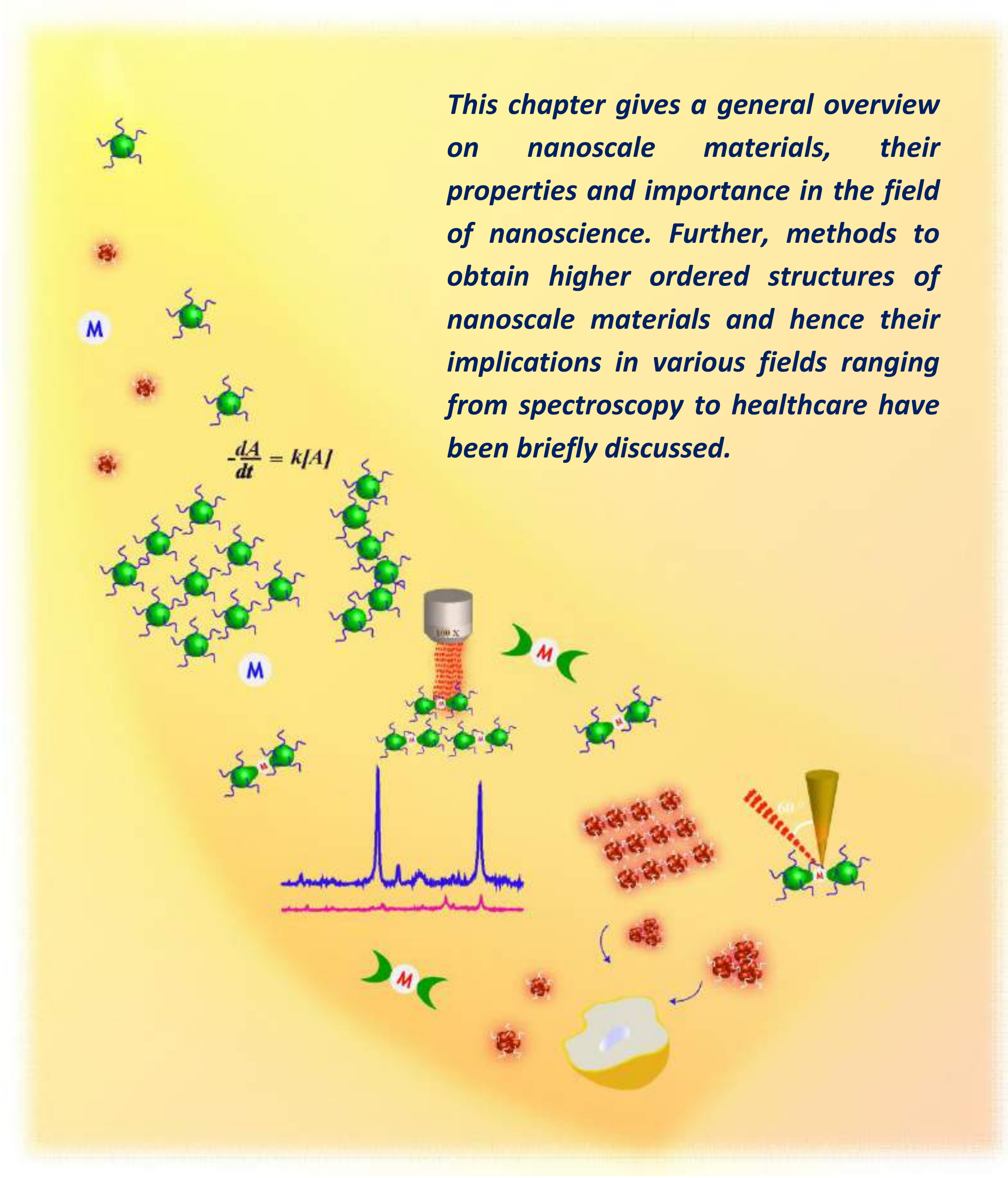

This chapter gives a general overview on nanoscale materials, their properties and importance in the field of nanoscience. Further, methods to obtain higher ordered structures of nanoscale materials and hence their implications in various fields ranging from spectroscopy to healthcare have been briefly discussed.

1.1. Introduction

"*Small is beautiful, nano is even better*" is the belief of present day's scientific community. The term "*nano"* refers to the matter in the scale regime – that is one billionth of a meter. Matter with dimension less than or equal to 100 nm are termed as nanoscale materials in general and nanoscale particles (nanoparticles, nanoclusters, quantum dots etc.) in particular. They fall in the size scale intermediate between individual atoms and their corresponding bulk dimensions. Although nanoscience is considered as the invention of 18th century however, it has been of interest to mankind since the classical times of the history.[1] Due to the interface, the nanoscale particles exhibit special attributes in terms of electrical, optical, magnetic and chemical properties that finds appeal not only in the area of fundamental scientific research, but also in biomedical, energy, chemical catalysis and technological applications.

1.2. Nanoscale Metal Particles and their Properties

At the nanoscale (1-100 nm), the properties of the matter (say metal particles) behave differently from their bulk as well as their atomic or molecular counterparts. The physical and chemical properties become size and shape dependent. As the size reduces, the electronic and optical properties of the metal are determined by the type of motion the electrons undergo in the space to which it is confined.[2] That is to say, particles in the size range 2-100 nm consisting of atoms less than 10^6 in number are termed as metal nanoparticles (NPs), which exhibit surface plasmon resonance by the collective oscillation of conduction electrons upon interaction with light.[3] On the other hand, particles consisting of a few to hundreds of atoms with size nearly approachable to Fermi wavelength of electrons (< 2 nm) are termed as metal nanoclusters (NCs) and exhibit photoluminescence that arise from the electronic transition between the discrete energy levels upon interaction with light.[4] This advent of new properties with the fine tuning of the size and shape can be attributed to (**i**) high surface to volume ratio, (**ii**) quantum–size effect, (**iii**) electrodynamic interaction etc. that is achieved upon reduction of size to nanoscale length.[5-7]

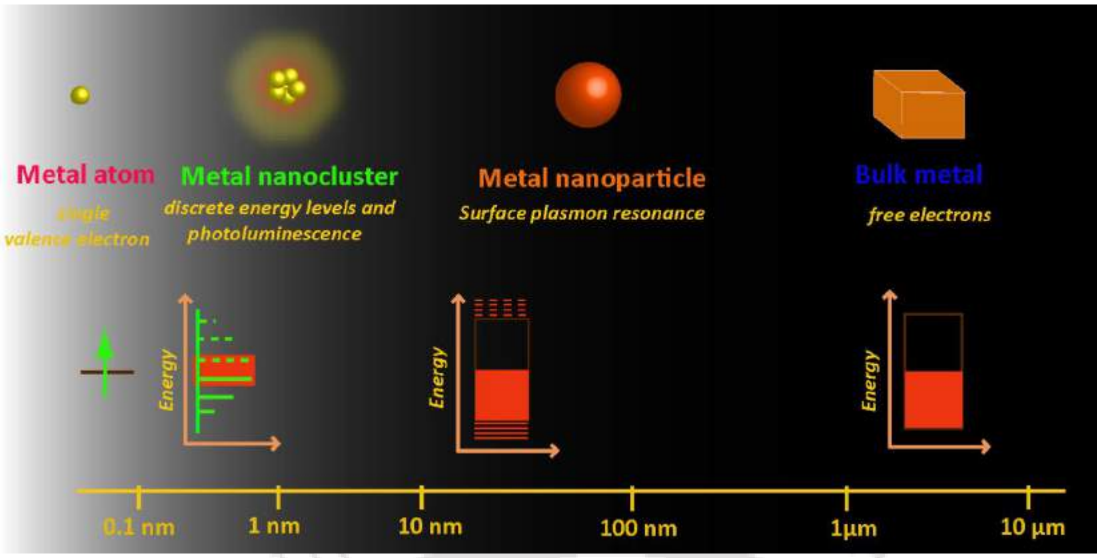

Figure 1.1. Hierarchy of materials (metals) from atom to bulk. Effect of size on the properties of nanoscale metal particles.

1.2.1. Metal Nanoparticles

Metal nanoparticles (NPs) are of immense scientific interest due to the ability of their surface plasmon to couple with light, which endows them with unique optical, electrical, chemical and magnetic properties that are again directed by their size, shape and composition. A plasmon is a collective oscillation of free electrons in metal. At the surface of a metal, plasmon is termed as surface plasmon or surface plasmon polaritons (SPPs). A special type of plasmon oscillation occurs at energies lower than the bulk plasmon when light is coupled to the coherent oscillation of free surface conduction electrons. When the frequency of collective oscillation of the conduction electrons is in resonant with the incident light frequency, the condition is termed as surface plasmon resonance (SPR).[8]

Two types of SPR can be generated. Surface plasmon propagating along the metal surface, when coupled with incoming light waves, are termed as propagating surface plasmons (PSPs) and the resonance condition is termed as propagating surface plasmon resonance (PSPR) as depicted in **Figure 1.2.A.**[9] However, when a surface plasmon is confined to a particle (NP) of size less than or comparable to the wavelength of incident light (**Figure 1.2.B**), particle's free electrons exhibit coherent oscillation, which is termed as localized surface plasmons and the resonance condition is termed as localised surface plasmon

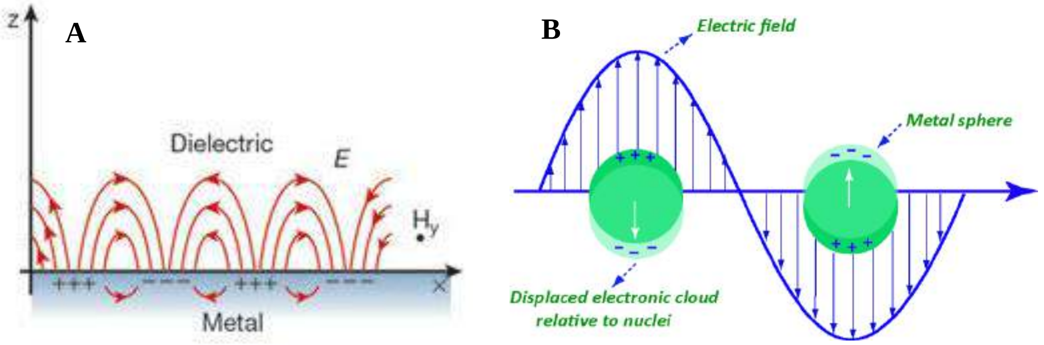

Figure 1.2. Schematic representation of a (**A**) propagating surface plasmon polaritons at the interface between metal and dielectrics, [Reprinted with permission from **reference 9**. Copyright 2003 Nature Publishing Group] (**B**) localised surface plasmon resonance.

resonance (LSPR). This results in an optical extinction peak at a wavelength corresponding to plasmon oscillation frequency.[8,10] Among all, NPs of coinage metals - gold (Au), silver (Ag) and copper (Cu) are the most widely studied because of the occurrence of their surface plasmon oscillation in the visible range of the electromagnetic spectrum which therefore, endows them with characteristic color.[3]

The frequency and position of SPR extinction peak is, however, strongly influenced by the size, shape, interparticle interactions, dielectric properties and refractive index of the surrounding medium.[11] For example, small spherical NPs exhibit single, sharp extinction band due to the absorption – called a dipole plasmon resonance where the entire charge distribution of the particle oscillates at the frequency of the incident electric field as illustrated in **Figure 1.2.B**. Larger spherical particles, on the other hand exhibits multiple absorption bands due to the generation of quadrupole and other higher ordered resonances where for example, half of the electron cloud moves parallel to the incident field and half moves antiparallel.[8] A quintessential example of size dependence of nanoparticles is metal nanorods. Due to particle anisotropy, the dipole resonance is split between transverse and longitudinal plasmon resonance associated with oscillations along the length of the nanorod (at longer wavelength) and that along the width of the nanorods (at shorter wavelength), respectively.[12]

Additionally strong enhancement in electromagnetic field occurs near to the surface of metallic nanoparticle owing to the interaction of incident light with the surface plasmon - the enhancement being highest at the surface and falls off rapidly with the distance.[13] This can be used to obtain enhanced optical signals (like fluorescence, Raman scattering etc.) for any molecule placed in the near vicinity of NPs which are otherwise barely observable, leading to the development of surface enhanced spectroscopic methods like surface enhanced Raman scattering (SERS),[14] surface enhanced fluorescence spectroscopy (SEFS)[14,15] etc. Additionally, metal NP exhibits redox property too.[16] Each of these features makes metal NPs a potent candidate in the study of nanoscience.

1.2.1.a. Gold Nanoparticles (NPs)

Gold on the nano-scale has received the most significance because of its tuneable electronic, optical properties, superior resistance to oxidation and its optical extinction in the visible region.[17] It was Michael Faraday who provided the first scientific description on colloidal gold and its color, in his classic 1857 paper, entitled, "Experimental relations of gold (and other metals) to light."[18] Gustav Mie in 1908, then provided description of the optical response (scattering and absorption) of spherical particles of arbitrary size immersed in a homogeneous solution by solving Maxwell's equation.[19] However, modern day numerical methods using discrete dipole approximation (DDA), finite difference time domain (FDTD) and finite element method (FEM) allows one to calculate surface plasmon properties of plasmonic NPs of any arbitrary geometry beyond spheres and spheroids.[3,5]

Later in 1951, Turkevich developed the most popular approach for the synthesis of gold NPs using sodium citrate reduction of chloroauric acid ($HAuCl_4$) in water that still finds its use in today's date.[20] Thereafter, a significant breakthrough in the synthesis of gold NPs was achieved by Brust and Schiffrin in 1994, after Mulvaney's initial attempt of stabilizing Au NPs with alkanethiols.[21] Brust and Schiffrin reported a two-phase synthetic strategy to obtain 1.5-5 nm gold NPs utilizing the strong thiol-gold interactions with thiol ligands in organic phase that exhibited superior stability.[22] Literature is therefore, replenished with diverse synthetic strategies employing various functional ligands like thiol/

thiolated ligands,[23-24] amines (including primary, secondary and quaternary amine ligands),[25-26] phosphine,[27] carboxylate ligands,[28-29] amino acids,[30-31] proteins,[32] hydroquinone[33] etc. along with shape modification strategies involving physical methods like thermolysis,[34] digestive ripening[35] and conventional ripening[36] for obtaining metal (gold) NPs. NPs shows optical extinction maximum at the localised surface plasmon resonance frequency that occurs at the visible wavelength in case of noble metal NPs. Hence, colloidal dispersion of gold NPs of size 50 nm exhibits a ruby red coloration due to absorption of green light (520 nm), corresponding to frequency at which plasmon resonance occurs in case of nano gold.[37] Further, as interesting electronic and optoelectronic properties can be originated from shape anisotropy extensive efforts have also been given towards shape controlled fabrication of nanocubes, hollow spheres, nanorods (or nanowires), triangular nanoprisms etc. through diverse synthetic routes from inorganic precursors of silver or gold.[8] Thus, Au NPs owing to their tuneable optoelectronic properties,[38] high surface to volume ratio and expansive functionalisation option with biocompatible ligands[39] provides a wide platform for surface enhanced spectroscopic studies, sensing studies based on binding event between recognition element and analyte molecule, catalysis, plasmon assisted hot-carrier devices, drug delivery vehicle, therapy, detection of biological targets etc.[40-43]

1.2.2. Metal Nanoclusters (NCs)

Metal NCs are a new class of fluorogenic nanoscale metal particles that have gained interest due to their molecular like properties and therefore form a missing link between individual atoms and plasmonic NPs.

When metal particles are reduced in size (less than ~1 nm in diameter) and reach a size comparable to electron Fermi wavelength of metal, they no longer behave like pieces of metal with loosely bound electrons but the continuous band structure of NPs break into discrete electronic states. This gives rise to phenomenon like strong photoluminescence through electronic transitions between the different energy levels and thus the tiny particles with molecule like properties are referred to as "metal nanocluster".[44] Photoluminescence can be termed as either fluorescence or phosphorescence, depending upon the type of relaxation mechanism (singlet-singlet or triplet-single) and emission lifetime.[39] Thus metal NCs exhibit different optical, electronic and chemical properties in terms of large Stokes shifted photoluminescence, photostability, high quantum yield, small size, large surface to volume ratio and biocompatibility which make them ideal fluorescent probes for biological applications like bio-imaging, bio-sensing in addition to their applicability in catalysis, as light harvesting materials and other luminescence based studies.[4,45]

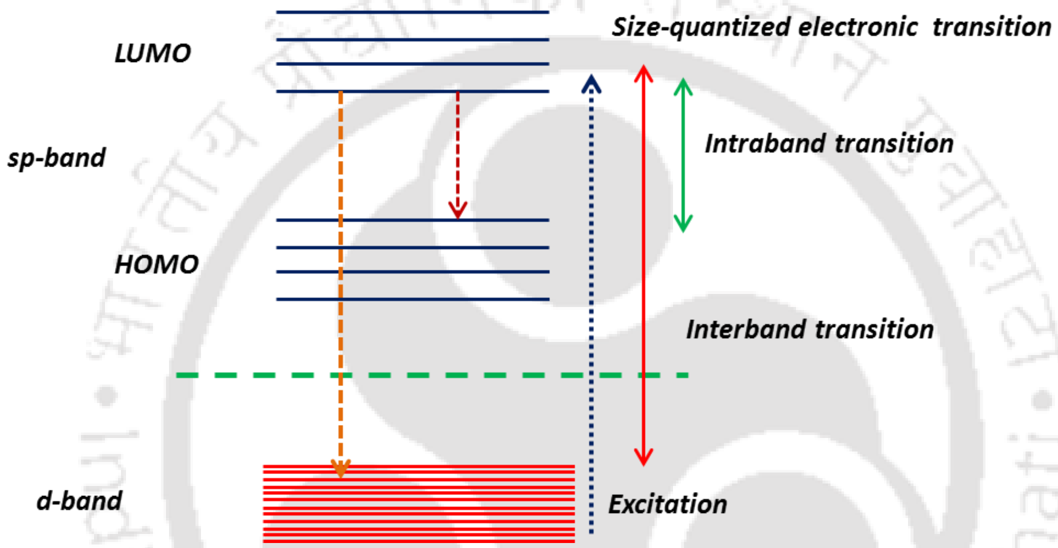

Figure 1.3. Solid-state model for the origin of the two luminescence bands from Au_{28} clusters. The high energy band is proposed to be due to radiative inter-band recombination between the sp and d-bands while the low energy band is thought to originate from radiative intra-band transitions within the sp-band across the HOMO–LUMO gap. [Modified from **reference 46**, Copyright 2002 American Chemical Society]

Photoluminescence observed in few-atom NCs mostly follows the free electron model and is suggestive of the fact that emission fundamentally arises from intra-band (sp-sp) and/or inter-band (sp-d) transition between the discrete energy levels.[39,46] (**Figure 1.3**) It is to be mentioned that although luminescence is attributed to particle size, other parameters like surface ligand assisted ligand-metal/ligand-metal-metal charge transfer (LMCT/LMMCT), valence states of metal atoms and particle crystallinity also have significant influence on emission properties.[4] However, with the increase in the number of atoms, the energy level spacing becomes smaller and eventually becomes comparable to thermal energy (kT), resulting in the disappearance of photoluminescence.

Therefore, control at the atomic level is necessary because of the sensitivity of the cluster's properties to the number of atom.[4] In this regard, considerable effort have been given to generate metal NCs employing appropriate reducing agent, surface protecting capping agents and template in a controlled manner *via* various synthetic methods. Thus, surface protecting stabilizer ligand and the template with different functional moieties plays critical role in determining the electronic structure, geometry and photoluminescence properties of the NCs. Generally employed template and stabilizer ligands involve amino acids, small thiols, nitrogen and carboxylic acid group containing molecule, DNA, peptide, protein, polymer, dendrimers etc.[47]

Additionally metal NCs also exhibit two-photon absorption (TPA) - involving simultaneous absorption of two photons of same or different frequencies in order to excite a molecule at a higher frequency from one state to a higher energy electronic state. The two-photon excitation in the near-infrared region unlike one-photon excitation therefore, increases the penetration depth, spatial resolution due to lower scattering and minimizes autofluroscence[4] which is suitable for photodynamic therapy and in-vivo imaging. Phenomenal progress has therefore been achieved in the studies of Au and Ag NCs so far and increasing interest has also been documented in the studies of Cu NCs in the recent times.

1.2.2.a. Gold Nanoclusters (Au NCs)

Au NCs have received increasing attention since Marcus and Schwentner reported the first observation of photoluminescence from Au_2^+ clusters embedded in a noble-gas matrix in 1987.[48] Since then large number of highly luminescent Au NCs with sizes ranging from 0.3 to 20 nm have been synthesized and fundamental understanding of the emission mechanism has also been gained. Common strategy to prepare Au NCs involves – ligand and template assisted wet chemical reduction technique, which uses reduction of Au^{3+} to Au^+ and then finally to Au in the presence of reducing and capping agents.[4] Thiol containing compounds are often used as a capping agent mainly because they can form strong Au−S bonding with

Au atoms/ions. The surface capping ligand influences the luminescence properties in two different ways: (**i**) charge transfer from the ligand to S and then to Au through the Au–S bond and (**ii**) direct donation of electrons from electron rich atoms or groups in the ligand to Au core.[49]

For example, single-crystal X-ray crystallographic studies[44] on Au_{25} NCs stabilized with phenylethanethiol ligands revealed that Au_{25} cluster is composed of a centered icosahedral Au_{13} core and an exterior shell made of 6 S–Au–S–Au–S staples units. Studies then revealed that the fluorescence of Au NCs arises from the metal centered free-electron transition (NC core) and LMCT/LMMCT. Thus, according to report by Goodson et al. dual emission in $Au_{25}(SG)_{18}$ fundamentally arises from the electron–hole recombination in the Au_{13} core at 500 nm with little perturbation from surface ligands but NIR emission at 700 nm originates from the electron –hole recombination in the ground core state and decay from core excited states to S–Au–S– Au–S semi rings (**Figure 1.4**).[50]

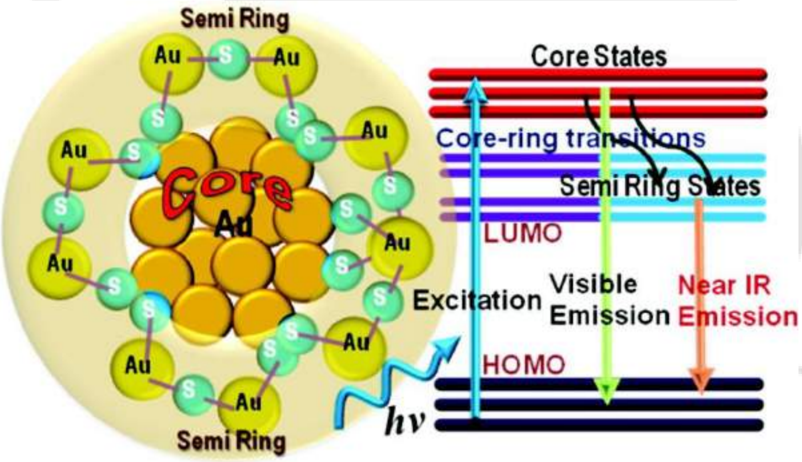

Figure 1.4. Cartoon diagram depicting the origin of luminescence from the gold core and semi-ring states along with the relaxation pathways in $Au_{25}L_{18}$ clusters. [Reprinted with permission from **reference 50**. Copyright 2010 American Chemical Society]

Additionally, the type of solvent used also affects the optical properties of NCs. Other route to obtain highly stable Au NCs involves the ligand induced chemical etching of metallic NPs. For example, Au NPs prepared from THPC as a capping and reducing agent was used to prepare Au NCs using thiol ligands like 11-

mercaptoundecanoic acid (11-MUA) as an etching agent under alkaline conditions.[51] Biomolecules like protein, peptides, DNA, RNA have also been used as scaffold for the nucleation and growth of Au NCs. This is a process similar to bio-mineralization[52] undergone by organisms in nature where biomolecule scaffold entraps the Au ions via complexation linkage, which then provides a nucleation site for the further growth of Au NCs under the scaffold. For example, BSA-Au_{25} NCs synthesized at pH 12 under physiological condition serves as an important example of biomimetic synthesis of NCs using BSA as the protein scaffold.[53] Thus these differently functionalised AuNCs being biocompatible in nature with interesting luminescence property finds real time application as sensors, bio-imaging agents and in light emitting devices.[4,47,54]

1.2.2.b. Copper Nanoclusters (CuNCs)

Despite copper being the earth abundant, inexpensive and biologically important metal, research focussed on the synthesis and application of Cu NCs is still in its infancy due to its inherent tendency towards oxidation. Synthesis of stable Cu NCs involves chemical technique with template and stabilizer (ligand), electrochemical and etching method alike AuNCs. However, judicious selection of surface ligands is the key to obtain stable and highly luminescent CuNCs and to further protect them from inherent oxidation. Crooks's group in 1998, reported the synthesis of CuNCs in the interior of poly (amidoamine) (PAMAM) starburst dendrimers.[55] Long term stability in terms of photoluminescence can be imparted to CuNCs when synthesized in presence of biomolecules like proteins, peptides, DNA etc.[56,57]

Additionally, small thiol containing ligands are also known to impart good stability to the cluster core in addition to their rich roles behind the origin of luminescence in CuNCs.[58] Ghosh et al. synthesized dihydrolipoic acid stabilized Cu NCs in the presence of PVP using a two-step reduction approach under ambient conditions.[59] Further, Goswami and co-workers reported the synthesis of Cu NCs in the presence of bovine serum albumin (BSA) as both the template and reducing agent.[60] The emission mechanism in CuNCs is however, the same as discussed in case of Au NCs in the previous section. Therefore, a wide variety of CuNCs with core atoms (n) ranging from 2-13 using thiolated and other functional ligands involving amines, carboxylic group etc. have been reported that provide stability under ambient conditions.[61] Therefore, owing to the synthetic advances, molecular like properties, strong luminescence extending to NIR region, photostability and small size, CuNCs have been considered for several applications such as chemical sensors, light emitting devices, bio-imaging and therapeutic potential too.[58,59,62]

1.3. Higher Ordered Assembly of Nanoscale Metal Particles

Though the scientific interests at the beginning was focussed at tailoring and tuning the size and shape of nanoscale particles via various synthetic strategies and functionalization techniques, the present day interests have changed the emphasis with the imagination to design and generate higher ordered architectures of nanoscale particles with superior properties. Judicious assimilation of as synthesized 0D nanoscale particles with different functionalities and properties allow one to obtain assembled structures of higher order architectures based on which they can be classified into categories of – 1D, 2D and 3D nanostructures as depicted in **Figure 1.5** below.

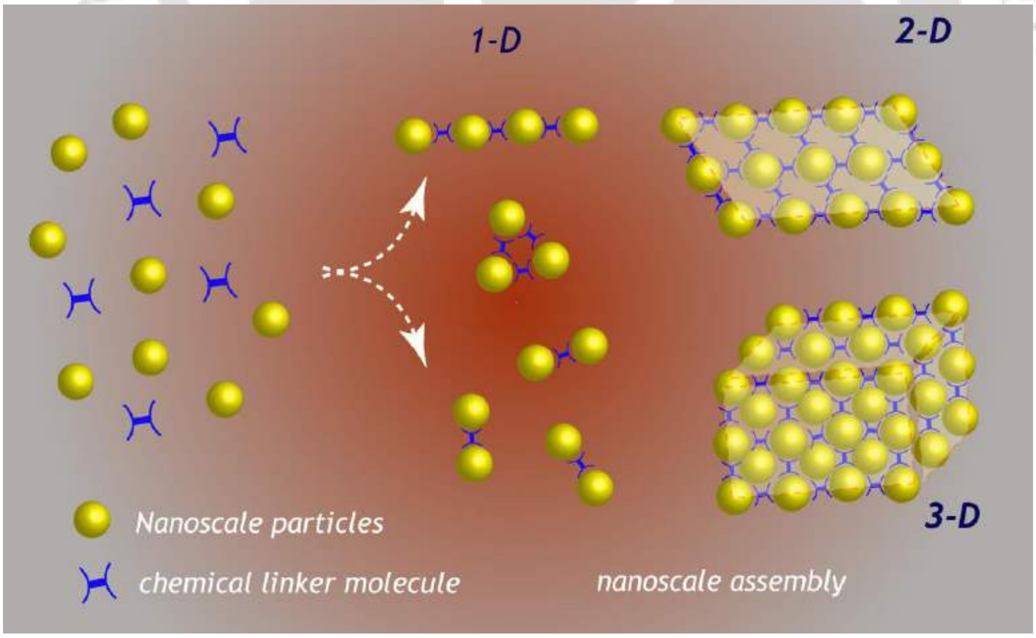

Figure 1.5. Schematic depiction of organizations of 0D nanoscale particles into 1D-, 2D- and 3D- nanostructures.

Ensemble of nanoscale particles exhibits newer collective properties, which in addition to improved mechanical properties also exhibits superior optical, electronic and magnetic properties.[63] Thus self-assembled structures of NPs and NCs therefore, provide us with much cost effective fabrication strategy for many useful nanodevices, including sensors, photonic circuits, optoelectronic devices in addition to their applicability in biology (as drug delivery vehicle, bio-sensors, bio-imaging agent, theranostics etc.) and other fundamental scientific studies.[63-65]

1.3.1. Methods to Design Higher Ordered Assembled Nanostructures

Self-assembly involves organization at the nanoscale with desired number of particles of specific orientation and dimension and therefore has been a challenge and also of great significance to the scientific community. The organization of structures being characterized by a minimum in the system's free energy.[66] Therefore, several methods to obtain assembled nanostructures have been discussed below:

1.3.1.a. Self-assembly in Solution

From physical force point of view, assembly in solution is governed by the balance of attractive and repulsive forces. Attractive forces involved in self-organization process are electrostatic attraction between oppositely charged ligands, covalent or hydrogen bonding, depletion forces or dipole–dipole interactions which are balanced by repulsive forces like steric forces and electrostatic repulsion between ligands of like charges.[63] For example, side-by-side or end-by-end assembly of Au nanorods can be driven by initiating attraction between the different ligands attached to the long and short facets of the Au nanorods.[67] Gryzbowski et al. presented a classic example of electrostatic interaction induced assembly where oppositely charged AuNPs and AgNPs interact with each other leading to the formation of diamond like crystal. The crystallization of particles being mediated by screened electrostatic interaction allowing the particles to react through short-range electrostatic potential.[68]

1.3.1.b. Directed Assembly

It involves assembly process induced by molecular interaction aided using directing agents, template, external field etc.

(i) Directing Agent induced Assembly. From chemical point of view, self-assembly of nanoscale particles in different dimensions can be induced by manipulating the surface ligand coverage with molecular linkers,[69] synthetic ligands,[70] metal ions,[71] polymers,[72] DNA,[73] biomolecules[74] as binders. Mirkin and co-workers reported the 3D crystallisation of AuNPs into micrometer sized face-centred-cubic or body-centred-cubic crystal structures via hybridisation of complementary DNA strand attached to the NP surface. It was observed that different DNA sequences guided the assembly of the same AuNP into different crystalline states.[73] Further, rationally designed peptides have also been used to direct the synthesis and assembly of AuNPs into 1D-NP superstructures of various morphologies.[75] Cooper et al. carried out step-wise growth of 15 nm Au NPs from metallic monomer to dimer to polymeric 1D-NP chain structure using alkanedithiol as linker moiety.[76]

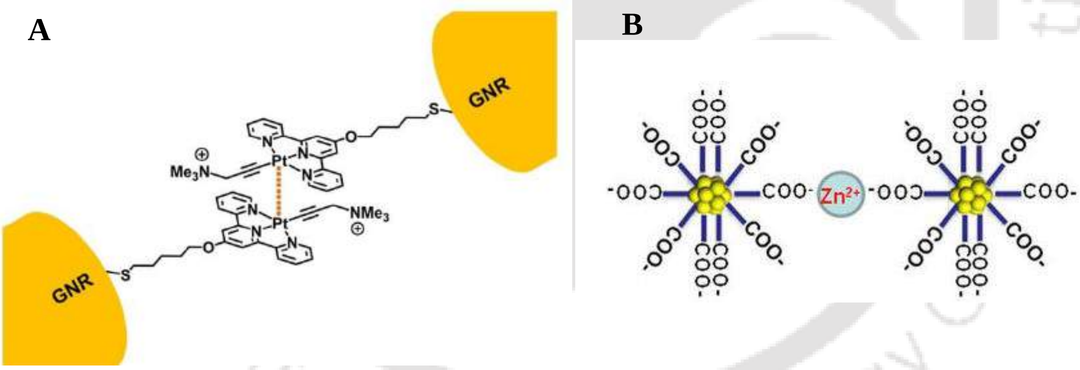

Figure 1.6. Schematic diagram of the proposed (**A**) end-to-end assembly of GNRs induced by Pt···Pt and π−π stacking interactions and (**B**) Zn^{2+} induced assembly of AuNCs. [**A**. Reprinted with permission from **reference 77** – "open access article published under an ACS Author Choice." Copyright 2016 American Chemical Society; **B**. Reprinted from **reference 71**. Copyright 2014 Nature Publishing Group]

A recent report by Yam et al. demonstrated the end-to-end assembly of gold nanorods (GNRs) functionalised by thioacetate containing alkylnylplatinum(II) terpyridine complex *via* Pt···Pt and π···π interaction.[77] (**Figure 1.6.A**) In another report, a facile approach to assemble fluorescent AuNCs have been demonstrated where negatively charged NCs underwent electrostatic interaction with divalent zinc ions selectively to assemble into fractal like spherical aggregates (**Figure 1.6.B**) with high order regularity.[71] Other methods include external stimuli to control the interaction of colloidal NPs. Common stimuli in this respect include pH, redox behaviour, solvent polarity etc. An ethanol induced assembly of 3-5 nm AuNPs is reported where the assembly is induced by altering the charge on AuNPs with the change in polarity of solvent. Addition of ethanol decreased the charges on AuNPs, triggering the dipole-dipole or van der Waals' interactions between the NPs to induce self-assembly and fusion forming nanowires of NPs.[78] In a report by Zhong and co-workers, the effect of pH on the behaviour of hydrogen bond guided glutathione-AuNP assembly was demonstrated. That is to say, low pH assisted the H-bonded assembly of glutathione Au NP dispersion whereas, increasing the pH of the dispersion lead to disruption of H-bond mediated assembly.[79]

(ii) **Templated Assembly.** It involves prefabricated nanostructures (1D, 2D or 3D) to guide the organization and deposition of nanoscale particles in well-ordered manner. A variety of substrate such as viruses, DNA, microstructures (like carbon nano tube, CNT or nanowires, NW) or block copolymers can serve as template in NP ensemble. Based on their classification, hard template like CNTs, NWs although provide solid structural support however, they fail to provide long range uniform spatial distribution. On the contrary, soft templates like small linker molecule, DNA, proteins, viruses etc. possess specific reactive sites with affinity toward certain particles, resulting in periodical arrangement of particles and eventual formation of hierarchical structures.[63]

For example, DNA scaffolds allow controlled organization of NPs of Au and Ag on their surfaces.[80,81] Mann et al. has demonstrated the utility of tobacco mosaic virus as template to synthesis and generate 1D assembly of the AuNPs.[82] Recently, Nann and co-workers have demonstrated a strategy to obtain controlled NP dimerization using a solid support of silica NP. The strategy involves a two-step approach via monofunctionalization of individual NP with terpy-amine ligand molecules on a solid support, followed by release of monofunctionalized particles and subsequent dimerization of AuNPs via co-ordination complexation.[83] Shang et al reported the synthesis of AuNC embedded peptide nanofibers via supramolecular self-assembly technique where the self-assembling peptides acted as a novel bioinspired scaffold.[57]

Another elegant example of templated assembly that needs mention is the modular approach adopted by Gwinn and co-workers to generate atomically precise arrays of AgNCs. Here, array of fluorescent DNA-stabilized AgNCs were obtained on a prototypical scaffold – a DNA nanotube – where the assembly process is mediated by designed DNA linkers that precisely locate the individual cluster on the nanotube surface and reserve its structure and purity following assembly.[84]

(iii) Assisted Assembly. The assembly process here is directed by external electric field, magnetic field, light, temperature or shear forces. For example, magnetic and metal NPs when placed under the influence of magnetic field undergo orientation in a homogeneous fashion to form 1D assembly (chains) or 3D superlattice.[85] 1D chain like assembly of Au NPs was generated from its aqueous dispersion under an a.c. field of 95–96 V cm^{-1}. The applied electric field induced polarization of NPs, where adjacent NPs interacted through dipole–dipole attractive force to form chains aligned parallel to the field lines.[86]

Further, Klajn and co-workers reported the light driven assembly of Fe_3O_4 NPs, stabilized with azobenzene-terminated catechol anchors. When the NPs were dissolved in solvents of low dielectric constant (e.g., toluene), the NPs underwent UV-induced azobenzene *trans* to *cis* isomerization where attractive electric dipole interactions between particles caused their rapid self-assembly into much larger aggregates.[87] Further, Yang and co-workers carried out the self-assembly of CuNCs into ribbon like structure by annealing CuNCs dispersion at 128 °C for 3 h. The annealing treatment facilitated the dynamic mobility of 1-dodecanethiol (DT) alkyl chain stabilizing the NCs, thus permitting the two-dimensional oriented self-assembly of NCs via dipole-induced asymmetric van der Waals attraction.[88]

1.3.1.c. Oriented Assembly

This is regarded as an assembly process where the strength of the driving forces is guided by interatomic bonding attraction of same crystal facets unlike van der Waals attractions and entropic factors being prevalent in other self-assembly process of colloidal NPs.[89] Lin et al, investigated the crystal growth kinetics of surfactant-free nanocrystalline SnO_2 in distilled water at 175–250 °C via multi-step OA mechanism.[90]

Further, ultrafine single-crystalline Au nanowire arrays have been synthesized via oriented attachment in solution phase. It was demonstrated that the growth of nanowire attachment was obtained such that two individual NP {111} facets fuse together to form a single particle.[91] Vanmaekelbergh and his group studied the formation of 1D and 2D superlattices via oriented attachment of PbSe nanocrystals in a thin film of a suspension casted on an immiscible liquid. Their findings suggested that by varying the concentration of PbSe and temperature, 1D and 2D superlattice (with square or honey-comb) periodicity can be obtained.[92]

1.3.2. Characteristic Features of Higher Ordered Assembled Nanostructures

Like nanoscale particles exhibit properties that differ from their bulk as well as atomic counterparts, ensemble of nanoscale particles also possess collective properties that would differ from the properties of their individual nanoscale particle and hence corresponding bulk.[63] Thus current interest in studying the ensemble of particles is driven by the superior functional properties that arise in the higher order assembled nanostructures as a result of the interaction between surface plasmons, excitons, plasmon-exciton or coherent state of the collections of individual NPs.

1.3.2.a Plasmon-Plasmon Coupling

An exciting feature of surface plasmons is that they can be coupled. When discrete plasmonic particles (two or more) are placed sufficiently close to each other, near-field coupling of the surface plasmons can lead to the generation of new surface plasmon resonance.[93]

Depending upon the polarization of incident light with respect to the symmetry of plasmon ensemble, the restoring force acting on the oscillating electrons of each particle undergo increase or decrease based on the charge polarization of the electrons in the ensemble and hence leading to red or blue shift of the extinction wavelength. For example, the near-field interactions between spherical NPs assembled in chains leads to red shift of the longitudinal band and blue shift of the transverse band.[63] Therefore, when gold NPs aggregate, the color of the solution changes from red to purple, which becomes apparent with concomitant red shift of SPR band.[94] In a study carried out by Capasso and co-workers, a hierarchy of tunable plasmonic structures made of self-assembled clusters of metal-dielectric spheres have been displayed where the plasmon modes exhibited strong electric, magnetic and Fano-like resonances depending upon the number and position of spheres in close-packed plasmonic clusters.[95] The "plasmon hybridization model" further allows us to gain better understanding of the plasmon coupling phenomenon.[96]

Additionally, plasmon coupling results in strong confinement of electromagnetic field at the hot-junction (or interparticle junction) of the coupled plasmons often referred to as "hot spots".[3,8] Plasmonic NPs are known to enhance spectroscopic signals of many molecules (that otherwise show very weak Raman scattering, say, for example). Therefore, the hot spot generation and the areas of concentrated electric field that arise in plasmonic ensemble may prove to be highly advantageous for many surface-enhanced spectroscopic studies like Raman,[40,97] infrared,[98] fluorescence[99] and tip-enhanced spectroscopic studies.[100]

To be precise, major issues that is of concern in SERS based studies are – (i) attainment of uniform spacing or control over the distance between the plasmons and (ii) precise location of the signature molecule at the hot-spot over surface, which induce several orders of magnitude increment of Raman signal.[69] Hence, rational design of plasmonic nanostructures to exploit the properties associated with coupled plasmons is highly desirable for their application in single molecule spectroscopy studies, in vivo cancer imaging, detection etc.[101-103]

1.3.2.b. Exciton Coupling

One of the important features observed in the ensemble of inorganic fluorophore (metal nanoclusters and semiconductor NPs) is that they undergo strong excited state electronic coupling. Electronic coupling affects the energy levels in the ground and excited state and strongly alters the quantum confinement effect.[104]

Excitonic coupling generally occurs through two mechanisms: electron exchange transfer (or Dexter transfer) and resonance energy transfer (Forster resonance energy transfer, FRET).[63] Electron exchange transfer requires an overlap of the wave functions of the inorganic fluorophores and is typically observed for small particles separated by short (<2 nm) distance. Electronic coupling therefore, generally leads to redshift in absorption and photoluminescence emission bands of inorganic fluorophore and the extent of coupling rapidly decreases with increasing size of the particle.[105] On the contrary, excitonic coupling through Förster resonance energy transfer occurs for particles separated by distance of approximately 2 nm and within 10 nm, resulting from interaction of transition dipoles of excited and ground states.[106] Meijerink et al, reported both exciton energy transfer and electronic coupling in molecular-like aggregates of CdTe quantum dots where the coupling energy (i.e., red-shifted emission peak) decreased from 40 to 0 meV when the size of the individual quantum dots was increased from 0.4 to 5.1 nm.[105]

Mtric and co-workers have recently demonstrated the design of 2D-AgNC array on porphyrin template that exhibited exciting optical properties due to excitonic coupling between Ag_3^+ cluster cores. Density functional theory calculations showed that metal cluster core undergoes J- and H- type excitonic coupling in the AgNC array resulting in controllable splitting of their excited states, which could serve as an efficient system for light–induced exciton transport.[107] Additionally, FRET based energy transfer can take place between same particles of different size due to size-dependent differences in the band-gap in semiconductor NP aggregates.[108]

Additionally, assembly in metal NCs with intriguing molecular-like properties often results in aggregation induced emission or enhancement (AIE or AIEE) phenomenon.[109] For example, gold NCs embedded peptide nanofibers resulted in the emission enhancement by 70-fold upon undergoing supramolecular self-assembly in solution.[57] Also, ZnS NPs upon aggregation showed an increase in band-edge PL emission.[110] The aggregation in NCs is capable of altering the ligand-

ligand, ligand-metal and metal-metal interactions.[88,111-112] Aggregation induced excitonic coupling affects the excited state relaxation dynamics due to restriction in intramolecular vibration and rotation of ligands. This results in the increased rate of radiative energy transfer by suppressing ligand-based nonradiative relaxation of excited states, which accounts for the origin or enhancement of luminescence.[88,111,113] Two major approaches for NC luminescence enhancement are solvent- and cation-induced aggregations.[71,114] Wang and co-workers reported highly stable CuNCs that exhibited intense red PL via AIE at pH 2.6, which however, existed as non-emissive isolated species when the pH of the dispersion was changed to 7.[62] Additionally, chiral gold clusters with strong circular dichroism (CD) but free of circularly polarized luminescence (CPL) when self-assembled and organized into uniform body-centered cubic (BCC) packed nanocubes, exhibits significantly enhanced CD intensity with remarkable CPL response.[115]

1.3.2.c. Plasmon–Exciton Coupling

Coupling between plasmons and excitons in a hybrid assembled structures comprising of metal NPs - metal NCs, semiconductors or chromophores leads to exciting phenomenon such as energy transfer,[116] surfaced enhanced emission,[117] emission quenching,[118] PL wavelength shift,[119] Fano resonance[120] etc. Photoluminescence enhancement originates from the amplification of the electromagnetic field induced by the plasmon resonance of metal NPs in the vicinity of excitonic particles, whereas quenching results from energy transfer from excitonic particles to plasmonic particles.[121]

However, plasmon-exciton interaction depends exclusively on the spatial orientation of plasmonic particles with respect to the excitonic particles (viz. QDs, NCs, chromophores), size,[105] shape[119] and distance between them.[117] Excitonic particles within ~5 nm of the surface of the metal NPs undergo their fluorescence quenching while particles at distances of ~10 nm or greater undergo surface enhanced fluorescence that may reach up to 100-fold. The excitonic particles within a distance of 5 nm of the surface can interact electronically with the surface plasmons to donate the excited electrons to the metal, thus quenching the fluorescence by non-radiative pathways available in the metal NPs.[3,122]

Halas and co-workers carried out a systematic study to compare and understand the electromagnetic coupling between indocyanine green (ICG) and Au NPs and nanoshells of different radii. Interestingly, a dramatic enhancement of molecular fluorescence by a factor of 50 was observed for the $[r_1, r_2]=[112,123]$ nm nanoshell, whose plasmon resonance overlaps with the ICG emission wavelength.[99] However, in a study of interaction between AuNCs and AgNPs, pronounced quenching in the emission of AuNCs was observed due to surface energy transfer assisted by surface plasmon resonance, which arises due to dipole–surface interaction between molecular clusters and NPs.[123] In another study, involving interaction between CdTe nanowires surrounded with AuNPs, huge enhancement of photoluminescence of CdTe was witnessed due to increase in emission of photons which was stimulated by a strong electromagnetic field generated by the AuNPs.[124]

1.4. Reaction Kinetics and Dynamics of Higher Ordered Assembly of Nanoscale Metal Particles

Understanding the mechanism of formation of nanoscale metal particles starting from atomic scale through various intermediate stage is important to have better control over their size and hence properties. Similarly, studying kinetic of reaction of nanoscale metal particles towards ensemble formation and hence understanding their dynamics allows us to gain insight of their assembly mechanism and hence stability in a system as a whole for rational utilisation in various applications.

With NPs of Au/Ag and their aggregates finding application as transport materials in natural environment, biomedical field etc.[125,126] colloidal stability of the same in natural environment and in solution of variable ionic strength is also important. The influence of solution chemistry on the aggregation kinetics of unmodified AgNPs was investigated by Li et al. where a critical coagulation concentration (CCCs) of the NP reaction was obtained through time-resolved dynamic light scattering (DLS).[127] In another report by Chen et al. the influence of NaCl, $MgCl_2$ and $CaCl_2$ on the colloidal stability and aggregation kinetics of AgNPs was delineated.[128] Further, Chen et al. adopted a single molecule approach for studying quantitative kinetics of nanoparticle catalysis with real-time monitoring of single-turnover resolution.[129]

As coupling of surface plasmons results in shift of SPR wavelength, therefore, Alivisatos and co-workers utilised this principle - as "plasmonic rulers" to follow the directed assembly of Au and Ag NPs dimers in real time and studied the kinetics of single hybridization events.[130] A significant blue-shift in absorption spectrum was observed upon addition of complementary DNA to an Au pair connected with single stranded DNA. Further, the plasmon rulers were also used to study dynamics of biophysical processes – i.e., bending and cleavage of DNA by the restriction enzyme EcoRV using ensemble kinetic measurements etc. which are important for biotechnology and nanoscience applications.[131]

Pelton et al. demonstrated a solvent mediated end-to-end assembly of Au nanorods by monitoring the assembly kinetics of the assembly process at different solvent composition and concentration of three different thiol ligands – undecanethiol, 11-mecpatoundecanoic acid and α, ω-undecanethiol to elucidate the mechanism responsible for assembly and optimize condition necessary to obtain desired product.[132] Aggregation rate study of neurological proteins is of importance for understanding the progress of many disease like Alzeimer's, disease, type II diabetes, Parkinson's disease (PDs) etc. Amyloid aggregates of α-synuclein (AS) in dopaminergic neurons of the brain are the hallmarks of PD. Therefore, understanding the mechanism of amyloid aggregation using various methodology and reagent that may provide control over the aggregation kinetics is essential. Stefani and co-workers have employed citrate capped AuNPs to investigate their effect on aggregation kinetics of AS using a fluorescent probe.[133] They found that gold NPs had a pronounced effect in accelerating protein aggregation with kinetic rate three-fold higher at concentration as low as 20 nM for NPs with 10 nm diameter. In another study, Giorgio et al. studied the kinetics of molecular recognition mediated NP assembly involving Ab conjugated QD with angiopoietin-2 antigen.[134] Such understanding of the aggregation kinetics and molecular mechanisms of interactions will be particularly important in developing the sensitivity and specificity of diagnostic methods in biomedical field.

1.5. Importance and Potential Applications of Higher Ordered Assembled Nanostructures

This section describes the various techniques that exploit the unique properties of NPs, NCs and the their higher order self-assembled nanostructures for utilization in the field of photocatalysis, sensing, bio-imaging, surface enhanced spectroscopy, drug delivery, cancer detection, optoelectronic devices, photonic crystals etc.[4,17,39,126,135-140]

AuNPs in general are sensitive to selective metal ions, anions, peptides, specific biomolecules etc. to undergo aggregation resulting in significant red-shift or broadening in the SP band accompanied by change in the solution color from red to blue. This phenomenon makes AuNP an attractive candidate as colorimetric sensors.[17] Geddes et al. have demonstrated a colorimetric glucose sensing assay via the dissociation of Con A-aggregated dextran coated AuNPs. The Con A cross-links the dextran coated AuNPs, which results in concomitant blue-shift in SPR. The addition of glucose diminishes the Con A-AuNP interaction releasing the individual dextran-coated AuNPs.[141-142] Kim and co-workers on the other hand, designed a pH sensitive surface ligand, which can switch its charge from negative to positive under acidic environment.[143] Further, they decorated as synthesized AuNPs with the pH sensitive ligand that responded to cellular acidic environment to undergo aggregation along with shift in the plasmon band to longer wavelength. The hence-formed Au plasmon aggregates with absorption in the NIR range was then utilised for photo thermal cancer therapy. Ensembles of NPs and NCs have also been used as platform for catalysis, nanoscale thermometers, pH sensors, as 'plasmon rulers' and as bio- and chemical sensors for disease or analyte detection.[57,62,99,144-146]

One of the striking features of plasmonic particles and their assemblies is that they support SERS. Assembled plasmonic structures can exhibit up to ten-fold enhancement in Raman scattering signal due to enhanced electromagnetic field at the hot-junction as compared to individual plasmonic particles.[147,148] Literature is therefore replete with engineered self-assembled plasmonic nanostructures for SERS based molecule and cancer bio-marker detection,[149] bio-imaging,[150] label free monitoring of catalysis[151] and single molecule studies.[152]

A self-assembled structure of NPs also serves as sensitive electrochemical biosensors.[153] Assembled NPs deposited on electrodes tends to increase the surface area of the electrode by generating a porous surface and also provided an intimate contact with redox analyte owing to the nanoscale curvature of nanoparticles thereby serving as an efficient bridge for the electron transfer between redox analyte and the surface of the electrode.[63] The electronic coupling between NPs in 3D-assemblies cross linked with organic matrix is highly sensitive to external chemical functionality. This property therefore opens up new possibilities of 3D assemblies of NPs to be used as chemiresistor type sensing application.[145] Also, 3D semiconductor NP assemblies possess unique electrical properties which make them attractive for the fabrication of photoconductive photodetectors.[154] Additionally, DNA directed assembly of NPs enables unprecedented control over the intrinsic photonic crystal property like – lattice parameter, crystal symmetry etc. by taking advantage of the programmability of DNA base pairing and hence finds utility in photonic research like metamaterials, quantum optics etc.[155] Self-assembled structures of metal NPs and NCs have also been proven to be excellent multifunctional carriers for delivery of drugs, sensors for cancer detection and superior one/two photon imaging agent.[126,156-158]

One of most striking features of NCs is the emergence of their strong tunable photoluminescence which makes them suitable for applications such as the color conversion layer for fabricating light-emitting devices (LEDs). For example, a WLED prototype with color coordinate at (0.32, 0.36) is fabricated by combining CuNC ribbons (blue-green), CuNC sheets (yellow), and AuNCs sheets (red) with the feed ratio of 1.2/1/ 1.5, which is the first of its kind that employs metal NCs to produce WLEDs.[87] Additionally, the unique AIE/AIEE property exhibited by Au NCs and Cu NCs makes them suitable for the design of various optoelectronic devices,[159] pH sensing[62] and fluorescent thermometers.[57] Further assembly of Au NCs stabilised with appropriate ligands supports modulation of electron transport by sorption of vapors with exceptional selectivity and sensitivity making it suitable for chemiresistor sensing.[146] On the other hand, metal mediated crystalline assembly of AuNCs have also been explored for hydrogen storage and sensing application.[160]

1.6. Objective of the Thesis

The current state of the art development of colloidal nanoscale metal particles and the scientific interest in the manipulation of the same at the nanoscale to design and fabricate assembled nanostructures are vast. However, there is plenty of room to explore newer techniques to pursue the field of nanoscale assembly for their utilisation as advanced nanomaterials. The present thesis initiates a step forward to design and explore newer techniques to generate advanced nanomaterials and understanding their reaction pathway for their utilization in the field ranging from spectroscopy to biology.

The salient features of the current issues concerning the present thesis are as follows:

- ***How do nanoscale metal particles react? Studying the reaction pathway and kinetics of nanoscale particles, employing Au NPs and NCs of Cu?***
- ***Can we achieve control over the reaction of these nanoscale particles in terms of dimers, trimers and higher order nanostructures?***
- ***How do pre-designed molecules, inorganic metal ions and their complexes allow us to achieve higher nanostructures of NPs and NCs and what advantageous physicochemical properties are induced therein?***
- ***How will the new collective properties – induced thereby in the higher ordered nanostructures – be utilised for their application in biology or spectroscopy study?***

Therefore, we have attempted to address the above issues through the experiments carried out and hence their results in the following chapter of the thesis.

1.7. References

1. Barber, D. J.; Freestone, I. C. *Archaeometry* **1990**, *32*, 33.
2. Díez, I.; Ras, R. Advanced Fluorescence Reporters in Chemistry and Biology II, *Springer*, **2010**, 307.
3. Eustis, S.; El-Sayed, M. A. *Chem. Soc. Rev.* **2006**, *35*, 209.
4. Zhang, L.; Wanga, E. *Nano Today* **2014**, *9*, 132.
5. Ghosh, S. K.; Pal, T. *Chemical Reviews* **2007**, *107*, 4797.
6. Volokitin,Y.; Sinzig, J.; de Jongh, L. J.; Schmid, G.; Vargaftik, M. N.; Moiseev, I. I. *Nature* **1996**, *384*, 621.
7. Kysylychyn, D.; Piatnytsia, V.; Lozovski, V. *Phys. Rev. E* **2013**, *88*, 052403.
8. Jones, M. R.; Osberg, K. D.; Macfarlane, R. J.; Langille, M. R.; Mirkin, C. A. *Chem. Rev.* **2011**, *111*, 3736.
9. Barnes, W. L.; Dereux, A.; Ebbesen, T. W. *Nature* **2003**, *424*, 824.
10. Maier, S. A. Plasmonics: Fundamentals and Applications; *Springer*: New York, **2007**.
11. Noguez, C. *J. Phys. Chem. C.* **2007**, *111,* 3806.
12. Link, S.; El-Sayed, M. A. *J. Phys. Chem. B* **1999**, *103*, 8410.
13. Campion, A.; Kambhampati, P. *Chem. Soc. Rev*. **1998**, *27*, 241.
14. Merlen, A.; Lagugne´-Labarthet, F.; Harte, E. *J. Phys. Chem. C* **2010**, *114,* 12878.
15. Lakowicz, J. R.; Geddes, C. D.; Gryczynski, I.; Malicka, J.; Gryczynski, Z.; Aslan, K.; Lukomska, J.; Matveeva, E.; Zhang, J.; Ramachandram, B.; Huang, J. *Journal of Fluorescence* **2004**, *14*, 425.
16. Quinn, B. M.; Liljeroth, P.; Ruiz, V.; Laaksonen, T.; Kontturi, K. *J. Am. Chem. Soc.* **2003**, *125*, 6644.
17. Saha, K.; Agasti, S. S.; Kim, C.; Li, X.; Rotello, V. M. *Chem. Rev*. **2012**, *112*, 2739.
18. Faraday, M. *Phil. Trans. Roy. Soc. London* **1857**,*147*, 145.
19. Mie, G. *Ann. Phys.* **1908**, *25*, 377.
20. Turkevich, J.; Stevenson, P. C.; Hillier, J. *Discuss. Faraday Soc*. **1951**, *11*, 55.
21. Giersig, M.; Mulvaney, P. *Langmuir* **1993**, *9*, 3408.
22. Brust, M.; Walker, M.; Bethell, D.; Schiffrin, D. J.; Whyman, R. *J. Chem. Soc., Chem. Commun*. **1994**, 801.
23. Cappellari, P. S.; Buceta, D.; Morales, G. M.; Barbero, C. A.; Moreno, M. S.; Giovanetti, L. J.; Ramallo-López, J. M.; Requejo, F. G.; Craievich, A. F.; Planes, G. A. *J. Colloid Interface Sci*. **2015**, *441*, 17.

24. Shelley, E. J.; Ryan, D.; Johnson, S. R.; Couillard, M.; Fitzmaurice, D.; Nellist, P. D.; Chen, Y.; Palmer, R. E.; Preece, J. A. *Langmuir* **2002**, *18*, 1791.

25. Leff, D. V.; Brandt, L.; Heath, J. R. *Langmuir* **1996**, *12*, 4723.

26. Chen, S.; Liu, Y.; Wu, G. *Nanotechnology* **2005**, *16*, 2360.

27. Weare, W. W.; Reed, S. M.; Warner, M. G.; Hutchison, J. E. *J. Am. Chem. Soc*. **2000**, *122*, 12890.

28. Sarkar, A.; Shukla, S. P.; Adhikari, S.; Mukherjee, T. *Int. J. Nano. Technol* **2010**, *7*, 1027.

29. Wang, W. X.; Chen, Q. F.; Jiang, C.; Yang, D. Z.; Liu, X. M.; Xu, S. K. *Colloid. Surface. A*. **2007**, *301*, 73.

30. Bhargava, S. K.; Booth, J. M.; Agrawal, S.; Coloe, P.; Kar, G. *Langmuir* **2005**, *21*, 5949.

31. Selvakannan, P.; Mandal, S.; Phadtare, S.; Gole, A.; Pasricha, R.; Adyanthaya, S. D.; Sastry, M. *J. Colloid Interface Sci*. **2004**, *269*, 97.

32. Housni, A.; Ahmed, M.; Liu, S.; Narain, R. *J. Phys. Chem. C*. **2008**, *112*, 12282.

33. Sirajuddin; Mechler, A.; Torriero, A. A. J.; Nafady, A.; Lee, C. Y.; Bond, A. M.; O' Mullane, A. P.; Bhargava, S. K. *Colloids Surf. A* **2010**, *370*, 35.

34. Tao, A. R.; Habas, S.; Yang, P. D. *Small* **2008**, *4*, 310.

35. Prasad, B. L. V.; Stoeva, S. I.; Sorensen, C. M.; Klabunde, K. J. *Langmuir* **2002**, *18*, 7515.

36. Maye, M. M.; Zheng, W. X.; Leibowitz, F. L.; Ly, N. K.; Zhong, C. J. *Langmuir* **2000**, *16*, 490.

37. Xia, Y.; Halas, N. J. *MRS Bull.* **2005**, *30*, 338.

38. Jain, P. K.; Huang, X.; El-Sayed, I. H.; El-Sayed, M. A. *Acc .Chem. Res*. **2008**, *41*, 1578.

39. Yang, X.; Yang, M.; Pang, B.; Vara, M.; Xia, Y. *Chem. Rev.* **2015**, *115*, 10410.

40. Wang X.; Li, Maohua.; Meng, L.; Lin, K.; Feng, J.; Huang, T.; Yang, Z.; Ren, B. *ACS Nano*, **2014**, *8*, 528.

41. Aslan, K.; Lakowicz, J. R.; Geddes, C. D. *Anal. Biochem*. **200**4, *330*, 145.

42. Zhao, J.; Nguyen, S. C.; Ye, R.; Ye, B.; Weller, H.; Somorjai, G. A.; Alivisatos, A. P.; Toste, F. D. *ACS Cent. Sci.* **2017**, *3*, 482.

43. Khandelia, R.; Jaiswal, A.; Ghosh, S. S.; Chattopadhyay, A. *J. Mater. Chem. B* **2014**, *2*, 6472.

44. Zheng, J.; Zhou, C.; Yu, M.; Liu, J. *Nanoscale*, **2012**, *4*, 4073.

45. Wilcoxon, J. P.; Abrams, B. L. *Chem. Soc. Rev*. **2006**, *35*, 1162.

46. Link, S.; Beeby, A.; FitzGerald, S.; El-Sayed, M. A.; Schaaff, T. G.; Whetten, R. L. *J. Phys. Chem. B*, **2002**, *106*, 3410.

47. Chakraborty, I.; Pradeep, T. *Chem. Rev*. **2017**, *117*, 8208.

48. Markus, R.; Schwentner, N. Physics and Chemistry of Small Clusters; *Springer-Verlag*: Berlin, **1987**, 611.

49. Wu, Z.; Jin, R. *Nano Lett.* **2010,** *10*, 2568.

50. Devadas, M. S.; Kim, J.; Sinn, E.; Lee, D.; Goodson, T.; Ramakrishna, G. *J. Phys. Chem. C*, **2010**, *114*, 22417.

51. Huang, C.-C.; Liao, H.-Y.; Shiang, Y.-C.; Lin, Z.-H.; Yang, Z.; Chang, H.-T. *J. Mater. Chem*. **2009**, *19*, 755.

52. Addadi, L.; Joester, D.; Nudelman, F.; Weiner, S. *Chem. Eur. J*. **2006**, *12*, 980.

53. Xie, J.; Zheng, Y.; Ying, J. Y. *J. Am. Chem. Soc.* **2009**, *131*, 888.

54. Bhandari, S.; Pramanik, S.; Khandelia, R.; Chattopadhyay, A. *ACS Appl. Mater. Interfaces*, **2016**, *8*, 1600.

55. Zhao, M.; Sun, L.; Crooks, R. M. *J. Am. Chem. Soc*. **1998**, *120*, 4877.

56. Mohanty, J. S.; Baksi, A.; Leeb, H.; Pradeep, T. *RSC Adv.* **2015**, *5*, 48039.

57. Zhang, W.; Lin, D.; Wang, H.; Li, J.; Nienhaus, G. U.; Su, Z.; Wei, G.; Shang, Li.; *Bioconjugate Chem*. **2017**, *28*, 2224.

58. Wang, Z.; Chen, B.; Rogach, A. L. *Nanoscale Horiz.,* **2017**, *2*, 135**.**

59. Ghosh, R.; Goswami, U.; Ghosh, S. S.; Paul, A.; Chattopadhyay, A. *ACS Appl. Mater. Interfaces*, **2015**, *7*, 209.

60. Goswami, N.; Giri, A.; Bootharaju, M. S.; Xavier, P. L.; Pradeep, T.; Pal, S. K. *Anal. Chem*., **2011**, *83*, 9676.

61. Lu, Y. Z.; Wei, W. T.; Chen, W. *Chin. Sci. Bull.* **2012**, *57*, 41.

62. Jia, X.; Yang, X.; Li, J.; Li, D.; Wang, E. *Chem. Commun.* **2014**, *50*, 237.

63. Nie, Z.; Petukhova, A.; Kumacheva, E. *Nature Nanotech.***2010**, *5*, 15.

64. Stolarczyk, J. K.; Deak, A.; Brougham, D. F. *Adv. Mater*. **2016**, *28*, 5400.

65. Jin, R.; Zeng, C.; Zhou, M.; Chen, Y. *Chem. Rev.*, **2016**, *116*, 10346.

66. Grzelczak, M.; Vermant, J.; Furst, E. M.; Liz-Marza´n, L. M. *ACS Nano* **2010**, *4*, 3591.

67. Nie, Z. H. *et al. Nature Mater.* **2007**, *6***,** 609.

68. Kalsin, A. M.; Fialkowski, M.; Paszewski, M.; Smoukov, S. K.; Bishop, K. J. M.; Grzybowski, B. A. *Science*, **2006**, *312*, 420.

69. Chen H. Y.; Lin, M. H.; Wang, C. Y.; Chang, Y-M.; Gwo, S. *J. Am. Chem. Soc.* **2015**, *137*, 13698.

70. Fruhnert, M.; Kretschmer, F.; Geiss, R.; Perevyazko, I.; Dana, C. M.; Steinert, M.; Janunts, N.; Sivun, D.; Hoeppener, S.; Hager, M. D.; Pertsch, T.; Schubert, U. S.; Rockstuhl, C. *J. Phys. Chem. C* **2015**, *119*, 17809.

71. Yao, Q.; Luo, Z.; Yuan, X.; Yu, Y.; Zhang, C.; Xie, J.; Lee, J. Y. *Sci. Rep.* **2015**, *4*, 3848.

72. Gao, B.; Alvi, Y.; Li, V.; Tao, A. R. *CrystEngComm*, **2014**, *16*, 9434.

73. Park, S. Y.; Lytton-Jean, A. K. R.; Lee, B.; Weigand, S.; Schatz, G. C.; Mirkin, C. A. *Nature* **2008**, *451*, 553.

74. Mout, R.; Tonga, G. Y.; Wang, Li-S.; Ray, M.; Roy, T.; Rotello, V. M. *ACS Nano* **2017**, *11*, 3456.

75. Zhang, C.; Song, C.; Fry, H. C.; Rosi, N. L. *Chem. Eur. J.* **2014**, *20*, 941.

76. Hussain, I.; Brust, M.; Barauskas, J.; Cooper, A. I. *Langmuir* **2009,** *25,* 1934.

77. Leung, F. C-M.; Leung, S. Y-L.; Chung, C. Y-S.; Yam, V. W-W. *J. Am. Chem. Soc.* **2016**, *138*, 2989.

78. Xie, J.; Zhang, Q.; Lee, J. Y.; Wang, D. I. C. *J. Phys. Chem. C* **2007,** *111,* 17158.

79. Lim, I-I. S.; Mott, D.; Ip, W.; Njoki, P. N.; Pan, Y.; Zhou, S.; Zhong, C- J. *Langmuir* **2008,** *24,* 8857.

80. Warner, M. G.; Hutchison, J. E. *Nature Mater.* **2003**, *2*, 272.

81. Niemeyer, C. M.; Simon, U. *Eur. J. Inorg. Chem*. **2005**, 3641.

82. Dujardin, E.; Peet, C.; Stubbs, G.; Culver, J. N.; Mann, S. *Nano Lett*. **2003**, *3*, 413.

83. Dewi, M. R.; Gschneidtner, T. A.; Elmas, S.; Ranford, M.; Moth-Poulsen, K.; Nann, T. *ACS Nano* **2015**, *9*, 1434.

84. Copp, S. M.; Schultz, D. E.; Swasey, S.; Gwinn, E. G. *ACS Nano* **2015**, *9*, 2303.

85. Ahniyaz, A.; Sakamoto, Y.; Bergstrom, L. *Proc. Natl Acad. Sci. USA,* **2007**, *104,* 17570.

86. Velev, O. D.; Bhatt. K. H. *Soft Matter* **2006**, *2*, 738.

87. Das, S.; Ranjan, P.; Maiti, P. S.; Singh, G.; Leitus, G.; Klajn, R. *Adv. Mater*. **2013**, *25*, 422.

88. Wu, Z.; Liu, J.; Gao, Y.; Liu, H.; Li, T.; Zou, H.; Wang, Z.; Zhang, K.; Wang, Y.; Zhang, H.; Yang, B. *J. Am. Chem. Soc.* **2015**, *137*, 12906.

89. Nai, J.; Guan, B. Y.; Yu, L.; Lou, X. W. (David). *Sci. Adv*. **2017**, *3*, 1.

90. Zhuang, Z.; Zhang, J.; Huang, F.; Wang, Y.; Lin, Z. *Phys. Chem. Chem. Phys.* **2009**, *11*, 8516.

91. Halder, A.; Ravishankar, N. *Adv. Mater.* **2007**, *19*, 1854.

92. Evers, W. H.; Goris, B.; Bals, S.; Casavola, M.; de Graaf, J.; van Roij, R.; Dijkstra, M.; Vanmaekelbergh, D. *Nano Lett.* **2013**, *13*, 2317.

93. Hao, E.; Schatz, G. C. *J. Chem. Phys.* **2004**, *120*, 357.

94. Mirkin, C. A.; Letsinger, R. L.; Mucic, R. C.; Storhoff, J. J. *Nature* **199**6, *382*, 607.

95. Fan, J. A.; Wu, C.; Bao, K.; Bao, J.; Bardhan, R.; Halas, N. J.; Manoharan, V. N.; Nordlander, P.; Shvets, G.; Capasso, F. *Science* **2010**, *328,* 1135.

96. Koh, A. L.; Bao, K.; Khan, I.; Smith, W. E.; Kothleitner, G.; Nordlander, P.; Maier, S. A.; McComb, D. W. *ACS Nano* **2009**, *3* ,3015.

97. Talley, C. E.; Jackson, J. B.; Oubre, C.; Grady, N. K.; Hollars, C. W.; Lane, S. M.; Huser, T. R.; Nordlander, P.; Halas, N. J. *Nano Lett.* **2005**, *5*, 1569.

98. Dong, L.; Yang, X.; Zhang, C.; Cerjan, B.; Zhou, L.; Tseng, M. L.; Zhang, Y.; Alabastri, A.; Nordlander, P.; Halas, N. J. *Nano Lett.* **2017**, *17*, 5768.

99. Tam, F.; Goodrich, G. P.; Johnson, B. R.; Halas, N. J *Nano Lett.* **2007**, *7*, 496.

100. Zhang, Z.; Sheng, S.; Wang, R.; Sun, M. Tip-Enhanced Raman Spectroscopy. *Anal. Chem.* **2016**, *88*, 9328.

101. Zrimsek, A. B.; Chiang, N.; Mattei, M.; Zaleski, S.; McAnally, M. O.; Chapman, C. T.; Henry, A.-I.; Schatz, G. C.; Van Duyne, R. P. *Chem. Rev.*, **2017**, *117*, 83.

102. Radziuk, D.; Moehwald, H. *Phys.Chem.Chem.Phys.***2015**, *17*, 21072.

103. Abramczyk, H.; Brozek-Pluska, B. *Chem. Rev.* **2013**, *113*, 5766.

104. Kasha, M.; Rawls, H. R.; El-Bayoumi, M. A. *Pure Appl. Chem*. **1965**, *11*, 371.

105. Koole, R.; Liljeroth, P.; Donega, C. de M.; Vanmaekelbergh, D.; Meijerink, A. *J. Am. Chem. Soc.* **2006**, *128*, 10436.

106. Lee, J.; Govorov, A. O.; Kotov, N. A. *Nano Lett.* **2006**, *6*, 984.

107. Röhr, M. I. S.; Lisinetskaya, P. G.; Mitric, R. *J. Phys. Chem. A* **2016**, *120*, 4465.

108. Tang, Z.; Ozturk, B.; Wang, Y.; Kotov, N. A. *J. Phys. Chem. B* **2004**, *108,* 6927.

109. Goswami, N.; Yao, Q.; Luo, Z.; Li, J.; Chen, T.; Xie, J. *J. Phys. Chem. Lett.* **2016**, *7*, 962.

110. Jassby, D.; Wiesner, M. *Langmuir* **2011**, 27, 902.

111. Luo, Z.; Yuan, X.; Yu, Y.; Zhang, Q.; Leong, D. T.; Lee, J. Y.; Xie, J. *J. Am. Chem. Soc.* **2012**, *134*, 16662.

112. Yam, V. W.-W.; Lo, K. K.-W. *Chem. Soc. Rev.*, **1999**, *28*, 323.

113. Valeur, B. Molecular Fluorescence: Principles and Applications; *Wiley–VCH: Weinheim*, Germany, **2002**.

114. Shi, L.; Zhu, L.; Guo, J.; Zhang, L.; Shi, Y.; Zhang, Y.; Hou, K.; Zheng, Y.; Zhu, Y.; Lv, J.; Liu, S.; Tang, Z. *Angew. Chem. Int. Ed.* **2017**, *56*, 1.

115. Jia, X.; Li, J.; Wang, E. *Small* **2013**, *9*, 3873.

116. Chen, C.-W.; Wang, C.-H.; Wei, C.-M.; Hsieh, C.-Y.; Chen, Y.-T.; Chen, Y.-F.; Lai, C.-W.; Liu, C.-L.; Hsieh, C.-C.; Chou, P.-T. *J. Phys. Chem. C* **2010**, *114,* 799.

117. Kulakovich, O.; Strekal, N.; Yaroshevich, A.; Maskevich, S.; Gaponenko, S.; Nabiev, I.; Woggon, U.; Artemyev, M. *Nano Lett.* **2002,** *2***,** 1449.

118. Mandal, G.; Bardhan, M.; Ganguly, T. *J. Phys. Chem. C* **2011**, *115*, 20840.

119. Lee, J., Hernandez, P., Lee, J., Govorov, A. O.; Kotov, N. A. *Nature Mater.* **2007,** *6***,** 291.

120. Zhang, W.; Govorov, A. O.; Bryant, G. W. *Phys. Rev. Lett.* **2006**, *97*, 146804.

121. Govorov, A. O.; Bryant, G. W.; Zhang, W.; Skeini, T.; Lee, J.; Kotov, N. A.; Slocik, J. M.; Naik, R. R. *Nano Lett.* **2006**, *6*, 984**.**

122. Thomas, K. G.; Kamat, P. V. *Acc. Chem. Res*. **2003**, *36*, 888.

123. Chen, C.-W.; Wang, C.-H.; Wei, C.-M.; Hsieh, C.-Y.; Chen, Y.-T.; Chen, Y.-F.; Lai, C.-W.; Liu, C.-L.; Hsieh, C.-C.; Chou. P.-T. *J. Phys. Chem. C* **2010,** *114,* 799.

124. Lee, J.; Govorov, A. O.; Dulka, J.; Kotov, N. A. *Nano Lett.* **2004**, *4*, 2323.

125. Badawy, A. M. E.; Hassan, A. A.; Scheckel, K. G.; Suidan, M. T.; Tolaymat, T. M. *Environ. Sci. Technol*. **2013**, *47*, 4039.

126. Khandelia, R.; Jaiswal, A.; Ghosh, S. S.; Chattopadhyay, A. *Small* **2013**, *9*, 3494.

127. Li, X.; Lenhart, J. J.; Walker, H. W. *Langmuir* **2010**, *26*, 16690.

128. Huynh, K. A.; Chen, K. L. *Environ. Sci. Technol*. **2011**, *45*, 5564.

129. Xu, W.; Shen, H.; Liu, G.; Chen, P. *Nano Res* **2009**, *2*, 911.

130. Sonnichsen, C.; Reinhard, B. M.; Liphardt, J.; Alivisatos, A. P. *Nat. Biotechnol* **2005**, *23*, 741.

131. Reinhard, B. M.; Sheikholeslami, S.; Mastroianni, A.; Alivisatos, A. P.; Liphardt, J. *Proc Natl Acad Sci USA* **2007**, *104*, 2667.

132. Wang, Y.; DePrince, A. E.; Gray, S. K.; Lin, X. M.; Pelton, M. *J. Phys. Chem. Lett.* **2010**, *1*, 2692.

133. Alvarez, Y. D.; Fauerbach, J. A.; Pellegrotti, J. V.; Jovin, T. M.; Jares-Erijman, E. A.; Stefani, F. D. *Nano Lett.* **2013**, *13*, 6156.

134. Soman, C.; Giorgio, T. *Nano Res* **2009**, *2*, 78.

135. Oshima, T.; Lu, D.; Ishitani, O.; Maeda, K. *Angew. Chem. Int. Ed.* **2015**, *54*, 2698.

136. Ouyang, L.; Ren, W.; Zhu, L.; Irudayaraj, J. *Reviews in Analytical Chemistry*, **2016**, *36*.1

137. Liu, S.; Tang, Z. *J. Mater. Chem*. **2010**, *20*, 24.

138. Park, H.; Lee, S.; Chen, L.; Lee, E. K.; Shin, S. Y.; Lee, Y. H.; Son, S. W.; Oh, C. H.; Song, J. M.; Kang, S. H.; Choo, J. *Phys. Chem. Chem. Phys*., **2009**, *11*, 7444.

139. Qin, W.; Lohrman, J.; Ren. S. *Angew. Chem. Int. Ed.* **2014**, *53*, 7316.

140. Parka, D. J.; Zhanga, C.; Kub, J. C.; Zhoub, Y.; Schatza, G. C.; Mirkin, C. A. **2015**, *112* ,977.

141. Aslan, K.; Lakowicz, J. R.; Geddes, C. D. *Anal. Biochem*. **2004**, *330*, 145.

142. Aslan, K.; Lakowicz, J. R.; Geddes, C. D. *Anal. Chem*. **2005**, *77*, 2007.

143. Nam, J.; Won, N.; Jin, H.; Chung, H.; Kim, S. *J. Am. Chem. Soc.* **2009**, *131*, 13639.

144. Chirea, M.; Pereira, C. M.; Silva, F. *J. Phys. Chem. C* **2007**, *111,* 9255.

145. Wohltjen, H. *Anal. Chem*. **1998**, *70*, 2856.

146. Snow, A. W.; Ancona, M. G.; Park, D. *Langmuir* **2012**, *28*, 15438.

147. Wei, H.; Xu, H. *Nanoscale*, **2013**, *5*, 10794.

148. Shiohara, A.; Wanga, Y.; Liz-Marzán, L. M. *J. Photochem. Photobiol., C*, **2014**, *21*, 2.

149. Sekhar, P. K.; Ramgir, N. S.; Bhansali, S. *J. Phys. Chem. C,* **2008**, *112,* 1729.

150. Xia, X.; Li, W.; Zhang, Y.; Xia, Y. *Interface Focus* **2013***, 3,* 20120092 DOI: 10.1098/rsfs.2012.0092.

151. Zhang, K.; Zhao, J.; Ji, J.; Li, Y.; Liu, B. *Anal. Chem* **2015**, *87*, 8702.

152. Qian, X.-M.; Nie, S. M. *Chem. Soc. Rev.* **2008**, *37*, 912.

153. Xiao, Y.; Patolsky, F.; Katz, E.; Hainfeld, J. F.; Willner, I. *Science* **2003**, *299*, 1877.

154. Jin, Y.; Wang, J.; Sun, B.; Blakesley, J. C.; Greenham, N. C. *Nano Lett.,* **2008**, *8*, 1649.

155. Park, D. J.; Ku, J. C.; Schatz, G. C.; Mirkin, C. A. *SPIE*, **2015**, doi: 10.1117/2.1201503.005823.

156. Qin, L.; He, X.; Chen, L.; Zhang, Y. *ACS Appl. Mater. Interfaces* **2015**, *7*, 5965.

157. Khandelia, R.; Bhandari, S.; Pan, U. N.; Ghosh, S. S.; Chattopadhyay, A. *Small*, **2015**, *11*, 4075.

158. Yahia-Ammar, A.; Sierra, D.; Mérola, F.; Hildebrandt, N.; Guével, X. L. *ACS Nano* **2016**, *10*, 2591.

159. Wang, Z.; Chen, B.; Zhu, M.; Kershaw, S. V.; Zhi, C.; Zhong, H.; Rogach, A. L. *ACS Appl. Mater. Interfaces* **2016**, *8*, 33993.

160. Basu, S.; Paul A.; Chattopadhyay, A. *J. Mater. Chem. A*, **2016**, *4*, 1218.

CHAPTER 2

Kinetics of Reaction of Gold Nanoparticles Following Partial Removal of Stabilizers

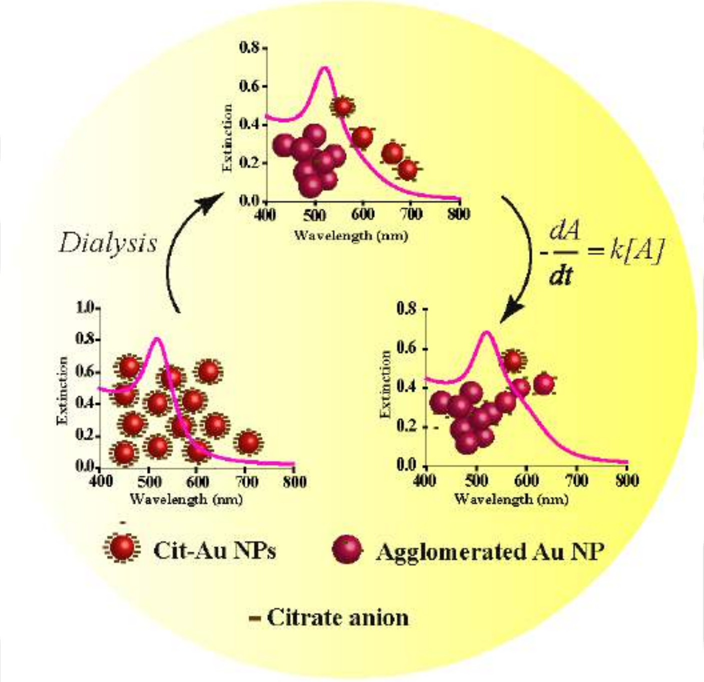

*In **Chapter 2** a new way to study kinetics of reaction of Au NPs in liquid medium is demonstrated via ligand desorption method. Citrate-stabilized Au NPs of 17 nm diameter were allowed to react following partial depletion of the stabilizer using dialysis. Kinetics of the reaction was then investigated by following time-dependent changes in the visible extinction spectrum. The reaction followed first order kinetics with respect to concentration of reactant (Au NP) with a rate constant on the order of (2.10 ± 0.34) × 10^{-3} min^{-1}. Further, product concentration (agglomerated structures) correspondingly increased with time. A model has therefore been proposed based on reaction of individual NPs with agglomerated structures which accounted for the observed kinetics.*

***[Dutta et al. J Nanopart Res. 2015, 17, 260] - Reproduced by permission of Springer. Copyright © 2015, Springer Science+Business Media Dordrecht**
https://link.springer.com/article/10.1007/s11051-015-3021-6*

2.1. Introduction

The inherent instability of inorganic nanoparticles (NPs) requires the presence of additional stabilizing molecular or ionic layer on their surface, which also prevents their reaction as such.[1] In contrast to this, the stability of individual molecular and ionic species in liquid media allows the ease of carrying out chemical reactions and of following the reactants or products (and thus kinetics of reaction) using optical and other physical techniques. However, literature reports suggest that the presence of a third reagent such as an inorganic ion (from a metallic salt) or electrolyte or a biomolecule leads to agglomeration of the NPs, following disruption of the electrical double layer surrounding them, which is accompanied by changes in the UV-vis spectrum.[2-4]

Although primary interest in this regard has been to obtain self-assembled NPs[5] for appropriate applications there are also reports of pursuing kinetics of reactions of the NPs leading to agglomeration.[6-7] For example, the rate of halide induced oxidative decomposition of the NP surface and agglomeration of the NP has been found to vary with a fractional order and order equivalent to two for the Ag NP concentration.[8] Interestingly, aggregation induced fast crystal growth of bulk-like SnO_2 nanocrystals has been shown to follow first order kinetics.[9]

On the other hand, there has been extensive interest in the formation and growth kinetics of NPs from clusters involving two mechanisms – the ostwald ripening and oriented attachment process.[10-11] It can be said that progress in the understanding of kinetics of aggregation of chemically synthesized colloidal NPs has been somewhat hindered by the lack of availability of sufficiently stable, bare and reactive NPs. However, even though complete removal may not be possible, partial removal of the stabilizers may provide enough stability (and thus instability) for studying the kinetics of reaction of the NPs. There are reports where dialysis of as-prepared nanomaterials has been carried out in order to remove excess ligands and free ions from the medium.[12-13] However, to the best of our knowledge, there is no literature on the use of dialysis to prepare the initial reaction conditions involving bare and reactive gold NPs to study the kinetics of the reaction in liquid medium. This is important as understanding kinetics of reactions of NPs are vital to their utilization as well as following their fate upon use.

2.2. Outline of the present work

Herein we report the kinetics of reaction of citrate-stabilized Au NPs following depletion of citrate concentration using dialysis. The reaction was followed using surface plasmon resonance (SPR) based UV-vis spectroscopy of the Au NPs. Investigation revealed that – following dialysis - the medium initially contained monomeric Au NPs along with low population of agglomerated NPs. The reaction led to the increase in the extent of agglomeration at the cost of individual particles followed by coalescence. Analyses of the extinction spectra revealed that the reaction was first order with respect to loss of monomeric Au NPs (reactants). The results were further substantiated by dynamic light scattering (DLS) based particle size analyses and transmission electron microscopy (TEM). The observations have been accounted for using a model where individual NPs reacted with agglomerated structures to produce larger agglomerates.

2.3. Experimental Section

2.3.1. Materials

Gold(III) chloride (30 wt%, anhydrous, Sigma-Aldrich), tri sodium citrate (Merck), dialysis tubing membrane, LA 393-10MT,12kDa, 2.4 nm pore size (HIMEDIA), sodium hydrogen carbonate (Merck) and ethylene diaaminetetraacetate, EDTA (Merck) were used as received. Milli-Q grade water (18.2 MΩcm) was used for synthesis as well as for carrying out analytical work.

2.3.2. Dialysis Tubing Membrane Activation

Dialysis membrane of desired length was cut and immersed in Milli-Q grade water containing 0.2% $NaHCO_3$ and 1.0 mM EDTA. The above solution containing dialysis membrane was heated at 90 ˚C, along with stirring for ~ 45 min. The activated dialysis membrane was then rinsed thoroughly with Milli-Q grade water thrice to wash out the excess $NaHCO_3$, EDTA and other by products, if any. Finally the rinsed dialysis membrane being immersed in fresh Milli-Q grade water was transferred to a beaker and stored at 4 ˚C for further use.

2.3.3. Synthesis of Citrate-Stabilised Gold Nanoparticles (Cit-Au NPs)

Synthesis of citrate-stabilised Au NPs (Cit-Au NPs) was carried out following a modified version of well-known citrate reduction method.[14] Tri sodium citrate (1.93 mM) added to Milli-Q grade water (50 mL) was allowed to reflux under stirring condition. As the citrate solution started to boil, 500 μL $HAuCl_4$ (1.72×10^{-2} M) was added all at once. The reaction was monitored by rapid change in color from purple to deep red, indicating the formation of Cit-Au NPs. The reaction was continued for another 30 min to ensure complete reduction of Au(III) ions, keeping the reaction condition same. The formation of Cit-Au NPs was confirmed by recording of UV-vis spectrum and TEM analysis. The area under the SPR band was obtained using function set in Origin 7.0 software.

2.3.4. Dialysis of Cit-Au NPs and their Kinetic Study

17 nm Cit-AuNP dispersion (6 mL) was transferred to pre-activated dialysis tubing membrane which was clipped tightly from both the ends so that Cit-Au NP dispersion volume was maintained throughout the dialysis time. Reaction was initiated by dialysing Cit-Au NPs against Milli-Q grade water at room temperature, with continuous stirring.[15] The volume of the Milli-Q grade water in the dialysis chamber was always fixed at 800 mL. After dialysing 0.62 nM Cit-Au NPs for 270 min (initial time), an aliquot (~3 mL) from the dialysed Cit-Au NP dispersion was transferred to the UV cuvette and thereafter time - dependent UV-vis spectra were recorded for next 30 min at a constant time gap of 3 min. Simultaneously, 1 mL aliquot of dialysed Cit-Au NP dispersion was transferred to DLS measurement glass cuvette to measure the size distribution at a time interval of six min during time-dependent UV-vis study. It is to be mentioned that the initial time (t = 0 min) at which the nearly bare Au NPs initiate to react was established empirically by carrying out the dialysis for multiple times, for a defined concentration of Au NP and therefore considered as the initial time. Therefore, the time for which the dialysis was to be carried out before the reaction kinetic study of Au NPs was pre-

established. Time-dependent experiment carried out for dialysis, duration of which was less than the above initial time showed no change in SPR band. Six different concentrations of Cit-Au NPs were dialysed to study the kinetics of NP reaction viz., 0.62, 0.49, 0.42, 0.39, 0.32 and 0.24 nM.

2.3.5. Reaction Order Calculation

Order of the reaction was determined following differential rate method. The rate was calculated considering initial rate of reaction for different initial concentrations of reactant (monomeric Cit-Au NPs) and agglomerates (product Au NPs). The initial rate values corresponding to six different concentration of Cit-Au NPs were calculated from the slope (obtained from the first four data points) of plot of Ext. Vs time of experimental spectra and from the plot of Absorbance Vs time of the primary deconvoluted band. Ext. and $(\text{Ext.})_0$ refer to extinction and initial extinction value from the SPR spectrum obtained during the time dependent study.

2.3.6. Reaction Rate Constant Calculation

Rate constant values were obtained from the slope of the integrated rate equation plot i.e, ln(Ext.) vs Time and $\ln[A]$ vs t as well as from the differential rate equation plot i.e, ln (rate) vs ln $(\text{Ext.})_0$ and ln (rate) vs $\ln[\text{A}]_0$ corresponding to six different concentration of Cit-Au NP dialysed. Six different sets of rate constant were obtained corresponding to six different concentration of Au NP dialysed and mean rate constant value is reported based on average of all measured rate constant data value.

2.4. Characterization

All UV-vis measurements were recorded with Perkin Elmer Lambda 25. TEM images were captured using a JEOL JEM 2100 transmission electron microscope, operating at maximum operating voltage of 200 kV. TEM sampling was done by drop casting 4 μL of Au NP dispersion on the carbon coated copper grid, and was allowed to air-dry. Size distribution analysis based on dynamic light scattering was done using Zetasizer Nano ZS90 instrument (MODEL NO. ZEN3690, MALVERN), operating with red He-Ne gas laser (λ=633 nm) at a temperature of 25°C.

2.5. Results and Discussion

Citrate stabilised Au NPs were prepared by citrate reduction method following a reported protocol.[16] A typical TEM image of as-prepared Cit-Au NPs as shown in **Figure 2.1.A** evidenced the presence of well-defined spherical Au NPs. The average particle size of 17±1.3 nm (diameter) was calculated from over hundred particles as indicated in the histogram in **Figure 2.1.B**. Assuming that all gold ions got converted to gold atoms, an average NP contains 197332 Au atoms and therefore, the concentration of as synthesized Cit-Au NPs was calculated to be 0.734 nM. The area under the SPR band of as synthesized Cit-Au NPs is proportional to the initial concentration of as synthesised Au NPs, $[Au]_0$ (containing 197332 atoms on an average per NP). The peak area value was found to be quite reproducible for different sets of as-synthesized Cit-Au NPs and was 69.81 AU (arbitrary unit). Therefore, peak area to concentration conversion was calculated to be 69.81 AU= 0.734 nM, following a literature report.[8] This was used as standard value to calculate the concentration of Cit-Au NPs dialysed at different concentrations and also for NPs during kinetic study, as described later in the discussion.

UV-vis extinction spectrum of dialysed citrate-stabilized Au NPs consisted of a single peak at 520 nm, which was close to the as-synthesized sample occurring at 518 nm (**Figure 2.1.C**). The broadness of the spectrum indicated that there might have been agglomeration following dialysis; however, the extent might not have been substantial, as there was no occurrence of a second peak at a higher wavelength. Further, time-dependent UV-vis spectra of the dialysed sample had two prominent changes - the lowering in intensity of the peak at 520 nm and appearance of a new peak at 600 nm and increase in its intensity (**Figure 2.1.D**). Also, when assembly of NPs form a linear or branched structure the resonance peak occurs at a longer wavelength (akin to longitudinal plasmon resonance).

Further, the position of the second peak did not seem to evolve substantially with time. Typically, it took about 270 min of dialysis in order to observe significant change in the spectrum. Dialysis for a shorter time resulted in no prominent changes in the spectrum. A schematic representation of the process of dialysis and the reaction of the dialyzed Cit-Au NPs is shown in **Figure 2.2**.

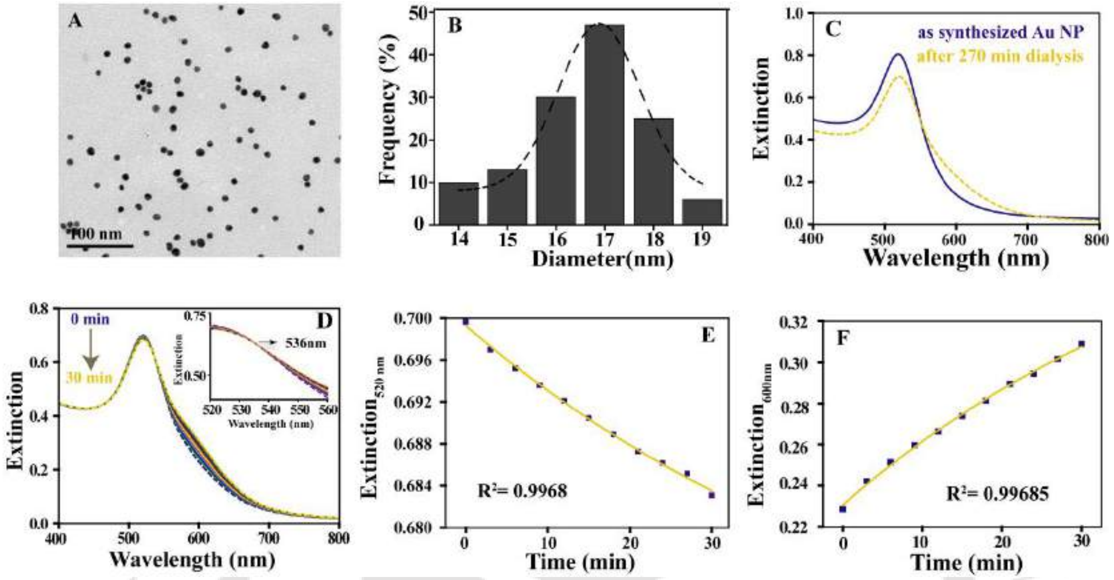

Figure 2.1. (**A**) Representative TEM image of as-synthesized Cit-Au NPs, (**B**) particle size histogram as calculated based on the TEM image, (**C**) Surface plasmon resonance (SPR) extinction spectra of as-synthesized Cit Au NP (with [Au NP] ~0.62 nM) dispersion (red line) and that immediately following dialysis for 270 min (blue dotted line), (**D**) Time-dependent (with time interval of 3 min) SPR extinction spectra of 0.62 nM Cit-Au NP dispersion recorded after 270 min of dialysis. Inset shows the expanded view of the isosbestic point, (**E**) Plot of decay of the SPR extinction maximum at λ_{max} = 520 nm as function of time. The curve could be fitted with single exponential function, (**F**) Plot of growth of the SPR extinction spectrum at λ_{max} = 600 nm. The graph was fitted with a growth function which changed exponentially with time. The data points in (**E**) and (**F**) were obtained from the spectra in (**D**).

On the other hand, longer dialysis period resulted in the appearance of two distinct peaks in the extinction spectrum initially, accompanied by rapid changes in its time-dependence and hence not pursued further. Recording of spectra typically for 30 min (with an interval of 3 min) - following dialysis - indicated changes significant enough to follow the kinetics. Additionally, observation of an isosbestic point at 536 nm in the extinction spectra (inset in **Figure 2.1.D**) indicated transformation of individual NPs into agglomerated structures, akin to chemical reaction involving reactants and products with overlapping extinction spectra.

In other words, it may be reasonable to assume that indeed the process could be considered as reaction of NPs into agglomerated product. The results were further substantiated by TEM measurements. TEM results (**Figure 2.3**) supported the spectroscopic observation, indicating the presence of smaller proportions of agglomerated structures in comparison to individual NPs at the beginning of the reaction i.e. right after dialysis (at t = 0 min). It was further observed that with the progress of reaction the extent of agglomeration increased. For example, TEM images recorded for samples at 15 min and 30 min of reaction indicated the formation of increasingly agglomerated structures at the expense of monomers (**Figure 2.3.B** and **2.3.C**). It is plausible that monomers might have reacted with agglomerated structures to produce larger agglomerates.

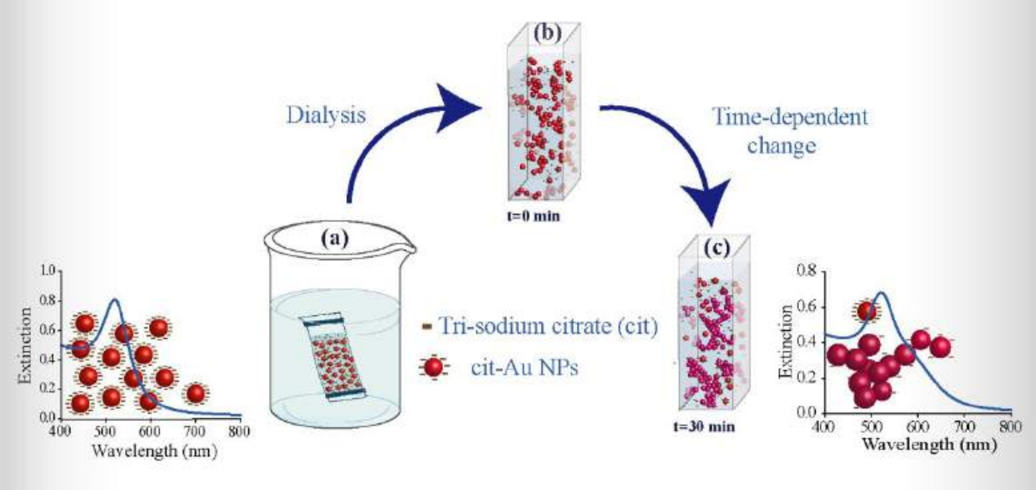

Figure 2.2. A schematic representation depicting the experimental procedure to monitor the reaction kinetics of nearly bare Cit-Au NPs. (**A**) As-synthesized Cit-Au NPs was dialysed in 12 kDa dialysis membrane, (**B**) dialysed Cit-Au NP dispersion was transferred (right after dialysis) to cuvette to study the reaction of nearly bare Cit-Au NPs and (**C**) represents formation of Au NP agglomerated species with time.

For a colloidal solution, the extinction for n NPs per unit volume is given by,[17]

$$A = \log_{10}\frac{I_0}{I} = nQ_{ext}l \qquad (1)$$

where I_o and I are the intensities of incident and transmitted light, l is the path length of the sample and Q_{ext} is the extinction coefficient of single Au NP, which is a function of metal core, surface layer and the medium in which it is present. Now, decrease in the extinction value at 520 nm is indicative of loss of individual reactive NPs and thus of occurrence of reaction. A plot of the extinction (at 520 nm) with time could be fitted with a single exponential decay (**Figure 2.1.E**) indicating first order reaction involving the NPs. This can be reasoned to be based on the linear relationship between the extinction and concentration of the NPs as mentioned above. On the other hand, a plot of extinction at 600 nm with time indicated growth, which could be fitted with an exponential function, showing a direct correlation of product (agglomerated NP) formation from reactant NPs. (**Figure 2.1.F**)

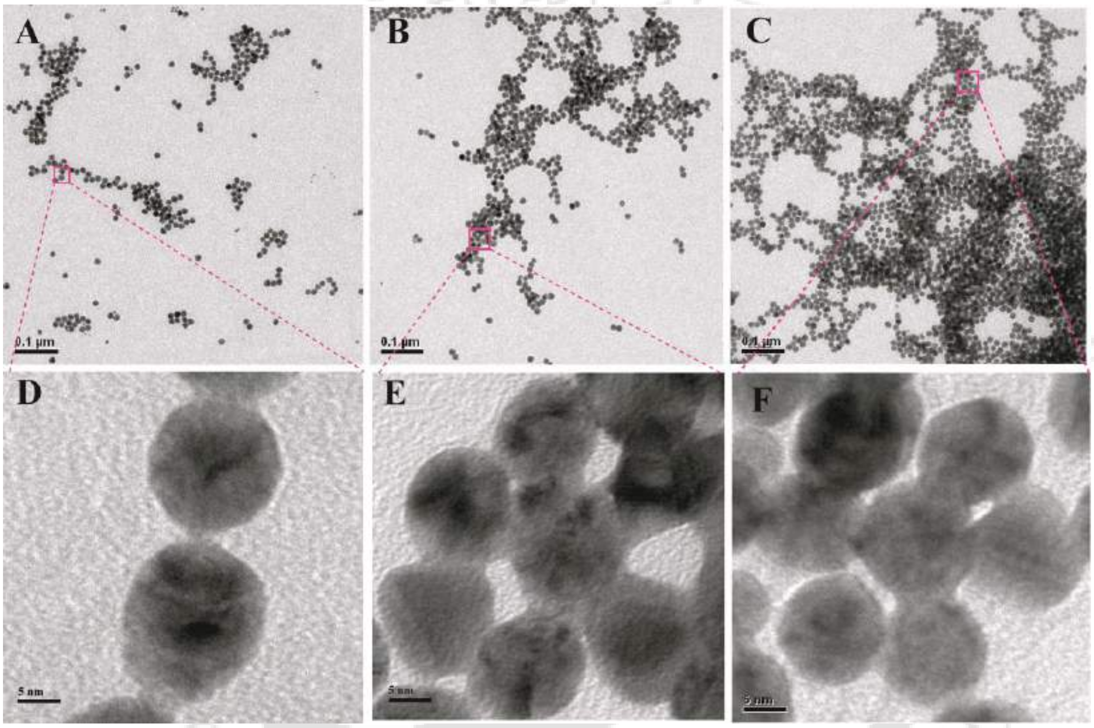

Figure 2.3. Representative TEM images of 0.62 nM dialyzed Cit-Au NPs recorded from samples of time-dependent study. Here (**A**) is for sample at t = 0 min (i.e. right after dialysis), (**B**) is for sample at t = 15 min and (**C**) is for the sample at t = 30 min. (**D**), (**E**) and (**F**) are the HRTEM images from a select region (purple solid boxes) corresponding to Figure (**A**), (**B**) and (**C**), respectively. The dialysis for the sample was carried out for 270 min.

It may be mentioned here that in general, assembly of plasmonic metallic NPs may agglomerate in the form of linear assembly of NPs.[18] They may also form branched structures or larger nearly spherical (highly branched) particles following fusion.[19-20] In the first instance, the extinction spectrum would consist of two peaks – one due to transverse plasmon resonance with peak occurring nearly at the single particle wavelength, while the other would be due to longitudinal plasmon resonance with peak appearing at higher wavelength, which would depend on the length of the assembly.[21] This would make it difficult to correlate the concentration of the remaining individual particle as well as the product particles with the extinction spectrum. On the other hand, extensively branched structures and nearly spherical fused particles as the case herein, may have single major peak at higher wavelengths with little contribution to the peak at the lower wavelength (520 nm) and may provide a better opportunity for analysis.[22] Thus, even if the branched structures have an additional peak at the lower wavelength, however, that may not be significantly contributing to the overall peak at the lower wavelength –at least for the initial period of reaction - and the analysis may still be carried out.

That the analysis could be pursued with the above assumption was evident from the measured extinction spectrum for longer time of reaction, where the major peak was at the higher wavelength and the peak at the lower wavelength (522 nm) was significantly weak (**Figure A2.1**, **Appendix**). The nature of the product formed was further pursued by HRTEM analysis as shown **Figure 2.3.D**, **E** and **F**, indicating the occurrence of fusion of particles in the extensively branched structures of the product formed from the reaction of dialysed Au NPs with starting concentration of 0.62 nM. A typical selected area electron diffraction (SAED) pattern of a particle in **Figure 2.3.D** is shown in **Figure A2.2**, **Appendix** indicating the presence of planes viz., (**111**), (**200**) and (**220**) corresponding to fcc Au NPs. Similar TEM image results were also obtained for sample containing 0.39 nM Au NP (refer to **Figure A2.3**, **Appendix**). The images also indicated absence of individual linear arrays in significant numbers, thus excluding major contribution of simultaneous transverse and longitudinal resonances in the extinction spectra.

Dynamic light scattering (DLS) based particle size analysis (**Figure A2.4.A**, **Appendix**) indicated that following dialysis the average particle size changed from as-prepared size of 29 nm (hydrodynamic diameter) to 47.1 nm. On the other hand, the particle size distribution and the average size did not change significantly during the reaction period (**Figure A2.4**, **Appendix**). In other words, as the reaction proceeded, the number of individual NPs decreased and the number of agglomerated particles increased.

However, since the time period of measurement was sufficiently small, the change in dimensions was sufficiently small to make any significant change in the DLS results. On the other hand, UV-vis spectroscopy, being a more sensitive probe, provided a more accurate representation of the observed changes. This means that during the initial period of reaction the concentration of reactants and products changed sufficiently small, thus providing an opportunity for analysis based on the concept of ordinary chemical reaction kinetics. Also, results for several other initial concentrations of Au NPs viz., 0.49, 0.42, 0.39, 0.32 and 0.24 nM following dialysis were obtained which are included in **Figure 2.4.**

If there are two kinds of species which are present in the liquid medium and if the plasmon resonance peaks due to the species are sufficiently separated, the overall extinction can be considered as summation of two spectra and thus can possibly be deconvoluted into two component spectra.

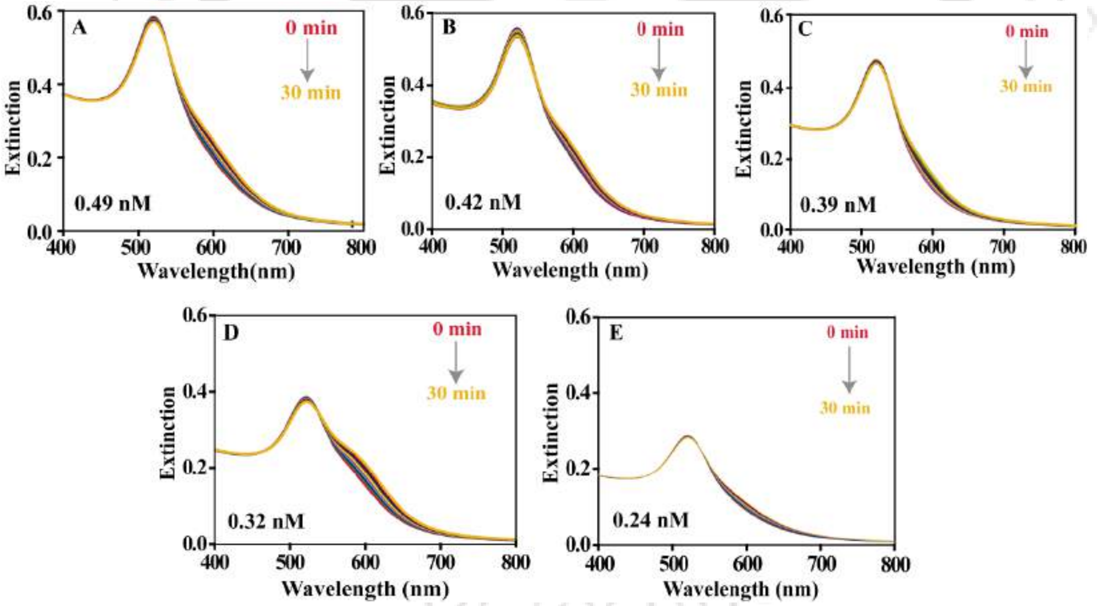

Figure 2.4. UV-Vis SPR extinction spectra of (**A**) 0.49 nM, (**B**) 0.42 nM, (**C**) 0.39 nM (**D**) 0.32 nM and (**E**) 0.24 nM Cit-Au NP dispersions recorded following dialysis for 270 min.

The total extinction of light by the individual and agglomerated NPs could then be written as[3],

$$A(\lambda) = Q_{ext,NP}(\lambda)C_{NP}\, l + Q_{ext,agg}(\lambda)C_{agg} l = A_{AuNP}(\lambda) + A_{AuNP,agg}(\lambda) \qquad (2)$$

Here, $A(\lambda)$ is wavelength dependent total extinction, $Q_{ext,NP}(\lambda)$ and $Q_{ext,agg}(\lambda)$ are the extinction coefficients due to free monomeric Cit-Au NPs and agglomerated Cit-Au NPs respectively; C represents the concentration of individual species and l is the path length. Indeed the time-dependent extinction spectra could be decomposed into three components – one with a peak at 522 nm, the other with a peak at 596 nm (**Figure 2.5**) and the background spectrum representing scattering and interband transition of the metallic NPs.[23]

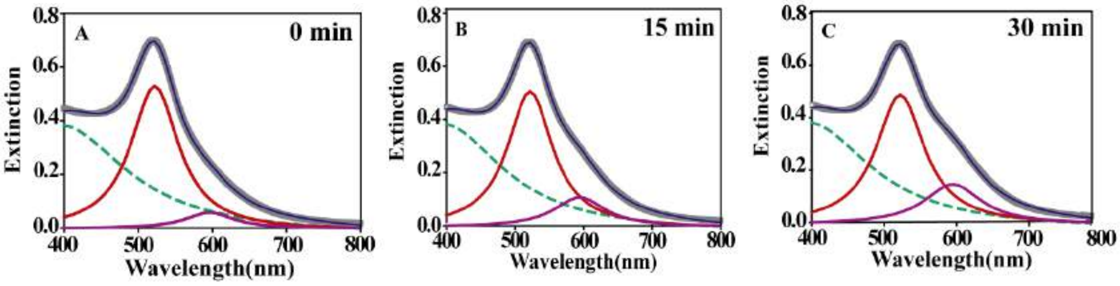

Figure 2.5. Selected deconvulated spectral SPR peaks during time dependent UV-Vis study at (**A**) t = 0 min, (**B**) t =15 min and at (**C**) t = 30 min of 0.62 nM Cit-Au NPs following dialysis for 270 min. The curve in grey is the experimental curve, that in blue is its Lorentzian fit, those in red and violet are the primary and the secondary bands and the green (dotted) curve is the background spectrum.

Figure A2.5 represents the deconvoluted SPR peak for as-synthesized Cit-Au NPs which shows two distinct curves, one corresponding to background scattering and the other due to primary absorption band. The spectra were deconvoluted using non-linear Lorentzian curve fitting analysis. The time-dependent decrease in intensity of the peak at 522 nm and increase in intensity of the peak at 596 nm could clearly be delineated. Further, deconvoluted bands obtained from spectra at 0, 15 and 30 min of reaction as shown in **Figure 2.5.A**, **B** and **C** indicated increase in the area of the secondary SPR band with concomitant decrease in the area of primary SPR band.

Plots of deconvoluted curves represented progress of reaction with time (**Figure 2.6.A** and **B**). The change in absorbance at the maximum wavelength corresponding to the curve with a peak at 522 nm could be fitted with a single exponential decay (**Figure 2.6.C**) and thus indicated a first order reaction of the monomeric Au NPs. Correspondingly, the absorbance maximum at 596 nm increased rapidly which could be fitted with an exponential function of time (**Figure 2.6.D**).

Considering the deconvoluted spectral plots, the orders of reaction with respect to the species contributing to the changes in absorbance at 522 nm and 596 nm were determined following the initial rate method. Concentration of monomer at time *t* was calculated using the peak area to concentration conversion as mentioned earlier. The plot of ln (initial rate) of disappearance of the reactant versus ln$[A]_0$ i.e. initial concentration of the NPs, as obtained from the deconvoluted SPR band at 522 nm resulted in the order of the reaction to be unity (**Figure 2.7.B**). This is in agreement with the order obtained from experimental spectral data (**Figure 2.7.A**) i.e. from the plot of ln(initial rate) versus ln$(Ext)_0$,. The data obtained from above plots were further used to calculate the rate constant for the reaction (with respect to individual NPs). The first order rate constant corresponding to six different concentrations of Cit-Au NPs obtained

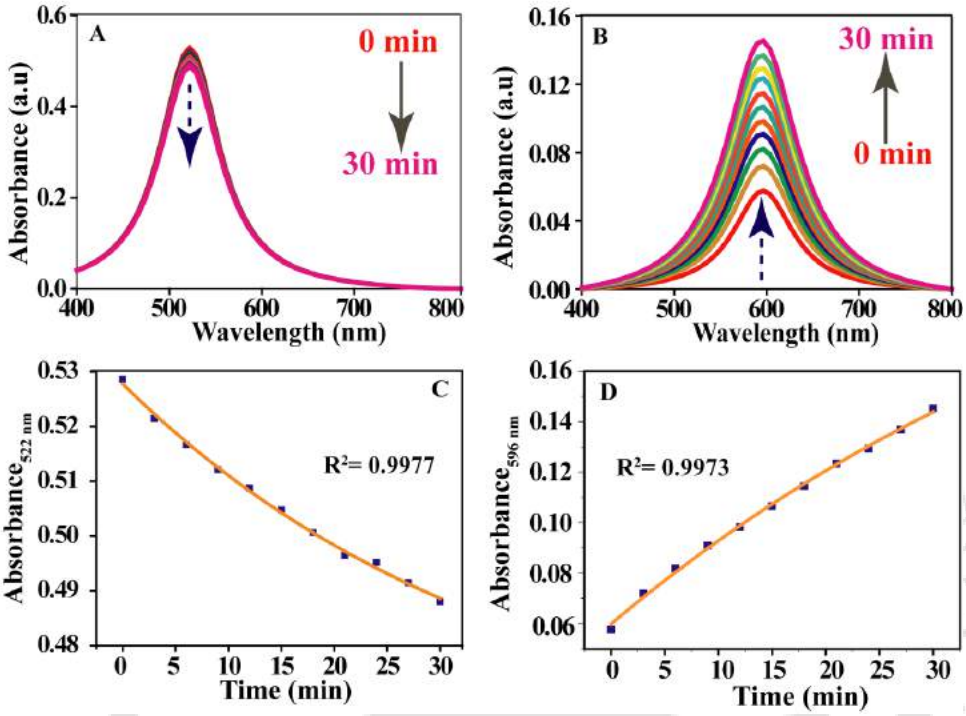

Figure 2.6. Deconvolution of time-dependent UV-vis spectra of Cit-Au NPs (after dialysis for 270 min). These graphs were obtained following deconvolution of spectra in **Figure 2.1.D**. (**A**) Deconvoluted UV-Vis absorption spectra of the primary SPR band, (**B**) growth curve of deconvoluted secondary SPR band, (**C**) time-dependence of UV-vis absorption maximum at 522 nm (fitted with a single exponential function) and (**D**) time-dependence of UV-Vis absorption maximum at 596 nm (fitted with a growth function which changed exponentially with time).

from the deconvoluted primary UV-vis band was calculated to be (1.58 ± 0.27) × 10^{-3} min^{-1} (**Table A2.1**, **Appendix** calculated following integrated rate method).

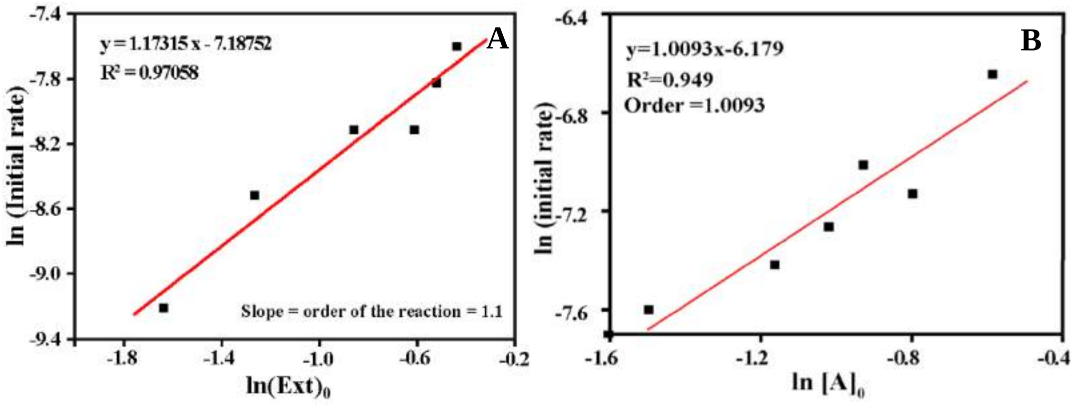

Figure 2.7. (**A**) Plot of ln(initial rate) vs ln(Ext)$_0$ to derive the order of the reaction from experimental data. (Ext)$_0$ refers to initial extinction maxima as obtained at 520 nm and at t=0 min of reaction. (**B**) Plot of ln(initial rate) versus ln[A]$_0$. Data points were fitted to a linear function and the slope was equal to order of the reaction (i.e. 1). [A]$_0$ refers to monomeric Au NP species absorbing at 520 nm.

The results mentioned above could be analysed based on the following model. The as-synthesized Cit-Au NPs existed as individual entities with an electrical double layer surrounding the NP. Electrostatic and van der Waals forces balance each other to stabilize the NPs in the medium. Once the NP containing dispersion medium was subjected to dialysis, the concentration of citrate went down. This in turn reduced the equilibrium surface concentration of the citrate ions surrounding the NPs. Thus, the structure of the electrical double layer changed with reduction in the citrate concentration, rendering the NPs unstable and they started to agglomerate, owing to attainment of lowered Gibbs free energy.[24] The extent of agglomeration would depend on the time of dialysis and initial concentration of citrate and NPs. However, if timed appropriately, the agglomeration can be controlled and the initial population of NPs and agglomerated particles could be 'chosen'. The two species can be allowed to react following increase in agglomeration at the cost of individual NPs. The concentrations of the NPs and agglomerated NPs immediately after dialysis could be considered as the initial concentrations of the reactants. Now, there could be three possible reactions between the species present in the medium. Firstly, the individual NPs could react among themselves producing dimers. Secondly, the larger agglomerated structures could react with themselves producing even larger structures. Finally, the individual NPs could also react with the agglomerated structures to produce further agglomeration, which is the predominant case herein during the time period of study. The high surface free energy of individual NPs drives the reaction process where the bare NPs i.e, particles devoid of stabilizers, preferentially approaches surface of agglomerates to undergo coalescence, mostly sharing the same crystallographic planes at the interface.[25] This is understood from the inverse fast Fourier transform (IFFT) analysis of a typical HRTEM image showing coalesced Au NPs (**Figure A2.6**, **Appendix**). Bare Au NPs are plausibly expected to react with each other limited by diffusion only. However, in the current situation, the NPs still retain some of the stabilizers on the surface and hence would have sufficient barrier to reaction. The barrier may originate from relocation of the remaining stabilizers so that fusion of two appropriate faces may occur. In addition, the fusion may be crystalline face specific and hence every collision may not lead to fusion. Thus there may be barrier to 'reactive collisions' with respect to appropriate orientation of faces and desorption of citrate stabilizer, before fusion of two particles. Literature reports suggest that Au and other NPs fuse preferably among the same crystalline faces.[25] Analysis showed lattice fringes with d-value ~0.23 nm, corresponding to (111) fcc Au lattice at the interface region, which underwent fusion sharing the same plane. Unlike perfect fusion to generate single crystalline adduct, there are also fusion along mismatched interface (image not shown).

The as-synthesized NPs had an average particle size of 17 nm. If a few of such NPs were to agglomerate the product particle would exhibit an extinction spectrum the maximum of which would be close to the original peak at 520 nm. Also, if the number of particles in the product in terms of average size increased gradually with a significant change in the percentage population, then the extinction spectrum is expected to shift gradually towards longer wavelength. This - not being the observed case - can be ruled out. On the other hand, the initial UV-vis extinction spectrum of the reacting medium lacked a clear second peak, thus indicating the population of agglomerated structures to be sufficiently low. Hence the reaction among the larger agglomerates could be ruled out. However, individual NPs could still react with initially formed agglomerated structures and increase their dimensions. Meanwhile, reactions of individual NPs –albeit smaller in number - in terms of binary or ternary (or similar) collisions would result in increase in the population of the larger particles, which may act as the seed particle for larger structures. The model can therefore be written in terms of the following two independent types of reactions.

$$A + A_n = A_{n+1} \qquad where\ n \geq 1 \qquad (3)$$

$$A_n + A_m = A_{n+m} \ where\ n > 1\ \ and\ \ m > 1 \qquad (4)$$

Considering the observation of a single plasmonic peak at the beginning of reaction i.e. following dialysis, it may be assumed that the concentrations of agglomerated species (A_n and A_m) are sufficiently low and the concentration of individual NPs (i.e. A) is high, hence the reaction among agglomerated species are negligible compared to reaction of monomeric species with agglomerated species at the initial time of the reaction. The reaction as proposed in **equation** (**4**) might happen at later times following dialysis (say at about 10 h or later) because by then the competing **reaction** (**3**) was nearly over. As a proof of concept, control experiment was carried out by transferring 3 mL aliquot of freshly made Au NP dispersion to a glass cuvette and then allowing it to stand for nearly 270 min. Thereafter, the time-dependent extinction spectrum was recorded for the same (**Figure A2.7**, **Appendix**) for next 30 min. which however did not show significant broadening or decrease in extinction. This is unlike the broadening observed in the time-dependent changes for the dialysed Au NPs (**Figure 2.1.D**). That the reaction was occurring between two species present in the medium was further confirmed by the following experiment. Following dialysis of the Cit-Au NPs and after 12 min of reaction citrate solution (1.93 mM) was added to the medium. It was observed that there was no further change in the UV-vis spectrum (**Figure A2.8**, **Appendix**). This means that even though reaction occurred following dialysis, addition of excess citrate led to 'halting' of further reaction. Additionally, if citrate was added at a later point of time of reaction then again the changes in UV-vis spectrum associated with the progress of reaction stalled immediately. In addition, that the aggregation of NPs was induced by the depletion of citrate ligands during dialysis was clear from repeating the dialysis against trisodium citrate aqueous solution (of equal concentration) instead of water only. Thus, dialysing Au NPs against citrate solution for over 12 h showed no spectral change as such as shown in **Figure A2.9.A**, **Appendix**. Further **Figure A2.9.B**, **Appendix** shows the FTIR spectrum (red) recorded from depleted tri-sodium citrate anion that has been recovered following dialysis (when carried out against water only) by boiling out the water solution from the dialysis chamber. The band occurring at 3442 cm^{-1} corresponds to H–O–H bending of water molecules.[26] The band occurring at 3442 cm^{-1} corresponds to stretching due to alcoholic O–H moiety of citrate recovered from the water in dialysis chamber after dialysis (**Figure A2.9.B**, **Appendix**, red). The bands at 1418 and 1580 cm^{-1} are characteristics of symmetric and asymmetric stretching vibrations due to carboxylate anion (having identical C-O bonds). The relatively broad feature at 1060 cm is due to C–O stretching of the C–OH group. Barring the broadness of the aforementioned peaks for the citrate recovered from dialysis chamber, the spectrum is in close match with that of the pure citrate salt (**Figure A2.9.B**, **Appendix**, blue). Therefore, the agglomeration of the NPs and the consequent change in the UV-vis spectrum was due to depletion of citrate.

As the reaction was monitored for a small time range, the evolution of product was observed in terms of increase in number density of agglomerated structures of similar nature (either branched or nearly fused and spherical) instead of observing rapid growth of agglomerated structures, which would be the case when the same is monitored for longer period (refer **Figure A2.1**, **Appendix**). Further, DLS based particle size analysis for the sample (showing characteristic SPR nature in **Figure A2.1**, **Appendix**) after 46 h of study showed considerable shift in hydrodynamic diameter from d=47.1 nm (at time 0 min) to d= 78.5 nm (at time 46 h) which is included in **Figure A2.10**, **Appendix** indicating the occurrence of reaction and agglomeration with time. This, however, did not contradict the observation that for the initial 30 min of reaction the average particle size did not change significantly. A representative TEM image in this regard is shown in **Figure A2.11**, **Appendix** corresponding to the sample at 46 h of reaction. Thus the increase in the extinction at 596 nm demonstrates the growth of agglomerated structures driven by higher surface free energy of smaller unstable agglomerate units. It is important to point out here that plots of the peak for the as-observed extinction at 600 nm (**Figure 2.1.F**) as well as the one corresponding to deconvoluted peak at 596 nm (**Figure 2.6.D**) indicated growth curve which could be fitted with an exponential function. Moreover, the initial rate of formation of agglomerated species, representing absorbance at 600 nm, when plotted as function of initial agglomerate concentration at initial time of reaction was found to be weakly dependent on agglomerate concentration (**Figure A2.12**, **Appendix**) and therefore the reaction rate can be said to be solely dependent upon the rate of loss of monomeric Au NP concentration (**Figure 2.6.C**). This is also evident from the rate constant values obtained from time-dependent study at different initial concentration of dialysed Cit-Au NPs, which appears to be close to each other. This means that the rate constant of the reaction is independent of the concentration of different reacting agglomerated species formed during dialysis of Cit-Au NP, which was dialysed for six different concentrations. Based on the initial rate law, the rate constant was calculated to be $(2.10 \pm 0.34) \times 10^{-3}$ min^{-1} (**Table A2.2**, **Appendix**). This value agrees reasonably well with the literature values with rate constant value ~ 2.79×10^{-3} min^{-1} for Ag NP aggregation in presence of halides.[8]

Therefore, the essential mechanistic steps of the reaction, consistent with the current experimental observations, can be written as below. Find detailed elucidation in the **Discussion A2.1**. This is based on the assumption that although, there would be an equilibrium between the citrate ions on the surface of the NPs and those in the medium, reaction between the individual NPs and agglomerates would dominate, due to their high surface free energy. Thus it is likely that the Au NPs would react to a more stable 'state', with more favourable surface to volume ratio and higher surface concentration of citrate^{3-} ions. Therefore we write,

$$\left\{Au(citrate)_{x+q}\right\}^{3(x+q)-} \leftrightharpoons \left\{Au(citrate)_{x}\right\}^{3x-} + q \times citrate^{3-} \qquad K_{eq} = \frac{k_{cit}^{q}}{k_{-cit}^{q}} \qquad (5)$$

In these reactions, citrate represents citrate^{3-}, q is average number of citrate ions removed from single Au NP to make it reactive. The above step represents equilibrium of the adsorption and desorption of citrate ions from the surface of the Au NP, which probably occurs during and after dialysis. The overall equilibrium constant will be product of the ratio of rate constants for each individual equilibrium reaction.

The following reaction is the first step towards formation of nucleation sites for formation of aggregated structures and which probably starts during the dialysis and may continue during the kinetic study period.

$$\{Au(citrate)_x\}^{3x-} + \{Au(citrate)_x\}^{3x-} \xrightarrow{k_1} \{Au_2(citrate)_{2x}\}^{3(2x)-} \tag{6}$$

Similar reactions may take place in a sequential manner, during the reaction, to give rise to products as below,

$$\{Au(citrate)_x\}^{3x-} + \{Au_{m-1}(citrate)_y\}^{3y-} \xrightarrow{k_{m-1}} \{Au_m(citrate)_{x+y}\}^{3(x+y)-} \tag{7}$$

$$\{Au(citrate)_x\}^{3x-} + \{Au_m(citrate)_y\}^{3y-} \xrightarrow{k_m} \{Au_{m+1}(citrate)_{x+y}\}^{3(x+y)-} \tag{8}$$

Here, m means the number of Au nanoparticles in the agglomerate with y meaning the number of citrate attached to the agglomerate. Also, $\{Au(citrate)_x\}^{3x-}$ represents the reactive species involved in reactions with the monomer and its concentration will be in steady state during the course of the reaction (at least in the initial period). The reactant $\{Au_m(citrate)_y\}^{3y-}$, in reaction (**8**) is unstable and is formed through a sequence of reactions starting from reaction (**6**) during and after dialysis. Reaction depicted in equation (**8**) is predominant during the initial period of study. Species on right of reaction (**8**) is the one that absorbs at 600 nm. All other aggregate species smaller than (m+1) are formed and subsequently consumed in steps preceding this step, and hence can be considered reactive intermediates forming this final state, $\{Au_{m+1}(citrate)_{x+y}\}^{3(x+y)-}$.

Further, bimolecular reaction of two agglomerated structures to give larger aggregated units (**9**) can also be possible.

$$\{Au_m(citrate)_y\}^{3y-} + \{Au_{m+1}(citrate)_{x+y}\}^{3(x+y)-} \xrightarrow{k^b_{m+1}} \{Au_{(2m+1)}(citrate)_{(x+2y)}\}^{3(x+2y)-} \tag{9}$$

This reaction will be in competition with reaction (**6**) above and will predominate only at longer reaction times when [$\{Au(citrate)_x\}^{3x-}$] will be low and [$\{Au_m(citrate)_y\}^{3y-}$] large and will be accompanied by large red shift in the secondary SPR peak, as observed in our results and shown in **Figure A2.1**.

Based on the above proposition, it can be shown (refer to **equation A13**, **Appendix**) that the decay of the reactant with initial concentration $\left[\{Au(citrate)_{x+q}\}^{3(x+q)-}\right]_o$ can be represented by,

$$\left[\{Au(citrate)_{x+q}\}^{3(x+q)-}\right] = \left[\{Au(citrate)_{x+q}\}^{3(x+q)-}\right]_o \exp\left(\frac{-k_{cit}^q}{2}t\right) \qquad \textbf{(10)}$$

The exponential decay fits exactly with the observations in **Figure 2.1.E** and **Figure 2.6.C** mentioned above. Further, the product formation with time can also be represented by,

$$\left[\{Au_{m+1}(citrate)_y\}^{3y-}\right]_t - \left[\{Au_{m+1}(citrate)_y\}^{3y-}\right]_o = Const\left\{1-\exp\left(-\frac{k_{cit}^q}{2}t\right)\right\} \qquad \textbf{(11)}$$

The growth with an exponential function fits exactly with observation in **Figure 2.1.F** and **Figure 2.6.D** for the agglomerates as discussed above. Further details of equation (**11**) are available in the **equation A21**, **Appendix**. The above equations (**10**) and (**11**) qualitatively account for the observed rate of loss of monomeric Au NPs and the formation of agglomerates with time. Although, there are several approximations which can be considered crude, the essential mechanistic steps delineating the formation of the product from monomeric Au NPs and agglomerated Au NPs capture the essence of the reaction under consideration.

2.6. Conclusions

Finally, we have been able to demonstrate a new way of studying reactions of metal (Au herein) NPs in a liquid medium. This has been achieved by making the NPs nearly bare of stabilizers by depletion of their population using dialysis. This created an initial population of individual NPs and agglomerated NPs, which reacted with each other to form further agglomerates. The driving force for the reaction of bare Au NPs arises due to additional increase in surface energy in the absence of effective stabilization. Interestingly, the reaction was found to follow first order kinetics with respect to the concentration of individual NPs, which also represented the overall reaction rate. Further, the experimental findings and interpretations of the results reported in the manuscript may be considered as a beginning of probing a rather complex chemistry. That the reaction of NPs could be studied using spectroscopic tools (as simple as UV-vis spectroscopy) augers well for pursuing reactions under more controlled conditions. This new approach is akin to kinetics of molecular reactions and may offer an interesting way of studying chemical kinetics of NPs in a classical way, by following the optical spectrum of the reactants and products.

2.7. Discussion

The deconvolution was done in Microcal Origin 7.0 software using non-linear curve fit analysis. The Lorentzian function was selected to fit the spectral curve. It is to be mentioned that the plot of extinction at 520 nm and 600 nm versus time of dialyzed Au NPs recorded during time–dependent study showed an exponential fit decay and growth respectively. (Figure 2.1E and F) Also, the extinction spectra obtained during time–dependent study corresponds to free Au NPs as well as aggregated Au NPs, hence the overall spectrum was approximated by superposition of three component spectral curve considering multiple Lorentzian - one correspond to background scattering, second band represents the primary band due to monomeric particles whereas third band represents the secondary band due to aggregated species.

2.8. References

1. Ott, L. S.; Finke, R. G. *Coordination Chemistry Reviews* **2007**, *251*, 075.
2. Allen, E.; Henshaw, J.; Smith, P. AEAT/R/PSEG/0398; AEA Technology Engineering Services, Inc.: Harwell, Oxford, **2001**.
3. Deka, J.; Paul, A.; Chattopadhyay, A. *J Phys Chem C* **2009**, *113*, 6936.
4. Huynh, K. A.; Chen, K. L. *Environ Sci Technol* **2011**, *45*, 5564.
5. Besson, C.; Finney, E. E.; Finke, R. G. *J Am Chem Soc* **2005**, *12*, 8179.
6. Finney, E. E.; Finke, R. G. *Chem. Mater* **2008**, *20*, 1956.
7. Besson, C.; Finney, E. E.; Finke, R. G. *Chem. Mater* **2005**, *17*, 4925.
8. Espinoza, M. G.; Hinks, M. L.; Mendoza, A. M.; Pullman, D. P.; Peterson, K. I. *J Phys Chem C* **2012**, *116*, 8305.
9. Zhuang, Z.; Huang, F.; Lin, Z.; Zhang, H. *J Am Chem Soc* **2012**, *134*, 16228.
10. Ribeiro, C.; Lee, E. J. H.; Longo, E.; Leite, E. R. *Chem Phys Chem* **2005**, *6*, 690.
11. Shields, S. P.; Richards, V. N.; Buhro, W. E. *Chem. Mater* **2010**, *22*, 3212.
12. Shalkevich, N.; Shalkevich, A.; Si-Ahmed, L.; Burgi, T. *Phys Chem Chem Phy*, **2009** *11*, 10175.
13. Yan, M.; Fresnais, J.; Berret, J. F. *Soft Matter* **2010,** *6*, 1997.
14. Jimenez, I. O.; Bastus, N. G.; Puntes, V. *J Phys Chem C*, **2011**,*115,* 15752.
15. Fresnais, J.; Lavelle, C.; Berret, J. F. *J Phys Chem C* **2009**, *113*, 16371.
16. Jimenez, I. O.; Bastus, N. G.; Puntes, V. *J. Phys Chem C* **2011**, *115*, 15752.
17. Mulvaney, P. *Langmuir* **1996**, *12*, 788.
18. Zhang, Y. X.; Zeng, H. C. *J Phys Chem B* **2006**, *110*, 16812.
19. Xie, J.; Lee, Z. Q.; Lee, J. Y.; Wang, D. I. C. *J Phys Chem C* **2007**, *111*, 17158.
20. Murugadoss, A.; Chattopadhyay, A. *J Phys Chem C* **2008**, *112*, 11265.
21. Das, S.; Murugadoss, A.; Sarkar, S.; Chattopadhyay, A. *J Chem Sci* **2008**, *120*, 547.
22. Kuo, C. H.; Huang, M. H. *Langmuir* **2005**, *21*, 2012.
23. Sendroiu, I. E.; Mertens, S. F. L.; Schiffrin, D. J. *Phys Chem Chem Phys* **2006**, *8*, 1430.
24. Cao, G. Imperial College Press: London, U.K, **2004**.
25. Zhang, J.; Huang, F.; Lin, Z. *Nanoscale* **2010**, *2*, 18.
26. Park, J. W.; Parry, J. S. S. *J. Am. Chem. Soc.* **2014**,*136*, 1907.

CHAPTER 3

Effect of Temperature on the Aggregation Kinetics of Partially Bare Gold Nanoparticles

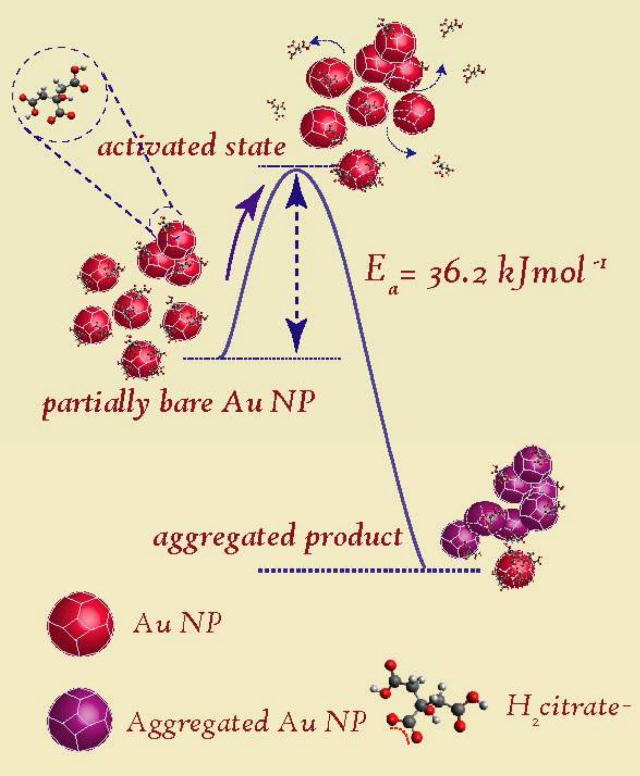

*In **Chapter 3**, we report the influence of temperature on the kinetics of aggregation reaction of Au NPs following controlled removal of tri-sodium citrate stabilizer by dialysis. UV-visible spectroscopy was used to monitor the aggregation of Au NPs in the temperature range of 20 °C - 60 °C which showed that the rate of aggregation had increased with increase in temperature. Detailed kinetic analysis showed that the aggregation process was reaction limited, demonstrating a first order kinetics with an activation energy of 36.2 ± 3.0 kJ mol^{-1}. Based on our observations a model is proposed taking into account various probable steps involved in the formation of NP aggregates to delineate the underlying reason towards barrier to activation.*

[Dutta et al. RSC Adv. 2016, 6, 82138] - Reproduced by permission of The Royal Society of Chemistry. http://pubs.rsc.org/en/content/articlelanding/2016/ra/c6ra17561a#!divAbstract

3.1. Introduction

Systematic organization of nanoscale particles into well-defined geometries, based on the principle of synthetic chemistry,[1] has primarily remained a challenge. The success in this regard has understandably been limited. Further, it is still worth pursuing research in transforming well dispersed, stable metal or semiconductor NPs into hierarchically ordered structures,[2-6]which are not ordinarily achievable through chemical route synthesis and which will have superior optical,[7] electronic,[8-9] magnetic[10] and chemical properties[11] in comparison to their monodispersed counterparts.[12-14] It has also been realized that aggregation of nanoscale particles takes place in the presence of biomolecules that carry information about the nature of their interactions[15-16] and hence has been applied in biosensing and bioassays and also finds importance in understanding the fate of nanoscale materials in human and other animal models.[17]

Recent efforts in studying the growth of nanoscale particles are based on two hypothesis: Ostwald ripening (OR) in which larger particles are grown at the expense of smaller particles and oriented attachment (OA), where two identical crystal lattice planes of the reacting NPs comes in contact with each other, leading to the formation of a larger particle via fusion at the contact planes.[18-19] While the mechanism of coalescence or attachment of particles have drawn significant attention, the future of the field may lie in improved understanding of the kinetics, the dynamics and also the thermodynamics of reaction of NPs. This may also help in fulfilling the great expectations of chemists with regard to using nanoscale particles as the building blocks of new materials. The above points are being addressed by probing the effects of temperature, stabilizing ligand and size of NPs in governing aggregation and growth processes of colloidal particles.

Apart from studying the kinetics of aggregation of NPs under various physical and chemical conditions, much effort has gone to understand the mechanism of aggregation process. Therefore, most of the studies reported so far are based on system where kinetics and aggregation mechanism have been followed for ligand (i.e. stabilizing agent) capped NPs, specifically those of transition metal oxide NP[20-21] and long chain containing ligand protected Au NPs in organic media.[22-23]

We have recently reported the dominance of first order kinetics in aggregation reaction of partially bare Au NPs - obtained after dialysis of as-synthesized citrate-stabilized Au NPs (Cit-Au NPs)[24] where the rate law was established based on a proposed model.

3.2. Outline of the Present Work

Herein, we have attempted to study the temperature-dependent kinetic behaviour of the aggregation reaction of partially bare Cit-Au NPs, obtained by depletion of citrate stabilizer via dialysis in the aqueous phase. Temperature dependence of aggregation was followed by using UV-vis spectroscopy and the resulting aggregate morphologies were analysed using transmission electron microscopy (TEM). Rate constant values obtained at five different temperatures from time-dependent kinetic study were then used to obtain the activation energy of the aggregation process. Further, plausible colloidal aggregation mechanism was delineated and a model has been proposed to account for the activation energy obtained herein.

3.3. Experimental Section

3.3.1. Materials

Tri-sodium citrate dihydrate (Merck), gold(III) chloride (30 wt% in HCl, Sigma-Aldrich), dialysis tubing membrane, LA 393-10MT, 12kDa, (HIMEDIA), sodium hydrogen carbonate (Merck), sodium chloride (Merck), disodium ethylene diaamine tetraacetate dihydrate ($Na_2EDTA.2H2O$, Merck) and HPLC-grade acetonitrile (Spectrochem) were used as received. Milli-Q grade water (18.2 MΩ cm, Millipore) was used for synthesis as well as for other experimental works.

3.3.2. Dialysis tubing membrane activation

Dialysis membrane of required length was cut and activated by stirring the membrane in Milli-Q grade water containing 1.0 mM Na_2EDTA and 0.2% $NaHCO_3$ at 100 °C for 60 min. Thereafter the activated membrane was rinsed thoroughly with Milli-Q grade water three times to wash out the excess $NaHCO_3$, Na_2EDTA

and other by products, if any. Finally, the activated dialysis membrane was transferred in fresh Milli-Q grade water and stored at 4 °C for further use.

3.3.3. Synthesis of citrate stabilised gold nanoparticles (Cit-Au NPs)

Synthesis of Cit-Au NPs was carried out following a reported method[25] with some modification. An aqueous solution (100 mL) of trisodium citrate (1.7 mM) was refluxed at 135 °C with continuous stirring. As the solution started boiling, 1.0 mL of 1.7×10^{-2} M stock $HAuCl_4$ solution was added and the reaction was continued for next 30 min, keeping the reaction condition same. The appearance of deep red color indicated the formation of Au NPs. The as-synthesized Au NPs were characterized using UV-vis spectroscopy and TEM analysis. Therefore, assuming full reduction of gold ions to gold atoms, concentration of as synthesized Cit-Au NPs was calculated to be 1.64 nM (Refer **calculation A3.1**, **Appendix**).[24] The area under the UV-vis spectrum (obtained after subtracting the background scattering following deconvolution) of as synthesized Cit-Au NPs integrated over the wavelength range 400 nm – 800 nm was taken to be proportional to its concentration and a standard conversion factor of 60.318 = 1.64 nM was arrived at and used throughout the experiment to calculate the concentration of Au NPs.

3.3.4. Time-dependent kinetic study of reaction of partially bare Au NPs at five different temperatures

The kinetic experiments were carried out using the same procedure as reported earlier.[24] A measured volume of Cit-Au NPs at a particular concentration was dialyzed against Milli-Q grade water. The dialysis was carried out by transferring 6 mL of Au NP dispersion (at a fixed concentration) to the pre-activated dialysis membrane tube (clamped tightly from both the ends to ensure that volume of Au NP dispersion was maintained) immersed in a beaker containing 800 mL of Milli-Q water. The sample dispersion was then dialyzed by stirring for 270 min, at room temperature, following which kinetic study was carried out. Immediately after 270 min of dialysis, an aliquot (3 mL) from the dialyzed Au NP dispersion was transferred to an UV-cuvette and allowed to attain the desired temperature, which typically took about 60 s. It may be mentioned here that the attainment of desired temperature by the dispersion was measured independently by using a thermometer. Thereafter time-dependent UV-vis spectrum was recorded for next 35 min, at an interval of 5 min. each. The initial time (t=0 min) was marked at the point at which the solution attained the desired temperature. Hence, the time-dependent kinetic study was carried out at five different temperatures viz. 20 °C, 30 °C, 40 °C, 50 °C and 60 °C for four different dispersions of Cit-Au NPs viz. 1.59 nM, 1.19 nM, 0.78 nM, 0.51 nM subjected to dialysis. Also to be mentioned, that the time for attainment of a particular temperature by the dispersion was sufficiently short – in comparison to the total kinetic measurement time - to affect the kinetics of the reaction significantly. In other words, the short initial time spent to attain a particular temperature did not alter the overall kinetics of the reaction.

3.3.5. Quantification of citrate removal following dialysis by high performance liquid chromatography (HPLC)

High performance liquid chromatography (HPLC) was employed to quantify the amount of citrate removed following dialysis of Cit-Au NPs with original dispersion concentrations of 1.59 nM, 1.19 nM, 0.78 nM, 0.51 nM. HPLC analyses were performed in an isocratic mode, with mobile phase consisting of water: acetonitrile (95:5; v/v) mixture. The system was operated at a flow rate of 1 mL min-1 with an injection volume of 20 uL at temperature 25^{o}C. The detection was carried out at 210 nm wavelength. Following dialysis of Cit-Au NPs, an aliquot from the solution in the dialysis beaker outside the dialysis bag was collected and 20 uL sample for each concentration was injected into the column. Under the above condition, the elution time for citrate was found to be 2.6 min. **Figure A3.1**, **Appendix** shows a typical chromatogram of a standard sodium citrate solution and **Figure A3.2**, **Appendix** shows a typical chromatogram obtained for citrate corresponding to the medium in contact with 1.59 nM Au NP dispersion subjected to dialysis for 270 min. A standard calibration plot for sodium citrate was then obtained based on the integrated area under chromatogram versus known concentration of sodium citrate. The identification and quantification of citrate for all samples were done by comparing the retention time and from the area under the chromatogram obtained in each run with that of the calibration obtained with the standard.

3.3.6. Calculation of rate constant and activation energy of reaction of partially bare gold nanoparticles

Kinetic parameters were obtained following both integrated rate method and differential rate method.

(a) Integrated rate method

The change in extinction in the UV-vis spectrum of dialyzed Au NPs at 521 nm was monitored as a function of time at five different temperatures i.e. 20 °C, 30 °C, 40 °C, 50 °C and 60 °C. The measurement was done five times at each temperature for 1.59 nM of dialyzed Au NP. Kinetic rate constant at each temperature was thereafter obtained from the slope of ln (Ext.) versus Time plot. The kinetic rate constant so obtained at five different temperatures were then fitted to Arrhenius equation to obtain activation energy from ln k versus T^{-1}(K) plot.

(b) Differential rate method

The time dependent extinction spectra obtained for all four concentrations of Au NP (i.e. 1.59 nM, 1.19 nM, 0.78 nM, 0.51 nM) at five different temperatures were deconvoluted into three component spectra – the first deconvoluted band represented spectrum due to background scattering (dotted green curve), the second represented the primary deconvoluted band (blue curve) and the third represented the secondary deconvoluted band (pink curve) (refer **Figure A3.3, Appendix**). The extinction spectra were deconvoluted using Lorentzian non-linear curve fitting function available in Origin 7.0 software.[24,26] Based on our previous report, the reaction followed first order rate law with respect to the partially bare monomer Au NP.[24] Therefore, we monitored the time-dependent change considering area under the primary absorption band (and hence the concentration of Au NP) with time to calculate initial rate of reaction, rate constant and hence the activation energy value for the reaction. The concentrations of Au NP during the time-dependent study were obtained from the peak area to concentration conversion factor (as stated above in experimental **Section 3.3.3**). Rate constants at five different temperatures were obtained from the slope of *Initial rate vs Initial concentration* plot. Initial rate was obtained from the slope (exponential fitting of first four data points) of rate of change of concentration of Au NP (during time-dependent study of dialyzed Au NPs corresponding to four different concentrations) with time at all five temperatures. (Refer **Figure A3.4-3.8**, **Appendix**). The rate constants so obtained at five different temperatures were further fitted to Arrhenius equation to obtain the value of activation energy.

3.3.7. Calculation of flocculation parameter for reaction of partially bare Au NPs at five different temperatures

In order to determine the flocculation parameter[27] we put forth the deconvolution method, where the extinction spectra obtained during time-dependent study were decomposed into three different components - as discussed in experimental **Section 3.3.6**(**b**). The flocculation parameter herein, have been calculated from the integrated area under the third deconvoluted band corresponding to peak at ~ 600 nm, that was obtained after deconvoluting each of the UV-vis spectra recorded sequentially with time for 35 min, at five different temperatures viz., 20 °C, 30 °C, 40 °C, 50° C, 60 °C for 1.59 nM dialyzed Au NP dispersion. The area gives a measure of extent of aggregates formed at any instant of time during the course of the reaction.

3.3.8. Calculation of Ionic Strength of the Cit-Au NP solution after dialysis

Ionic strength of the Au NP dispersion was calculated using following equation,

$$Ionic\ Strength = I = 0.5 \sum C_i Z_i^2 \qquad (1)$$

where C_i and Z_i are respective molar concentration and charge present on each ion in the medium. The concentration of ions in the solution was measured, as described below:

[Na^+] that was removed by dialysis was measured using atomic absorption spectroscopy (AAS). The [Na^+] remaining in the dialysis bag was obtained by subtracting the amount of Na^+ removed (by dialysis) from the initial amount of Na^+ taken in the bag. $[H^+]$ and $[OH^-]$ were obtained from the measured pH value and ionic constant of water respectively. Chloride ion concentration $[Cl^-]$ that was removed by dialysis was measured using ion chromatography and therefore total $[Cl^-]$ remaining in dialyzed Au NP dispersion was accounted for by considering initial concentration of $HAuCl_4$ present before dialysis.

Citrate concentration in dialyzed Au NP dispersion was obtained by considering the following dissociation equilibria for sodium citrate in water,

$$H_3citrate \Leftrightarrow H_2citrate^- + H^+ \quad , pK_a = 3.12 \qquad (2)$$

$$H_2citrate^- \Leftrightarrow Hcitrate^{2-} + H^+ \quad , pK_a = 4.76 \qquad (3)$$

$$Hcitrate^{2-} \Leftrightarrow citrate^{3-} + H^+ \quad , pK_a = 6.39 \qquad (4)$$

Applying Henderson-Hasselbalch equation, concentration ratio between citrate species present at the experimental pH was obtained. Amount of citrate removed during dialysis was estimated from HPLC measurement (Refer **Table A3.1**, **Appendix**). Thus total citrate amount present in the Au NP dispersion after dialysis was obtained by considering the amount of citrate initially present before dialysis. Thereafter, the concentration of all the citrate species in the dialyzed Au NP dispersion was determined from the total calculated citrate concentration after dialysis. It is to be noted that under the given experimental conditions, $[citrate^{3-}]$ would be the predominant species present in the medium.

Finally, using the measured concentration of each ion in the solution and their respective charge, the ionic strength was calculated using **equation 5**. (**Table A3.1**, **Appendix**)

$$\begin{aligned} I = 0.5\,[\,& C_{H_3Citrate} Z_{H_3Citrate}^2 + C_{H_2Citrate^-} Z_{H_2Citrate^-}^2 \\ & + C_{HCitrate^{2-}} Z_{HCitrate^{2-}}^2 + C_{Citrate^{3-}} Z_{Citrate^{3-}}^2 \\ & + C_{H^+} Z_{H^+}^2 + C_{OH^-} Z_{OH^-}^2 + C_{Na^+} Z_{Na^+}^2 \\ & + C_{Cl^-} Z_{Cl^-}^2 \;] \qquad \ldots\ldots \quad (5) \end{aligned}$$

3.4. Characterization

UV-vis measurements were recorded using double beam UV-vis spectrophotometer - Perkin Elmer Lambda 25 assembled with PTP (1+1) Peltier Temperature Programmer. TEM images were obtained using JEOL JEM 2100 transmission electron microscope, operating at maximum operating voltage of 200 kV. Sample preparation for TEM was done by drop casting 5 µL of Au NP dispersion on the carbon coated copper grid, which was allowed to air dry. Citrate estimation was performed on a Shimadzu spectrophotometer (Shimadzu Corporation, Kyoto, Japan) equipped with reverse-phase C18G-column (4.6 mm × 250 mm, 5 µm particle size) with a photo diode array UV-vis detector. Chloride ion concentration in the samples were measured using a Metrohm 792 Basic Ion Chromatograph (IC) (Metrohm AG, Herisau, Switzerland) fitted with a Metrosep A Supp 5 column (250 mm × 4 mm), a guard column, and a conductivity detector. The eluent used was Na_2CO_3, $NaHCO_3$ (32 mmol, 1 mmol) with a flow rate of 0.7 mL/min. Sodium ion concentrations in the samples was determined using atomic absorption spectrometer (Varian, AA240, Netherlands).

3.5. Results and Discussion

Cit-Au NPs were synthesised using an established protocol (refer to Experimental **Section 3.3.3**). TEM and UV-visible measurements shown in **Figure 3.1A** and **Figure 3.1.B (i)** respectively confirmed the formation of well dispersed Cit-Au NPs. The NPs so formed showed an SPR band at 518 nm in the UV visible spectrum. TEM measurement established the formation of spherical Au NPs with an average diameter of 15.0 ± 1.3 nm. The Cit-Au NPs of size ~ 15 nm are known to adopt an equilibrium truncated octahedron shape, with (111) followed by (100) face being the major exposed surface planes.[28]

Reactivity of Cit-Au NPs leading to agglomeration of particles can be initiated by change in pH of the medium,[29] addition of inorganic salt (such as NaCl, KCl etc.)[30] or by interaction with biomolecules such as proteins and DNA.[15,31] However, we have recently demonstrated that dialysis leads to lowering of concentration of the citrate in the medium thus making the NPs partially bare of the stabilizers.[24] This results in a metastable state where NPs react with each other during dialysis and thereafter. The amount of citrate that was removed after

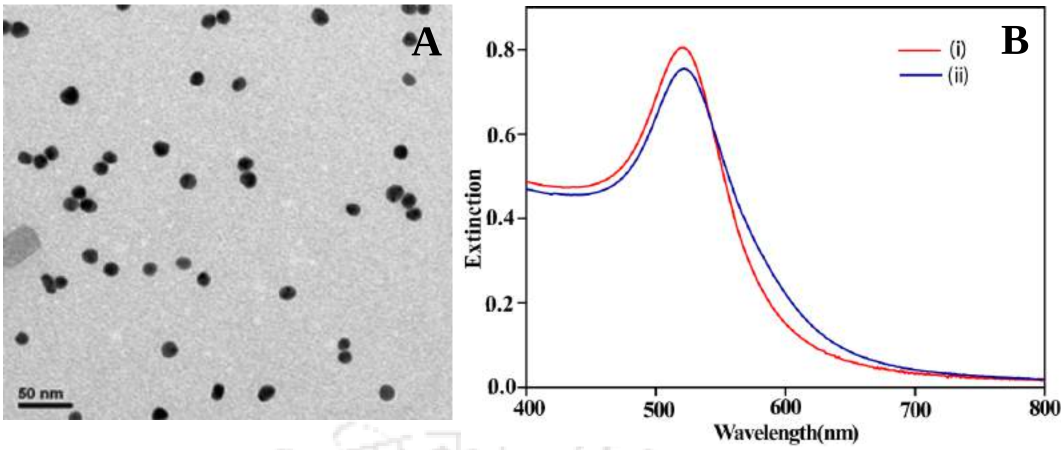

Figure 3.1. (**A**) Representative TEM image of as-synthesized Cit-Au NPs before dialysis. (**B**) The UV-Vis spectrum of (**i**) as-synthesized Cit-Au NPs before dialysis and (**ii**) that of Au NPs (1.59 nM) recorded following dialysis for 270 min.

dialysis was quantified by HPLC measurement of the aqueous mixture accumulated in the dialysis beaker outside the dialysis bag. (**Table A3.1**, **Appendix**) The amount of citrate removed during 270 min dialysis of the four different Cit-Au NP dispersions was found to linearly increase with the concentration of NPs in the dispersion. Further we have measured the pH and ionic strength of the dialyzed Au NP dispersion (as tabulated in **Table A3.1**, **Appendix**), which could have a marked effect on the reaction rate. Careful control of dialysis time and concentration of the NPs led to control over citrate in the medium, which in turn helped in controlling the aggregation reaction of the NPs following dialysis. Experimentally, UV-vis spectrum of the Cit-Au NP dispersion, which was subjected to dialysis for 270 min, showed a major peak at 521 nm with slight broadening at ~ 600 nm as is evident from **Figure 3.1.B**(**ii**). The broadening is attributed to the presence of aggregated NPs in the medium. The broadening was minimally present when dialysis was carried out for a shorter period (i.e., 250 min) while it increased for the samples which were dialyzed for a longer period of time (i.e., 320 min). It has been observed earlier that the intensity of the peak at 600 nm increased with time when the dialyzed sample was left to react at room temperature.[24] This has helped follow kinetics of reaction of the NPs. Importantly, the reaction led to the increase in extinction accompanied by broadening of the UV-vis spectrum of the Au NPs at ~ 600 nm with concomitant decrease in extinction at 521 nm due to monomeric Au NPs.

Specifically, contribution due to the second peak associated with the aggregated particles could be deconvoluted[24] and can be used to follow the mechanism of kinetics of the reaction. In a colloidal medium, the extinction of n NPs per unit volume can be written as,[32]

$$A = \log_{10}\frac{I_0}{I} = \frac{nQ_{ext}l}{2.303} \qquad (6)$$

Here, I_o and I are the intensities of incident and transmitted light, l is the path length of the sample and Q_{ext} is the extinction coefficient of single Au NP. The same equation can be considered valid for both individual NPs and aggregated NPs. Thus, when both the species are present in the medium, total extinction of light may be written as,[16,24]

$$\begin{aligned} A(\lambda) &= Q_{ext,NP}(\lambda) C_{NP}\, l + Q_{ext,agg}(\lambda) C_{agg} l \\ &= A_{Au\ NP}(\lambda) + A_{Au\ NP,agg}(\lambda) \qquad (7) \end{aligned}$$

Here, $A(\lambda)$ is wavelength dependent total extinction, and $Q_{ext,NP}(\lambda)$ and $Q_{ext,agg}(\lambda)$ are the extinction coefficients due to free monomeric Cit-Au NPs and aggregated Cit-Au NPs, respectively. C refers to the concentration of above mentioned species and l is the path length. It has been observed that the increase in intensity of the second peak at ~ 600 nm is commensurate with the rate of decrease in intensity due to single NP peak at 521 nm. The reaction followed first order rate law with respect to the concentration of the monomeric NPs. This has been explained based on the reaction of the monomer with aggregated particles, formed during dialysis, the concentration of which increased at the expense of the monomers. Since [citrate^{3-}] is the predominant species (see experimental **Section 3.3.8**) the primary reaction can be written as,

$$\left\{Au(citrate)_x\right\}^{3x-} + \left\{Au_n(citrate)_y\right\}^{3y-} \xrightarrow{k} \left\{Au_{n+1}(citrate)_{x+y}\right\}^{3(x+y)-} \quad where\ n \geq 1 \qquad (8)$$

Here, x and y are the number of citrate ions attached to individual NP and aggregated NPs (with n number of NPs in the aggregated) respectively. The kinetic expression for the first order loss of individual NP concentration can be represented by,[24]

$$\left[\left\{Au(citrate)_x\right\}^{3x-}\right] = \left[\left\{Au(citrate)_x\right\}^{3x-}\right]_0 \exp(-kt) \text{.....} \quad (9)$$

In order to pursue studies related to temperature-dependent kinetics of aggregation, time-evolution of the UV-vis spectra were recorded for the dialyzed Au NP dispersions in the temperature range of 20 °C – 60 °C for four different concentrations of dialyzed Au NP. The details of the procedure are given in the Experimental **Section 3.3.4**. **Figure 3.2**(**A-E**) shows the time evolution of the UV-vis spectra recorded at 20 °C, 30 °C, 40 °C, 50 °C and 60 °C, respectively for 1.59 nM Cit-Au NP dispersions dialyzed for 270 min at room temperature. Two distinct primary changes in the spectra were observed for all the samples. The value of the peak at 521 nm decreased monotonically with time, while that due to peak at ~ 600 nm increased monotonically along with broadening. Further, this gradual broadening of the SPR band at ~600 nm is accompanied with the appearance of an isosbestic point at all the temperature-dependent spectral evolutions. (**Figure 3.2**) The decrease in the peak intensity at 521 nm, due to monomeric species is indicative of decrease in their population in the medium; whereas the increase in peak intensity at 600 nm indicated the increase in the population of the aggregated products with time.

The changes in the UV-vis spectra indicated reactions of individual NPs leading to the increase in the concentration of the aggregated products. Further, as shown in the insets of all the panels in **Figure 3.2**, the logarithm plots of extinction at 521 nm with time are linear for all the spectra. This is consistent with the first order loss of monomeric NPs in the reaction medium at all temperatures mentioned (**Equation 9**).

Further similar observations were made during time dependent study carried out at five different temperatures for three different Au NP dispersions viz., 1.19 nM, 0.78 nM, 0.51 nM (which were dialyzed for 270 min. at room temperature). In addition, the extinction spectra so obtained (within experimental temperature range) corresponding to four different concentrations of dialyzed Au NPs were

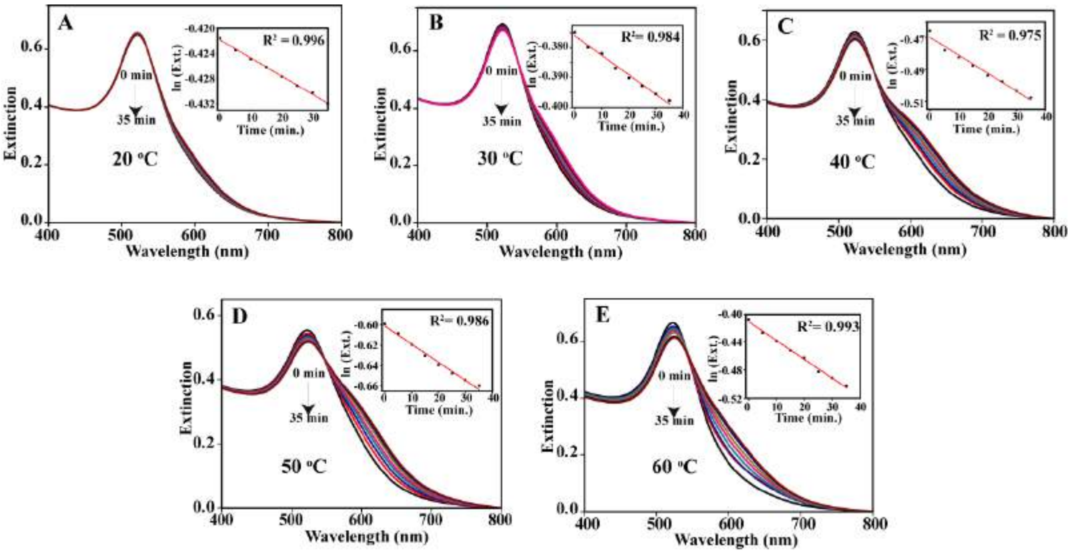

Figure 3.2. Time evolution of the surface plasmon extinction spectra of partially bare Au NPs formed after 270 min of dialysis of 1.59 nM Cit-Au NP dispersion monitored at five different temperatures viz. (**A**) 20 °C, (**B**) 30 °C, (**C**) 40 °C, (**D**) 50 °C and (**E**) 60 °C. Data points were fitted to a linear function the slope of which is equal to the rate constant. The insets show the corresponding *ln(Ext.) versus time* plot, where the *Ext.* in the y-axes refers to extinction.

deconvoluted and the rate of change of concentration of monomeric Au NP corresponding to peak at 521 nm (as obtained from primary deconvoluted band) with time was monitored. The results indicated exponential decay in the concentration of the monomeric NPs with time (**Figure A3.4-3.8**, **Appendix**) i.e., the first order rate law prevailed for the reaction at all the temperatures measured (as far as the concentration of the monomeric species was concerned). Control experiments were also performed, wherein 1.59 nM Au NP dispersion was transferred to an UV cuvette and allowed to stand for 270 min. This was followed by measuring time-dependent extinction spectra for the Au NP dispersion at five different temperatures viz., 20 °C, 30 °C, 40 °C, 50 °C, 60 °C (**Figure A3.9**, **Appendix**) for the next 30 min. Such spectra revealed no broadening, shift or decrease in extinction. The results supported the stability of the dispersion of as-synthesized Au NPs at different temperatures, which is consistent with established literature.[33]

Importantly, the observed enhanced rate of colloidal aggregation with temperature is similar to the general trend observed in ordinary chemical reaction. It is noteworthy that the peak position of the SPR band of the aggregated units (**Figure 3.2**) red-shifted by approximately 25 nm, which is also reflected in a similar shifting of the isosbestic point, with increasing temperatures (20 °C to 60 °C). This is indicative of increase in the size of the aggregated units. It is thus likely that the aggregation process is a reaction limited process, as temperature is expected to have a marked effect on the surface reactivity and hence influence the final size of the aggregate units so formed. That the rate of the reaction increased with temperature (**Figure A3.4-3.8**, **Appendix**) provided an impetus to further investigate the kinetic parameters.

Table I. Mean rate constant values obtained at five different temperatures calculated following the integrated rate law method. Mean constant was calculated from the average of five data set, obtained from the slope of *ln(Extinction) versus time (min)* plot at five different temperatures.

Temperature (°C)	**Mean rate constant, k (min^{-1})/ 10^{-3}**
20	**0.3±0.1**
30	**0.4±0.1**
40	**0.7±0.1**
50	**1.2±0.2**
60	**1.5±0.5**

Kinetic rate constants (k) were calculated based on the UV-vis spectra shown in **Figure 3.2**. The rate constants as obtained following integrated rate law were found to increase monotonically with temperature from 20 °C to 60 °C (**Table I**). The dependence of the experimental kinetic rate constant on the temperature was further used to fit into Arrhenius equation[34] to extract the activation energy, E_a, of reaction of partially bare Au NPs. The plot of ln(k) versus T^{-1}, as shown in **Figure 3.3.A**, could be fitted well in a straight line with a negative slope, which indicated that the reaction rate constant followed Arrhenius behaviour. The activation energy, E_a of the reaction was calculated from the slope (negative), which resulted in a value of 36.2 ± 3.0 kJmol^{-1}. It is apparent that for the reaction of partially bare Au NPs leading to aggregation of particles the Arrhenius equation remained valid in the temperature range 20 ° – 60 °C (as measured) and therefore, validated the temperature independent activation energy.[35] In addition, temperature dependent kinetics of three different Au NP dispersions viz. 1.19 nM, 0.78 nM, 0.51 nM subjected to dialysis were also followed.

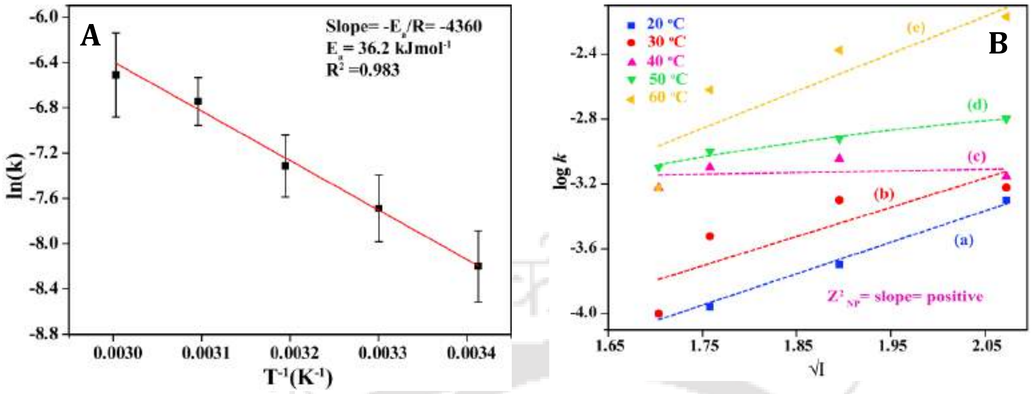

Figure 3.3. (**A**) Arrhenius plot of ln(k) versus temperature inverse (in absolute temperature scale). Data points were fitted to a linear function in order to obtain the activation energy from the slope (Ea = slope × R). (**B**) Plot of $\log_{10}$ k versus the square root of ionic strength of the Au NP dispersion (corresponding to samples with 1.59 nM, 1.19 nM, 0.78 nM, 0.51 nM) at temperatures (**a**) 20 °C, (**b**) 30 °C, (**c**) 40 °C, (**d**) 50 °C and (**e**) 60 °C.

The rate constant values were then calculated from the *initial rate vs concentration* plot as shown in **Figure 3.4**(**A-E**). Further, the kinetic rate constant values so obtained at five different temperatures were then fitted into Arrhenius equation as discussed above to find the activation energy of the reaction. The slope obtained from the linear fit of $ln(k') \ vs \ T^{-1}$ plot as evident from **Figure 3.4.F** gave the activation energy equal to 36.0 kJ mol^{-1}, which is in close match to the activation energy value so obtained following integrated rate law (**Figure 3.3.A**). Therefore enthalpy of activation was obtained from the slope of Eyring plot[36] i.e, $\ln\frac{k}{T} vs \frac{1}{T}$ (**Figure A3.10**, **Appendix**) with an enthalpy of activation equal to 33.9±3.0 kJmol^{-1}. Further, the influence of ionic strength on the reaction rate constant obtained from time-dependent kinetic study of partially bare Au NP dispersions at concentrations 1.59 nM, 1.19 nM, 0.78 nM, 0.51 nM, was investigated using Bronsted - Bjerrum equation,

$$\log k = \log k_O + 2AZ_A Z_B \sqrt{I} \qquad .... \qquad (10)$$

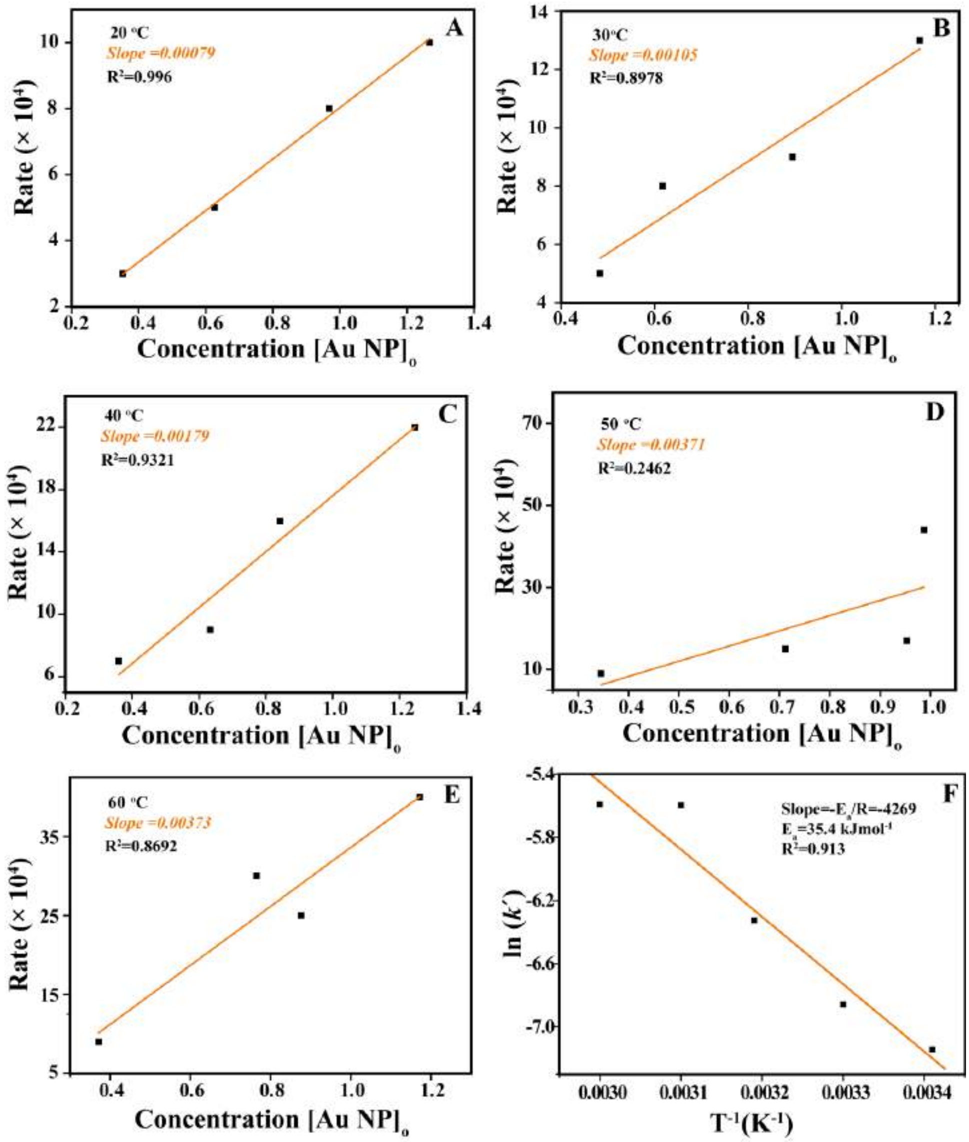

Figure 3.4. Plot of *Initial rate versus concentration* (at t = 0 min) of dialysed Au NP at five different temperatures viz. (**A**) 20 °C, (**B**) 30 °C, (**C**) 40 °C, (**D**) 50 °C and (**E**) 60 °C. Data points were fitted to linear function and kinetic rate constant at the respective temperature was obtained from the slope of the linear fit. (**F**) Plot of $ln(k')$ *Vs* T^{-1} where k' represents the rate constant (obtained using initial rate method) and T represents temperature in Kelvin unit. Data points were fitted to linear function to obtain activation energy from the slope of the linear fit.

where k refers to the experimentally observed rate constant, k_o refers to the rate constant at zero ionic strength, A refers to Debye-Huckel constant which varies with the temperature and dielectric constant of the medium, Z_A and Z_B refer to ionic charge of the reacting NPs and I refers to total ionic strength of the medium. Therefore, experimental rate constant obtained from the time-dependent kinetic study at five different temperatures were compared with the ionic strength of the dispersion corresponding to four different concentrations of Cit-Au NPs subjected to dialysis at room temperature. Following **equation** (**10**), the logarithm of the rate constant was plotted versus square root of the ionic strength at temperature 20 °C – 60 °C as shown in **Figure 3.3.B**. Data points so obtained were fitted to linear graph, which provided a positive slope that equals to the product of ionic charge on two reacting species carrying similar charges. **Figure 3.3.B** implies that at all the temperatures the reaction rate constant showed an increasing trend with increase in ionic strength of the medium.

In order to probe the mechanism of the reaction of the NPs, transmission electron microscopy (TEM) studies of the aggregation process with time were performed. Microscopic images were recorded for samples collected from the medium, after the reactions were allowed to proceed for 20 min. at respective temperatures as shown in **Figure 3.5**. The representative images recorded for three different temperatures viz., 20 °C, 40 °C and 60 °C are depicted in **Figure 3.5.A**, **3.5.B** and **3.5.C**, respectively; while **Figure 3.5.D** shows the magnified view of aggregates from a select region in **Figure 3.5.C**. It is evident from the images that the extent of aggregation increased with temperature for the same reaction time and initial state. Though it is likely that aggregation may occur due to evaporation induced drying of colloids on the TEM grid; however, we have also observed coalescence of partially bare Au NPs to occur along with the increase of aggregation, the extent of which increased with the increase of reaction time. Thus, while at 20 °C there were a few and smaller aggregate units, at 60 °C not only were there extensive aggregation to larger units but there was also coalescence of the NPs which could be observed. However, the Au NPs did not aggregate in any particular order (such as linear), but were attached with each other in random fashion, forming compact aggregates. The observation of extensive aggregated structures with increasing temperature correlated well with the UV-vis extinction spectra, which showed increased broadening with temperature. In other words, growing size of the aggregates with the formation of branched and three dimensional units, as seen over extended regions in typical TEM images, represented the second peak appearing at ~ 600 nm in the UV-vis extinction spectra. It has been reported that the second peak, occurring in the extinction spectrum of aggregated Au NPs indicated the size of the aggregates, the peak wavelength of which increased with increasing size.

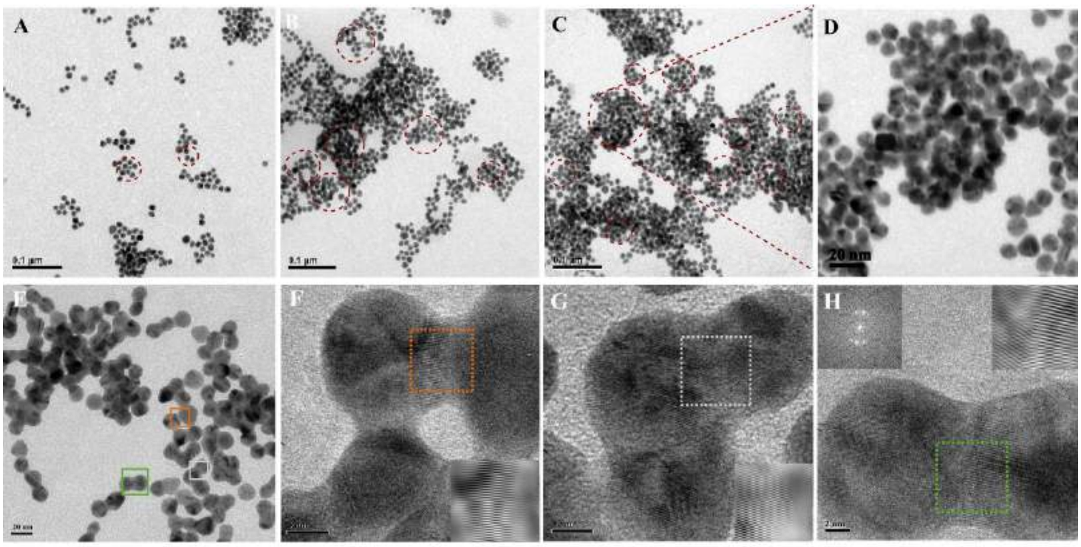

Figure 3.5. Representative TEM images of partially bare Au NPs of the samples collected at 20 min after commencement of the reaction at temperature (**A**) 20 °C, (**B**) 40 °C, (**C**) 60 °C, (**D**) magnified view from a select region of the image in **Figure 3.5.C**, (**E**) Additional TEM image of Au NPs recorded for the sample collected after 20 min of reaction at 40 °C. Corresponding HRTEM images shown in (**F**), (**G**) and (**H**) represents three different regions from image (**E**). Insets of (**H**) are the FFT (left) and IFFT (right) images, showing twinning defect due to oriented attachment of two Au NPs.

For an fcc crystal, the following order holds in terms of surface free energy[28] i.e. $Au_{\gamma}(100) > Au_{\gamma}(111)$. Structural based modelling studies have revealed that citrate adlayers on AuNP surface show ordered adsorption where citrate tends to adsorb on the (111) and (100) surfaces through 1-D chain network, thereby rendering electrostatic stabilization to the Au NP surface.[37-38] It is likely that during dialysis the Cit-Au NPs were partially stripped off the stabilizer, exposing the (111) surface facet, as this face has the least surface free energy. To reduce the surface energy, the partially exposed colloidal particles, undergoing random thermal collisions in the medium, tend to attain surface passivation by forming aggregate units. However, not all collisions are successful, and only a small fraction of collisions lead to sticking of these NPs yielding aggregates, which further coalesce with time. Nature of the product so formed after only 20 min of commencement of the reaction at 40 °C were examined by HRTEM and is shown in **Figure 3.5.(F-H)** Note that while large-scale aggregation of Au NPs is evident in **Figure 3.5.E**, closer inspection from select regions on the TEM grid revealed large scale coalescence of two or more particles mostly sharing common crystallographic orientations (**Figure 3.5.F**, **G** and **H**). Inverse fast Fourier transform (IFFT) analysis of selected region (as shown in insets) of HRTEM images in **Figure 3.5.F** and **3.5.**G revealed fused Au NPs having (111) common lattice fringe with d-spacing value of ~ 0.23 nm. At times twinning faults[39,40] could be observed in some of the region in the grid as represented in **Figure 3.5.H**. Insets to **Figure 3.5.H** show the fast Fourier transform (FFT) of the twinned region (top left inset) and the corresponding IFFT image (top right inset).

The aggregation reaction of partially bare Au NPs need to transverse the following four basic steps: (**a**) diffusion of the NPs towards each other, (**b**) collision and reorientation of NPs, (**c**) sticking/attachment of the NPs to form larger aggregate units, followed by (**d**) coalescence. Based on this general scheme, two types of models have been proposed for colloidal aggregation widely in the literature: namely - diffusion limited colloidal aggregation (DLCA) and reaction limited colloidal aggregation (RLCA). In a stable colloidal suspension, the stability of NPs is determined by the repulsive energy[41-42] barrier between two approaching particles, according to Derjaguin-Landau-Verwey-Overbeek (DLVO) theory. In DLCA, the rate of aggregate formation is limited by the time taken by the individual colloidal particles to approach towards each other in the medium and coalesce i.e., a situation feasible when the repulsive barrier between particles is much less than the thermal energy, k_BT.[43] In this scenario, the individual particles stick as soon as they collide. On the other hand, in the RLCA[44] the rate of product formation is limited by the actual reaction step, and is applicable when the energy barrier E_a for the reaction step is either comparable or larger than k_BT, such that particles undergo many random collisions before successfully attaching with each other and forming aggregates.

According to the report by Kraus et al, and Schreiber et al,[22,45] a model based on Smoluchowski theory, DLCA follows a power law growth of mean radius of aggregate with time, whereas RLCA shows an exponential dependent growth of mean radius of aggregate with time. The growth of aggregate, in terms of mean radius, with time can be related to an empirical parameter called *"flocculation* *parameter”*,[27] I, which has been defined as the integral of absorbance[45] under the secondary deconvoluted band (i.e., the third deconvoluted band herein) corresponding to the aggregated NPs and is as noted below (**equation 11**).

$$Flocculation\ Parameter,\ I = \int_{400}^{800} I_{Abs}(\lambda)d\lambda \qquad (11)$$

where $I_{Abs(\lambda)}$ refers to absorbance of aggregates at a particular wavelength, λ, and the flocculation parameter is its integral in the wavelength range 400 nm to 800 nm corresponding to the secondary deconvoluted band. Flocculation parameter (refer to experimental **Section 3.3.7**) was determined at five different temperatures (viz., 20 °C, 30 °C, 40 °C, 50 °C, 60 °C) as obtained from the time-dependent study of 1.64 nM Au NPs (dialyzed). The same when plotted as a function of time in a *log-log* plot as in **Figure3.6.A** showed an exponential aggregate growth rate, indicative of the operation of RLCA mechanism at these temperatures for the reaction of partially bare Au NPs obtained after dialysis. Further, TEM analysis of aggregates obtained at three different temperature viz., 20 °C, 40 °C and 60 °C was used to obtain fractal dimension value (Hausdorff dimension) d_f, from the plot of $ln\ N\ vs\ ln\ L$. The slopes obtained from the plots (**Figure 3.6**.(**B**, **C** and **D**) gave $d_f \sim 2.07$, $d_f \sim 2.00$, and $d_f \sim 1.96$ at 20 °C, 40 °C and 60 °C, respectively. The values being close to 2.00 supports the slow aggregation regime[46] and substantiate our claim of RLCA mechanism. Also it is interesting to note that the values of the rate constants (as obtained by integrated rate law) for the NP aggregation reaction in the aqueous medium, as shown in (**Table I**) as well as those obtained from initial rate method as depicted from **Figure 3.4**.(**A-E**) are much lower than those expected for a diffusion limited reaction in aqueous medium[22] within the said temperature regime. Hence, the observed aggregation reaction most likely followed the RLCA mechanism, possibly governed by a rate determining step with activation energy barrier 36.2 ± 3 kJ mol^{-1}.

Recent literature report[37] reveals that citrate forms a bilayer consisting of unit of citrate trimer consisting of two citrate anions adsorbed through central carboxylate and dangling citrate moiety hydrogen bonded with the two adsorbed

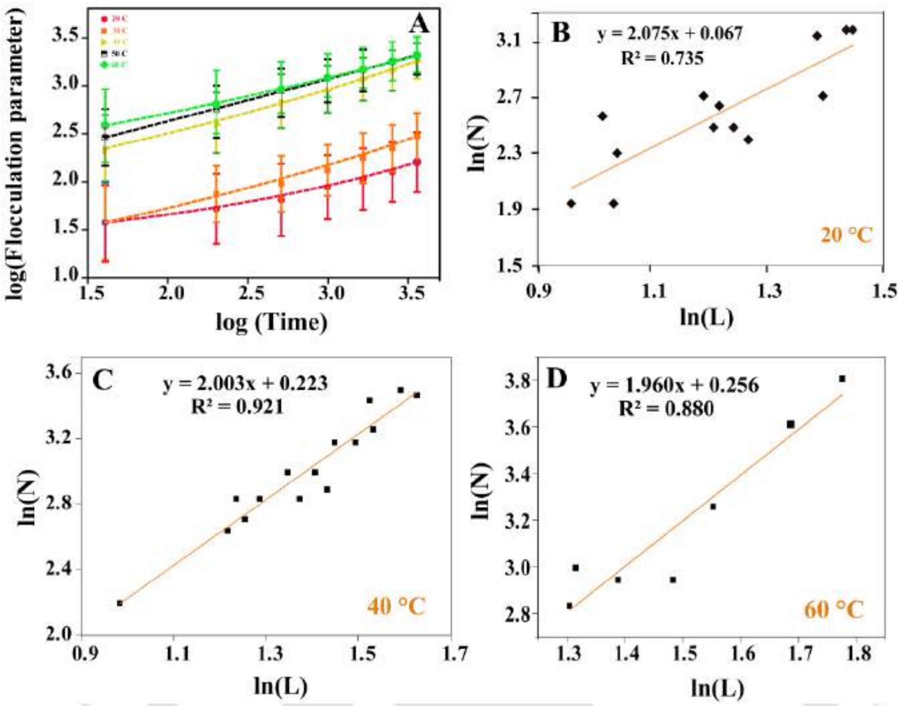

Figure 3.6. (**A**) Plot of *log (Flocculation parameter) versus log (Time)* at five different temperatures corresponding to 1.64 nM of dialyzed Au NPs. The error bars are the standard deviation of the mean integrated area obtained from five different data sets. Logarithmic plot of N vs L obtained from TEM analysis data of NP aggregates obtained from samples of time-dependent study measured at (**B**) 20 °C, (**C**) 40 °C and (**D**) 60 °C. The slope obtained from the linear regression least square fits of the data sets gives the value of fractal dimension of the aggregates, d_f. Here N refers to number of particles in the nanoparticle aggregate (cluster) and L refers to the geometric mean of longest linear dimension of the aggregate (cluster) and the length perpendicular to the former axis.

anions via formation of acyclic carboxylate dimers. In the initial stages of the reaction, as also discussed in our earlier work,[24] citrate removal from the surface of NPs was found to be crucial for the onset of the aggregation process of Au NPs (**equation 12**).

$$\{Au(citrate)_{x+q}\}^{3(x+q)-} \rightarrow \{Au(citrate)_{x}\}^{3x-} + q \times citrate^{3-} \qquad (12)$$

Thus the measured activation energy of ~ 36.2 kJmol^{-1}, could be associated with

desorption energy of a citrate ion from the surface of Au NP marking it as the rate limiting step. Molecular dynamic simulation studies using force fields and concept of soft epitaxy, has revealed that the free energy of adsorption of trisodium citrate on Au (111) surface, in aqueous medium is ~ -39.7 kJ mol^{-1}.[47] Based on this report, the conformational freedom of citrate anion gained through desorption is balanced by the loss of translational freedom of surface-bound water molecules. That is to say that the adsorption free energy for trisodium citrate is nearly equal to its enthalpy of adsorption in the aqueous medium. The best estimate of desorption energy of a single citrate anion based on this computation is reported to be 35.5 kJmol^{-1}. By microscopic reversibility, if the desorption process can be considered to be reverse of adsorption process, then the enthalpy of desorption of citrate ion from Au(111) will be an energetically uphill task, requiring roughly 35.5 kJmol^{-1}, provided the barrier to conversion from physisorbed to chemisorbed state is nearly zero in the medium.

To the best of our knowledge simulation studies on activation barrier to desorption/adsorption of citrate ions from Au surface in aqueous solution have not been carried out. As the experimentally obtained enthalpy of activation of ~ 33.9 kJ mol^{-1} correlates well with the minimum enthalpy energy that citrate ion would require to desorb off from the (111) surface of Au NPs (35.5 kJ mol^{-1}), this step maybe the rate limiting step for the aggregation reaction. Note that, the adsorption energy of water at various stable sites on the Au faces[48] ranges from -8.68 kJ mol^{-1} to -18.33kJ mol^{-1}; hence desorption of water from the Au NPs surface is a much more facile process as compared to desorption of citrate anion and is not likely to be the rate limiting step. TEM images in **Figure 3.5.**(**F-H**) attest to the fact that the individual Au NPs in the aggregated structures not only stick to each other but also undergo extensive coalescence. It could be that the coalescence process is rate-limited by the attainment of correct crystallographic alignment at the interface to generate a continuum lattice in three dimensions yielding aggregated structures mostly via oriented attachment.[18] Such a mechanism has been commonly proposed in the thermal and electron beam irradiated reactions of Au NPs supported on graphene layer,[49] formation of ultrafine gold nanowire array at room temperature[39] and low temperature annealing of semiconductor nanocrystal.[50]

OA involves the unification of particles sharing common crystallographic face and is therefore, driven by the high energy of the atoms at the point of attachment and inter particle misalignments. It is generally accepted that OA involves three dimensional rotation to eliminate dislocations at the boundaries, or could involve atom by atom reorientation at dislocations or grain boundaries, depending on the orientation of the approaching NPs. The former occurs via atom diffusion on surface followed by three dimensional rotation, while the latter mechanism involves atom diffusion on surface followed by growth of one grain at the cost of the other grain, till the grain boundary[51] is pushed to the surface via atom diffusion resulting in a defect free lattice of coalesced structure. Secondly, there is a possibility of twin boundary generation along with stacking faults during the attachment process. Therefore, energies for adatom diffusion,[52-53] grain boundary diffusion,[54] twin boundary,[39] surface relaxation[55] etc. which might be contributing factors to the rate determining step can be examined from literature available for nanostructured gold as well as from their bulk and surface counterparts. Towards this effort, activation energy for nanocrystallite grain growth in gold[54] has been reported to be 29.5 $kJmol^{-1}$, while the energy barrier for self-diffusion of adatoms over (111) fcc plane of growing Au clusters[53] involving various mechanism lies in the range 10.6 $kJmol^{-1}$ to 27.9 $kJmol^{-1}$. Both these processes therefore have lower activation energy from our measured activation energy of 36.2 $kJmol^{-1}$ or, the enthalpy of activation determined in this study, suggesting that these processes probably do not limit the rate of aggregation of partially bare Au NPs.

In addition, twin boundary and stacking faults (if any) generates low energy interfaces,[39] the occurrence of which is possible and is also observed in our case. (**Figure 3.5.H**). On the other hand, occurrence of grain boundary generates high energy interfaces frequently observed in high temperature studies,[49] and is not observed in our study. Thus these two processes do not affect the rate determining step. It is to be noted that in the OA mechanisms for aggregation, surface relaxation also plays an important role. Interestingly, surface relaxation, a phenomenon which occurs or takes place to relief surface strain, depends on the presence or absence of surface adsorbate as well as on the nature of the adsorbate. For example, nanostructured gold lattice in presence of ozone is known to contract and upon exposure to CO is restored to the original dimensions.[56] While similar studies in aqueous medium in presence of citrate would have helped us to delineate this process from the rate limiting step, presumably once the strongly adsorbed citrate stabilizer is removed from the surface, such surface relaxation does help in coalescence of the aggregated structures with time as seen from the TEM images in **Figure 3.5** and reported in other thermal and electron induced aggregation studies.[49] In addition, as a rule of thumb, the surface diffusion barrier of adsorbate on metal surface is approximately 12% of the binding energy of the adsorbate, thereby, striking out adsorbate diffusion on surface as one of the rate limiting step.[57] The overall process of Au NP aggregation under partially bare condition followed by coalescence is illustrated schematically in **Figure 3.7**.

To sum up, a reactive collision is met when particles overcome the energy barrier in terms of citrate desorption from the surface at the point of attachment, and the two NPs after sticking further reorganize on atomic scale and finally coalesce sharing the same crystallographic faces with or without defects, most of the times. The energy barrier that arises in due course of citrate desorption represents the activation energy in partially bare Au NP aggregation reaction. To sum up, a reactive collision is met when particles overcome the energy barrier in terms of citrate desorption from the surface at the point of attachment, and the two NPs after sticking further reorganize on atomic scale and finally coalesce sharing the same crystallographic faces with or without defects, most of the times. The energy barrier that arises in due course of citrate desorption represents the activation energy in partially bare Au NP aggregation reaction. In this regard, it is expected that the desorbing citrate ions from the surface of Au NP will have more polar transition state with respect to the reactant state, a fact substantiated by our kinetic salt effect studies in **Figure 3.3.B**, where the rate constant was found to increase with increase in ionic strength of the medium. Thus, the adsorbed species are known to have a marked effect on the structure and dynamics of surface atoms, for example, in adatom diffusion and surface relaxation. Hence it is plausible that once citrate desorbs off the surface, particles approach towards each other more readily followed by rotation to attain 3D alignment at the interface resulting in coalescence via surface relaxation preceded by adatom diffusion to finally form stable aggregate structures. In fact such surface relaxation and atom diffusion may continue even after two NPs have joined, giving rise to the extensive coalescence with common lattice planes.

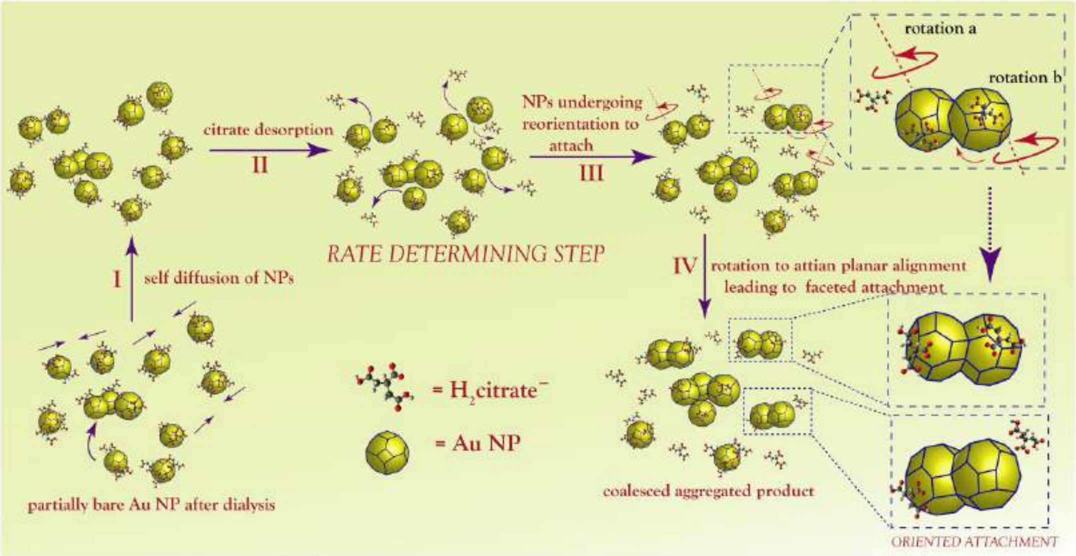

Figure 3.7. Schematic representation of the overall aggregation reaction of partially bare Cit Au NPs. (**I**) diffusion of partially bare Cit-Au NPs obtained after dialysis, (**II**) citrate desorption from the surface (crystallographic faces) of Au NPs (rate determining step), (**III**) reorientation and favourable rotation of NPs to attain correct crystallographic accord at the interface (**IV**) leading to coalescence.

The reaction is therefore, limited by citrate desorption step, representing the highest activated state in the whole series of plausible steps (such as diffusion of NPs, relative orientation of NPs, desorption of adsorbed species, rotation to planar alignment, self-diffusion of Au adatoms towards attachment site and surface relaxation) that take place following the dialysis of Cit-Au-NPs resulting into the coalescence of the partially bare Au NPs. Hence, the experimentally observed barrier to activation of 36.2 ± 3 kJ mol^{-1} can be explained to arise exclusively from the citrate anion desorption from the Au NP surface, limiting the overall reaction and is therefore termed as the rate determining step.

3.6. Conclusion

In conclusion, we have demonstrated that the rate of the aggregation of partially bare Au NPs in aqueous solution, obeys first order kinetics with an activation barrier of 36.2 kJ mol^{-1} in the temperature range 20°C – 60°C. Time-dependent aggregation kinetic study within the experimental temperature range reflects exponential growth behaviour of aggregates with time, defining the colloidal aggregation to be reaction limited. From energy consideration, it can be concluded that the desorbing citrate moiety from the surface of Au NPs involved a polar transition state and, therefore, that appeared to be the rate limiting step in the overall reaction process. Thus, the slow citrate desorption is followed by faster, downhill processes such as faceted approach of bare NP, planar alignment, surface relaxation via adatom diffusion resulting in correct crystallographic accord at the interface, leading to OA and ultimately fusion. The preferential orientation of NPs, rearrangement of adatoms such that faces share the same crystallographic planes, is desired to minimize the surface energy and surface curvature of the coalescing particles. The proposed model hereby accounts for the activation energy of 36.2 kJ mol^{-1} obtained from this study.

3.7. References

1. Grzelczak, M.; Vermant, J.; Furst, E. M.; Liz-Marza´n, L. M. *Nano Lett.* **2010**, *4*, 3591.

2. Yang, M.; Chen, G.; Zhao, Y.; Silber, G.; Wang, Y.; Xing, S.; Han, Y.; Chen, H. *Phys. Chem. Chem. Phys.* **2010**, *12*, 11850.

3. Wang, Y.; DePrince, A. E.; Gray, S. K.; Lin, X. M.; Pelton, M. *J. Phys. Chem. Lett.* **2010**, *1*, 2692.

4. Padalkar, S.; Capadona, J. R.; Rowan, S. J.; Weder, C.; Moon, R. J.; Stanciu, L. A. *J Mater Sci*. **2011**, *46*, 5672.

5. Roy, S.; Tyler, B. N.; Rotello, V. M. *Adv. Mater.* **2005**, *17*, 657.

6. Schreiber, R.; Do, J.; Roller, E. M.; Zhang, T.; Schuller, V. J.; Nickels, P. C.; Feldmann, J.; Liedl, T. *Nat. Nanotech*. **2014**, *9*, 74..

7. Lim, D. K.; Jeon, K. S.; Kim, H. M.; Nam, J. M.; Suh, Y. D. *Nat. Mater.* **2010**, *9*, 60.

8. Liu, D.; Chen, W.; Sun, K.; Deng, K.; Zhang, W.; Wang, Z.; Jiang, X. *Angew. Chem*. **2011**, *50*, 4103.

9. Park, S. J.; Lazarides, A. A.; Mirkin, C. A.; Brazis, P. W.; Kannewurf, C. R.; Letsinger, R. L. *Angew. Chem.* **2009**, *21*, 3845.

10. Sahoo, Y.; Cheon, M.; Wang, S.; Luo, H.; Furlani, E. P.; Prasad, P. N. *J. Phys. Chem. B* **2004**, *108*, 3380.

11. Cheetham, A. G.; Zhang, P.; Lin, Y.; Lock, L. L.; Cui, H. *J. Am. Chem. Soc.* **2013**, *135*, 2907.

12. Kelly, K. L.; Coronado, E.; Zhao L. L.; Schatz, G. C. *J. Phys. Chem. B.* **2003**, *107*, 668.

13. Magdassi, S.; Grouchko, M.; Kamyshny, A. *Materials* **2010**, *3*, 4626.

14. Nealon, G. L.; Donnio, B.; Greget, R.; Kappler, J. P.; Terazzib, E.; Gallani, J. L. *Nanoscale* **2012**, *4*, 5244.

15. Zhang, D.; Neumann, O.; Wang, H.; Yuwono, V. M.; Barhoumi, A.; Perham, M.; Hartgerink, J. D.; Stafshede, P. W.; Halas, N. J. *Nano Lett.* **2009**, *9*, 666.

16. Deka, J.; Paul, A.; Chattopadhyay. A. *J. Phys. Chem. C.* **2009**, *113*, 6936.

17. Saha, K.; Agasti, S. S.; Kim, C.; Li, X.; Rotello, V. M. *Chem. Rev.* **2012**, *112*, 2739.

18. Lv, W.; He, W.; Wang, X.; Niu, Y.; Cao, H.; Dickerson, J. H.; Wang, Z. *Nanoscale* **2014**, *6*, 2531.

19. Zhang, Q.; Liu, S. J.; Yu, S. H. *J. Mater. Chem.* **2009**, *19*, 191.

20. Zhuang, Z.; Zhang, J.; Huang, F.; Wang, Y.; Lin, Z. *Phys. Chem. Chem. Phys.* **2009**, *11*, 8516.

21. Zhuang, Z.; Huang, F.; Lin, Z.; Zhang, H. *J. Am. Chem. Soc.* **2012**, *134*, 16228.

22. Born, P.; Kraus, T. *Phys. Rev. E.* **2013**, *87*, 062313(1)-062313(11).

23. Meli, L.; Green, P. F. *ACS Nano* **2008**, *2*, 1305.

24. Dutta, A.; Das, S.; Paul, A.; Chattopadhyay, A. *J Nanopart Res.* **2015**, *17*, 260.

25. Jimenez, I. O.; Bastus, N. G.; Puntes, V. *J Phys Chem C* **2011**, *115*, 15752.

26. Sendroiu, I. E.; Mertens, S. F. L.; Schiffrin, D. J. *Phys. Chem. Chem. Phys.* **2006**, *8*, 1430.

27. Weisbecker, C. S.; Merritt, M. V. *Langmuir*, **1996**, *12*, 3763.

28. Skriver, H. L.; Rosengaard, N. M. *Phys. Rev. B*, **1992**, *46*, 7157.

29. Nam, J.; Won, N.; Jin, H.; Chung, H.; Kim, S. *J. Am. Chem. Soc.* **2009**, *131*, 13639.

30. Espinoza, M. G.; Hinks, M. L.; Mendoza, A. M.; Pullman, D. P.; Peterson, K. I. *J Phys Chem C* **2012**, *116*, 8305.

31. Aslan, K.; Luhrs, C. C.; Pe´rez-Luna, V. H. *J. Phys. Chem. B* **2004**, *108*, 15631.

32. Mulvaney, P. *Langmuir* **1996**, *12*, 788.

33. Link, S.; El-Sayed, M. A. *J. Phys. Chem. B* **1999**, *103*, 4212.

34. Li, Y.; Petroski, J.; El-Sayed, M. A. *J. Phys. Chem. B* **2000**, *104*, 10956.

35. Ribeiro, C.; Lee, E. J. H.; Longo, E.; Leite, E. R. *Chem Phys Chem* **2005**, *6*, 690.

36. Han, X.; Lee, R.; Chen, T.; Luo, J.; Lu, Y.; Huang, K. W. *Sci. Rep.* **2013**, *3*, 2557.

37. Parry, J. S. S.; Park, J. W. *J. Am. Chem. Soc.* **2014**, *136*, 1907.

38. Lin, Y.; Pan, G. B.; Su, G. J.; Fang, X. H.; Wan, L. J.; Bai, C. L. *Langmuir* **2003**, *19*, 10000.

39. Halder, A.; Ravishankar, N. *Adv. Mater.* **2007**, *19*, 1854.

40. Huang, Z.; Li, H.; Pan, Z.; Wei, Q.; Chao, Y. J.; Li, X. *Sci. Rep.* **2011,** *1*, 148.

41. Verwey, E. J. W.; Overbeek, J. T. G. Elsevier Publishing Company Inc.: Amsterdam, **1948**.

42. Derjaguin, B. V.; Churaev, N. V.; Muller, V. M. Springer: US, **1987**.

43. Lint, M. Y.; Lindsay, H. M.; Weitz, D. A.; Klein, R.; Ball, R. C.; Meakin, P. *J. Phys.: Condens. Matter* **1990**, *2*, 3093.

44. Lint, M. Y.; Lindsay, H. M.; Weitz, D. A.; Ball, R. C.; Klein, R.; Meakin, P. *Phys. Rev. A* **1990**, *41*, 2005.

45. Zhang, F.; Dressen, D. G.; Skoda, M. W. A.; Jacobs, R. M. J.; Zorn, S.; Martin, R. A.; Martin, C. M.; Clark, G. F.; Schreiber, F. *Eur Biophys J.* **2008**, *37*, 551.

46. Weitz, D. A.; Huang, J. S.; Lin, M. Y.; Sung, J. *Phys. Rev. Lett.*, **1985**, *54*, 1416.

47. Feng, J.; Pandey, R. B.; Berry, R. J.; Farmer, B. L.; Naik, R. R.; Heinz, H. *Soft Matter*, **2011**, *7*, 2113.

48. Huzayyin, A.; Chang, J. H.; Lian, K.; Dawson, F. *J. Phys. Chem. C* **2014**, *118*, 3459.

49. Yuk, J. M.; Jeong, M.; Kim, S. Y.; Seo, H. K.; Kimab, J.; Lee, J. Y. *Chem. Commun.* **2013**, *49*, 11479.

50. Huis, M. A. v.; Kunneman, L. T.; Overgaag, K.; Xu, Q.; Pandraud, G.; Zandbergen, H. W.; Vanmaekelbergh, D. *Nano Lett.* **2008,** *8*, 3959.

51. Surrey, A.; Pohl, D.; Schultz, L.; Rellinghaus, B. *Nano Lett*. **2012**, *12*, 6071.

52. Baker, T. A.; Friend, C. M.; Kaxiras, E. *J. Phys. Chem. C* **2009**, *113*, 3232.

53. Baletto, F.; Mottet, C.; Ferrando, R. *Surf. Sci.* **2000,** *44*, 631.

54. Yevtushenko, O.; Natter, H.; Hempelmann, R. *Thin Solid Films* **2006**, *515*, 353.

55. Brako, R.; Sokcevic, D. *Surf. Sci.* **2000**, *469*, 185.

56. Biener, J.; Wittstock, A.; Zepeda-Ruiz, L. A.; Biener, M. M.; Zielasek, V.; Kramer, D.; Viswanath, R. N.; Weissmüller, J.; Bäumer, M.; Hamza, A. V. *Nat. Mater*. **2009**, *8*, 47.

57. Nilekar, A. U.; Greeley, J.; Mavrikakis, M. *Angew. Chem.* **2006**, *45*, 7046.

CHAPTER 4

Surface and Tip Enhanced Raman Spectroscopy at the Plasmonic Hot Spot of a Co-ordination Complex Conjugated Gold Nanoparticle Dimer

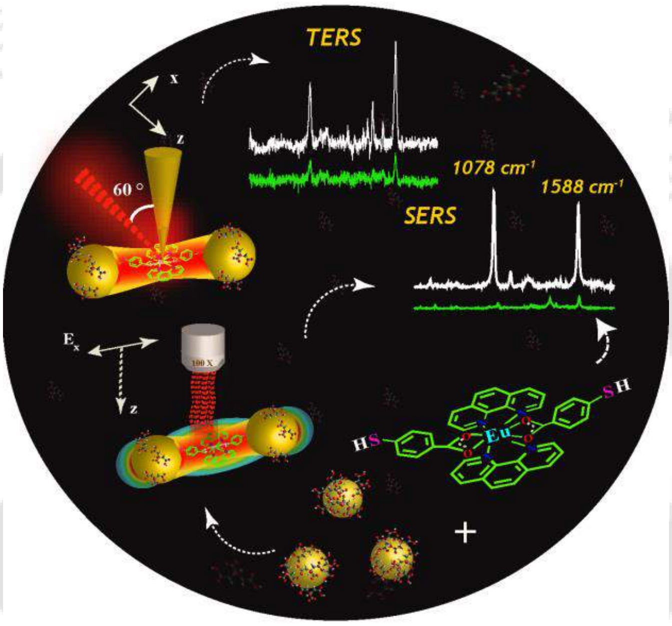

Chapter 4 *demonstrates a new idea to design and generate uniform Au NP dimer (nano-dimer) in considerable yield, using a pre-designed Raman active co-ordination complex of europium (Eu) metal, which was used to probe its potential as a Raman substrate at a plasmonic hotspot. The reaction between the Raman active 4-MBA ligand of the Eu-complex and citrate-stabilized Au nanoparticles (cit-Au NPs) led to selective dimerization in considerable yield and precise control over hot-spot engineering to maximize SERS. Additionally, scanning probe microscopy (SPM) correlated tip-induced Raman enhancement using He-Ne laser focusing on the plasmonically coupled Au nano-dimers helped obtain intense Raman signal at the spatial resolution of single dimer. Based on this the average SERS and TERS amplification was measured to be on the order of* 10^9 *and* 10^4 *respectively.*

***** "Reprinted with permission from (Dutta et al. J. Phys. Chem. C 2017, 121, 18854). Copyright © 2017, American Chemical Society." http://pubs.acs.org/doi/abs/10.1021/acs.jpcc.7b07301**

4.1. Introduction

The unique ability of metal nanoparticles to support localized surface plasmons (LSPs) and hence light driven strong electromagnetic field enhancement near the vicinity of metal surfaces, provides an opportunity for applications – among others - in surface enhanced Raman spectroscopy (SERS).[1] Of the three prominent ones (Au, Ag and Cu), the Au nanoparticles (NPs) and nanorods (NRs) along with their higher ordered structures have received the greatest attention as plasmonic materials with applicability in SERS, owing to their ease of synthesis, stability and bio-friendliness.[2-3] The plasmon coupling induced field enhancement is found to be strongest near the vicinity of inter-particle gap distance called the hot-spot, which is key to obtaining higher sensitivity - down to a single molecule - in SERS.[4] In that regard, dimer, trimer, tetramer or hierarchical assemblies of metal nanoparticles could serve as important candidates.[2,5-6]

In principle, information about a chemical bond at the resolution of a single molecule should be obtainable using SERS. However, in practice, the best spatial resolution that could be achieved depends on the diffraction limited laser focus size. In that regard, tip-enhanced Raman spectroscopy (TERS) provides a more convenient approach, which utilizes the concept of SERS in combination with scanning probe microscopy (SPM) imaging in order to obtain structural and Raman spectral information at the nanometric scale spatial resolution.[7-8] Based on this, it could be inferred that if the induced plasmon at the tip could be combined, with plasmon enhancement at the hot-spot owing to dimeric or oligomeric metal NPs, the signal intensity enhancement may be the highest.[9]

Principles of chemistry offer a repertoire of techniques for assembling nanoparticles in liquid dispersion.[10-15] Most of these attempts for programmed assembly of plasmonic nanoparticles in terms of dimers, trimer or their hierarchical assemblies are intended to achieve maximum enhancement for SERS. Thus the key to achieve large-scale electromagnetic field enhancement for Raman signal lies in the appropriate localization of molecules in between the plasmonic particles (hot-spot), with the ability to tune the distance of separation and control steric alignment of the functional groups of interest.[16] Importantly, 98% of SERS signals are generated by the molecules that are localized in the inter-junction of probe nanostructures or the hot-spot than that on the surface.[4] This has led to the development of synthetic methods for controlled hot-spot engineering with Raman enhancement on the order of 10^7 – 10^5[5,16-17] Although organic linker and DNA – based assemblies offer some degrees of control, inorganic coordination complexes, with the ability to host ligands with extraordinary stereoelectronic manoeuvrability may offer far superior engineering options based on the use of a whole gamut of ligands and metals.

4.2. Outline of the present work

A new idea to design and generate uniform Au NP dimer (nano-dimer) in considerable yield, using a pre-designed Raman active co-ordination complex of europium (Eu) metal have been demonstrated, which was then used to probe its potential as a Raman substrate at the plasmonic hotspot. The ligating moiety was designed by taking advantage of the complex co-ordination chemistry employing heterocyclic phenanthroline and 4-mercaptobenzoic acid (4-MBA) as precursors for the Eu complex. The Eu metal in the complex - being oxophilic in nature - underwent complexation through the carboxyl group of 4-MBA – a Raman active molecule. On the other hand, affinity of the sulphydryl group of 4-MBA towards Au NP surface helped attain selective dimerization. In addition, the phenanthroline ring imparted structural rigidity to the complex, thereby inducing steric crowd in the near vicinity of metal centre that resulted in the dimerization of the Au NPs nearly exclusively. Thus the availability of the probe ligand (4-MBA) in the gap between the nano-dimer positioned using the complexation affinity of 4-MBA towards the Eu as well as towards gold surface helped attain extraordinary electromagnetic field (EF) enhancement at the hot-spot appropriate for single molecule studies.

4.3. Experimental Section

4.3.1. Materials

Tri-sodium citrate dihydrate (Merck), gold(III) chloride (30 wt% in HCl, Sigma-Aldrich), europium chloride hexahydrate (Sigma), 1,10-phenanthroline monohydrate (Merck), 4-mercaptobenzoic acid (Sigma-Aldrich), sodium hydroxide (Merck) were used as received. Milli-Q grade water (18.2 MΩcm, Millipore) was used for synthesis as well as for other experimental work.

4.3.2. Synthesis of $[Eu(Phen)_2(MBA)_2]Cl$

In a typical reaction, phenanthroline (20.7 mg, 0.1044 mmol) was dissolved in 12 mL methanol to which 4-mercaptobenzoic acid dissolved (with 1M, NaOH) in 4 mL methanol (16.4 mg, 0.1063 mmol) was added sequentially at 60 °C under stirring condition. After 5 min, 4 mL methanolic solution of $EuCl_3.6H_2O$ (20.7 mg, 0.0565 mmol) was added dropwise under continuous stirring condition resulting in milky white appearance. The mixture was refluxed at 60 °C for 3 h, during which the milky white suspension turned into light orange dispersion. The dispersion was allowed to cool to room temperature and was filtered to remove any insoluble material. The filtrate so obtained was solvent dried and excess water was added to precipitate the complex. The precipitate so obtained was then dried in dessicator (following decantation of water) overnight to obtain solid orange powder and was then used for further characterization.

4.3.3. Synthesis of citrate stabilised gold nanoparticles (cit-Au NPs)

In a typical synthesis, 100 mL aqueous solution containing 50 mg tri-sodium citrate refluxed at 135 °C with continous stirring for 30 min. At the boiling condition, 1 mL of $HAuCl_4$ (1.72×10^{-2} M) was then added and the reaction was further allowed to continue for next 30 min. The formation of cit-Au NPs was ensured by appearance of deep red color dispersion, which was further characterised by UV-Vis and TEM studies.

4.3.4. Synthesis of gold nanoparticle (Au NP) dimer

1 mL of as-synthesized cit - Au NP dispersion was diluted in 5 mL aqueous solution. To the above dispersion, 50 µL (30 µM) methanolic solution of $[Eu(Phen)_2(MBA)_2]Cl$ was added dropwise, with vigorous stirring at room temperature. The resulting mixture was stirred for 2 min to obtain metal complex ligated Au NP dimer. Similarly, the reaction was carried at two other different

concentrations of metal complex viz., 15 µM and 90 µM. In each 5 mL aqueous dispersion of Cit - Au NPs, 50 µL (15 µM or 90 µM) of metal complex was added dropwise and stirred vigorously for 2 min under the same condition. The resulting NP dispersion was then centrifuged at 20267 rcf for 10 min; the pellet was collected and was finally redispersed in 5 mL water for storage and further use.

4.3.5. Sample preparation for normal Raman and SERS experiment

SERS measurements were carried out in 1.7×1.7 cm^2 pre-cleaned oven-dried glass slides. The glass slides were cleaned following three-step cleaning process: The glass slides were first dipped in piranha solution (H_2SO_4/H_2O_2) for 30 min and then rinsed with Milli-Q water. Those were then transferred to acetone solution and sonicated for 30 min. That was followed by repeated washing of the glass slides with Milli-Q water, which was then oven-dried at 60 °C for further use. For all Raman measurements, 100 uL of the sample was dropcast on the clean glass slide to make a thin film of it, which was dried in vacuum dessicator. The Raman spectra for the samples were then recorded in a LabRam HR Raman instrument using 532 nm and 633 nm laser source as per requirement. All measurements were carried out with 100× objective with an acquisition time of 20 s.

4.3.6. Tip enhanced Raman spectroscopy (TERS) experimental set-up

The TERS set-up consists of Bruker's Innova- IRIS (Integrated AFM Raman Imaging system) system integrated with LabRAM HR evolution Raman (Horiba Jobin Yvon) spectrometer using an optic coupler that focuses laser into the scanning probe microscope (SPM, Bruker) probe. For SPM-TERS operation, a sharp gold metallic tip (Bruker) was used. At first, STM or SFM gold tip was engaged to obtain topographic information from the region of interest (ROI) that was pre-identified using optical microscope. TERS acquisition was then carried out using a side illumination optical set-up. A long working distance objective (Olympus, 50x, NA=0.42) placed at 60° angle with respect to the tip-axis was used to focus the He-Ne (632.8 nm) laser at the tip-apex. The Raman signal was then collected in back-scattered mode through the same objective, which was sent to

Horiba Jobin Yvon spectrograph, at 600 lines per mm grating. TERS acquisition was done employing two types of SPM technology: scanning force microscopy (SFM)-TERS and scanning tunnelling microscopy (STM)-TERS mode. For carrying out TERS, we have assumed that a single complex had ligated Au nano-dimer through the Raman active 4-MBA. The enhanced electric field at the SPM tip-apex when aligned with 632.8 nm laser allowed us to achieve Raman spectral information from individual Au nano-dimer at the spatial resolution of less than 100 nm.

(a) **SFM-TERS:** SFM-TERS set up consisted of a fine gold probe (with tip radius of about 20 nm) attached to quartz tuning fork, which was mounted on a tuning fork cartridge that included a piezoelectric element to induce oscillation of the tuning fork.

Sample preparation: SFM-TERS measurements were done on pre-cleaned silicon substrate. The silicon substrate was first sonicated in piranha solution (H_2SO_4/H_2O_2) for 30 min and then rinsed with Milli-Q water. This was then rinsed in acetone solution (thrice) followed by repeated washing with Milli-Q water, which was then dried overnight at room temperature for further use. The as-synthesized Au nanodimer dispersion (~ 8 µL) was dropcast on the pre-cleaned silicon substrate and was then allowed to dry overnight.

Imaging condition: The SFM images were obtained by engaging the gold tip with the sample at set point value of 4.5 V. The scan was then performed in tuning fork amplitude feedback mode. TERS acquisition was then carried out with 632.8 nm laser (ND filter = 25 %) focussed at the gold tip-apex with an acquisition time of 20 s.

(b) **STM-TERS**: The STM-TERS set-up involved a solid gold etched wire and a conductive substrate and sample for operation at a constant current feedback loop.

Sample preparation: For STM-TERS sample preparation, 8 µL as-synthesized Au nanodimer dispersion was dropcast on carbon coated copper TEM grid, which was then allowed to dry overnight. The dried copper TEM grid was then placed on the sample holder by applying silver paste on the edge of the TEM grid to generate conduction between the sample and the substrate.

Imaging Condition: The STM-TERS operation was conducted by engaging the etched gold tip at a set-point current of 1.0 nA and a bias voltage of 0.5 V. For TERS acqusition, 632.8 nm laser was aligned with the gold tip-apex and spectral acqusition was recorded at ND filter = 25 % with an acqusition time of 20 s.

4.4. Characterization

UV-Vis measurements were carried out in Perkin Elmer Lambda 750 double beam UV-Vis spectrophotometer. (ii) Fluorescence spectra were recorded in HORIBA Jobin Yvon FluoroMax-4 spectrofluorimeter. (iii) FT-IR spectra for all dried solid samples were recorded in Perkin Elmer spectrophotometer (Model- spectrum one) in the range 400-4000 cm^{-1}, using KBr pellet method. FT-IR of the as-synthesized complex was done with solid powder obtained from synthesis. The as-synthesized Au NPs and Au nano-dimer dispersion were centrifuged at 20627 (rcf) for 15 min at 20 °C. The precipitate so obtained in each case was then dried in vacuum dessicator and further used for FT-IR measurement. (iv) Transmission electron microscopic images were obtained using JEOL JEM 2100 transmission electron microscope (TEM), operating at maximum operating voltage of 200 kV. TEM samples were prepared by drop casting 7 μL of colloidal dispersion on the carbon coated copper grid and drying under ambient condition. The inter-dimer gap was calculated using gatan digital micrograph software equipped with TEM. (v) ESI-MS measurements were performed in quadrupole time–of–flight (QTOF)–MS spectrometer (Waters, Model: Q–Tof Premier). The as-prepared complex was dissolved in methanol (HPLC grade) solvent and filtered using 0.2 micron filter paper. ESI-MS measurements for the filtered solution were then carried in positive ion mode. (vi) NMR spectra for the samples were recorded in a BRUKER (400 MHz) NMR machine with $CDCl_3$ as the solvent. (vii) Raman spectra were recorded in a LabRAM HR evolution microscope Raman system (Horiba Jobin Yvon) equipped with air-cooled diode laser operating at 532 nm and 633 nm. The laser power used for 532 nm and 633 nm sources was 7.96 mW and 4.94 mW, respectively, with ND filter set at 50 %. Spectral acqusitions were carried out with 1800 lines per mm grating using 100 × objective (numerical aperture = 0.9) if otherwise not mentioned. Baseline subtraction for all spectra was done using line fit option available in LabSpec software equipped with the Raman instrument.

4.5. Results and Discussions

4.5.1. Characterisation of as synthesized Eu-complex

The synthesis of red luminescent Eu complex was carried out at 60 °C using 4-MBA and phenanthroline as described in the Experimental **Section 4.3.2**. The UV-vis spectrum of the as-synthesized complex was characterized by intense ligand centered $\pi - \pi *$ absorption bands (E - bands) at 230 nm and 264 nm with a broad band at 315 nm attributed to B-band corresponding to the aromatic ring of phenanthroline and 4–mercaptobenzoic acid ligands. (**Figure 4.1 A**).

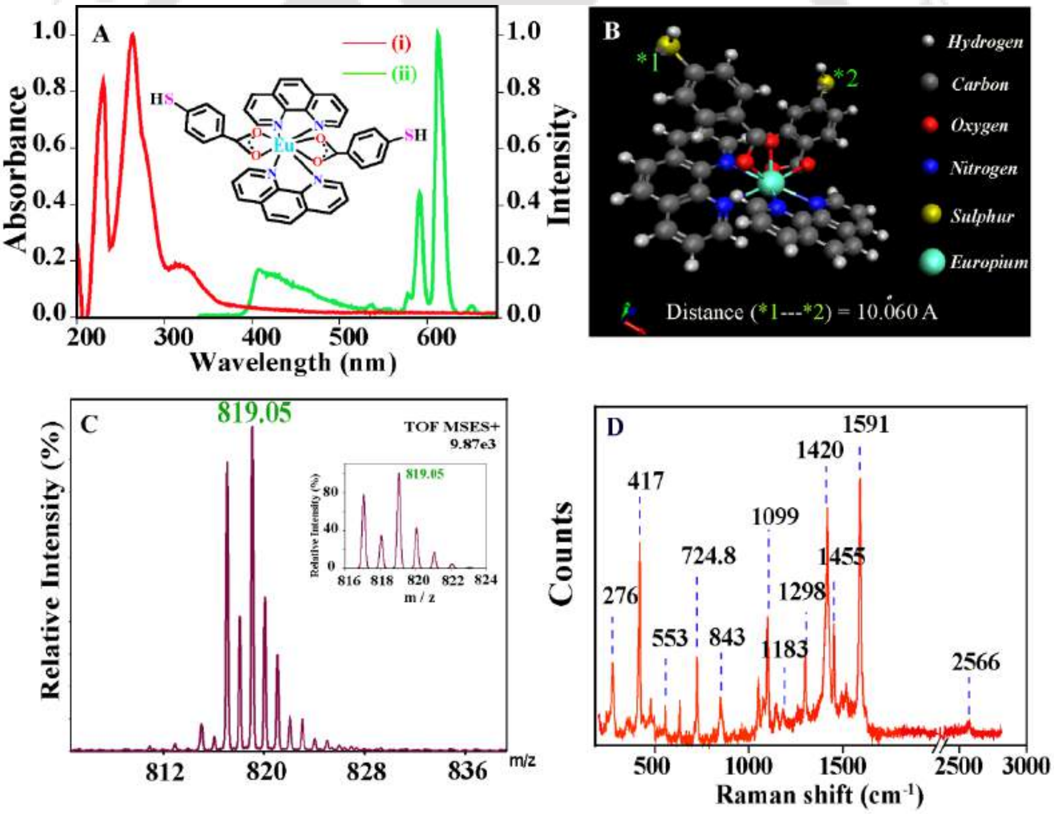

Figure 4.1. (**A**) UV–vis (red band) and photoluminescence (green band) spectra of [Eu(phen)$_2$(MBA)$_2$]Cl. (**B**) The energy optimized structure of the as-synthesized complex computed using Avogadro software. (**C**) ESI-MS spectrum of [Eu(phen)$_2$(MBA)$_2$]Cl in positive ion mode (HPLC methanol). (**D**) Raman spectrum of the as synthesized europium complex [Eu(phen)$_2$(MBA)$_2$]Cl.

On the other hand, **Figure 4.1 A** also showed multiple emission bands in the range 550-750 nm (λ_{ex}= 320 nm) corresponding to bright red luminescent complex. This is attributed to the ligand sensitized emission associated with 4f–4f transition involving the $^5D_0$ excited state and the low-lying ^7F_J (J = 0 - 4) levels of Eu(III) ions. The weak emission band centered at 580 nm and 650 nm appeared due to forbidden $^5D_0 \rightarrow ^7F_{0,3}$ transition; whereas the band at 593 nm was relatively strong, occurring due to magnetic $^5D_0 \rightarrow ^7F_1$ transition and is independent of co-ordination environment. On the other hand, the sharp peak centered at 614 nm due to $^5D_0 \rightarrow ^7F_2$ transition arising from induced electric dipole transition was indicative of slightly polarizable chemical environment around the Eu(III) site.**[18]** However, the considerably low intensity ratio of the electric dipole transition to the magnetic dipole transition was suggestive of symmetric environment around the co-ordination sphere. **Figure 4.1 B** shows the proposed computed structure of the as synthesized complex using "Avogadro".

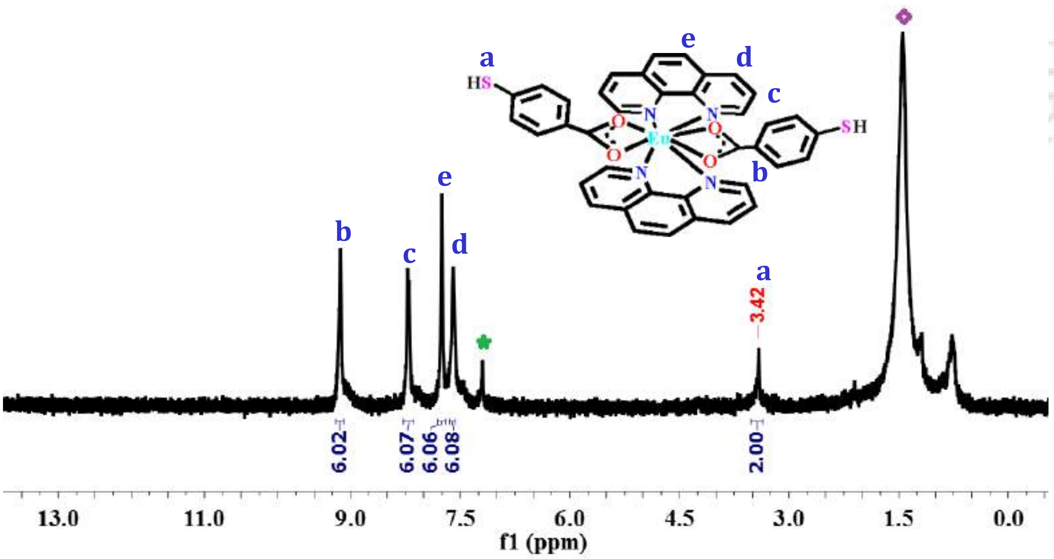

Figure 4.2. ^{1}H-NMR (400 MHz) spectra of [Eu (phen)$_2$(MBA)$_2$]Cl in CDCl$_3$. The peak in the range 7-9.5 ppm corresponds to the aromatic protons. The peak at 3.42 ppm corresponds to sulphydryl group of p-mercaptobenzoic acid. The green asterisked peak corresponds to solvent peak (CDCl$_3$) and the red asterisked one corresponds to solvent water.

The complex was further identified by electrospray ionization mass spectrometric (ESI-MS) analysis. The experimentally measured m/z peak at 819.05 indicated a composition of $C_{38}H_{26}EuO_4N_4S_2$ (**Figure 4.1.C**) corresponding to $[Eu(phen)_2(MBA)_2]^+$, which matched exactly with the theoretically calculated isotope distribution pattern, as shown in the inset of **Figure 4.1 C**. Further, ^1H-NMR spectra (recorded in $CDCl_3$) exhibited six characteristic signals downfield, with two distinct signals from the aromatic ring of 4-MBA found overlapping with phenanthroline peaks at 9.14 ppm, 8.21 ppm, 7.75 ppm and 7.59 ppm (**Figure 4.2**), thus substantiating the symmetric co-ordination environment around the Eu^{3+} ion. The bonding and co-ordination mode of ligand with the metal and hence the plausible structure of complex was further substantiated with the help of FTIR (see **Figure 4.3**) and Raman spectral (**Figure 4.1D**) analyses. The disappearance of characteristic C=O stretching vibration at 1678 cm^{-1} upon complexation and appearance of peaks due asymmetric ($\nu_{as}(COO^-)$) and symmetric ($\nu_s(COO^-)$) stretching vibrations of carboxylate group at 1543 cm^{-1} and 1406 cm^{-1}, respectively, as shown in **Figure 4.3A**, indicated the participation of carboxyl group of 4-MBA ligand in metal co-ordination.

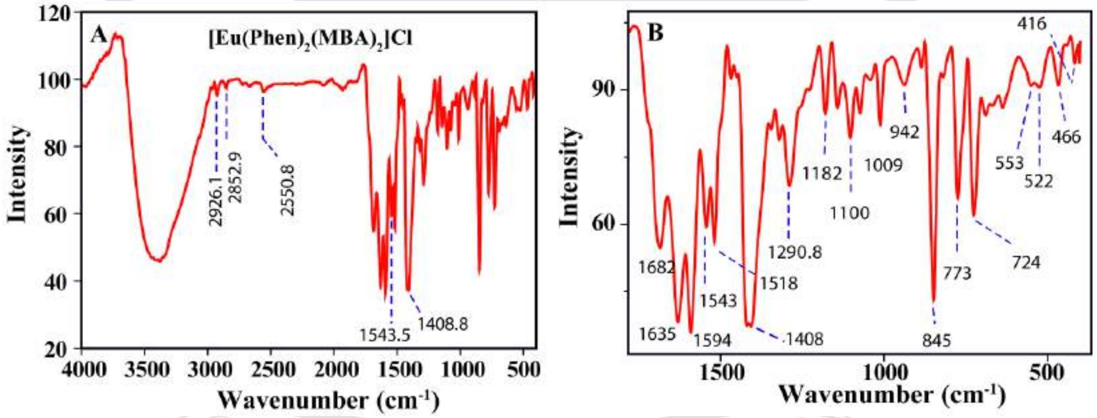

Figure 4.3. FTIR spectra of (**A**) as synthesized $[Eu(phen)_2(MBA)_2]Cl$ complex and (**B**) expanded view of **Figure 4.3.A** in the range 400-1800 cm^{-1}.

In addition, the direction of their frequency shift and the corresponding shift difference ($\Delta\nu = \nu_{as(COO)} - \nu_{s(COO)} = 137\ cm^{-1}$) with respect to free ligand (4-MBA) indicated the bidentate co-ordination mode of the carboxyl group with the metal ion.[19] The peak at 2550 cm^{-1} corresponds to the stretching vibration of the -SH group in 4-MBA ligated to the metal centre through carboxyl group. The shift in the quadrupole vibrational bands appearing at 1682 cm^{-1}, 1635cm^{-1}, 1518 cm^{-1} and 1465 cm^{-1} due to ring vibration in phenanthroline along with weak band in the range 466-690 cm^{-1} indicated the metal ion co-ordination to the phenanthroline ring.[20] (**Figure 4.3B**) Sharp peaks appearing at 416 cm^{-1} and 1594 cm^{-1} were attributed to $Eu - O$ stretching vibration and $C = C$ aromatic stretch of the benzene ring. Further the peak appearing at 721 cm^{-1} and 850 cm^{-1} can be assigned to out of plane motion of hydrogen atoms on the heterocyclic ring of phenanthroline and hydrogen on the centre of the ring, respectively.[21]

Figure 4.1D shows the Raman spectrum of the as-synthesized europium complex, $[Eu(phen)_2(MBA)_2]Cl$. Raman peaks appearing at 276 cm^{-1} and 2566 cm^{-1} (**Figure 4.1D**) correspond to $Eu - N$ and $-SH$ stretching vibration of free thiol group, respectively. In addition, a sharp peak appearing at 417 cm^{-1} due to polarised Raman line of phenanthroline supported the co-ordination with metal and that at 553 cm^{-1} corresponds to Eu-O-C-C vibration. The complex spectra exhibited a weak bands at 843 cm^{-1} and 1183 cm^{-1} due to $\gamma_{bend}(COO^-)$ and C-COOH stretching vibration of 4-MBA group; whereas strong peaks at 1591 cm^{-1} and 1099 cm^{-1} were assigned to C=C stretching and ring breathing vibration corresponding to the aromatic ring in 4-MBA. Strong peak appearing at 724 cm^{-1} corresponds to out of plane γ(C-C) vibration comprising both phenanthroline and 4-MBA ligand.[22] Additionally, peak appearing at 1420 cm^{-1} is attributed to ($\nu_{C=C}$, $\nu_{C=N}$) vibration and that peak at 1298 cm^{-1} and 1455 cm^{-1} corresponds to ($\nu_{C=C}$ + δ_{CH}) vibration of aromatic ring in phenanthroline.[23-24] Thus the designed europium complex $[Eu(phen)_2(MBA)_2]Cl$ consisted of two planar phenanthroline and two Raman active 4-MBA moiety preferably in trans orientation to each other with its free thiol directed outward in space. Hence affinity of thiols towards Au - surfaces makes the designed metal complex - an ideal linker moiety to generate gold nano-dimers with controlled interparticle gap-distance.

4.5.2. Characterization of as synthesized Au NP dimer

Cit-Au NPs of 13.3 ± 6.5 nm in diameter were synthesized following an earlier reported method[25] (Refer Experimental **Section 4.3.3**) and were characterized by the plasmonic extinction band centered at 520 nm (**Figure 4.4.A(i)**, red band) and transmission electron microscopy (TEM). The selective dimerization using the metal complex as ligating moiety was achieved via a one-step process as described in the Experimental **Section 4.3.4**. Briefly, 30.0 µM of the as-synthesized Eu complex (in methanol) was added dropwise to 10 mL Cit-Au NPs aqueous dispersion followed by stirring for 2 min at room temperature.

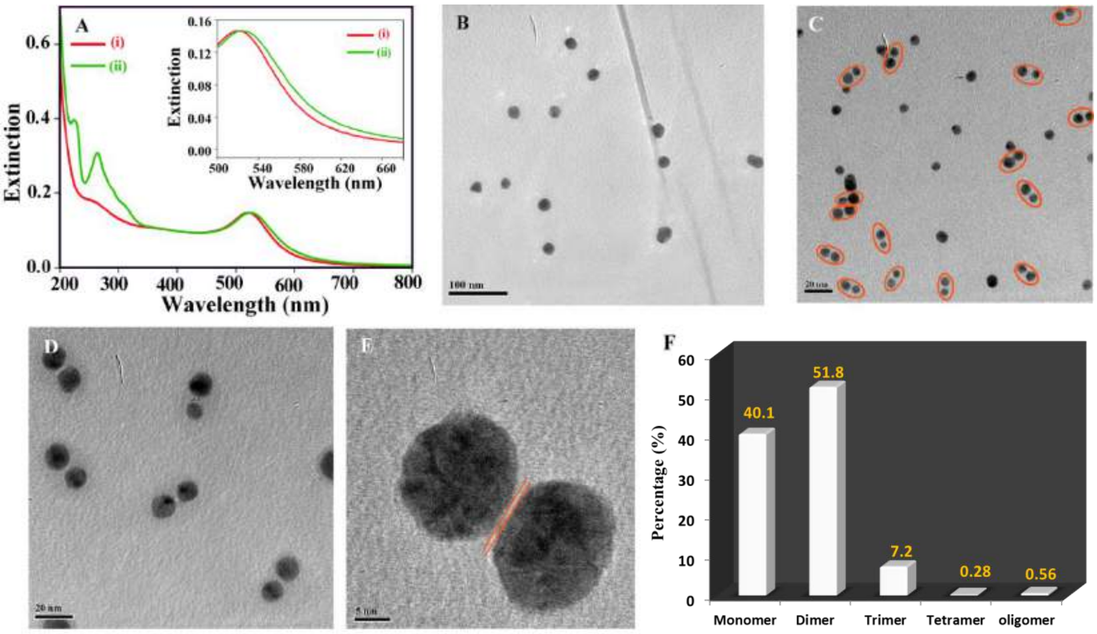

Figure 4.4. (**A**) UV-vis spectra of (**i**) as synthesized Cit-Au NPs (red band) and (**ii**) Au nano-dimer (green band). Representative TEM image of (**B**) as-synthesized Cit-Au NPs, (**C**) Eu-complex bridged Au nano-dimer (in addition to monomers), (**D**) magnified view of Au nano-dimers, (**E**) typical HR-TEM image of a Au NP dimer showing a gap distance of 0.954 nm. (**F**) Plot of statistical yields of dimers, trimers and other oligomers obtained following reaction of Cit-Au NPs with the metal complex at concentration of $[Eu(phen)_2(MBA)_2]Cl$ = 30 μM.

The selective dimerization led to a 5 nm red-shift of the extinction band with peak centered at 525 nm along with broadening in the range 580-600 nm as shown in **Figure 4.4.A(ii)**, which is in well agreement to previous literature reports. Literature reports suggest that whereas dimerization of larger NPs (> 20 nm) may lead to appearence of longitudinal peak at a longer wavelength,[12,26] however, that of relatively smaller NPs (< 20 nm) does not necessarily lead to a large shift in the peak position.[17,27-28] Considering that in the reaction mixture the population of the dimers may be much less than 100%, the 5 nm red-shift, along with broadening in the range 580-600 nm, is indicative of significant dimer formation even in the presence of unreacted monomeric Au NPs. **Figure 4.4.B** shows the TEM images of the as-synthesized Au NPs (with average particle size 13.3 ± 6.5 nm) and that of the Au NPs from the dispersion treated with Eu-complex is represented in **Figure 4.4.C**. **Figure 4.4.D** represents the magnified view of as synthesized dimers indicating clear formation of dimers with uniform separation distance. The inter-dimer gap calculated[17] from the high resolution (HR)-TEM image of a representative Au nano-dimer shown in **Figure 4.4.E** was found to be 0.95±0.06 nm which is close to the theoretically calculated S···S distance of 1.006 nm in space (using "Avogadro") of the as-synthesized metal complex (**Figure 4.1.B**).

Figure A4.1.B (Appendix) shows the high resolution TEM (HRTEM) image of a typical Au nano-dimer (**Figure A4.1.A, Appendix**). The corresponding IFFT image shown in **Figure A4.1.C** obtained from select region of **Figure A4.1.B** clearly revealed gold lattice fringe with d-value of 0.20 nm corresponding to (200) Au-plane. Selected area electron diffraction (SAED) analysis of a representative Au nano dimer also clearly revealed diffraction corresponding to various planes of gold viz., (111), (200), (220), (222) and (311), respectively, as shown in **Figure A4.2, Appendix**. It may be mentioned here that the dimer formation in considerable yield depended on the concentrations of the precursors and time of reaction. **Figure A4.3.A** and **B, Appendix** show the changes recorded in UV-vis spectrum of Cit Au NPs with increasing concentration (15 μM, 30 μM and 90 μM) of the ligating complex in the dispersion. At higher complex concentration (90 μM), metal complex bridged discrete assemblies of Au nanoparticles (as depicted in TEM image of **Figure A4.4.C** and **D**) were predominately formed rather than Au nano-dimers that were obtained at lower complex concentrations viz. 15 μM (**Figure A4.4.A** and **B**) and 30 μM (**Figure 4.4.C**), respectively. At lower concentration of the complex, the UV-vis spectrum showed slight red shift with broadening (**Figure A4.3.A(ii)**), which increased to a certain extent with increasing the concentration of ligating complex in the Cit-Au NP dispersion, as depicted in **Figure A4.3.B(iii-iv)**. The dimerization was carried out in very dilute dispersion of Au NPs, maintaining a constant stoichiometry with the metal complex, in order to avoid aggregation during the reaction. This - on the other hand - limited the overall yield of the dimers in the reaction mixture, which otherwise competes for the remaining Au NP monomers. (Refer Experimental **Section 4.3.4** for details). Further, statistical analysis of several TEM images, indicated an overall percentage yield of 40% monomer, 52% dimer, 7% trimer and the rest % are in the form of higher order agglomerates (**Figure 4.4.F**) obtained corresponding to Cit Au monomeric dispersion treated with 30 μM metal complex. Additional TEM images of samples consisting of Au nano-dimers are shown in **Figure A4.5**(**A-F**), **Appendix**. The schematic depiction of Au nano dimer formation using pre-designed metal complex for SERS and TERS studies and mechanism of electromagnetic field enhancement therein is shown in **Figure 4.5**.

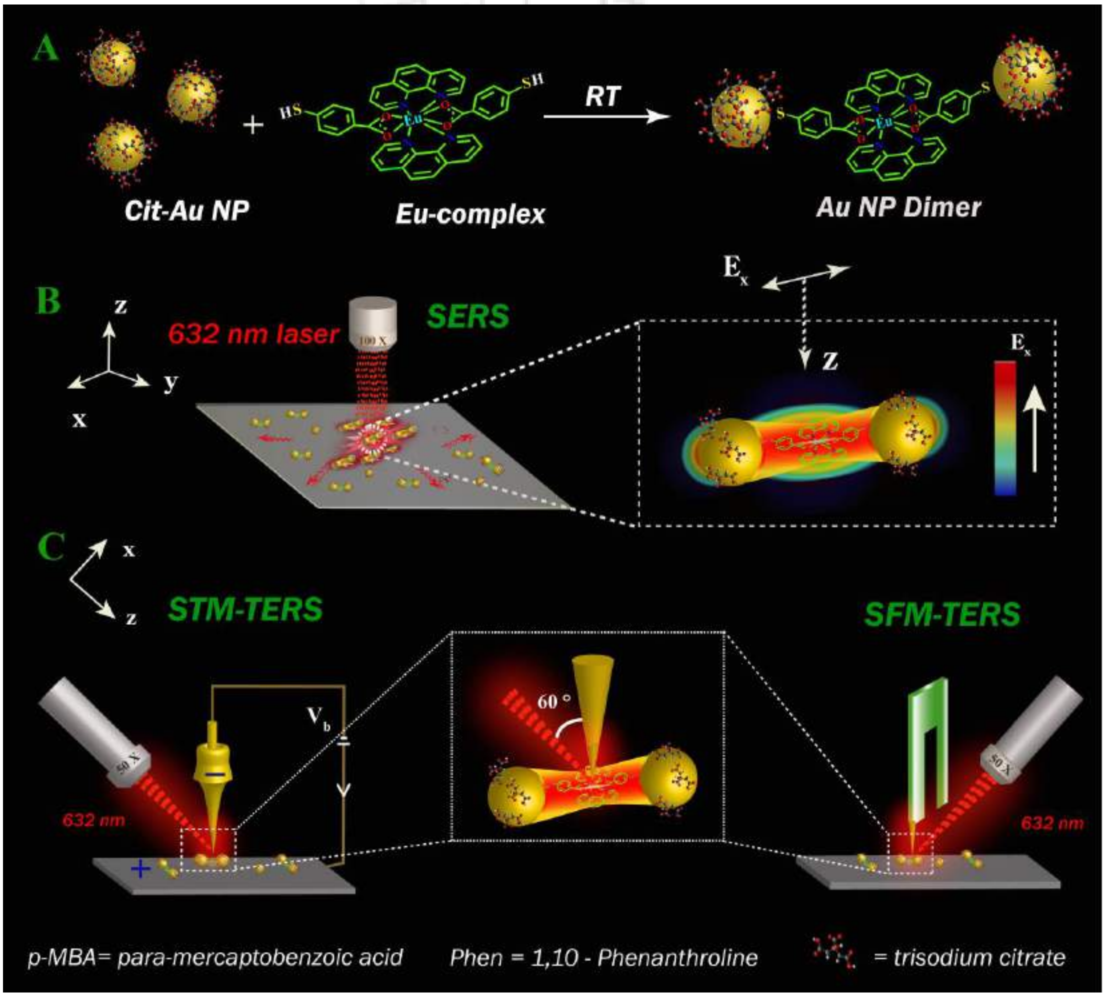

Figure 4.5. Schematic depiction of (**A**) Au nano dimer formation using pre-designed europium complex with cit-Au NPs; mechanistic depiction of the electromagnetic field enhancement at the hot-spot using (**B**) surface enhanced Raman (SER) and (**C**) tip-enhanced Raman (TER) spectroscopy.

4.5.3. SERS and TERS study of as-synthesized AuNP dimer

In order to investigate SERS, two laser sources were used with wavelengths at

532 nm and 632.8 nm. For this, the ligating complex only and as - synthesized Au nano-dimers with the ligating complex positioned in the hot-spot, were evaporated on glass substrate by liquid drop-cast method (refer to Experimental **Section 4.3.5** for further details). **Figure 4.6.A(i)** (red peak) represents the Raman spectrum of the as-synthesized Eu-complex (3 mM) with multiple peaks in the range 200-2700 cm^{-1}. Interestingly, the SERS spectrum of the Eu-complex in the Au nano-dimer was dominated by two strong bands (**Figure 4.6.A(ii)**, green peak) due to the aromatic ring stretches at 1078 cm^{-1} and 1588 cm^{-1}, respectively, when the excitation source was set to 632.8 nm. However, no clear peaks at the above positions could be observed for as-synthesized cit-Au NPs when excited at the same wavelengths (refer **Figure 4.6.B(i)**). However, upon excitation at 532 nm, two peaks – albeit could be observed occurring at 1078 cm^{-1} and 1588 cm^{-1} – but were very weak (refer **Figure 4.6.B(ii)**). This therefore supports the UV-vis spectral data obtained for monomeric Au NP and that obtained after dimerization in **Figure 4.4.A** and hence suitability of 632.8 nm laser for observation of enhanced Raman peaks due to the dimeric species. Thus, the near-resonant condition achieved with 632.8 nm laser, which reasonably matches with the gold nano-dimer absorption wavelength (as supported by the broadening of the spectrum in the range 580-600 nm in **Figure 4.4.A (ii)**), led to the enhanced plasmon field at the hot-spot than 532 nm laser source, which considerably improved the Raman scattering signal of the complex positioned in between the dimer.[29] Hence, superior SERS results could be obtained from the Au nano-dimer samples in presence of laser excitation at the higher wavelength which is also well supported by previous literature report.[29] Further, the appearance of a new weak peak at 343 cm^{-1}, attributed to Au-S vibration and simultaneous disappearance of the peak due to free thiol group at 2566 cm^{-1} (**Figure 4.6.A, inset**), supported the binding of Eu-complex via the sulphydryl of 4-MBA ligand leading to dimerization of Au nanoparticles selectively.

The SERS spectra allowed us to make a qualitative inference regarding the orientation of the ligands in the Eu-complex in the hot-spot region of the as - synthesized dimers based on the surface selection rule. The preferential enhancement of the Raman modes at 1078 cm^{-1} and 1588 cm^{-1}, assigned to

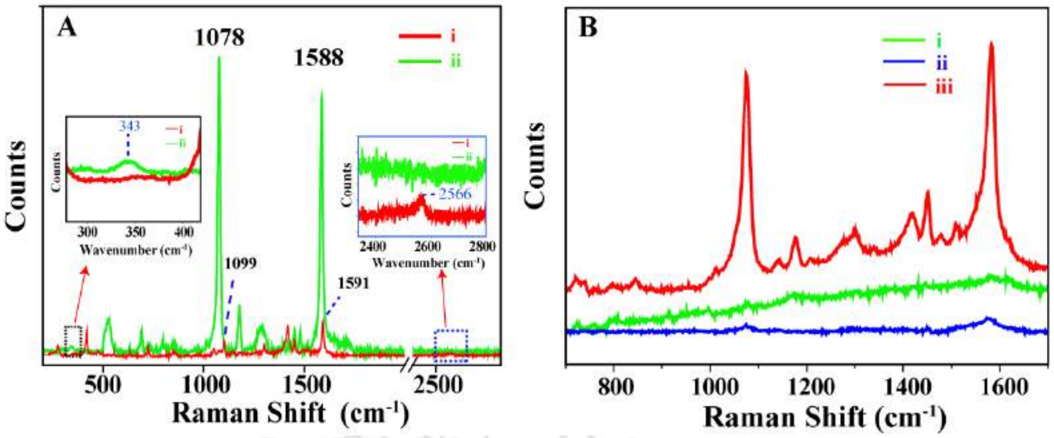

Figure 4.6. (**A**) (**i**) Raman spectrum of 3×10^{-3} M $[Eu(phen)_2(MBA)_2]Cl$ complex, (**ii**) SERS spectrum of $[Eu(phen)_2(MBA)_2]Cl$ complex ligated Au nano-dimer at a laser excitation wavelength of 632.8 nm. Magnified view of Raman spectra (**i**) and (**ii**) in the range 280-420 cm^{-1} (left) and 2350-2800 cm^{-1} (right) are shown in the inset. (**B**) (**i**) Raman spectrum of cit-Au NPs obtained after centrifugation at 20627 rcf for 15 min at 15 °C, SERS spectra of metal complex bridged Au nano-dimer at laser excitation wavelength (**ii**) 532 and (**iii**) 632.8 nm. (Objective -100×, time - 20 s)

aromatic ring vibrations respectively of 4-MBA in the Eu-complex along with the peak at 343 cm^{-1} being attributed to Au-S vibration - compared to their normal Raman modes - indicated strong field polarization of these modes normal to the metal surface plane (as depicted in **Figure 4.5**). Hence it can be inferred that the two 4-MBA groups in the Eu-complex bearing the benzene ring must preferably be in trans-orientation to each other (either perpendicular or preferably in tilted geometry with respect to the metal surface plane) around the Eu metal facilitating the binding via sulphydryl group leading to Au-Au dimerization and hence accounts for effective Raman enhancement.**[30]** The SERS intensity detected in any Raman measurement is the sum of signal enhancement from all the probe moieties that lie within the laser focus region. In addition, the field enhancement in nanoshell or nanosphere dimers has been found to be maximum for field polarization parallel to the interparticle axis of the dimer, irrespective of all other laser polarization directions.**[29]** Therefore, taking into account the above factors, we report the average SERS enhancement factor using equation (1),

$$E = \frac{I_{SERS} N_{bulk}}{I_{normal} N_{SERS}} \qquad (1)$$

where N_{bulk} and I_{normal} are the number of molecules and measured average intensities of normal Raman scattering of metal complex in bulk, whereas N_{SERS} and I_{SERS} are the number of metal complex and average SERS intensity obtained from the population of Au nano-dimer, trimer, tetramer etc under the laser illumination beam, when measured with 632.8 nm laser source (objective - 100×, time - 20 s). The average SERS enhancement factor calculated using equation (1) considering peak at 1078 cm^{-1} for the designed Au nano-dimer was determined to be 1.6×10^{9} which is quite suitable for carrying out measurements down to single molecule level.[17] (Refer **Section 4.7.1** for SERS EF calculation)

Further, we have carried out scanning probe microscopy (SPM) correlated Tip-enhanced Raman spectroscopy (TERS) to support the SERS result with an attempt to reach higher spatial resolution and to elucidate the origin of Raman signal from individual dimeric nanostructures. For this, it is assumed that a single complex had ligated Au nano-dimer through the Raman active 4-MBA. **Figure 4.7.A** shows the tuning fork amplitude feedback-SFM topograph of the as-synthesized Au-nano dimer imaged on 4.5×3.5 μm^2 sampled area on silicon substrate. Refer Experimental **Section 4.3.6** for detailed discussion on TERS configuration and imaging condition. Prominently present single Au nano-dimers are identified in white circles in **Figure 4.7.A**, although Au-nanodimer assemblies arising out of evaporation induced aggregation could also be observed in several locations. TER spectrum recorded in tip-down mode as shown in **Figure 4.7.B(i)** when probed with 632.8 nm laser, showed clear vibrational peaks at 1078 cm^{-1} and 1588 cm^{-1}, akin to the ones observed in the SER spectrum (**Figure 4.6.A(ii)**). However, no vibrational peak at 1078 cm^{-1} and 1588 cm^{-1} could be clearly observed when TER spectrum was recorded using 532 nm laser (**Figure 4.7.B(ii)**).

In addition, when the tip was retracted back by 50 nm above the laser focus from the sampled area, characteristic vibrational bands obtained in TER spectrum in tip-down mode could hardly be observed (**Figure 4.7.B(iii)**) which indicated strong TERS signal enhancement. Although the signal to noise ratio in tip-retracted mode was poor to get a discernible far-field signal, howbeit, the far field effect would still be there. Similar observations were made when the Raman spectral acquisition was carried out in STM-TERS mode. Here TER spectra were

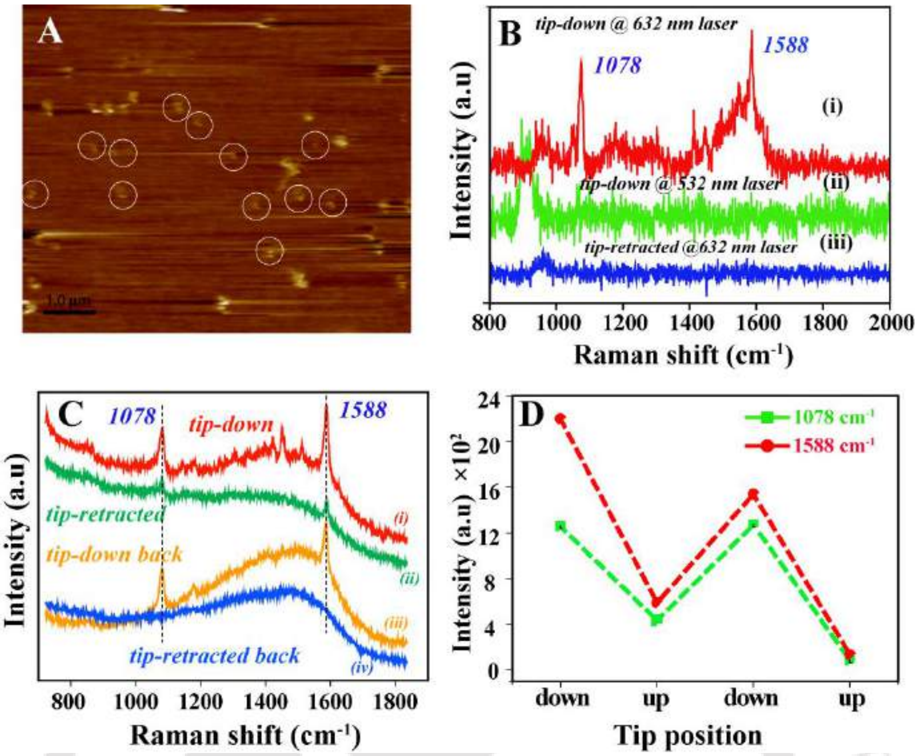

Figure 4.7. (**A**) Tuning fork (TF) amplitude feedback-SFM topograph of the as-synthesized Au-nano dimer on silicon substrate. (**B**) SFM-TER spectra of Au nano dimer obtained (when tip was placed at one of the representative Au-nano dimers obtained in image (**A**)) at different conditions: (**i**) tip-down mode (632.8 nm, 20 s); (**ii**) tip-down mode (532 nm, 20 s); (**iii**) tip-retracted (by 50 nm) mode (632.8 nm, 20 s). (**C**) STM-TER spectral cycle corresponding to STM topograph (image not shown, 0.5V, 1 nA) of Au nano-dimer at tip-down (**I, iii**) and tip-retracted (**ii, iv**) mode. (632.8 nm, 20 s) (**D**) Respective change in frequency at 1078 cm^{-1} (green) and 1588 cm^{-1} (red) during tip-down and tip-up spectral acquisition cycle as shown in (**C**).

collected by performing two spectral acquisition cycles in tip-down and tip-up modes, each successively for gold tip positioned over the same area as represented in **Figure 4.7.C (i-iv)**. **Figure 4.7.D** clearly shows the results of frequency sweep at 1078 cm^{-1} and 1588 cm^{-1} during a tip-up and down cycle. Interestingly, signal obtained at tip-retracted mode was very weak. The results therefore provided a strong evidence for the presence of near-field effect in signal enhancement arising out of tip-sample interaction in conjunction with the far-field effect at the hot-spot of the dimer and hence the reproducibility of the tip induced Raman enhancement. Additionally, SFM (TF) topograph correlated TER spectra were also recorded as shown in **Figure A4.6.** It was observed that the dimeric Au NP (marked in area 2) showed detectable TER signal at 1588 cm^{-1} (strong) and

1078 cm^{-1} (weak) characteristic of Eu-complex (**Figure A4.6.C**). However, no such discernible peak signal could be observed for single Au nanoparticle for gold tip positioned over area 1 (**Figure A4.6.B**). As a control study, TER spectrum was recorded by positioning the gold tip over particle free area (marked area 3, **Figure A4.6.D**), which exhibited a featureless spectrum. The results, therefore, provided further evidence that the observed TER signal obtained with 632.8 nm laser originated from the ligated Eu-complex trapped in the hot-site of single Au nano-dimer. It is to be noted that, characteristic spectral peaks observed in all the recorded TER spectra exhibited low intensity as when compared to SER spectra which however originated from ensemble average of large number of molecules (metal complex positioned in a hot spot) for diffraction limited laser focus. Additionally, it is to be mentioned that although TERS acquisition in ambient condition often result in generation of rough features in SPM topographic image[7] resulting in poor image and signal (as also observed in our case), however, it did help obtain Raman signal with optimal signal to noise ratio herein.

Thus, overall enhancement in TERS that constitutes far-field signal and near field signal would be higher than each of them in isolation, resulting in a discernible signal to noise ratio as seen in **Figure 4.7.B**(**i**) and **4.7.C**(**i, iii**) in tip-down configuration. Now, since major part of the TERS signal is generated due to enhanced field at the tip-apex (near field effect), quantification of the tip induced enhancement factor is important. TERS enhancement factor (EF) was calculated using contrast factor obtained from the ratio of measured near-field and far-field Raman intensity values and their respective scattering areas following equation (**2**) and (**3**),

$$Contrast = \frac{I_{near\ field}}{I_{far\ field}} = \frac{I_{tip\ down} - I_{tip\ up}}{I_{tip\ up}} \qquad (2)$$

$$Enhancement\ Factor = Contrast \times \frac{A_{focus}}{A_{tip}} = Contrast \times \frac{d^2_{focus}}{d^2_{tip}} \qquad (3)$$

where $I_{near\ field}$ and $I_{far\ field}$ refers to the tip-enhanced near-field and far-field Raman signal intensities, A_{focus} and A_{tip} refers to far-field and near-field laser scattering area, d_{focus} and d_{tip} refers to diameter of laser focus and to two times the radius of curvature of the tip respectively.

Thus TERS-EF calculated following equation (**2**) and (**3**) based on SFM (TF)-TERS data with respect to peak at 1078 cm^{-1} and 1588 cm^{-1} was found to be *3.2* × 10^4 and *3.6* × 10^4 respectively. (Refer Experimental **Section 4.7.2** for TERS EF calculation) It is to be mentioned that actual field enhancement depends upon many other factors, which include tip-size, tip material, tip radius, tip-sample distance, tip-sample alignment, dielectric properties of the probe molecule including optimal laser focussing. Additionally, for the case herein, there can be redistribution of hot-spot in the presence of the tip as interaction between field generated by the tip and each nanoparticle may also become part of the system (Refer **Figure A4.7**, **Appendix**). Thus the enhancement at the hot-spot in the presence of the tip would be more complex than simple interaction between the field generated by the tip and the molecular bond. (Refer **Discussion A4.1**, **Appendix** for detailed discussion on tip induced enhancement) Thus considering the above factors, TERS enhancement factor of 10^4 can be considered as lower bound here in contrast to SERS EF of 10^9, which is quite consistent with the literature reports of such enhancements.[31-32]

4.6. Conclusion

Thus, we report a new synthetic method to generate SERS active Au nano-dimer (SERS substrate) using co-ordination complex of Eu metal as ligating moiety. The metal complex bridged Au nano-dimer exhibited exclusive SERS when compared to normal Raman spectrum obtained for the as-synthesized metal complex only. Therefore, the present approach of attaining dimerization of Au nanoparticles using metal complex allowed us to overcome the limitations of most SERS based measurement by ensuring the availability of probe molecule in the hot-spot, based on complexation chemistry. Secondly, metal complex based dimerization allowed us to achieve control over the uniform gap in the hot-site, which has been one of the prime concerns towards the attainment of reproducible SERS data in most Raman based studies. Further, results from SERS and TERS experiments demonstrated superiority of the design in achieving unprecedented Raman signal enhancement using both tip and laser light induced plasmons – at appropriate laser wavelength. Thus, the availability of metal of choice based on the probe molecule to be studied in the hot-site may provide us with a new platform to study complex chemistry therein. Hence, it can be inferred that the proposed gold based nanostructures which offered an enhancement factor on the order of 10^9 could serve as potent SERS substrate for Raman based detection, single molecular spectroscopic studies along with their applicability in the field of bio-sensing, photocatalysis and photovoltaics.

4.7. Calculation of SERS and TERS Enhancement Factor

4.7.1. SERS Enhancement Factor (EF)

The average SERS enhancement factor[33] is given by,

$$EF = \frac{I_{SERS} N_{bulk}}{I_{normal} N_{SERS}} \qquad (1)$$

where N_{bulk} and N_{SERS} are the number of molecules of the metal complex in bulk and the number of metal complex in the Au nano-dimers under the laser excitation beam; whereas I_{norm} and I_{SERS} are the measured intensities for normal Raman scattering from the bulk complex and SERS intensity of the metal complex in Au nano-dimers, measured with 632.8 nm laser source. The measurement was carried out with 100× objective (numerical aperture = 0.9) with an acqusition time of 20 s for each measurement. We considered the average Raman scattering intensities - I_{norm} and I_{SERS} - obtained from the average of at least 10 different Raman measurements, for acquisition carried over different probed area under 632.8 nm laser illumination. We assumed in our calculation that one hot-site contained only one complex molecule.

Concentration of as synthesized Cit-Au NPs = 0.95 nM[34]

Therefore, number of moles of Cit-Au NPs in the 5 mL reaction volume = 0.95×10^{-12}

Therefore, total number of NPs in 5 mL reaction volume = $0.95\times 10^{-12} \times N_A$

$= 5.721 \times 10^{11}$

The percentage yield of dimer, trimer and tetramer as obtained after reaction of Cit-Au NP dispersion with Eu-complex in the reaction mixture was found to be 51.8 %, 7.2 % and 0.28 % respectively.

Therefore,

Number (population) of dimers in 5 mL reaction volume = 1.4817×10^{11}

Number (population) of trimers in 5 mL reaction volume = 0.2059×10^{11}

Number (population) of tetramers in 5 mL reaction volume = 0.0085×10^{11}

Now,

Total number of ligating complex molecules in the 5 mL Au NP dispersion undergoing reaction to yield 51.8 % dimers, 7.2 % trimer and 0.28 % tetramer - neglecting the contribution from multimers - can be calculated as follows:

Number of complex molecule in 5 mL reaction volume forming dimer = Number of dimer in 5 mL reaction volume = 1.4817×10^{11}

Number of complex molecule in 5 mL reaction volume forming trimer = 2 × Number of trimer in 5 mL reaction volume = $2 \times 0.2059 \times 10^{11} = 0.4118 \times 10^{11}$

Number of complex molecule in 5 mL reaction volume forming tetramer = 4 × Number of tetramer in 5 mL reaction volume = $4 \times 0.0085 \times 10^{11} = 0.0340 \times 10^{11}$

Total number of complex molecules ligating Au NPs in 5 mL dispersion

$= (1.4817 + 0.4118 + 0.0340) \times 10^{11} = 2 \times 10^{11}$

Volume of the Au NP dimer dispersion dropcast (probed under laser illumination) = 0.1 mL

Therefore, total number of complex molecule ligating Au NPs in probed volume, N_{SERS}

$$= \frac{2 \times 10^{11} \times 0.1}{5}$$

$$= \quad 4\times10^{9}$$

Average SERS intensity = I_{SERS} = 9459.7

Now,

Concentration of the Eu-complex molecule considered for normal Raman measurement = 3 mM

Volume of Eu-complex molecule dropcasted = 0.1mL

Total number of Eu-complex molecule in the probed volume, N_{bulk} can be calculated as follows:

Moles of Eu-complex in 0.1 mL solution **=** 3×10^{-7}

Therefore total number of complex molecule probed = $3\times10^{-7}\times N_A$ = 18.069×10^{16}

Normal Raman scattering intensity, I_{norm} =267

Considering **equation** (**1**), average enhancement factor was estimated to be,

$$EF = \frac{9459.7\times18.069\times10^{16}}{267\times4\times10^{9}} = 1.6\times10^{9}$$

4.7.2. TERS Enhancement Factor (EF)

The TERS enhancement factor is calculated taking into account the contrast factor obtained from the ratio of near-field and far-field Raman scattering intensity and their corresponding scattering area.[35,36] The enhancement factor is calculated using equation 1 and 2 as below:

$$Contrast = \frac{I_{near\ field}}{I_{far\ field}} = \frac{I_{tip\,down} - I_{tip\,up}}{I_{tip\ up}} \qquad (1)$$

$$Enhancement\ Factor = Contrast \times \frac{A_{focus}}{A_{tip}} = Contrast \times \frac{d^2_{focus}}{d^2_{tip}} \qquad (2)$$

where $I_{near\,field}$ and $I_{far\,field}$ refers to the tip-enhanced near-field and tip-retracted far-field Raman signal intensity , A_{focus} and A_{tip} refers to far- field laser scattering area and near-field laser scattering area at the tip-apex, d_{focus} refers to diameter of laser focus and d_{tip} refers to two times the radius of curvature of the tip. It is to be noted that during TER spectra collection, far field signal may be present as background. Therefore, the near-field Raman scattering intensity $I_{near\,field}$ is defined as difference between the Raman scattering intensity in tip-down and tip-up mode whereas far-field Raman scattering intensity $I_{far\,field}$ refers to Raman intensity at tip-up mode. The EF is calculated with respect to peak at 1078 cm^{-1} and 1588 cm^{-1} obtained using SFM(TF)-TERS. The calculated diameter of laser focal spot is 1838 nm and tip radius of TF-TERS probe (Bruker) = 20 nm. The Raman peak intensity values obtained using TF-TERS set-up are tabulated below (**Table 1**):

Table 1: Raman peak intensity values corresponding to wavenumbers 1078 cm^{-1} and 1588 cm^{-1} at tip-down and tip-up modes as obtained from SFM (TF)-TER spectra.

Wavenumber (cm^{-1})	**Intensity (Tip-down)**	**Intensity (Tip-up)**	**Contrast Factor**
1078	196	12	15.3
1588	258	14	17.4

Therefore,

TERS-EF with respect to peak at 1078 cm^{-1}:

$$Enhancement\ Factor = Contrast \times \frac{d^2_{focus}}{d^2_{tip}} = 3.2 \times 10^4$$

and TERS-EF with respect to peak at 1588 cm^{-1}:

$$Enhancement\ \ Factor\ =\ Contrast \times \frac{d_{focus}^{2}}{d_{tip}^{2}}\ =\ 3.6 \times 10^{4}$$

4.8. References

1. Jensen, L.; Aikens, C. M.; Schatz, G. C. *Chem. Soc. Rev.* **2008**, *37*, 1061.

2. Ko, H.; Singamaneni, S.; Tsukruk, V. V. *Small* **2008**, *4*, 1576.

3. Zhang, C. L.; Lv K. P.; Cong, H. P.; Yu, S. H. *Small* **2012**, *8,* 648.

4. Wang, X.; Li, M.; Meng, L.; Lin, K.; Feng, J.; Huang, T.; Yang, Z.; Ren, B. *ACS Nano* **2014**, *8*, 528.

5. Li, W.; Camargo, P. H. C.; Lu, X.; Xia, Y. *Nano Lett.* **2009**, *9*, 485.

6. Thomas, R.; Swathi, R. S. *J. Phys. Chem. C* **2012**, *116*, 21982.

7. Zhang, Z.; Sheng, S.; Wang, R.; Sun, M. *Anal. Chem.* **2016**, *88*, 9328.

8. Wang, H.; Schultz, Z. D. *Analyst* **2013**, *138*, 3150.

9. Kusch, P.; Mastel, S.; Mueller, N. S.; Azpiazu, N. M.; Heeg, S.; Gorbachev, R.; Schedin, F.; Hubner, U.; Pascual, J. I.; Reich, S. *Nano Lett.* **2017**, *17*, 2667.

10. Tsai, D. H.; Cho, T. J.; DelRio, F. W.; Gorham, J. M.; Zheng, J.; Tan, J.; Zachariah, M. R.; Hackley, V. A. *Langmuir* **2014**, *30*, 3397.

11. Fruhnert, M.; Kretschmer, F.; Geiss, R.; Perevyazko, I.; Dana, C. M.; Steinert, M.; Janunts, N.; Sivun, D.; Hoeppener, S.; Hager, M. D.; Pertsch, T.; Schubert, U. S.; Rockstuhl, C. *J. Phys. Chem. C* **2015**, *119*, 17809.

12. Liu, M.; Fang, L.; Li, Y.; Gong, M.; Xuc, A.; Deng, Z. *Chem. Sci.* **2016**, *7*, 5435.

13. Homberger, M.; Schmid, S.; Timper, J.; Simon, U. *J. Cluster Sci*. **2012***,* *23*, 1049.

14. Chak, C. P.; Xuan, S.; Mendes, P. M.; Yu J. C.; Cheng, C. H. K.; Leung, K. C. F. *ACS Nano* **2009**, *3*, 2129.

15. Chen, G.; Wang, Y.; Tan, L. H.; Yang, M.; Tan, L. S.; Chen, Y.; Chen, H. *J. Am. Chem. Soc.* **2009**, *131*, 4218.

16. Chen, H. Y.; Lin, M. H.; Wang, C. Y.; Chang, Y. M.; Gwo, S. *J. Am. Chem. Soc.* **2015**, *137*, 13698.

17. Lim, D. K.; Jeon, K. S.; Kim, H. M.; Nam, J. M.; Suh, Y. D. *Nat. Mater.* **2010**, *9*, 60.

18. Divya. V.; Biju, S.; Varma, R. L.; Reddy, M. L. P. *J. Mater. Chem.* **2010**, *20*, 5220.

19. Nakamato, K.; McCarthy, P. J. JohnWiley & Sons, New York, NY, USA, **1968**.

20. Schilt, A. A.; Taylor, R. C. *J. Inorg. Nucl. Chem.* **1959**, *9*, 211.

21. Qin, W.; Zhang, Y.; Liu, W.; Tan, M. *Spectrochimica Acta Part A* **2003**, *59*, 3085.

22. Michota, A.; Bukowska, J. *J. Raman Spectrosc.* **2003**, *34*, 21.

23. Tsaryuk, V.; Zolin, V.; Legendziewicz, J.; Szostak, R.; Sokolnicki, J. *Spectrochimica Acta Part A* **2005**, *61*,185.

24. Tsaryuk, V.; Zolin, V.; Puntus, L.; Savchenko, V.; Legendziewicz, J.; Sokolnicki, J.; Szostak, R. *Journal of Alloys and Compounds* **2000**, *300*, 184.

25. Dutta, A.; Paul, A.; Chattopadhyay, A. *RSC Adv.* **2016**, *6*, 82138.

26. Zheng, Y.; Rosa, L.; Thai, T.; Ng, S. H.; G´omez, D. E.; Ohshima, H.; Bach, U. *J. Mater. Chem. A* **2015,** *3*, 240.

27. Dewi, M. R.; Gschneidtner, T. A.; Elmas, S.; Ranford, M.; Moth-Poulsen, K.; Nann, T. *ACS Nano* **2015**, *9*, 1434.

28. Maye, M. M.; Nykypanchuk, D.; Cuisinier, M.; Lelie, D.; Gang, O. *Nat. Mater.* **2009**, *8*, 388.

29. Talley, C. E.; Jackson, J. B.; Oubre, C.; Grady, N. K.; Hollars, C. W.; Lane, S. M.; Huser, T. R.; Nordlander, P.; Halas, N. J. *Nano Lett*. **2005**, *5*, 1569.

30. Le Ru, E. C.; Meyer, S. A.; Artur, C.; Etchegoin, P. G.; Grand, J.; Lang, P.; Maurel, F. *Chem. Commun*. **2011**, *47*, 3903.

31. Zrimsek, A. B.; Chiang, N.; Mattei, M.; Zaleski, S.; McAnally, M. O.; Chapman, C. T.; Henry, A. I.; Schatz, G. C.; Van Duyne, R. P. *Chem. Rev.* **2017**, *117*, 7583.

32. Sabanes, N. M.; Driessen, L. M. A.; Domke, K. F. *Anal. Chem.* **2016**, *88*, 7108.

33. Wang, T.; Zhang, Z.; Liao, F.; Cai, Q.; Li, Y.; Lee, S. T.; Shao, M. *Sci. Rep.* **2014**, *4*, 4052.

34. Dutta, A.; Paul, A.; Chattopadhyay, A. *RSC Adv.* **2016**, *6*, 82138.

35. Sabanes, N. M.; Driessen, L. M. A.; Domke, K. F. *Anal. Chem.* **2016**, *88*, 7108.

36. Mehtani, D.; Lee, N.; Hartschuh, R. D.; Kisliuk, A.; Foster, M. D.; Sokolov, A. P.; Maguire, J. F. *J. Raman Spectrosc.* **2005**, *36*, 1068.

CHAPTER 5

Probing Cancer Cells through Intracellular Aggregation Induced Emission Kinetic Rate of Copper Nanoclusters

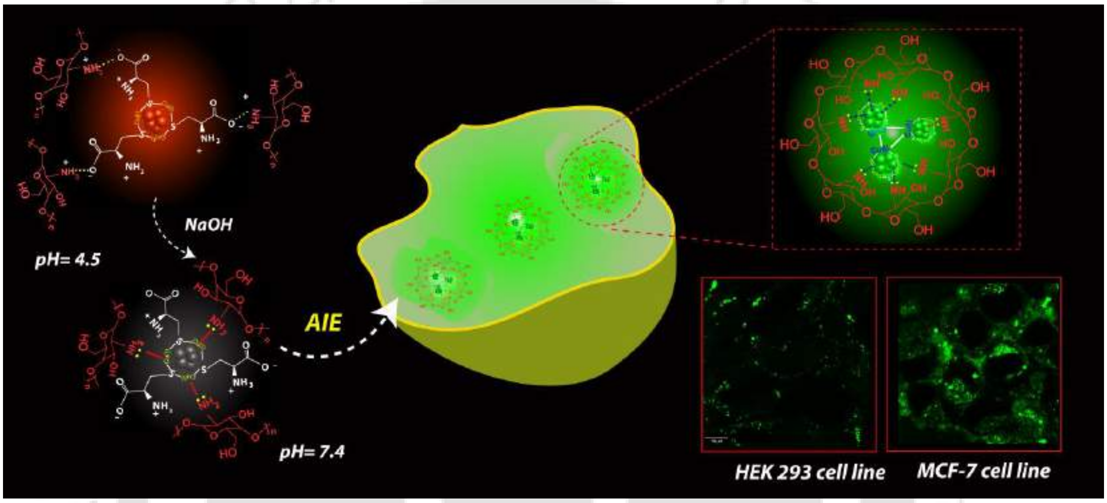

***Chapter 5** reports a pH responsive luminescent copper nanocluster (Cu NC) with aggregation induced emission (AIE) characteristics. The CuNCs synthesized in presence of L-cysteine and chitosan, responded distinctly to pH 4.5 and above 7.0. Thus upon internalization into living cells, the NCs displayed real time response to intracellular pH (pH_i) change exhibiting orange-red emission at pH_i 4.5 while bright green emission was observed over time at pH_i 7.4, through their AIE attributes. Intriguingly, intracellular rate constant value derived for AIE kinetics in MCF-7 cells was found 3-fold higher than that in HEK-293 cell lines whereas the value was 2-fold higher than that observed in the aqueous medium. This provided a new platform to study different cell lines based on intracellular AIE in living cells, with additional potential for future applications in cellular imaging, diagnostic and disease detection.*

**** ACS Appl. Mater. Interfaces 2017 American Chemical Society (Under Revision)***

5.1. Introduction

While it is important to pursue identifying specific molecular signatures of health, it can also be considered equally important to probe the collective effect of the state of the health on any probe.[1] Research in molecular understanding of state of health has helped develop intracellular probes, which depend on specific interactions between the molecules or organelles of interest and the externally added probes.[2-4] This is based on the idea that a cell or tissue is more than just a simple collections of molecules. Thus understanding the complex interactions within the cell may be the key to improved identification of health parameters. A case in point could be the identification of cancer cells. Cancer tumours exhibit a series of abnormal molecular events such as change in intracellular pH, temperature, enhanced receptor mediation, protein overexpression and reactive oxygen/nitrogen generation.[3,5-6] Therefore, there is a need to develop probe the property of which would reflect specificity of the intracellular environment of the cancer cells as compared to non-cancerous cells. Literature is replete with the use of luminescence materials - e.g., organic dyes, inorganic metal complexes, synthetic organic molecules or their nanoscale counterparts - to probe the abovementioned parameters, organelles of interests and various intracellular phenomena in vitro.[7-9] However, their limited photostability and occurrence of photo bleaching have led to the advent of quantum dots, carbon dots and atomic clusters as viable alternatives.[10-12]

In that regard, an important candidate that is under current focus for development with intriguing molecule - like properties is luminescent metal nanoclusters (NCs) that exhibits large Stokes - shifted photoluminescence, high photostability, ease of synthesis and option for specific surface functionalization.[13-14] The NCs are proven to be suitable as cellular imaging probes as well as in theranostics.[15] Additionally, it has been reported that Au and Cu NCs exhibit facile aggregation induced emission (AIE) in liquid medium,[16] which may make them useful for observing intracellular complex interactions. However, most NC based AIEs have been demonstrated via cation or solvent mediated strategy, which, however, limits their applicability in biological systems.[17-18] Meanwhile, single wavelength emissive pH guided AIE active fluorescent "on-off" NC probe has been demonstrated.[19-20] Howbeit, NCs being differentially sensitive to pH at two distinct emission wavelengths with AIE attribute as cellular probe has not yet been established. Additionally, distinction of cell lines based on different AIE kinetic rate specific for each may also be of considerable importance.

5.2. Outline of the present work

Herein, we report a pH stimulus responsive luminescent CuNCs, synthesized in the presence of L-cysteine and chitosan. The as-synthesized CuNCs showed bright orange-red emission at pH 4.5 and intriguingly at pH 7.0 and above they exhibited aggregation induced emission (AIE) behaviour with cyan-green emission. Importantly, the rate constants derived for first order aggregation observed for AIE kinetics was observed to be higher in MCF-7 cells than that in HEK-293 cells. The results indicated the difference in the nature of intracellular environment of the MCF-7 cells compared to the HEK-293 cells with higher expression levels of proteins and other biomolecules in cancerous cells (MCF-7 cells) triggering faster aggregation. The presence of L-cysteine and chitosan biopolymer as ligands in the as-synthesized CuNCs imparted stability, provided AIE attribute and biocompatibility for intracellular probe.

5.3. Experimental Section

5.3.1. Materials

Copper (II) nitrate hexahydrate (Merck, India), L-cysteine (Sigma Aldrich, USA), chitosan (high molecular weight, deacetylated chitin, viscosity average molecular weight 310-375 kDa, Sigma Aldrich, USA), sodium hydroxide (Merck, India), quinine sulphate (Sigma Aldrich, USA), sulphuric acid (Merck), coumarin 153 (Sigma Aldrich, USA), bovine serum albumin (BSA, Sisco Research Laboratories Pvt. Ltd., India), lysozyme (Sisco Research Laboratories Pvt. Ltd., India), 3-(4,5-dimethylthiazol-2-yl)-2,5-diphenyltetrazolium bromide (MTT, Himedia, India) were purchased and used as received without further purification. Milli-Q grade water (18.2 MΩ cm, Millipore) was used for all experimental works.

5.3.2. Preparation of Chitosan solution (pH= 5.5)

15 mg chitosan was dissolved in 3 mL water by adding a few drops of glacial acetic acid (99-100%) under constant stirring. The pH of the resulting solution was then adjusted to pH= 5.2±0.2 with 1.0 M NaOH.

5.3.3. Synthesis of cysteine stabilized copper nanoclusters (CuNCs)

(a) ***Red emitting CuNCs.*** In a typical synthesis, 30 mg L-cysteine was added to 4 mL aqueous solution of chitosan-water mixture (containing 0.5 mL, 5mg/mL as prepared chitosan solution). The resulting mixture was stirred vigorously for 3 h at room temperature. At the end of 3 h of stirring, 75 mM $Cu(NO_3)_2.6H_2O$ solution was added dropwise to the reaction mixture, which was then allowed to stir for 30 min at the same condition. The resulting transparent CuNCs so obtained exhibited bright orange-red emission under 365 nm UV-light illuminations. (pH= 4.5) The so obtained Cu NCs were further purified by dialysis using 1kDa dialysis membrane for 1 h and was stored at 4 °C for further use.

(b) ***Green emitting CuNCs.*** The as-synthesized Cu NCs obtained at pH=4.5 was then further treated with 1.0 M NaOH to gradually increase the pH of the medium to 7.4. The clear solution immediately turned into semi-transparent dispersion, which was allowed to age for 1-6 h. During the aging time, the semi-transparent dispersion turned into a yellow-brown dispersion, which exhibited striking green fluorescence under 365 nm UV-light illuminations.

(c) ***Time-dependent PL study of CuNC dispersion at pH 7.4.*** 4 mL of the as - synthesized CuNC dispersion was taken and pH of the dispersion was adjusted to 7.4 (using 0.1 M NaOH). PL spectra of the dispersion were then recorded at different intervals of time to monitor the change in emission intensity.

(d) ***Cysteine stabilized CuNCs in absence of chitosan.*** Freshly prepared $Cu(NO_3)_2.6H_2O$ (75 mM) was added dropwise to 4 mL aqueous solution containing 30 mg L-cysteine. The mixture was allowed to stir for 30 min when a cloudy dispersion of CuNCs was formed. The solution was allowed to stand for 1 h when white precipitate of the as-synthesized CuNCs separated out. Thereafter, the precipitate was collected and redispersed in 4 mL water for further use.

5.3.4. Control experiment

(i) Time dependent AIE study in presence and absence of chitosan

4 mL from each of the dispersions containing CuNCs and synthesized in the presence and absence of chitosan was taken in a vial and the pH of dispersion was slowly adjusted to 7.4 using 0.1 M NaOH. Thereafter, time-dependent kinetic study was continued till 240 min.

(ii) Time dependent AIE study of as - synthesized CuNCs and in presence of BSA and lysozyme at pH 7.4

BSA and lysozyme were chosen as representative proteins for the experiments. A stock solution of 12 mg/mL of BSA and lysozyme were prepared. 4 mL as - synthesized CuNCs was diluted to 10 mL and was kept for three different set of experiment. 3 mL each of diluted dispersions of CuNCs was taken in three different vials. Thereafter, 1 mL as prepared BSA and lysozyme solution (12 mg/mL) each was added to two respective vials and the mixture was allowed to homogenize by gentle shaking. The pH of the dispersion of all three sets was then adjusted to 7.4 using 0.1M NaOH and time-dependent kinetic study was carried out at various time intervals till 240 min. Each set of experiments were carried out in triplicate.The rate of AIE kinetics was obtained from the plot of intensity ratio (I/I_0) versus time. For all experiments, intensity at 470 nm was monitored. Thereafter, rate constant values were obtained from the slope of corresponding integrated rate equation plot i.e., $\mathrm{Ln}(I/I_0)$ *versus* time.

5.3.5. Cell Culture Studies

Human breast adenocarcinoma cells (MCF-7) and Human embryonic kidney cells (HEK-293) for cellular study were acquired from the National Centre for Cell Sciences (NCCS), Pune, India. MCF-7 cells and HEK-293 cells were cultured in Dulbecco's modified Eagle's medium (DMEM) supplemented with 10% (v/v) fetal bovine serum (PAA Laboratories, Austria), L-glutamine (4mM), penicillin (10000 units), streptomycin (10 mg/mL, Sigma-Aldrich) and maintained in 5% CO_2 humidified incubator at 37 °C.

5.3.5.a. Cell viability assay

To carry out cell viability assay, MCF-7 cells and HEK-293 cells (5×10^3 cells/well) were seeded in a 96 well microplate, containing DMEM growth medium supplemented with 10% (v/v) fetal bovine serum (FBS) under 5% CO_2 humidified incubator at 37 °C, overnight. The MCF-7 cells as well as HEK-293 cells were first treated with varying concentrations of CuNCs (0.072–0.362 µg/mL with respect to copper). Copper content in the NC probe was estimated by atomic absorption spectroscopic (AAS) measurements. After 24 h incubation, MTT based cell viability assay was carried out. The absorbance at 570 nm due to formazan formation in DMSO was recorded using a TECAN microplate reader. The assay was carried out in triplicates for each concentration of NC probe mentioned above. Cell viability was calculated as follow:

$$\%\ \text{viable cell} = \frac{(A_{570} - A_{690})\ \text{of treated cells}}{(A_{570} - A_{690})\ \text{of control cells}} \times 100$$

where A_{570} corresponds to absorbance of formazan and A_{690} arises due to background.

5.3.5.b. Intracellular pH adjustment

To carry out live cell imaging at two different pH conditions, pH of culture media (phenol red free) was adjusted to pH 4.5 with 0.1 M HCl and pH 7.4 with 0.1 M NaOH, and measured by pH-meter. For imaging in acidic condition, the intracellular pH was attained by incubating the cells (MCF-7 or HEK-293) in pH adjusted culture media (pH-4.5) and allowing it to homogenize for 10 min before addition of the probe. Whereas for imaging in pH 7.4, the probe was incubated in fresh DMEM (pH 7.4) media followed by repeated washing and fixing.

5.3.5.c. Cell culture and confocal laser scanning microscopic (CLSM) imaging

(i) Fixed cell imaging: For confocal imaging at two different pH conditions in both MCF-7 and HEK-293, cells were seeded onto a microscopic coverslip placed in two 35 mm culture plates and were allowed to grow overnight in DMEM growth medium. Before treating the cells with the NC probe, for imaging at acidic conditions, the cells were washed with PBS twice, which was replaced with phenol red free culture media (pH 4.5). After homogenization for 10 minutes at acidic conditions the probe (0.144 µg/mL) was added and incubated for 1h. In case of imaging at pH 7.4, the cells were incubated in fresh DMEM (phenol red free, pH 7.4) media with the probe for 1 h. After incubation, the cells from both pH conditions were washed with PBS and were fixed with 70% chilled ethanol. Similarly, for imaging with cytopainter green, the cells incubated with the probe at pH 4.5, were washed twice with PBS followed by incubation with 1.0 mL cytopainter green for 1 h and fixing. Finally, the fixed cells were mounted on a glass microscopic slide, which was sealed from the edges. The fixed samples were then imaged under Zeiss LSM 880 confocal microscope (λ_{ex} = 405 nm) and (λ_{ex} = 488 nm) for the probe and cytopainter green, respectively.

(ii) Live cell imaging: For live cell confocal imaging, cells (MCF-7 and HEK-293) were seeded onto a 35 mm live cell culture plate and allowed to grow overnight in DMEM medium. The cells were then washed with PBS twice, which was replaced with phenol red free culture media (pH 4.5) and were allowed to homogenize for 10 min before treating them with NC probe (0.144 µg/mL). After treating the MCF-7 cells for 30 min under CO_2 incubation at 37 °C, live cell imaging was carried out in red channel with the diode laser (λ_{ex}= 405 nm). To observe intracellular behavior of the probe at pH 7.4 and to get insight of AIE therein, the cells (incubated at pH 4.5) were washed with PBS, which was replaced with fresh DMEM media (pH 7.4, phenol red free). That was then followed by time-dependent live cell confocal imaging under Zeiss LSM 880 confocal microscope. The live cell imaging was recorded for total 8 cycles with a time lag of 5 min and was obtained in green channel with diode laser (λ_{ex} =405 nm).

5.3.6. FACS Analysis

The uptake of NC probe and their intracellular behavior at pH 4.5 and 7.8 was monitored by flow cytometry method. For FACS study, MCF-7 cells (5 × 10^3) grown overnight in DMEM medium were washed with PBS twice before proceeding for uptake study. The overnight grown cells were first homogenized in phenol red free culture medium (pH=4.5) for 10 min followed by incubation with NC probe (0.144 μg/mL with respect to copper) for 1 h before harvesting them. To confirm the uptake, the MCF-7 cells treated with NC probe for 1 h in acidic culture medium (pH 4.5) were collected by trypsinization. The fluorescence was then recorded in PE-H channel (band-pass filter, 585/42 nm), which corresponds to red emission in Cyto FLEX flow cytometer (Beckman Coulter). Similarly, for AIE study, MCF-7 cells (5 × 10^3) were grown in 6 well plates followed by homogenization in acidic medium and incubation with the probe (0.144 μg/mL with respect to copper) for an hour as mentioned above. Thereafter cells were washed with PBS, which was replaced with fresh culture medium (pH=7.4). The treated cells were then harvested at different time points viz., 30 min, 60 min, 120 min and 180 min each, trypsinized and time - dependent fluorescence was then recorded in FITC channel (530/30nm) corresponding to green emission, using CytoFLEX flow cytometer (Beckman Coulter).

5.3.7. Kinetic assay to measure the intracellular AIE rate

To carry out kinetic assay, MCF-7 cells (5×10^3 cells/well) and HEK 293 cells (5×10^3 cells/well) were seeded in 96 well microplates containing DMEM growth medium supplemented with 10% (v/v) fetal bovine serum (FBS) under 5% CO_2 humidified incubator at 37 °C overnight. The cells were then washed with PBS twice, which was replaced with acidic culture medium (pH 4.5). After homogenization for 10 min at acidic condition, the respective cell lines were then treated with 0.144 μg/mL NC probe (with respect to copper) and were then incubated for an hour. To study AIE kinetics in the respective cell lines, the culture media of the treated cells at pH 4.5 was replaced with fresh culture media (pH 7.4) after 1 h of incubation. This was then followed by time dependent kinetic study in 96 well microplate reader. The kinetic measurements were monitored by recording the emission intensity at 470 nm for λ_{ex} = 365 nm at an intervals of 5 min each. The assay was carried out in triplicates for both the cell lines at the aforementioned concentrations of the NC probe.

The AIE rates were obtained from the plot of ratio of fluorescence intensity at a given time to the fluorescence intensity at initial time (I/I_0) with respect to time. Rate constant values were then obtained from the slope of the integrated rate equation plot of Ln (I/I_0) vs time (t).

5.4. Characterization

(i) UV-vis spectra of nanocluster (NC) dispersion were recorded using Perkin Elmer Lambda 750 UV-vis spectrophotometer. **(ii)** PL spectra of NC dispersion were recorded in HORIBA Jobin Yvon FluoroMax-4 spectrofluorimeter. **(iii)** Solid state FT-IR spectra were recorded in Perkin Elmer Spectrophotometer (Model-spectrum one) in the range 450-4000 cm^{-1} using KBr pellet method. The solid samples for FTIR were obtained by lyophilization method. **(iv)** Transmission electron microscope (TEM) images of particles were obtained using JEOL JEM 2100 (TEM), at maximum operating voltage of 200 kV. TEM samples were prepared by drop casting 5 μL of NC dispersion on the carbon coated copper grid, which were then allowed to air dry. **(v)** Copper ion concentrations in the as - synthesized Cu NCs were determined using atomic absorption spectrometer (Varian, AA240, Netherlands). **(vi)** Particle size distribution analysis based on dynamic light scattering **(**DLS) and surface zeta potential was done using Zetasizer Nano ZS90 instrument (MODEL NO. ZEN3690, MALVERN), operating with red He–Ne gas laser (λ = 633 nm) at a temperature of 25 °C. **(vii)** Time-resolved photoluminescence (TRPL) intensity decay of the NCs was recorded using a Life Spec II spectrofluorimeter. The samples were excited by 375 nm and 405 nm LED sources. The decay curves were then analyzed by FAST software, provided by Edinburgh instrument. **(viii)** ESI-MS measurements were run using Q-TOF LC/MS mass spectrometer (6520, Agilent Technologies). **(ix)** X-ray photoelectron spectroscopy (XPS) measurements were done on a PHI 5000 Versaprobe II XPS system with AlK_α source and a charge neutralizer at room temperature, maintaining a base pressure about 6×10^{-10} mbar and energy resolution of 0.6 eV.

(**x**) Cellular imaging was carried out using Zeiss LSM 880 confocal microscope. (λ_{exc} = 405 nm and λ_{exc} = 488 nm).

5.5. Results and Discussions

A "green" aqueous method of synthesis of cysteine stabilized CuNCs (pH=4.5) in presence of chitosan biopolymer have been reported (Refer Experimental **Section 5.3.3** for detailed synthesis). The essential concepts involved in the synthesis of the NCs, its emission at different pH and the AIE feature helping the differentiation of the MCF-7 cells from HEK-293 cells are portrayed in **Figure 5. 1**.

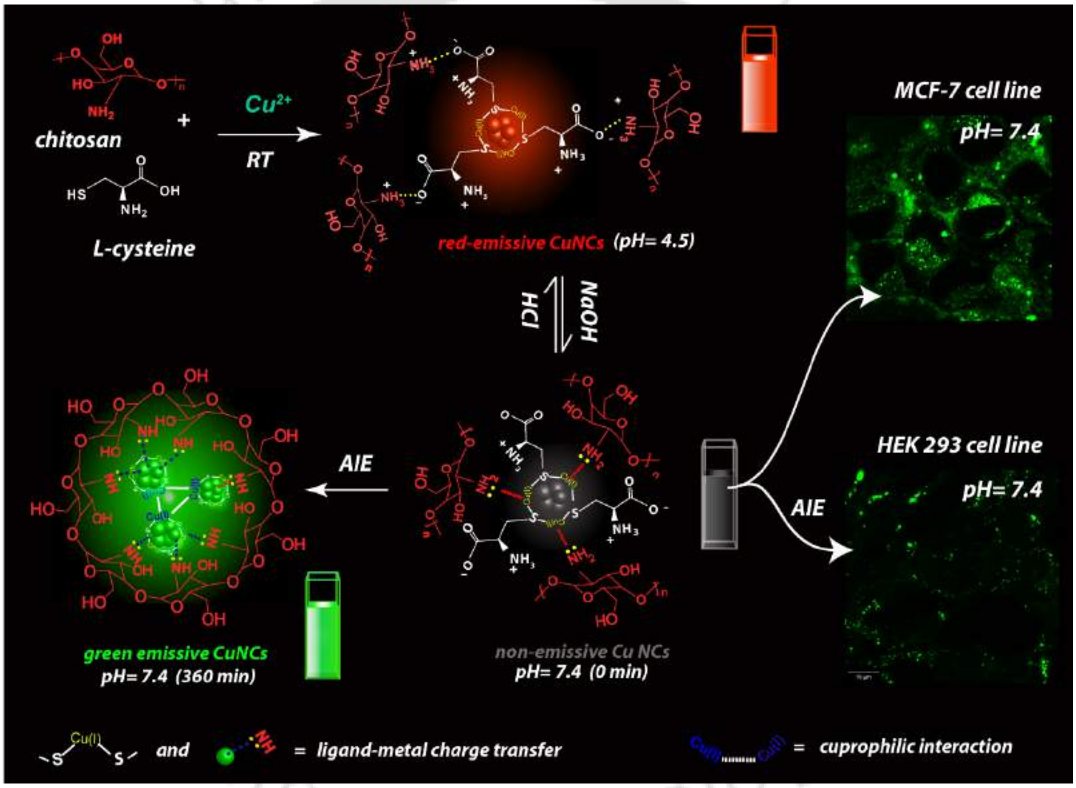

Figure 5.1. Schematic depiction of synthesis of red-emitting Cu NCs at pH 4.5 and pathway towards emergence of green emission at pH 7.4 *via* AIE attribute.

Transmission electron microscopy (TEM) study revealed the formation of well dispersed isolated particles of size 2.2±0.5 nm as shown in **Figure 5.2.A** (refer **Figure A5.1**, **Appendix**). The product exhibited distinct orange-red emission at pH 4.5 (**Figure 5.2.B**, red curve) centered at 615 nm (λ_{ex}=365 nm). The high energy extinction band at 260 nm characteristics of bridging Cu(I) cysteine complexes[21] (**Figure 5.2.C**(**i**)) and disappearance of cysteine –SH vibrational band at 2548 cm^{-1} in the FTIR spectrum (**Figure A5.2**(**i**)) recorded for as-synthesized

CuNCs at pH 4.5 suggested the active participation of thiol moiety in bonding with the metal core. Additionally, the absence of absorption band in the visible region (**Figure 5.2.C**) ruled out the possibility of the formation of Cu nanoparticles in the dispersion. However, a broad band is observed in the range 2800 - 3500 cm^{-1} in the FTIR spectrum of as-synthesized CuNCs (**Figure A5.2.**(**i**), **Appendix**) along with the blue shift of the NH_3^+ vibrational band to 1511 cm^{-1}. This indicated the possible existence of strong hydrogen bonding interaction (Refer **Discussion A5.1, Appendix** for details) between the protonated amine group (pK_a =6.3) of chitosan and carboxylic group (pK_a = 1.92) of cysteine surrounding the metal core at pH 4.5.[22]

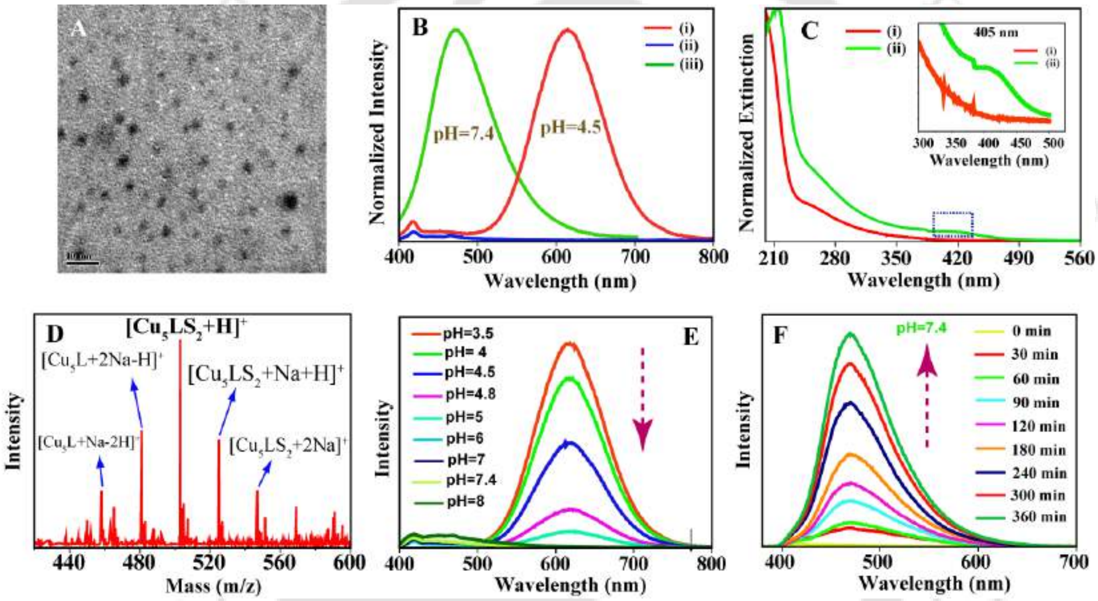

Figure 5.2. (**A**) Representative TEM image of as synthesized CuNC at pH 4.5. (**B**) Photoluminescence (PL) spectra of as synthesized CuNCs at (**i**) pH 4.5, (**ii**) pH 7.4 (0 min) and (**iii**) pH 7.4 (360 min); (**C**) corresponding UV-vis spectra at (**i**) pH 4.5 and (**ii**) pH 7.4 (360 min). (**D**) Positive mode ESI-MS spectrum of as synthesized CuNCs (L= $C_3H_6NO_2S$). (**E**) PL spectra of as synthesized CuNCs at different pH values as mentioned in legends. (**F**) Time-dependent change in PL spectra of as synthesized CuNCs recorded at pH 7.4 showing AIE feature when monitored with λ_{ex}=365 nm.

The chemical composition of the as-synthesized CuNCs determined using electrosprays ionization mass spectrometry (SI-MS) revealed the presence of Cu_5 atoms characterized by a major peak at *m/z* 503.1. This corresponds well with the molecular formula $[Cu_5LS_2+H]^+$ where L= $C_3H_6NO_2S$ followed by presence of multiple peaks in the form of sodium adducts as shown in **Figure 5.2.D**. The as-synthesized CuNCs showed high photoluminescence (PL) sensitivity towards pH change (**Figure 5.2.E**) as pH of the dispersion was varied from 4.5 to 8. Notably, in the pH range of 5.5-7.4, the dispersion became non-emissive as can be observed from **Figure A5.3.A**. Importantly, the characteristic emissions were reversible when pH cycling was carried out between pH 4.5 and 6.5 (using 0.1M HCl and NaOH) as shown in **Figure A5.3.B**, **Appendix**.

Intriguingly, the non-emissive CuNCs at pH 7 (and above) - upon aging for 30-60 min at room temperature - exhibited cyan green emission that increased with time. **Figure 5.3.A**, **B** and **C** shows the digital image recorded for NC dispersion at pH 4.5 and then pH 7.4 at 0 min and that after 6 h of aging, respectively. The as-synthesized CuNC dispersion, when aged at pH 7.4, exhibited striking cyan-green PL at 470 nm (λ_{ex}=365 nm) and 500 nm (λ_{ex}=405nm) as shown in **Figure 5.2.F** and **Figure A5.4**, **Appendix**, respectively. The emission intensity reached its maximum at 6 h. The excitation spectra recorded for CuNC at pH 4.5 and 7.4 are shown in **Figure A5.5.A**, **Appendix**. In addition, the NCs exhibited excitation tuneable emission (refer **Figure A5.5.B, Appendix**) i.e., CuNC dispersion - after aging at pH 7.4 - showed shift in emission maximum from 470 nm to 510 nm when the excitation wavelength was changed from 365 nm to 410 nm.

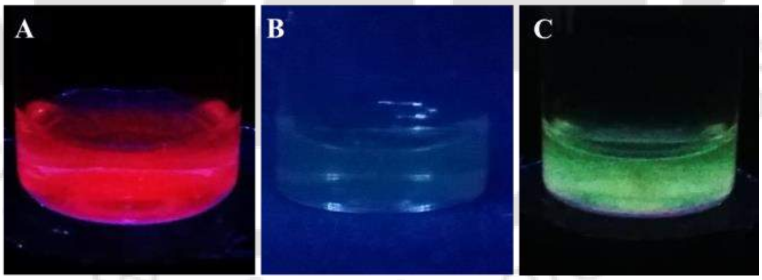

Figure 5.3. Digital photograph of as synthesized CuNC dispersion at (**A**) pH 4.5, (**B**) immediately after the as-synthesized dispersion was adjusted to pH 7.4 and (**C**) that after aging the dispersion for 6 h at pH 7.4.

The as-synthesized CuNCs also exhibited large Stokes shift (250 nm) and a long excited-state PL lifetime of 12.3 µs (**Figure 5.4.A**), which could be attributed to triplet excited state ligand-to-metal charge transfer (LMCT) transition, arising from capping ligand being coordinated with the copper core mixed with metal centered states.[18] Now, as the pH of the dispersion was raised above 7, chitosan moiety tended to become less soluble, and at the same time the amino group of chitosan (with pK_a=6.5) was rendered reactive.[23] On the other hand, the NC dispersion at pH 7.4 was also characterized by an additional extinction band in the range 380 nm – 450 nm with a weak shoulder at ~ 405 nm (**Figure 5.2.C(ii)**). The relative drop in emission intensity at 615 nm upon raising the pH of the NC dispersion can, therefore, be ascribed to gradual weakening of the H-bonded interaction between the protonated amine of chitosan and carboxylic moiety of L-cysteine that otherwise strengthen the effective triplet state charge transfer mechanism responsible for the luminescence therein.

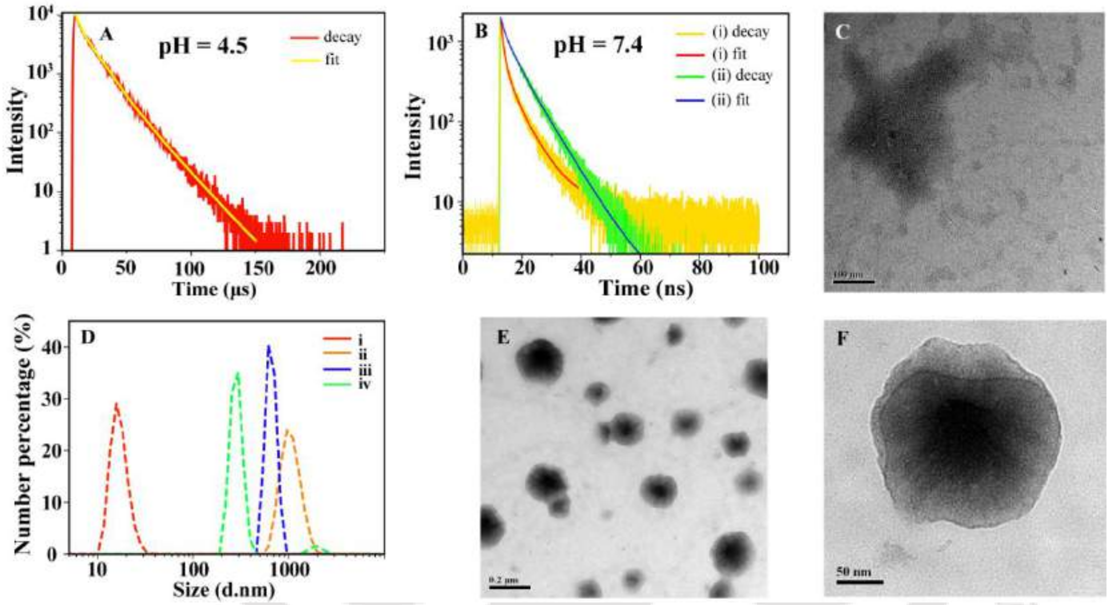

Figure 5.4. Photoluminescence lifetime decay curve of as synthesized CuNCs at (**A**) pH 4.5 (red) showing fitted line (yellow) and the same at (**B**) pH 7.4 showing (**i**) decay curve (yellow) and fitted line (red) at 0 h; (**ii**) decay curve (green) and fitted line (blue) after 6 h of aging. (**C**) Representative TEM image of CuNC dispersion recorded immediately after pH adjustment at 7.4 (0 h). (**D**) DLS-based particle size distribution obtained for as-synthesized CuNCs (**i**) at pH 4.5 (red curve) and at different time intervals of aging at pH 7.4 - (**ii**) 0 h (orange); (**iii**) 3 h (blue curve) and (**iv**) 6 h (green curve). Representative TEM image of CuNCs obtained at pH 7.4 (**E**) after aging for 4 h showing spherical aggregated structures and (**F**) enlarged view of a typical aggregate showing CuNCs clustered together.

Figure 5.4.C shows the TEM image recorded for CuNC dispersion immediately after the pH was changed to 7.4. This indicated the formation of aggregates of no particular shape at the initial time (0 min) of the study. The above was also

supported by the time-dependent dynamic light scattering (DLS) results (**Figure 5.4.D**, Refer **Table A5.1**, **Appendix**) which indicated hydrodynamic diameter, d_H *883.3±69.8* nm recorded immediately after the dispersion was adjusted to pH 7.4. (**Figure 5.4.D** (**ii**)) However, that recorded at pH 4.5 was found to be 15.4±5.2 nm (**Figure 5.4.D** (**i**)). Interestingly, d_H value recorded for the same dispersion at pH 7.4 after 3 h was *593.3±30* nm, which underwent a shift *to 303.6±86.9 nm* (**Figure 5.4.D** (**iii-iv**)) at the end of 6 h. It is to be mentioned here that copper exhibits strong inter NC dipolar attraction.[24] It is to be mentioned that owing to the inherent inter NC-dipolar attraction, the surface capping ligands re-organize during the random aggregation process to overcome the steric crowd, which would allow the occurrence of facile inter-cluster cuprophilic interaction via anisotropic van der Waals attraction.[6] Therefore, it can be concluded that the decrease in size was due to the aggregate formation as is evident from the DLS results. This must be associated with increased inter-NC cuprophilic interaction (Cu(I)···Cu(I)), which would be enhanced in compact aggregated structures. This is also supported by TEM data (**Figure 5.4.E**) obtained for NC dispersion at pH 7.4 that appeared as compact spherical aggregates comprising of CuNCs (**Figure 5.4.F**), which was unlike their morphologies observed at pH 4.5 (**Figure 5.2.A**). Additional TEM images of CuNC dispersion obtained at pH 7.4 are shown in **Figure A5.6, Appendix**.

Thus the results indicated that the enhancement of emission at higher pH could be aggregation induced, being mediated by gradual precipitation of chitosan. It is to be mentioned that the enhanced inter-cluster cuprophilic interaction induced by the compact aggregated structures over intra-cluster cuprophilic interaction led to the emergence of luminescence at pH 7.4 thus generating cyan-green emission (**Figure 5.2.F**).[24] This on the other hand, augmented the excited state relaxation via radiative pathway and reducing the non-radiative relaxation of the excited states (due to restriction in intramolecular vibration of capping ligands), resulting in the enhancement of emission intensity.[18] This is accompanied by enhanced PL average lifetime of 7.1 ns (**Figure 5.4.B**, λ_{em} = 470 nm) recorded after aging NC dispersion at pH 7.4 for 6 h in contrast to the average lifetime of 4.9 ns recorded for the same at initial time of time-dependent study.

Additionally, as the extinction spectrum of the NC dispersion at pH 7.4 showed a new band at ~ 405 nm (**Figure 5.2.C**(**ii**)), the green emission could also be tentatively attributed to the LMCT transition from nitrogen atom of the capping ligands towards the copper centre.[25] The quantum yield for the orange-red emitting CuNCs synthesized at pH 4.5 was calculated to be 0.4 % (λ_{ex} = 365 nm). However, that of green emitting CuNCs measured at pH= 7.4 was calculated to be as high as 4.6% (λ_{ex} = 365 nm) and 1.3% (λ_{ex} = 405 nm) using quinine sulphate and coumarin-153 as references, respectively. FTIR spectra recorded for CuNCs at both pH further helped elucidate the underlying surface chemistry herein (refer **Figure A5.2**, and **Discussion A5.1**, **Appendix**).

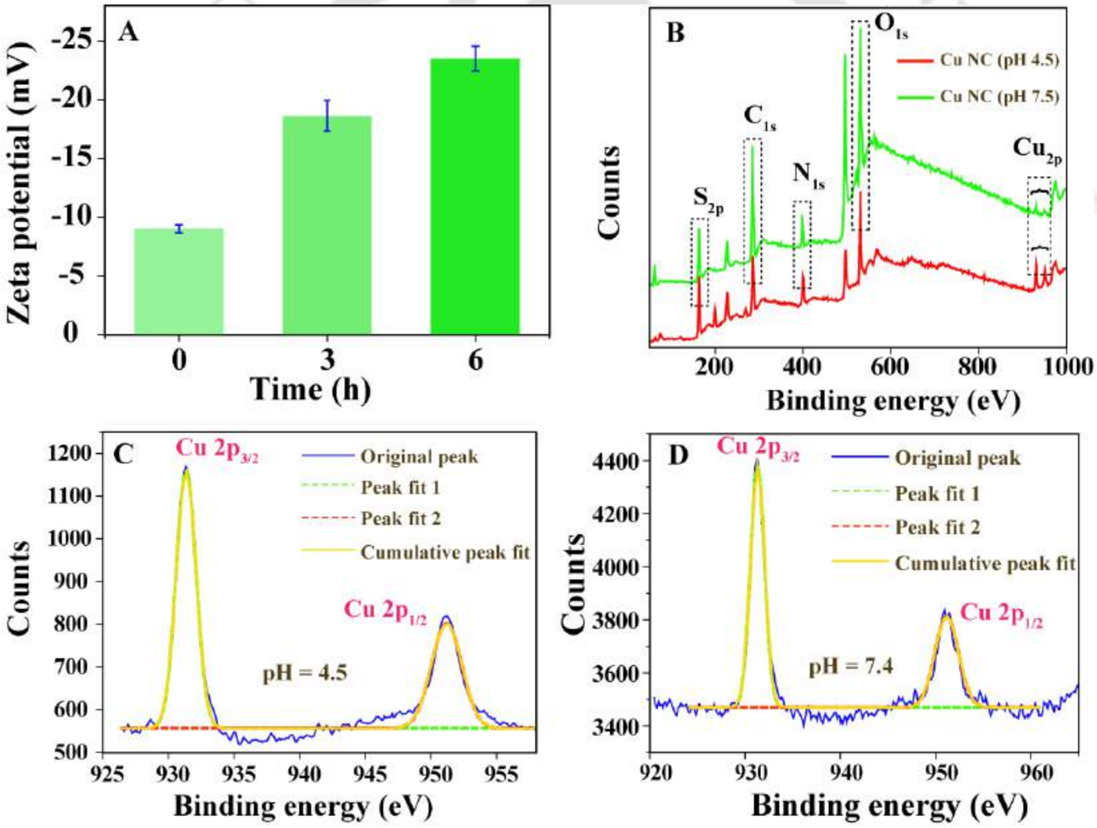

Figure 5.5. (**A**) Zeta potential measured for as synthesized CuNCs (pH 7.4) at different time interval (**i**) 0 h, (**ii**) 3h and (**iii**) 6 h. (**B**) XPS survey spectra of CuNCs at (**i**) pH 4.5 and that obtained at (**ii**) pH 7.4 after aging CuNCs for 6 h; core level Cu2p XPS spectra of as synthesized CuNCs at (**C**) pH 4.5 and that obtained after pH adjustment to (**D**) 7.4.

Additionally, pH dependent behaviour of surface ligand and hence surface charge of CuNC was further substantiated with the help of zeta-potential (ζ) measurements. The as-synthesized CuNCs at pH 4.5 showed value of +43.3 ± 0.27

mV, which gradually decreased to +32.9 ± 1.13 mV as the pH of the dispersion medium was changed from 4.5 to 6 (**Figure A5.7** and **Table A5.2**). At pH 7.4, ζ-potential of the CuNC dispersion was measured to be -9.01±0.34 mV. Interestingly, time dependent measurement of ζ-potential at pH 7.4, showed change in negative potential value from -9.01 ± 0.34 mV to -23.5 ± 1.05 mV at the end of 6 h (**Figure 5.5.A**.). This could possibly be due to increasing availability of free negatively charged carboxylic group owing to disruption of hydrogen bonding interaction between carboxylic group of cysteine and amino group of chitosan that otherwise was dominant at pH 4.5.

X-ray photoelectron spectroscopy (XPS) analyses (refer **Figure 5.5.B** and **Discussion A5.2**, **Appendix**) revealed the presence of elements Cu, N, O, C and S in the sample at pH 4.5 as well as 7.4. Further, core level spectra of these elements recorded for dispersions at pH 4.5 and pH 7.4 are shown in **Figure A5.8** (**A-B**) and **A5.8**(**C-D**), **Appendix** respectively. Cu$_{2p}$ core spectrum exhibiting two sharp peaks appearing at 951.9 eV and 932.2 eV assigned to copper 2p$_{1/2}$ and 2p$_{3/2}$ levels indicated the existence of copper in Cu(0) or Cu(+1) state (**Figure 5.5.C** and **D**) in the dispersion at both the pH.[20] Further, the absence of any satellite peak at 942 eV in both indicated the absence of Cu(II) in the dispersion. Unlike synthesized in the presence of chitosan, CuNCs synthesized in its absence did not show considerable increment in intensity (**Figure 5.6.A** and **B**, Refer Experimental **Section 5.3.4.**(**i**)) when monitored at pH 7.4. It is therefore speculated that the steric crowding induced by chitosan moiety and the enhanced cuprophilic interaction was responsible for AIE at pH 7.4.

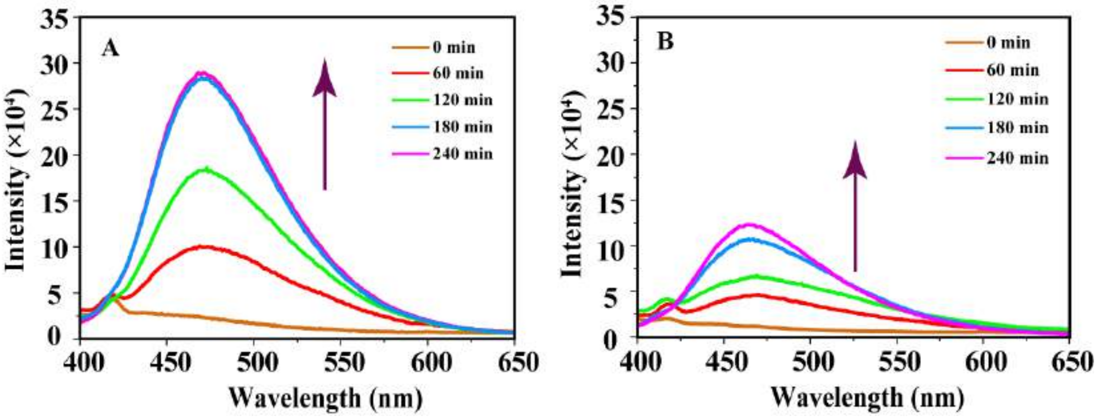

Figure 5.6. Time-dependent change in PL spectra of CuNCs synthesized (**A**) in presence of chitosan and (**B**) in absence of chitosan when pH of the dispersions was maintained

at pH 7.4 (λ_{ex}=365 nm) and monitored for 240 min.

In order to ensure the biocompatibility of the NC probe, cytotoxicity on human embryonic kidney cells (HEK-293) and human breast adenocarcinoma cell (MCF-7) was checked *via* cell viability assay (refer Experimental **Section 5.3.5.a**). Results revealed that more than 80% of the cells were viable in the presence of maximum (with respect to copper) in both HEK-293 (**Figure 5.7.A**) and MCF-7 (**Figure 5.7.B**) cells after 24 h of treatment. Therefore, 0.144 μg/mL of as-synthesized CuNCs was considered optimum and biocompatible to be used for all experiments herein. The pH of the NC probe was adjusted to 7 prior to all cellular investigations.

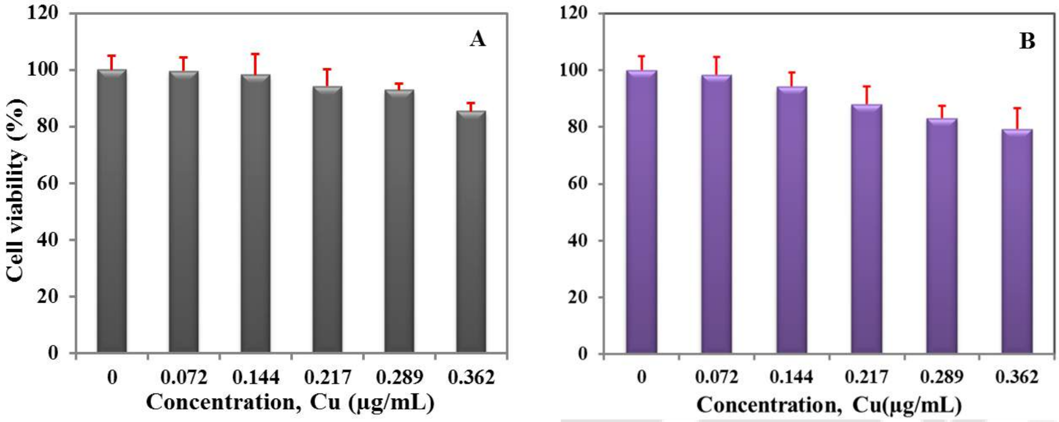

Figure 5.7. Cell viability of (**A**) HEK-293 cells and (**B**) MCF-7 cells treated with varying concentrations of as synthesized CuNCs for 24 h in DMEM media.

Interestingly, confocal laser scanning microscopy (CLSM) images of MCF-7 cells incubated with the NC probe for an hour exhibited two separate PL emissions from different regions of the cells in green and red channel upon using λ_{ex} =405 nm (Refer Experimental **Section 5.3.5.c** for details). The bright green emission was predominant in the entire cell when observed under green channel (**Figure 5.8.B**); whereas punctuated red spots were observed from some regions of the cell when observed under red channel (**Figure 5.8.C**). A subcellular co-localization experiment of the NC probe carried out with cytopainter green lysosome staining kit (Abcam) confirmed its prevalence in the lysosomes (validated by yellow spots in the merged image **Figure 5.8.J**). **Figure 5.8.H** revealed the red emission (punctuated red spots) from the probe (λ_{ex}= 405 nm) along with green emission of the cytopainter green (λ_{ex}= 488 nm, **Figure 5.8.I**) localized in the lysosome.

Interestingly, no emission of the NC probe could be observed under diode laser excitation of 488 nm (**Figure A5.9**, **Appendix**). It is to be mentioned that the affinity of N-acetylglucosamine unit of chitosan moiety towards lysosomal membrane protein, which are heavily glycosylated with N-linked glycans, in addition to lysosomal affinity for free basic amines, might have aided in lysosomal targeting by the probe.[26]

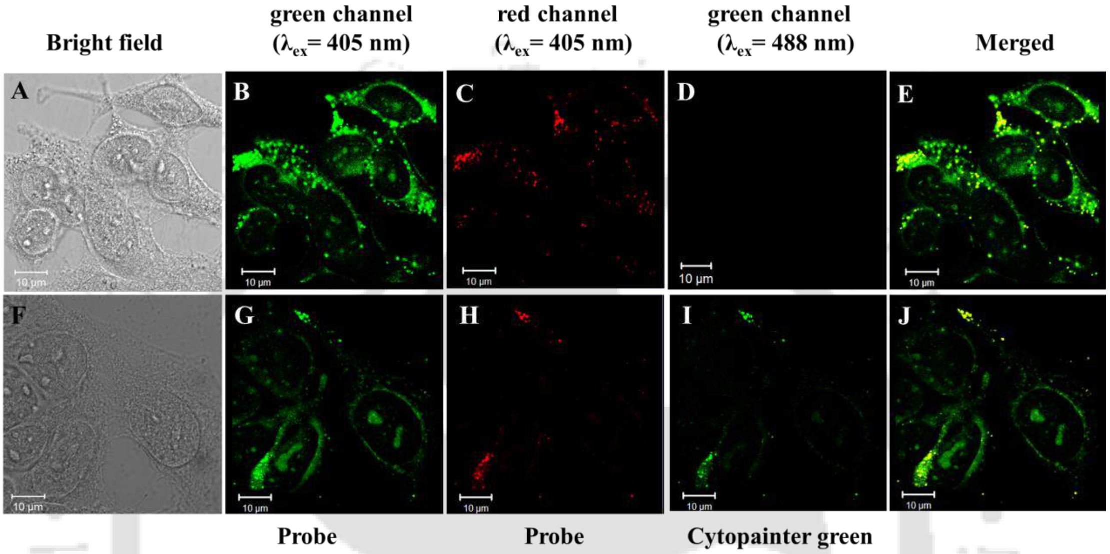

Figure 5.8. CLSM images of MCF-7 cells showing intracellular distribution of NC probe incubated for 1 h at 37 °C. (**A**) Bright-field image and fluorescence image of NC probe collected in (**B**) green and (**C**) red channel under laser excitation 405 nm; (**D**) green channel (laser excitation 488 nm) and (**E**) merged image of (**B**) and (**C**). CLSM images of MCF-7 cells incubated with NC probe for 1 h and then counterstained with cytostainer green showing (**F**) bright field image and fluorescence image of NC probe in (**G**) green and (**H**) red channel (λ_{ex}= 405 nm); (**I**) Fluorescence image of cytostainer green localized in lysosome which was collected in green channel (λ_{ex}= 488 nm). (**J**) Merged image of (**G**), (**H**) and (**I**) showing co-localization of NC probe in the in the lysosome. All images were acquired using 63× oil immersion objective.

The depth-projection shown in **Figure A5.10**, **Appendix** of the typical CLSM image in **Figure 5.8.A** further confirmed the internalization of the probe. Next, the pH response of the NC probe under two different cellular environments (pH 4.5 and 7.4) was investigated. At pH_i 4.5, red emission was observed from the entire cell (**Figure 5.9.B**) instead of punctuated spot that was observed at pH 7.4 (**Figure 5.8.C**, λ_{ex}=405 nm). On the other hand, cells kept at pH_i 7.4 exhibited AIE featured green emission (**Figure 5.9.D**, **Appendix**) similar to the observation made in **Figure 5.8.B.** The pH responsive AIE attribute of the NC probe was then delineated via live cell time-dependent CLSM study (refer Experimental **Section 5.3.5.c**(**ii**), for detailed procedure of live-cell imaging).

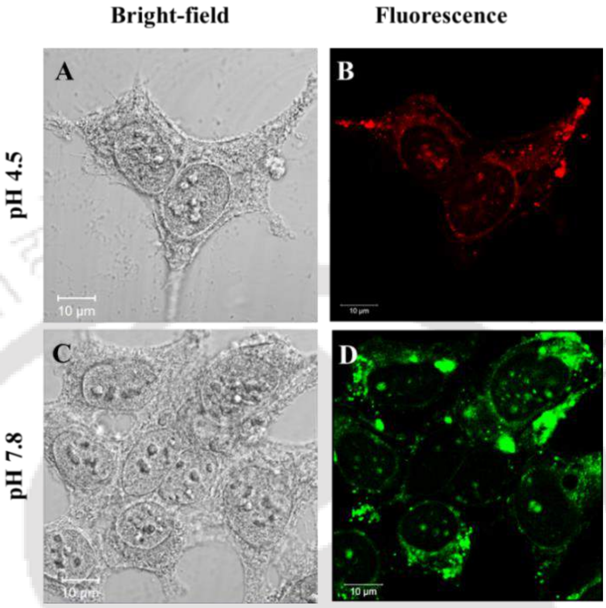

Figure 5.9. CLSM images of MCF-7 cells treated with the NC probe for 1 h at pH 4.5 culture medium. (**A**) Bright field image and (**B**) fluorescence image acquired in red channel for MCF-7 cells treated with NC probe for 1h at pH 4.5 culture media; (**C**) Bright field image and (**D**) fluorescence image acquired in green channel for MCF-7 cells treated with NC probe for 1h at pH 7.8 culture media (excitation source: 405 nm laser; images were acquired using 63× oil immersion objective).

Confocal microscopy study carried out after 30 min of incubation in acidic culture medium showed bright red–emission as shown in **Figure A5.11.A**, **Appendix** thus confirming internalization. Further time-lapsed experiment performed under the same live-cell condition at pH_i 7.4 showed weak green emission from various intracellular regions at the initial times, which gradually emerged with time to give bright green emission at the end of 45 min (λ_{ex} = 405 nm, **Figure 5.10.A-J**). The PL intensity increased significantly with time as revealed from the intracellular intensity versus time plot, which is shown in **Figure A5.11.B**, **Appendix**.

Quantitative analysis using flow cytometry confirmed uptake of the probe by

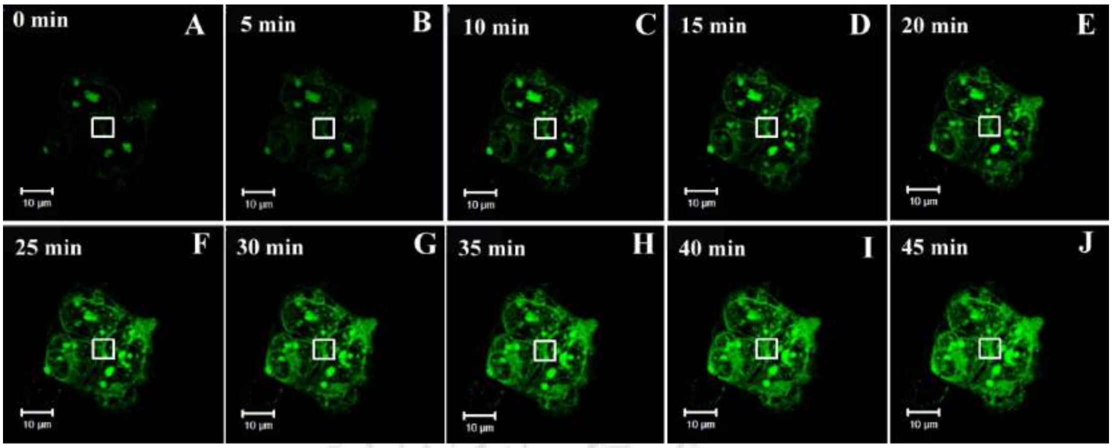

Figure 5.10. (**A-J**) Time-lapse live cell confocal microscopic imaging of the MCF-7 cells treated with CuNCs at pH=7.4 (culture medium) which were first stained in acidic culture medium (pH 4.5) for 30 min to ensure internalization prior to imaging. Images (**A-J**) were obtained after every 5 min interval. The pH_i of living MCF-7 cells was adjusted by adding required amount of HCl and NaOH to the cell culture medium. Scale bar is 10μm.

MCF- 7 cells, which showed shift in fluorescence intensity (**Figure 5.11.A**) when monitored at pH 4.5. Details of method of flow cytometry analysis are available in Experimental **Section 5.3.6**. Further, time-dependent flow cytometry carried at pH_i 7.4 exhibited apparent shift of fluorescence intensity with time when monitored in FITC-channel (**Figure 5.11.B**) and hence substantiating the AIE phenomenon inside the cellular environment.

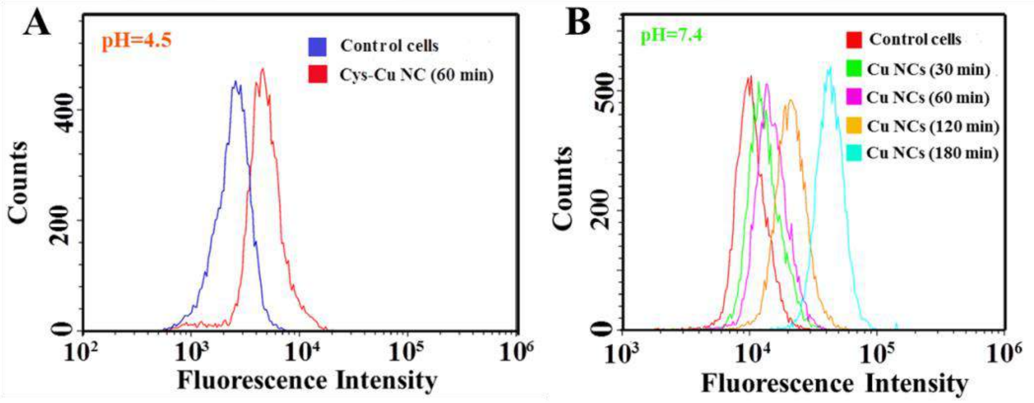

Figure 5.11. Flow cytometry analysis of MCF-7 cells treated with NC probe at (**A**) pH 4.5 showing fluorescence signal corresponding to red emission recorded in PE-H channel and (**B**) pH 7.4 showing fluorescence signal corresponding to green emission recorded in FITC channel at different time intervals as shown in legends. Non-treated cells refer to control here.

Additionally, depth projection shown in **Figure 5.12.E**, **Appendix** of a typical CLSM image (HEK-293 cell) obtained in **Figure 5.12.A-D**, **Appendix** confirmed the successful internalization of the probe. **Figure A5.12.B** and **A5.12.D**, **Appendix** clearly depict the pH_i response of the probe in HEK 293 cells similar to that observed in case of MCF-7 cells (**Figure 5.9**) when maintained at pH 4.5 and 7.4.

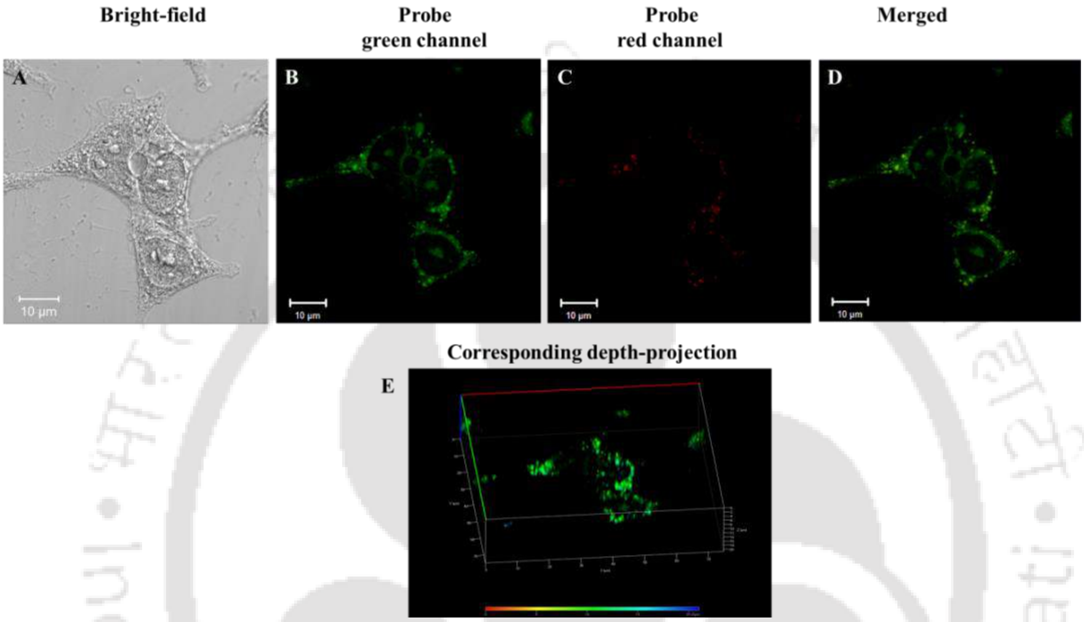

Figure 5.12. CLSM images of HEK-293 cells showing intracellular distribution of NC probe incubated for 1 h at 37 °C. (**A**) Bright-field image and fluorescence image of NC probe collected in (**B**) green channel, (**C**) red channel under laser excitation 405 nm, (**D**) merged image of (**B**) and (**C**); (**E**) Corresponding depth-projection of the image obtained in **Figure A5.12** showing successful internalization. Images were acquired using 63× oil immersion objective.

The results established the versatility of the NCs embedded in chitosan as imaging probe for monitoring cellular pH variation. It is to be noted here that the emission intensity appeared less in HEK cells as compared to MCF-7 cells when observed at both pH_i conditions. This could be tentatively ascribed to lower uptake efficiency of HEK-293 cells than those of MCF-7 cells. However, the amount of CuNCs internalized by both HEK-293 and MCF-7 cells, deducted using inductively coupled plasma atomic emission spectroscopy (ICP-AES) was estimated to be 0.002 ppm and 0.0023 ppm (with respect to copper ions), respectively, where the difference is nearly negligible. Therefore, based on ICP-

AES result, the uptake efficiencies of HEK-293 cells and MCF-7 cells might be considered identical. The difference in the nature of the cells used could primarily be responsible for the difference in the emission intensities observed. Further, time-dependent live-cell imaging carried out in HEK-293 cells (stained with NC probe) at pH_i 7.4 showed emergence of green fluorescence from various region of the cell (**Figure 5.13.(A-H)**, **Appendix**). However, the increment in emission with time observed in HEK-293 cells was comparatively feeble unlike observed in MCF-7 cells. Additionally, pH value in cancer cells is different from that in the healthy (non-cancerous) cells. That is to say, in healthy (non-cancerous cells), intracellular pH is generally ~ 7.2 and lower than extracellular pH (pHe), which is nearly 7.4. However, in cancer cells pHi is higher ~ 7.4 (in the cytosol) with acidic organelles experiencing pH value of 4.5 to 6.0 whereas pHe varies between ~ 6.7-7.1 that is nearly acidic, which therefore seems to be commendatory for the cellular studies herein. However, it is to be mentioned that the cellular experiments to study the AIE behaviour in case of both MCF-7 and HEK-293 cells in the present study were carried out by incubating the cells at pH 7.4 medium before treatment with NC probe. Hence the effect of difference in pH of the two cell lines can be neglected herein. Thus considering the fact that various proteins, peptides and enzymes are overexpressed in cancerous cells than the healthy (non-cancerous) cells[6,27] it is worth to consider the active participation of these biomolecules in exhibiting enhanced AIE feature in MCF-7 cells than HEK-293 cells.

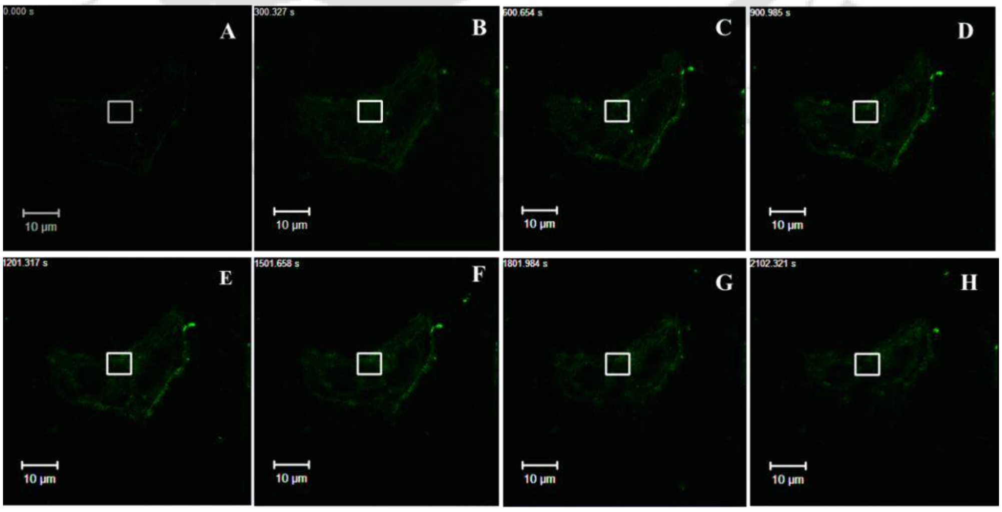

Figure A5.13 Time lapse confocal microscopy image of living HEK-293 cells post 10 min incubation at pH 7.4. The HEK-293 cells were first incubated with Cu NC probe (0.144

μg/mL) for 30 min in pH = 4.5 culture media prior to time-lapsed experiment to allow internalization of the NC probe.

The above fact is further supported by the experimental result obtained from time-dependent AIE studies (**Figure 5.14.A**, **C** and **E**) carried out for CuNC only and those in the presence of bovine serum albumin (BSA) and lysozyme being chosen as representative proteins.

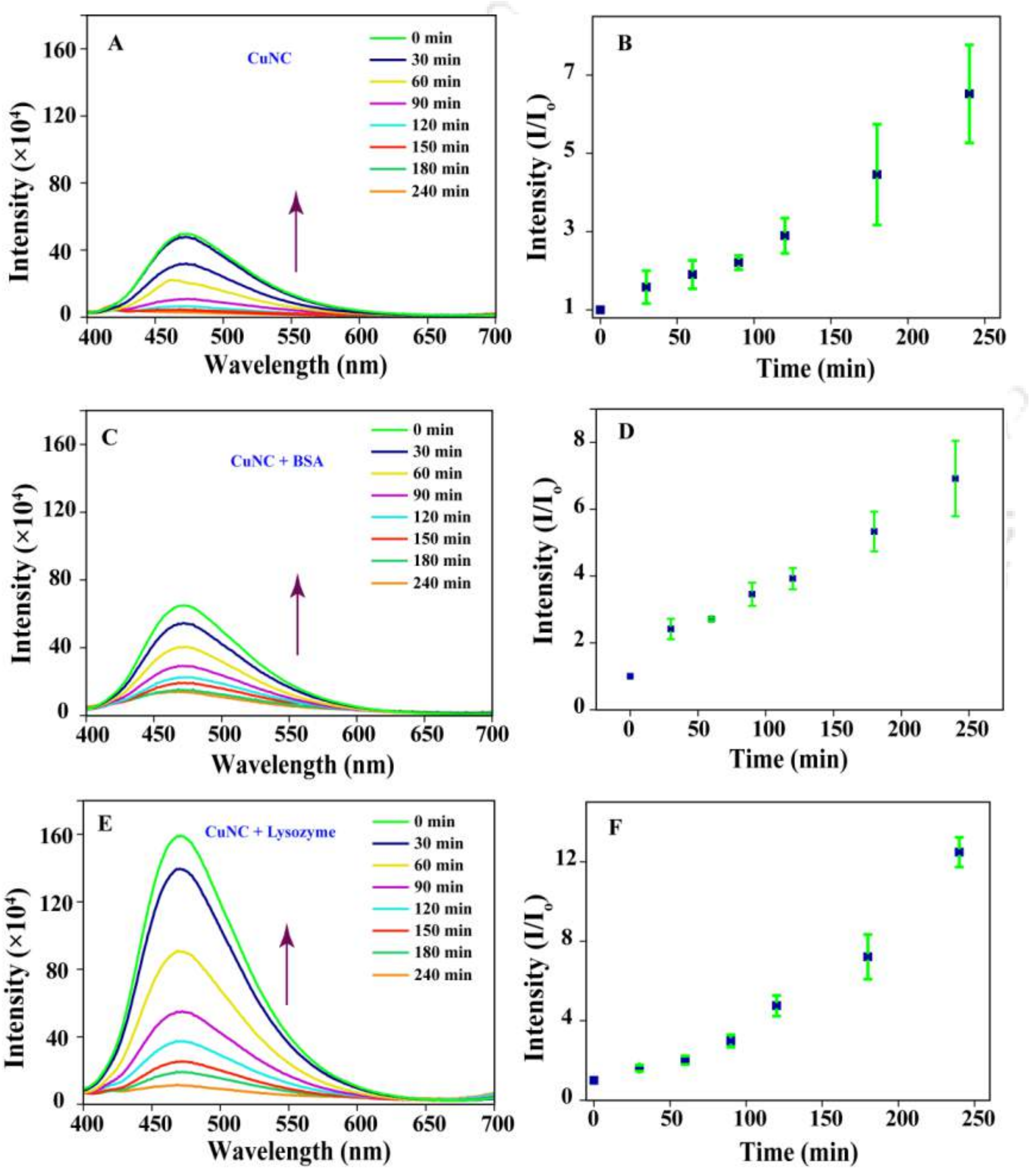

Figure 5.14. Time-dependent change in PL spectrum of (**A**) as synthesized CuNCs only; as synthesized CuNCs in presence of (**B**) BSA and (**C**) lysozyme when pH of the dispersion was maintained at pH 7.4 and monitored for 240 min (λ_{ex} = 365 nm).

The respective plot of change in ratio of emission intensity recorded with time at 470 nm (obtained from the above mentioned time-dependent AIE studies) is shown in Figure 5.14.B, D and F. The corresponding kinetic rate constant values derived following integrated rate equation, for first order kinetics, has been tabulated in Table A5.3 (refer Experimental Section 5.3.4.(ii) for experimental details and kinetic calculation). It is to be noted that the rate constant obtained for AIE monitored in the presence of lysozyme (kCuNC-Lyz = 1.35±0.22 × 10-2 min-1) was the highest followed by that in the presence of BSA (kCuNC-BSA = 8.92 ± 0.76 × 10-3 min-1) when compared to the rate constant obtained for CuNC only (kCuNC = 6.86±0.70 × 10-3 min-1) at pH 7.4. It may be argued that steric crowding induced by the protein in the medium augmented the AIE, thereby inducing enhanced cuprophilic interaction and hence luminescence.

We, therefore, tried to find the rate (hence rate constant) of AIE kinetics featured by the probe in MCF-7 cells and then establish a comparison to that of HEK 293 cells by carrying out time-dependent fluorescence–based analyses (refer Experimental **Section 5.3.7**, for details). **Figure 5.15** shows the plot for the change in fluorescence intensity ratio of the NC probe over time in MCF-7 as well as HEK-293 cells. In case of HEK-293 cells, constant green emission was attained

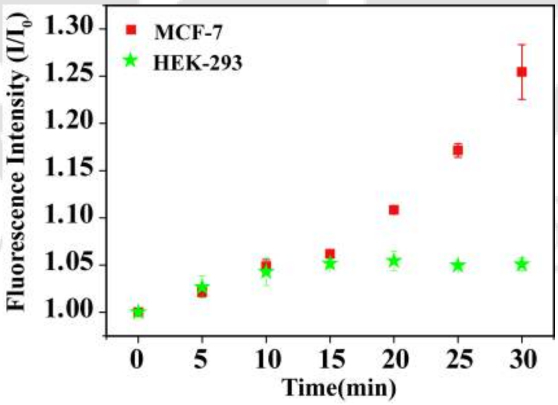

Figure 5.15. Change in fluorescence intensity ratio (I/I_0) of the probe over time (min) recorded in MCF-7 and HEK-293 cells

Table 1. Rate constant values obtained from the slope of the integrated rate equation plot of Ln (I/I_0) vs time. Mean constants were reported from the average of slopes obtained from the Ln (I/I_0) vs time plot.

Cell line	**Integrated rate law, I/I_0= fluorescence intensity at 470 nm**	**Mean rate constant (min^{-1})**
MCF-7	**Ln (I/I_0) vs t (min)**	**$1.12 \pm 0.14 \times 10^{-2}$**
HEK-293	**Ln (I/I_0) vs t (min)**	**$3.46 \pm 0.90 \times 10^{-3}$**

over time within a short period of time; however, in the MCF-7 cells the NCs exhibited an exponential rise in emission intensity with time as depicted from **Figure 5.15**. Intriguingly, intracellular rate constant calculated based on first order AIE kinetics showed 3-fold higher value in MCF-7 cells than HEK-293 cells (Refer **Table 1**, $k_{MCF-7} = 1.12 \pm 0.14 \times 10^{-2}$ min^{-1}, $k_{HEK-293} = 3.46 \pm 0.90 \times 10^{-3}$ min^{-1}). It is to be noted that the rate constant of AIE kinetics measured in MCF-7 cells was two-fold higher than that obtained for CuNC only in the aqueous medium when measured at pH 7.4 ($k_{CuNC} = 6.86 \pm 0.70 \times 10^{-3}$ min^{-1}). Thus it can be said that the difference in rate constant exhibited by two different cell lines might be an indication of different intracellular cytoplasmic crowding being prevalent, although the claim demands further detailed specific studies.[28]

5.6. Conclusions

Thus pH stimulus responsive AIE active Cu NCs have been synthesized, which exhibited red and green PL at pH 4.5 and above pH 7.4, respectively. The as-synthesized CuNCs – being composed of cysteine and chitosan, in addition - were found biocompatible in nature and showed internalization by both MCF-7 and HEK-293 cells. Time-dependent live-cell confocal microscopy studies clearly revealed the intracellular AIE phenomenon - featured by MCF-7 cells at pH 7.4 leading to bright green emission. Remarkably, MCF-7 cell line exhibited enhanced efficacy in featuring AIE than HEK-293 cell line. Based on this, the intracellular rate constant derived for AIE kinetics featured inside MCF-7 cells was found 3-fold higher than HEK-293 cells, thereby paving a new way of differentiating specific cell lines. (MCF-7 and HEK-293 herein) Additionally, the biocompatible and pH stimulus emission behaviour of the NC probe may be useful as sensitive probe for sensing specific organelles, biomolecules and overexpressed proteins and also as diagnostic tool for disease detection *in vitro* as well as *in vivo*. Thus, the present experimental results led us to propose the AIE characteristics of the as synthesized probe however, further extensive study may be helpful for complete understanding of any other plausible mechanism involved.

5.7. References

1. Situ, B.; Chen, S.; Zhao, E.; Leung, C. W. T.; Chen, Y.; Hong, Y.; Lam, J. W. Y.; Wen, Z.; Liu, W.; Zhang, W.; Zheng, L.; Tang, B. Z. *Adv. Func. Mater.* **2016**, *26*, 7132.

2. Zhu, B.; Li, P.; Shu, W.; Wang, X.; Liu, C.; Wang, Y.; Wang, Z.; Wang, Y.; Tang, B. *Anal. Chem.* **2016**, *88*, 12532.

3. Chen, S.; Hong, Y.; Liu, Y.; Liu, J.; Leung, C. W. T.; Li, M.; Ryan, T.; Kwok, T. K.; Zhao, E.; Lam, J. W. Y.; Yu, Y.; Tang, B. Z. *J. Am. Chem. Soc.* **2013**, *135*, 4926.

4. Wang, Y.; Zhou, K.; Huang, G.; Hensley, C.; Huang, X.; Ma, X.; Zhao, T.; Sumer, B. D.; De Berardinis, R. J.; Gao, J. *Nature Mater.* **2013**, *13*, 204.

5. Panizzi, P.; Nahrendorf, M.; Wildgruber, M.; Waterman, P.; Figueiredo, J. L.; Aikawa, E.; McCarthy, J.; Weissleder, R.; Hilderbrand, S. A. *J. Am. Chem. Soc.* **2009**, *131*, 15739.

6. Wang, K.; Ramji, S.; Bhatena, A.; Lee, C.; Riddick, D. S. *Xenobiotica* **1999**, *29*, 155.

7. Zhang, X. X.; Wang, Z.; Yue, X.; Ma, Y.; Kiesewetter, D. O.; Chen, X. *Mol. Pharmaceutics* **2013**, *10*, 1910.

8. Jin, C.; Liu, J.; Chen, Y.; Guan, R.; Ouyang, C.; Zhu, Y.; Ji, L.; Chao, H. *Sci. Rep.* **2016**, *6*, 22039.

9. Murtagh, J.; Frimannsson, D. O.; O'Shea, D. F. *Org. Lett.* **2009**, *11*, 5386.

10. Michalet, X.; Pinaud, F. F.; Bentolila, L. A.; Tsay, J. M.; Doose, S.; Li, J. J.; Sundaresan, G.; Wu, A. M.; Gambhir, S. S.; Weiss, S. *Science* **2005**, *307*, 538.

11. Liu, J. H.; Cao, L.; LeCroy, G. E.; Wang, P.; Meziani, M. J.; Dong, Y.; Liu, Y.; Luo, P. G.; Sun, Y. P. *ACS Appl. Mater. Interfaces* **2015**, *7*, 19439.

12. Wang, J.; Zhang, G.; Li, Q.; Jiang, H.; Liu, C.; Amatore, C.; Wang, X. *Sci. Rep.* **2013**, *3*, 1157.

13. Lin, C. J.; Lee, C. H.; Hsieh, J. T.; Wang, H. H.; Li, J. K.; Shen, J. L.; Chan, W.H.; Yeh, H. I.; Chang, W. H. *J. Med. Biol. Eng.* **2009**, *29*, 276.

14. Wang, Z.; Chen, B.; Rogach, A. L. *Nanoscale Horiz.* **2017**, *2*, 135.

15. Chen, L. Y.; Wang, C. W.; Yuan, Z.; Chang, H. T. *Anal. Chem.* **2015**, *87*, 216.

16. Goswami, N.; Yao, Q.; Luo Z.; Li, J.; Chen, T.; Xie, J. *J. Phys. Chem. Lett.* **2016**, *7,* 962.

17. Yao, Q.; Luo, Z.; Yuan, X.; Yu, Y.; Zhang, C.; Xie, J.; Lee, J. Y. *Sci. Rep.* **2015**, *4*, 3848.

18. Luo, Z.; Yuan, X.; Yu, Y.; Zhang, Q.; Leong, D. T.; Lee, J. Y.; Xie, J. *J. Am. Chem. Soc.* **2012**, *134*, 16662.

19. Jia, X.; Yang, X.; Li, J.; Li, D.; Wang, E. *Chem. Commun.* **2014**, *50*, 237.

20. Su, X.; Liu, J. *ACS Appl. Mater. Interfaces* **2017**, *9*, 3902.

21. Pecci, L.; Montefoschi, G.; Musci, G.; Cavallini, D. *Amino Acids* **1997**, *13*, 355.

22. Dong, C.; Chen, W.; Liu, C.; Liu, Y.; Liu, H. *Colloids and Surfaces A: Physicochem. Eng. Aspects* **2014**, *446*, 179.

23. Li, M.; Hong, Y.; Wang, Z.; Chen, S.; Gao, M.; Kwok, R. T. K.; Qin, W.; Lam, J. W. Y.; Zheng, Q.; Tang, B. Z. *Macromol. Rapid Commun.* **2013**, *34*, 767.

24. Wu, Z.; Liu, J.; Gao, Y.; Liu, H.; Li, T.; Zou, H.; Wang, Z.; Zhang, K.; Wang, Y.; Zhang, H.; Yang, B. *J. Am. Chem. Soc.* **2015**, *137*, 12906.

25. Azzellini, M. A. A.; Abbott, M. P.; Machado, A.; Miranda, M. T. M.; Garcia, L. C.; Caramori, G. F.; Gonçalves, M. B.; Petrilli, H. M.; Ferreira, A. M. C. *J. Braz. Chem. Soc.*, **2010**, *21*, 1303.

26. Chen, X.; Bi, Y.; Wang, T.; Li, P.; Yan, X.; Hou, S; Bammert, C. E.; Ju, J.; Gibson, K. M.; Pavan, W. J.; Bi, L. *Sci.Rep.*, **2015**, *5*, 9004.

27. Ma, L.; Teruya-Feldstein, J.; Weinberg, R. A. *Nature*, **2007**, *449*, 682.

28. Phillip, Y.; Kiss, V.; Schreiber, G. *Proc. Natl. Acad. Sci. U.S.A.,* 2012, **109**, 1461.

CHAPTER 6

Biomimetically Crystallized Protease Resistant Zinc Phosphate decorated with Gold Atomic Clusters for Bio-Imaging

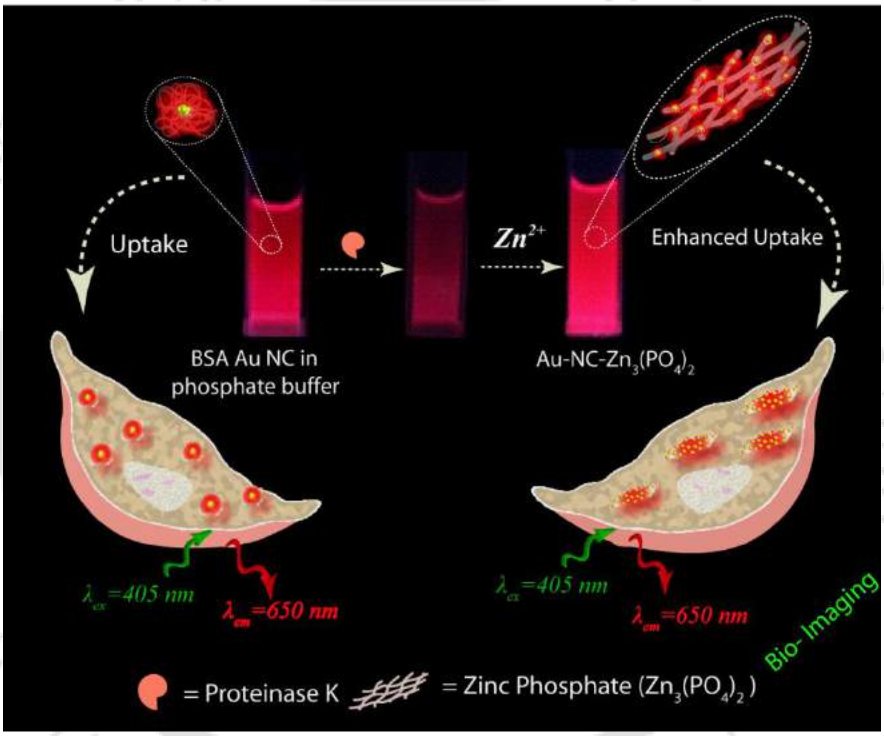

Chapter 6 *reports a new strategy to develop a luminescent probe via biomimetic crystallization of zinc phosphate in the presence of protein fragment stabilised gold (Au) nanoclusters for cellular imaging. The as-developed hybrid organic-inorganic nanostructure offered clustering of the Au NCs in one platform for efficient internalization by cancer cells (HeLa). The engineered probe - with Au nanoclusters assembled on the crystal - was protease resistant which offered a facile platform for efficient bio-imaging and uptake study.*

[Dutta et al. Chem. Commun. 2017, 53, 1277] - Reproduced by permission of The Royal Society of Chemistry. http://pubs.rsc.org/en/content/articlelanding/2017/cc/c6cc09092c#!divAbstract.

6.1. Introduction

Advanced materials - for potential theranostic applications – must possess essential features that are based on their sizes (for enhanced permeation and retention, EPR),[1] physical properties (such as optical and magnetic properties for diagnosis, imaging and therapy)[2] and long term stability in the circulatory system.[3] For targeted imaging, delivery and release, incorporation of functional moieties facilitating receptor mediation, temperature or pH trigger is necessary.[4] In this regard, traditional organic based drug delivery vehicles have new contenders in the form of nanoscale inorganic-organic hybrid materials with their ease of formation and stability for imaging and delivery as multimodal vehicles.[5]

Recent interests in the use of luminescent atomic clusters for imaging and as delivery vehicles, as opposed to conventional metal nanoparticles or quantum dots, is due to low cytotoxicity, high quantum yield and large Stokes-shifted photoluminescence, availability of protocols for size-selected synthesis and easy functionalization with organic moieties.[6] Additionally, the feasibility of two-photon excitation for working in the biological window of wavelength (650 – 950 nm) and the clusters themselves working as imaging and therapeutic agents provide unique opportunity for using them as precursor for fabrication of hybrid materials.[7]

A popular system of choice for the composite material is based on the use of proteins such as human serum albumin (HSA) or bovine serum albumin (BSA).[8] Thus nanoscale materials comprised of protein and Au nanoclusters (Au NCs) have been used for delivery of drugs as well as imaging using one photon and two-photon excitations.[7] Additionally, Au-Ag bimetallic nanoclusters embedded in proteins have been shown to enhance the efficacy of the drugs thus providing synergy of action.[9] However, there are fundamental challenges in using proteins as vehicles, as in circulation they are susceptible to degradation by proteases. In some cases polyethylene glycol (PEG) has been used as a coating substrate to overcome the issue. However, this approach has the inherent limitation in the form of loss of size selection, surface functionalization and inhibited cellular uptake in the process.[10] Thus there is a genuine need for the development of theranostic materials at the nanoscale, which would have the required stability in the circulatory system.

6.2. Outline of the present work

Herein we demonstrated a biomimetic way[11] to generate zinc phosphate ($Zn_3(PO_4)_2$) nanocrystals decorated with protein fragment stabilised Au NCs for bio-imaging. The luminescence of the composite - in the dispersion medium as well as in cancer cells - was comparable to that of parent BSA-Au-NCs from which the fragments were obtained following digestion using protease. The nanocomposite had long term stability in the presence of protease thus indicating the potential application in vivo imaging. The protein fragments acted as structure directing agent in the mineralization of $Zn_3(PO_4)_2$ via their consequent assembly with the zinc ions. The clustering of Au-NCs in the as synthesized composite, achieved through crystallization of $Zn_3(PO_4)_2$, helped in efficient internalization of the particles by cancer cells (HeLa) and convenient fluorescence imaging using confocal microscopy.

6.3. Experimental Section

6.3.1. Materials

Gold(III) chloride solution (30 wt %, HCl, Sigma Aldrich, USA), bovine serum albumin (BSA, Sisco Research Laboratories Pvt. Ltd., India), sodium hydroxide (Merck, India), proteinase K (Sigma Aldrich, USA), zinc acetate dihydrate (Merck, India), sodium dihydrogen phosphate dihydrate ($NaH_2PO_4.2H_2O$), Merck, India), di-Sodium hydrogen phosphate dihydrate ($Na_2HPO_4.2H_2O$, Merck, India), 3-(4,5-dimethylthiazol-2-yl)-2,5-diphenyltetrazolium bromide (MTT, Himedia, India) and sinapinic acid (Sigma-Aldrich USA) were purchased and used as received without further purification. Milli-Q grade water (18.2 MΩ cm, Millipore) was used for all experimental work.

6.3.2. Synthesis of BSA stabilised gold nanoclusters (BSA-Au-NCs)

The synthesis of BSA stabilised Au nanoclusters was carried out following a report by Xie et al.[12] An aqueous solution of $HAuCl_4$ (2.5 mL, 10 mM) was added dropwise to an aqueous solution of BSA (2.5 mL, 50 mg/mL) under vigorous stirring at 37 °C. After stirring for 3 minutes, freshly made NaOH solution (350 μL, 1M) was introduced to the reaction mixture and pH adjusted to ~12. The reaction was allowed to proceed under this condition for 12 h at 37 °C which resulted in the appearance of deep brown color solution, ensuring the completion of reaction.

6.3.3. Preparation of Phosphate Buffer (pH=7.4)

The phosphate buffer solution of pH=7.4 was made by mixing 18 mL of NaH_2PO_4 (0.02M, monobasic) and 82 mL of Na_2HPO_4 (0.02M, dibasic) stock solutions. The resulting solution was mixed thoroughly and pH was tested to be 7.4. The final volume of the solution was then adjusted to 200 mL.

6.3.4. Proteolytic digestion of BSA-Au-NCs

The proteolytic digestion was carried out in phosphate buffer pH=7.4 by proteinase K at 37 °C.[13] In a 3 mL fluorescence cuvette, 100 μL of as synthesized BSA-Au-NC dispersion was added to 2.3 mL phosphate buffer at 37 °C. After 5 minutes of incubation at 37 °C, proteinase K (100 μL, 0.8 mg/mL) was added and the mixture was further incubated for 90 min. The proteolytic process was monitored by recording the time dependent emission spectra of BSA-Au-NC at an excitation wavelength of 500 nm.

6.3.5. Formation of Au-NC decorated zinc phosphate nanocrystal (Au-NC-$Zn_3(PO_4)_2$)

Following proteolytic digestion of BSA-Au-NCs, the temperature of digested Au-NC suspension was then fixed at 27 °C. This was then followed by addition of zinc acetate solution (300 μL, 68.3 mM) to the digested Au-NC dispersion. In brief, to 2.5 mL digested Au-NC dispersion, 50 μL of zinc acetate solution was added successively and the emission spectra recorded simultaneously at an interval of 1 min each. This led to gradual recovery of fluorescence which reached a saturation in emission maxima after final addition of 300 μL, $[Zn^{2+}]$ = 68 mM. Immediately, after addition of zinc acetate salt solution, white suspension of zinc phosphate appeared which on standing for ~ 1 h settled down to form light brown powder of Au NC decorated with zinc phosphate (Au-NC-$Zn_3(PO_4)_2$). The powder so obtained was dried under vacuum for further characterization.

6.3.6. Synthesis of zinc phosphate hydrate

A 6 mL of 100 mM $Zn(NO_3)_2.6H_2O$ solution was added to 20 mL Milli-Q water. This is followed by dropwise addition of 5 mL of 100 mM $Na_3PO_4.12H_2O$ solution under constant stirring at 27 °C. The mixture was stirred for 6 h and the resultant white precipitate was collected by centrifugation and finally redispersed in 20 mL Milli-Q water.

6.3.7. Control experiments to validate the fluorescence recovery in digested Au NC

The as synthesized BSA Au NCs were digested with proteinase K in water (pH=7.4), instead of buffer which has no phosphate constituent in it for 90 min as two different simultaneous experiment – case(**i**) and case (**ii**).

This is then followed by addition of zinc acetate (100 μL, 68.3 mM) to the digested Au NC dispersion as obtained in **case** (**i**)**,** whereas digested Au NC dispersion as obtained in **case** (**ii**) was treated with as prepared zinc phosphate solution (300 μL, 68.3 mM; Refer Experimental **Section 6.3.6** for detailed synthesis of zinc phosphate hydrate) and luminescence spectra recorded.

6.3.8. Control experiments validating role of peptide fragments as structure directing agent

Case (**i**) Native BSA-Au-NC dispersion (5 mg/mL, 100 μL) was taken in phosphate buffer (2.3 mL) solution and then zinc acetate (300 μL, 68.3 mM) was added to the buffer mixture at 37 °C successively (i.e, 50 μL of zinc acetate solution was added successively at an interval of 1 min each) and mixed rapidly. **Case** (**ii**) 100 μL (50 mg/mL) native BSA solutions in 2.3 mL phosphate buffer medium was mixed and then digested with proteinase K at 37 °C for 90 min. This was then followed by sequential addition of zinc acetate salt solution as described above in case (**i**), (300 µL 68.3 mM). **Case** (**iii**) Zn^{2+} ions (300 µL, 69.3 mM) was added successively (as described in case(i)) to the phosphate buffer solution (2.3 mL) at 37 °C and mixed rapidly.

6.3.9. Cell Culture Studies

Human cervical carcinoma cells, (HeLa) for cellular study were acquired from the National Centre for Cell Sciences (NCCS), Pune, India. HeLa cells were cultured in Dulbecco's modified Eagle's medium (DMEM) supplemented with 10% (v/v) fetal bovine serum (PAA Laboratories, Austria), L-glutamine (4 mM), penicillin (50 units/mL), streptomycin (50 mg/mL, Sigma-Aldrich) and maintained in 5% CO_2 humidified incubator at 37 °C.

6.3.9.a. Cell viability assay

Cell viability assay was carried out by seeding HeLa cells (5×10^3 cells/well) in a 96 well microplate and grown in DMEM medium under 5% CO_2 humidified incubator overnight. Then cells were treated with varying concentrations of BSA-Au-NC (1−4.9 µM with respect to gold) and Au-NC-$Zn_3(PO_4)_2$ (50−200 µM, with respect to zinc). For cytotoxicity test of the composite on normal human cell line, cell viability assay was carried out by seeding HEK 293 cells (5×10^3 cells/ well) in a 96 well microplate and thereafter cells were treated with varying concentration of Au-NC-$Zn_3(PO_4)_2$ (50−200 µM, with respect to zinc). It may be mentioned here that the gold and zinc contents were estimated by atomic absorption spectroscopic (AAS) measurements. After 24 h incubation, MTT based cell viability assay was carried out. The absorbance at 570 nm due to formazan formation in DMSO was recorded using a TECAN microplate reader. The assay was carried out in triplicates for each aforementioned concentration of composite. Cell viability was calculated as follow:

$$\%\ viable\ cell\ = \frac{(A_{570} - A_{690})\ of\ treated\ cells}{(A_{570} - A_{690})\ of\ control\ cells} \times 100$$

where A_{570} corresponds to absorbance of formazan and A_{690} arises due to background interference.

6.3.9.b. Confocal laser scanning microscopic (CLSM) analyses

For confocal analyses, 1 × 10^5 HeLa cells/well were seeded onto a microscopic coverslip placed in a 35 mm culture plate and allowed to grow overnight. The cells were then treated with as synthesized BSA-Au-NC (4.9 µM), digested Au-NC (4.9 µM), Au-NC-$Zn_3(PO_4)_2$ composite (204.9 µM with respect to total zinc and gold present) and further incubated for 4 h in humidified atmosphere containing 5 % CO_2 at 37 °C. For endocytosis inhibition experiment, HeLa cells were first treated with 0.1% sodium azide for 10 min followed by treatment with Au-NC-$Zn_3(PO_4)_2$ nanocomposite (204.9 µM with respect to total zinc and gold present) and then incubated under the same condition as described above. For confocal analyses of the composite on normal human cell line, 1 × 10^5 HEK 293 cells/well were seeded onto a microscopic coverslip placed in a 35 mm culture plate and thereafter treated with Au-NC-$Zn_3(PO_4)_2$ composites (204.9 µM with respect to total zinc and gold present) following above described procedure. After this, the cells were washed with PBS and were fixed with 0.1% formaldehyde and 70% chilled ethanol. Finally the fixed cells were mounted on a glass microscopic slide and properly sealed. The samples were then imaged under Zeiss LSM 880 confocal microscope. (λ_{exc} = 405 nm).

6.3.9.c. Quantitative analysis of the luminescence intensity of the confocal Images

The cellular uptake of Au-NC-$Zn_3(PO_4)_2$ by HeLa cells in absence and presence of 0.1 % sodium azide (NaN_3) were expressed by the mean luminescence intensity (calculated from quantitative image analysis of CLSM images (3 different cell images) using Image J software). To compare the amount of luminescence in respective HeLa cells incubated with (i) Au-NC, (ii) digested Au-NC and (iii) Au-NC-$Zn_3(PO_4)_2$, the confocal images so obtained in three different cases (i-iii) were also independently analysed using Image J software (considering at least 5 different cells). Then each HeLa cells were selected and background subtracted corrected total cell fluorescence (CTCF) were measured using Image J software. The mean luminescence intensity was then obtained by dividing the CTCF by cell area under consideration. The values obtained from the measurements in each case were then represented as mean ± standard deviation.[14]

6.3.10. Stability of AuNC- $Zn_3(PO_4)_2$ against protease degradation

The protease assay was carried out in phosphate buffer (pH=7.4) by Proteinase K at 37 °C. The as synthesized Au-NC-$Zn_3(PO_4)_2$ was centrifuged at 20627 relative centrifugal force (rcf) for 2 minutes at 20 °C and the pellet so obtained was re-dispersed in 2.4 mL phosphate buffer solution. After 5 minutes of incubation of the dispersion at 37 °C, proteinase K (100 µL, 0.8 mg/mL) was added and the mixture was incubated for 120 min. The proteolytic process was monitored by recording the time dependent emission spectra of BSA-Au-NC at an excitation wavelength of 500 nm.

6.3.11. Stability of Au-NC-$Zn_3(PO_4)_2$ in human blood serum

Blood serum required for the experiment was obtained by centrifugation of the human blood sample collected from healthy individual, following the standard guidelines laid by Indian Institute of Technology Guwahati, Guwahati, India. The as synthesized Au-NC-$Zn_3(PO_4)_2$ was centrifuged at 20627 rcf for 2 minutes at 20 °C and the pellet so obtained was redispersed in phosphate buffer. Then, equal volume (1:1) of the composite in buffer and as obtained blood serum was mixed and spectra recorded immediately. The resultant dispersion was then incubated at 37°C and emission spectra were recorded for the composite at different time intervals at λ_{ex}=500 nm. As control, emission spectra of the blood serum only was also recorded at the same excitation.

6.4. Characterization

UV-vis spectra were recorded using Perkin Elmer Lambda 750 UV-vis spectrophotometer. Fluorescence studies were carried out in HORIBA Jobin Yvon FluoroMax-4 spectrofluorimeter. FT-IR spectra were recorded in Perkin Elmer Spectrophotometer (Model- spectrum one) in the range 450-4000 cm^{-1} for solid samples using KBr pellet method. The solid samples for FTIR were prepared by drying the samples (aqueous dispersion) in dessicator overnight. Matrix assisted laser desorption ionization (MALDI-TOF) spectra for the samples were obtained using Applied Bio systems 4800 Plus MALDI TOF/TOF analyser employing sinapinic acid as the matrix. Particle size and morphologies of all samples were obtained using JEOL JEM 2100 transmission electron microscope (TEM), operating at maximum operating voltage of 200 kV. Sample preparation for TEM was done by drop casting 7 µL of colloidal dispersion on the carbon coated copper grid and which was allowed to air dry. Powder X-ray diffraction (PXRD) data of as synthesized Au NC-$Zn_3(PO_4)_2$ was acquired using a Bruker AXS D8 Advance x-ray diffractometer with $CuK_{\alpha 1}$ radiation (λ~ 1.54060 Å), under 40 kV and 40 mA operating condition. Field emission scanning electron microscopy (FESEM) was carried out in a IGMA, Carl Zeiss FESEM. For sample preparation, 15 µL dispersion of Au NC decorated zinc phosphate nanocomposite was drop-casted on a pre-cleaned glass slide (wrapped with an aluminium foil), dried overnight in vacuum and further double coated with a gold film before sample mounting using SC7620 “Mini”, Polaron Sputter Coater, Quorum Technologies, Newhaven, England. Brunauer–Emmett–Teller (BET) surface area and Barrett-Joyner-Halenda (BJH) average pore width of the samples were analysed using Beckman-Coulter SA 3100 N_2 adsorption-desorption analyzer by degassing the samples at 80 °C for 3 h. Zinc and gold ion concentrations in the samples was determined using atomic absorption spectrometer (Varian, AA240, Netherlands). Size distribution analysis based on dynamic light scattering **(**DLS) and surface zeta potential was done using Zetasizer Nano ZS90 instrument (MODEL NO. ZEN3690, MALVERN), operating with red He–Ne gas laser (λ = 633 nm) at a temperature of 25 °C.

6.5. Results and Discussions

BSA stabilized Au-NCs of 1.6 ± 0.3 nm in size, were synthesized, following a previously reported protocol (Experimental **section 6.3.2**, **Figure A6.1**).[12] Subsequently, the as-synthesized BSA-Au-NCs, having photoluminescence emission at 650 nm (λ_{ex} = 500 nm, **Figure 6.1.A**), were subjected to enzymatic digestion by proteinase K (Experimental **Section 6.3.4**) for 90 min at 37 °C in phosphate buffer (pH= 7.4).[13] It may be mentioned here that protease treatment was carried out for 90 min because experimental results demonstrated very minute drop in PL intensity beyond 90 min of incubation, reaching a saturation at the end of 120 min. (**Figure A6.2, Appendix**) Proteinase K treatment resulted in gradual loss of emission intensity at 650 nm with consequent 10 nm red shift of the emission maximum (**Figure 6.1.A**). The digestion of BSA-Au-NCs resulted in loss of BSA shell and generation of protein fragments. This was confirmed by matrix assisted laser desorption ionisation - time of flight (MALDI-TOF) measurements, which revealed the disappearance of the characteristic peak at 71 kDa due to BSA-Au- NCs (**Figure A6.3**).

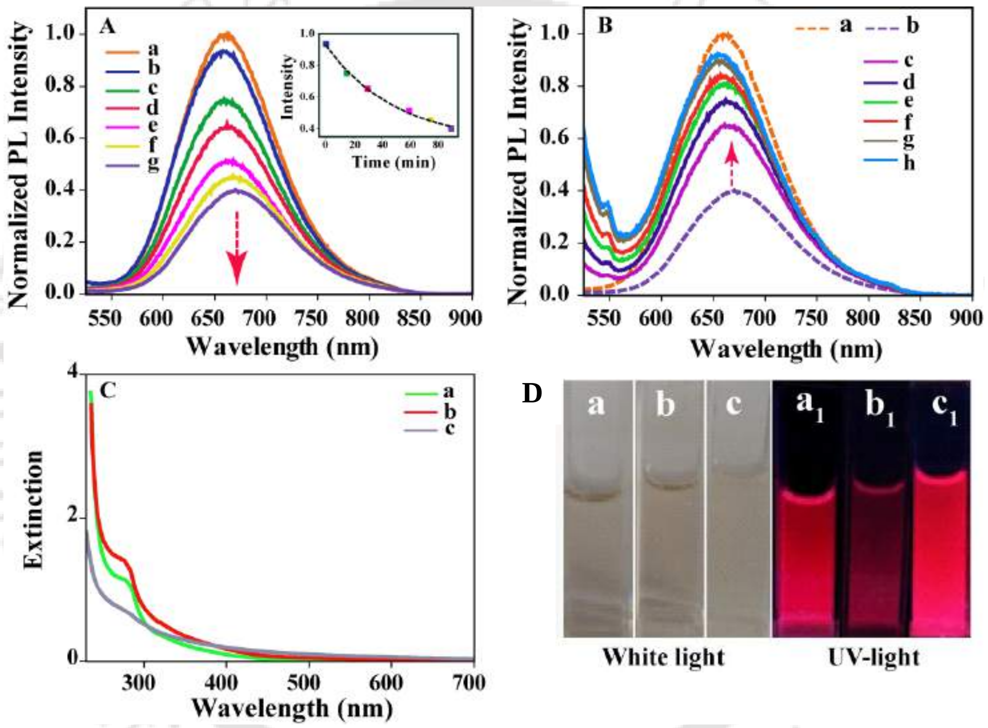

Figure 6.1. (**A**) Time dependent photoluminescence spectra recorded for BSA-Au-NC dispersion (**a**) in phosphate buffer; incubated at 37 C° with Proteinase K at (**b**) 0 min, (**c**) 15 min, (**d**) 30min, (**e**) 60 min (**f**) 75 min and (**g**) 90 min. Inset - shows time dependent loss of emission intensity, (**B**) Photoluminescence spectra of (**a**) original BSA-Au-NC, (**b**) digested BSA-Au-NC after 90 min incubation; gradual emission increment upon addition of (**c**) 50 µL, (**d**) 100 µL, (**e**) 150 µL, (**f**) 200 µL, (**g**) 250 µL and (**h**) 300 µL of [Zn^{2+}] =68 mM to 2.5 mL digested Au NC dispersion. (λ_{ex}= 500 nm for all measurements) (**C**) UV-Vis spectra and (**D**) digital image under white light (**a-c**) and UV-light (a_1-c_1; λ_{ex}= 365 nm) of (**a**) as made BSA-Au-NC, (**b**) digested Au-NC and (**c**) Au-NC-$Zn_3(PO_4)_2$ respectively.

The protease treatment disrupted the effective charge transfer in the triplet state due to S–Au–S–Au–S semi rings of BSA Au NCs,**[15]** leading to reduction in emission intensity, as is also evident from the drop in average lifetime from 1.50 μs to 0.99 μs measured from time-resolved photoluminescence (TRPL) study. (**Figure 6.2.A**)[13] Additionally, the red shift in the luminescence indicated change in the Au(I)-ligand interactions involving the atoms at the periphery of NC cores due to enhanced Au(I)–Au(I) interaction after enzymatic digestion.[16] Interestingly, addition of zinc acetate (68.3 mM) to the digested BSA-Au-NC dispersion resulted in zinc mediated assembly of the protein fragments stabilising the NCs.[17] This eventually led to the formation of zinc phosphate decorated with AuNCs (Au-NC_$Zn_3(PO_4)_2$); pH=6.2) via biomimetic pathway.[18]

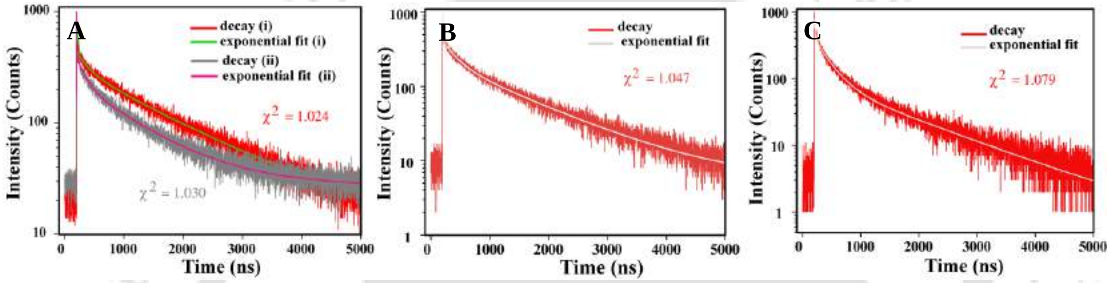

Figure 6.2. Photoluminescence lifetime decay curve of (**A**) as synthesized BSA-Au-NC (red) with fitted line (green); BSA Au NC treated with proteinase K for 90 min (grey) with fitted line (pink), (**B**) liquid dispersion of Au-NC-$Zn_3(PO_4)_2$ with fitted line (white) and (**C**) solid powder of Au-NC- $Zn_3(PO_4)_2$ with fitted line (white).

This was accompanied with simultaneous recovery of luminescence by about 90%, with a concomitant blue shift in emission maximum by 15 nm (**Figure 6.1.B**; Refer **Section 6.3.5** for experimental details). The blue shift in emission energy indicated possible predominance of inter-cluster aurophilic interaction in the assembly.[19] On the other hand, the characteristic absorption peak at ~ 280 nm attributed to tryptophan group in BSA showed an increase in extinction after proteolytic digestion, as is evident from the **Figure 6.1.C**, which nearly disappeared following zinc salt addition.[20] This is possibly due to change in the microenvironment surrounding the NC core upon digestion. The aromatic group of the tryptophan moiety, buried inside the hydrophobic environment in the protein was thus exposed to more polar aqueous environment, resulting in increase in extinction.[3] Further, the peak nearly disappeared upon zinc acetate addition (**Figure 6.1.C(c)**) which might be due to complexation between oppositely charged zinc ion and protein fragments (containing tryptophan residues) stabilising the Au NC core.

Digital photographic images, recorded under white light and UV-light (λ_{ex}=365 nm), respectively, clearly demonstrated the loss of luminescence following digestion of BSA-Au-NC and subsequent recovery upon addition of the zinc salt (**Figure 6.1.D**). It has been reported that when Zn^{2+} ions are added to peptide stabilized Au-NCs, there is enhancement in intensity of luminescence owing to metal mediated assembly of the NCs.[17]

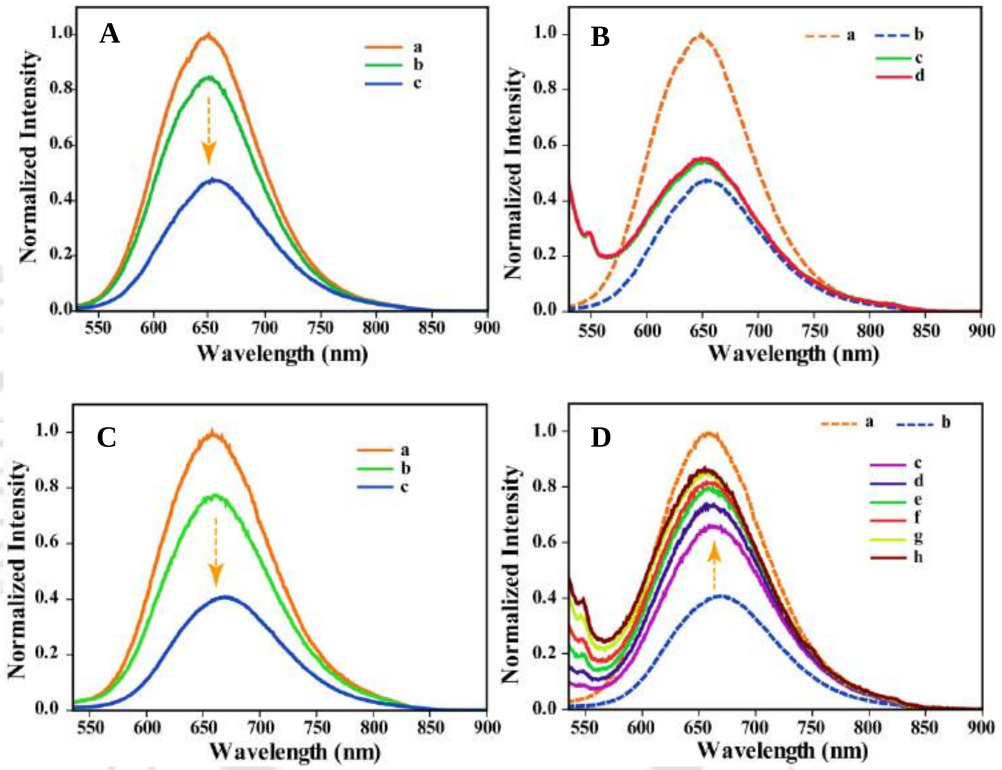

Figure 6.3. (**A**) and (**C**) Photoluminescence spectra recorded for dispersion of BSA-Au-NC (**a**) in water (pH=7.4); after incubation with Proteinase K at 37 °C for (b) 5 min and (c) 90 min, (**B**) Photoluminescence spectra of (**a**) original BSA-Au-NC; (**b**) digested BSA-Au-NC after 90 min incubation in water; upon addition of (**c**) 50 µL and (**d**) 100 µL of $[Zn^{2+}]$ =68 mM to digested Au NC dispersion whereas (**D**) showing considerable increment in emission upon addition of varying concentration of (**c**) 50µL, (**d**) 100 µL, (**e**) 150 µL , (**f**) 200 µL , (**g**) 250 µL and (**h**) 300 µL of zinc acetate hydrate to digested Au-NC dispersion as obtained in **Figure 6.3.C**.

However, control experiments (Experimental **Section 6.3.7**) suggested that it is the zinc phosphate formation in situ that lead to the emission intensity recovery as shown in

Figure 6.3.D rather than zinc ion only as shown in **Figure 6.3.B**. It is to be mentioned that no considerable emission increment in case (**i**) was observed as evident from **Figure 6.3.B**, however case (**ii**) exhibited considerable increment in luminescence (**Figure 6.3.D**) alike the one seen in the case corresponding to **Figure 6.1.B**. It is to be noted that phosphate only has no role in luminescence enhancement (data not shown). Therefore, it is the zinc phosphate which predominately plays the role in *luminescence recovery* rather than zinc ions only. This is also supported by the rise in average lifetime from 0.99 µs to 1.19µs and 1.22 µs for liquid dispersion (**Figure 6.2.B**) and that for solid powder (**Figure 6.2.C**) of Au-NC-$Zn_3(PO_4)_2$ respectively upon zinc addition. (**Table A6.1**) It is to be mentioned that the structural restraintment caused from the assembly induced aggregation of NCs and further entrapment of them in growing zinc phosphate nanostructure caused immediate arrest of their non-radiative relaxation decay from the excited state leading to luminescence recovery.[17]

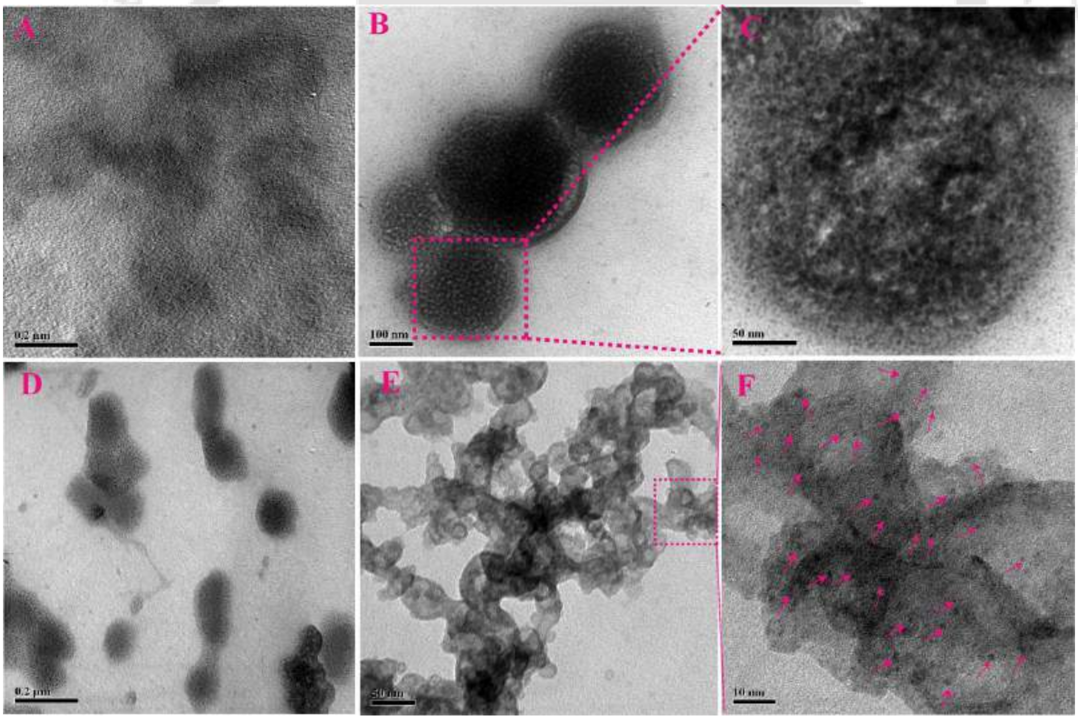

Figure 6.4. Representative TEM images depicting the Au-NC-$Zn_3(PO_4)_2$ growth. TEM image of (**A**) proteinase K treated Au NC (scale= 0.2µm), (**B**) at 4 min of reaction time after addition of 100 µL $[Zn^{2+}]$=68mM, (**C**) magnified view from select region of (**B**), (**D**) at 8 min of reaction time after addition of 200 µL $[Zn^{2+}]$ representing the amorphous stage of zinc phosphate (scale= 0.2µm), (**E**) Au-NC-$Zn_3(PO_4)_2$ obtained at 20 min of reaction time

after addition of 300 µL [Zn^{2+}] (Scale - 50 nm) (**F**) magnified view from a select region of (**E**) clearly depicting the Au NC (shown by green arrow) embedded in the crystal.

Figure 6.4.A represents the transmission electron microscopy (TEM) image of Au-NCs just after protease treatment. In order to understand the formation mechanism of zinc phosphate in situ, they were further probed by TEM measurements by probing the aliquots taken from the reaction mixture after addition of different concentrations of zinc salt and at different times (further details are available in **Discussion A6.1**, **Appendix**). TEM images shown in **Figure 6.4.B** and **C** indicated the formation of spherical assemblies at the initial stage (4 min) of the reaction, via complexation of protein fragments (stabilising the Au-NCs) with zinc ion. This provided the primary nucleation sites for the zinc phosphate growth.[21] It was further observed that the sizes of the structures increased with time and concentration of the zinc salt as is clear from TEM image in **Figure 6.4.D** obtained at 8 min of reaction (no featured SAED pattern was observed, **Figure A6.4, Appendix**). This later formed thermodynamically stable branched structures of zinc phosphate decorated with Au-NCs (indicated by green arrow) after 20 min of reaction time (**Figure 6.4.**(**E-F**)).[22]

Dark field scanning TEM (STEM) image of zinc phosphate in **Figure A6.5.A, Appendix** and the elemental mapping analysis of same confirmed the existence of Au, O, P and Zn as the constituent elements of the composite (**Figure A6.5**(**B-E**)). Also, selected area electron diffraction (SAED) pattern obtained for $Zn_3(PO_4)_2$ corresponding to (111), (221) and (002) planes[23] indicated their polycrystalline nature. (**Figure 6.5.A**) Further, inverse fast Fourier transform (IFFT) analysis from selected region of HRTEM image in **Figure 6.5.B** clearly revealed the lattice fringes (bottom inset in **Figure 6.5.B**) due to (321) plane of zinc phosphate. Powder X-ray diffraction (XRD) pattern of the as-synthesized composite revealed the formation of orthorhombic hopeite, $Zn_3(PO_4)_2.4H_2O$, as supported by the presence of characteristic peaks at 2θ values of 9.68, 18.2, 19.4, 20.0, 22.1, 26.4, 31.2, 33.7, 35.5, 39.7, 45.2, 46.8 and 49.9° (**Figure 6.5.C**; (RRUFF ID: R130562.9)).[24] The thermogravimetric and differential scanning calorimetry traces (as obtained under nitrogen atmosphere) for the as-synthesized composite (**Figure A6.6** and **A6.7**, (**Discussion A6.2**, **Appendix**) conforms to the β-hopeite polymorph of $Zn_3(PO_4)_2.4H_2O$.[25] The amount of zinc and gold present in the composite as quantified by atomic absorption spectroscopy was found to be 7.31 mM and 0.15 mM. FTIR spectroscopic analysis matched with the vibrational modes attributed to BSA stabilised Au NCs and zinc phosphate (**Figure A6.8, Appendix**). (Detailed spectral analysis in **Discussion A6.3**, **Appendix**) Overall, the results indicated the formation of nanocrystalline $Zn_3(PO_4)_2$ decorated with protein fragment-stabilized Au-NCs via biomimetic pathway.

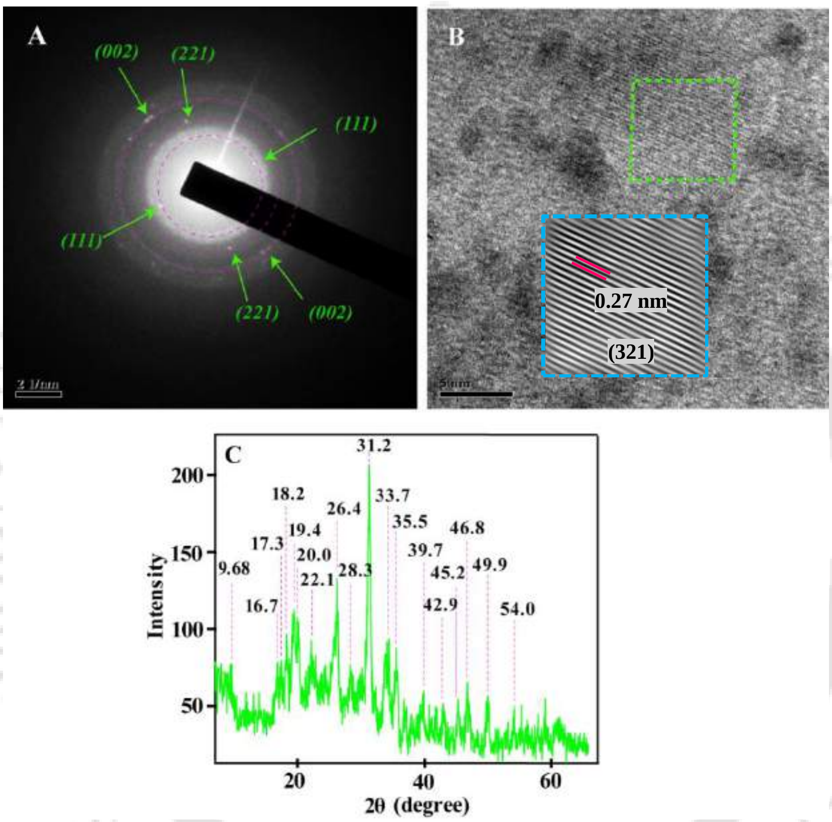

Figure 6.5. (**A**) SAED pattern of as synthesized Au-NC-$Zn_3(PO_4)_2$, (**B**) HRTEM image of as synthesized Au-NC-$Zn_3(PO_4)_2$ showing lattice plane corresponding to zinc phosphate; Inset: IFFT image representing the lattice spacing corresponding to hopeite (321) plane and (**C**) Powder X-ray diffraction pattern of Au-NC-$Zn_3(PO_4)_2$.

It was further observed that the protein fragments not only took part in metal binding to provide nucleation site but played a structure directing role in the zinc phosphate growth[26] (Refer Experimental **Section 6.3.8**). For example, when zinc salt was added to the medium containing as-synthesized BSA-Au-NCs, no such well-defined nanostructured crystals of zinc phosphate could be observed. (**Figure 6.6.**(**A-B**)) In this case, the Au-NC seems to remain scattered in the zinc acetate-phosphate buffer matrix with undefined morphology as revealed from TEM image **Figure 6.6.A**.

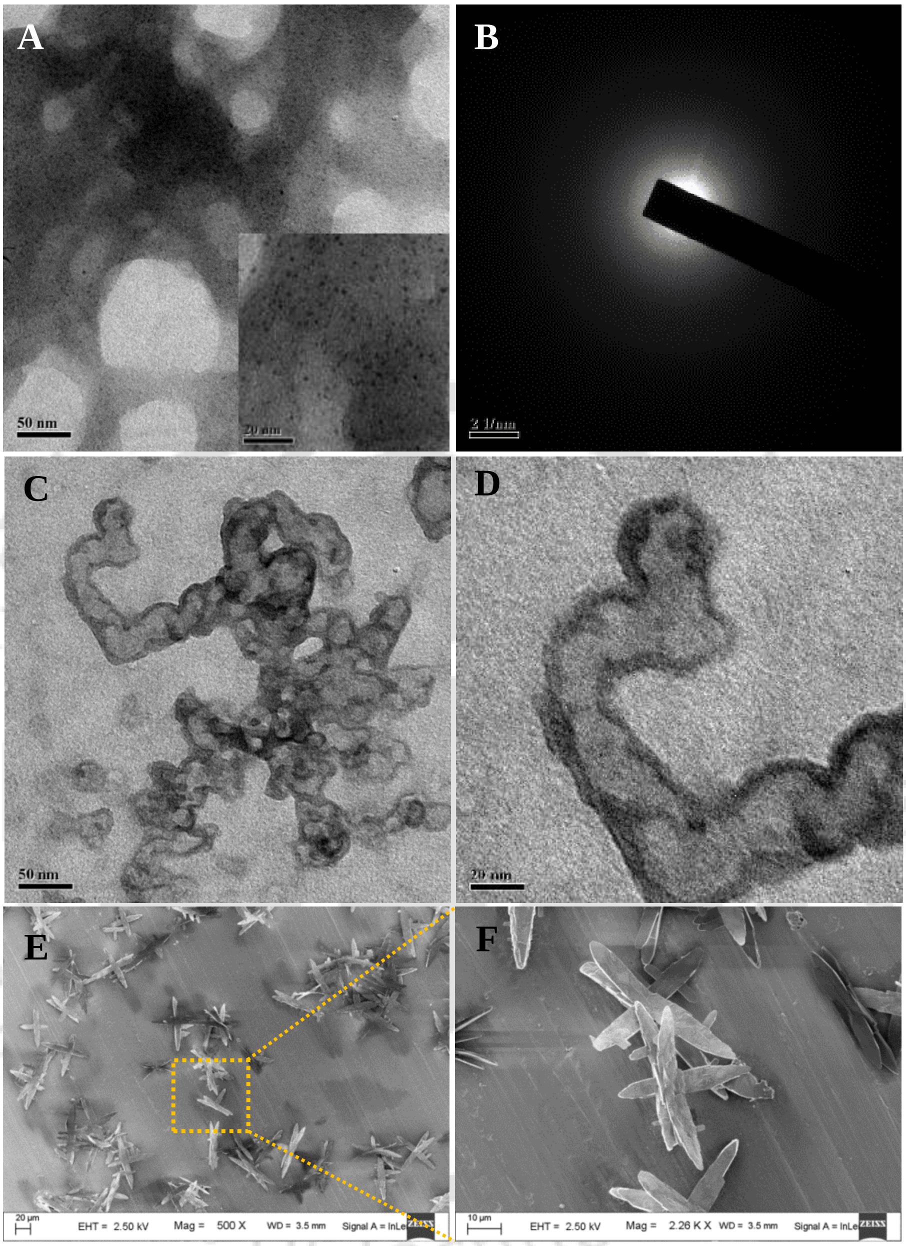

Figure 6.6. (**A**) Low magnification TEM image (Inset: High magnification image from select region of (**A**)) and (**B**) SAED image (scale size = 2 nm^{-1}) of 300 µL zinc acetate dihydrate (68.3 mM) treated BSA-Au-NC in phosphate buffer (pH=7.4). (**C**) TEM image of zinc phosphate ($Zn_3(PO_4)_2$) obtained from 300 µL zinc acetate dihydrate (68.3 mM) treated digested BSA solution at 37 °C for 90 min and (**D**) high magnification image from select region of (**C**). (**E**) FESEM image of $Zn_3(PO_4)_2$ obtained by treating phosphate buffer solution (pH=7.4) with 300 µL [Zn^{2+}] = 68mM showing star shaped structure and (**F**) high magnification image of $Zn_3(PO_4)_2$ from a select region of (**E**).

In addition, no characteristic SAED features (**Figure 6.6.B**) corresponding to zinc phosphate formation was seen. Also, the same well-defined nanostructured zinc phosphate crystal formation took place in the presence of digested BSA protein only (**Figure 6.6.C**); whereas addition of zinc salt to phosphate buffer only, led to formation of micron sized star shaped zinc phosphate structures (**Figure 6.6.(E-F)**). **Figure 6.6.C** shows the TEM image of the zinc phosphate obtained by digestion of native BSA in phosphate buffer which is similar to the one obtained from digestion of BSA-Au-NC (**Figure 6.4.E**). **Figure 6.6.D** is the magnified view from a select region of **Figure 6.6.C**. **Figure 6.6.F** is the magnified view of star shaped zinc phosphate nanostructure shown in **Figure 6.6.E.**

Hence, the peptide fragments bearing specific amino acids plays important role in directing the size and morphology of the zinc phosphate from micrometer to nanometer size range. Plausibly, the structure directing property of amine moieties might arise from the coulombic attraction between the positively charged amine moieties e.g., histidine[26] (system pH= 6.26) present in the peptide fragments and negatively charged phosphate group. Also, contribution from metal – amino acid coordination and hydrogen bond cannot be neglected.

The average hydrodynamic size of the as-synthesized BSA-Au-NC (Z_{avg} = 10.7 ± 1.5 nm) as recorded in aqueous medium underwent a shift to Z_{avg} = 6.6 ± 0.8 nm after proteolytic digestion. Upon zinc addition, the particle size distribution was significantly shifted to 503.7 ± 54 nm. (**Figure 6.7**(**C**)) This indicated the aggregated nature of the Au-NC-$Zn_3(PO_4)_2$ composite. This was also accompanied by an increase in the surface zeta potential of mineralized composite from -40.7 ± 1.4 mV to -19.6 ± 1.4 mV, measured at 25 °C. The abrupt increase in zeta potential might be due to the surface charge neutralization upon addition of [Zn^{2+}], which acted as the counter cation, as summarized in **Table A6.2**. The hydrodynamic diameter (Z_{av}) and surface charge measured for the as developed mineralized luminescent nanocomposite were deemed suitable for use in bio-imaging as their size favors easy extravasation through tumor tissues.[27] BET surface analysis of the mineralized nanocrystal composite showed Type IV isotherm (**Figure A6.9**(**A-B**), **Appendix**) confirming the mesoporous nature of the material with a pore diameter in the range 2-17 nm (Refer **Table A6.3**), which may be exploited for

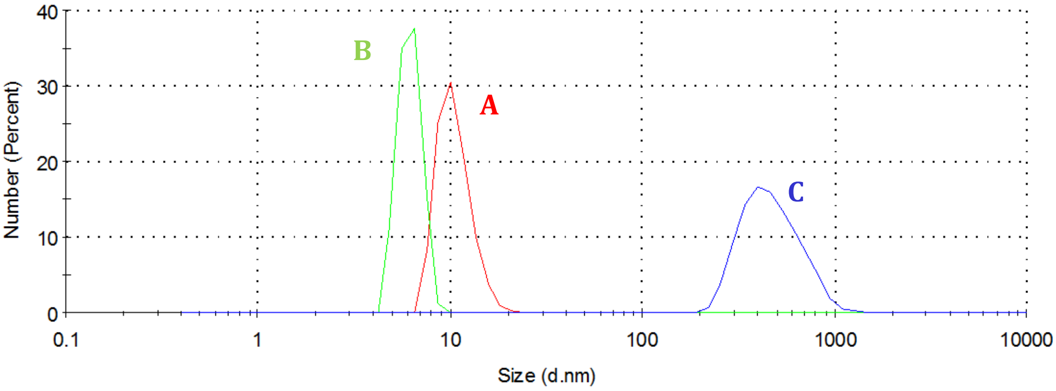

Figure 6.7. DLS-based particle size distribution obtained for (**A**) BSA-Au-NC (red curve), (**B**) digested BSA-Au-NC (green curve) and (**C**) Au-NC- $Zn_3(PO_4)_2$ (blue curve).

loading of therapeutics for delivery applications.[27] The overall schematic depiction of biomimetic crystallisation of Au-NC-$Zn_3(PO_4)_2$ and their internalisation in cancer cells for bio-imaging is depicted in **Figure 6.8.**

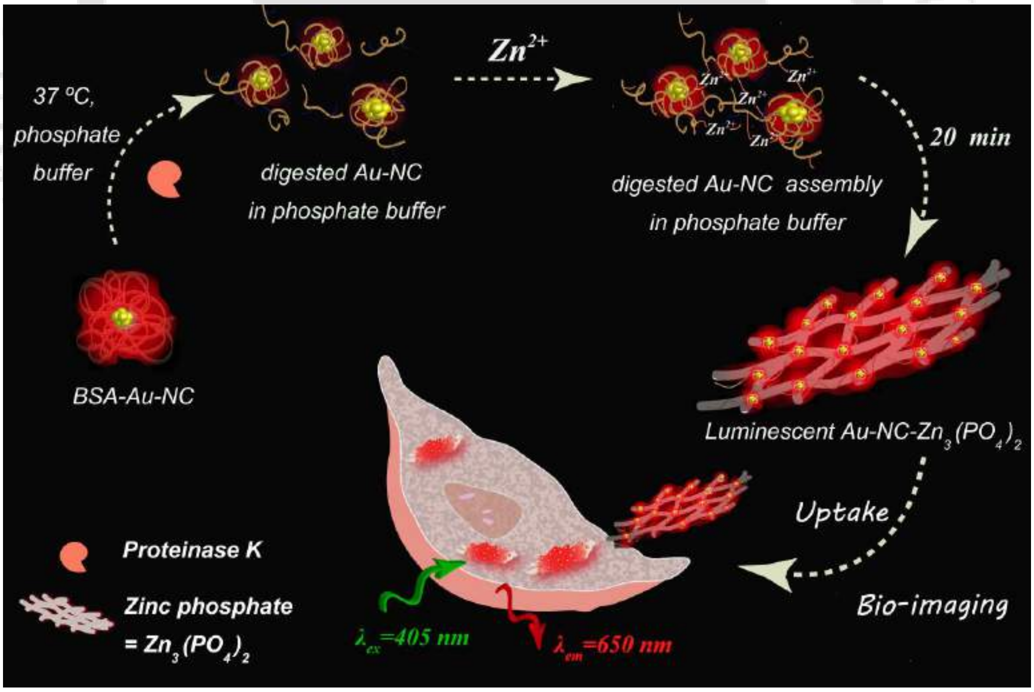

Figure 6.8. Schematic description of the biomimetic pathway towards zinc phosphate crystallization in protein fragment stabilised Au-NC assembly and their uptake in cancer (HeLa) cell for bio-imaging.

In order to evaluate the potential of the AuNC-$Zn_3(PO_4)_2$ nanocomposite as bio-imaging agent, first their cytotoxicity was investigated in-vitro on normal human kidney epithelial cells (HEK 293) as well as human cervical cancer (HeLa) cells by viability assay (Refer Experimental **Section 6.3.9.a**).

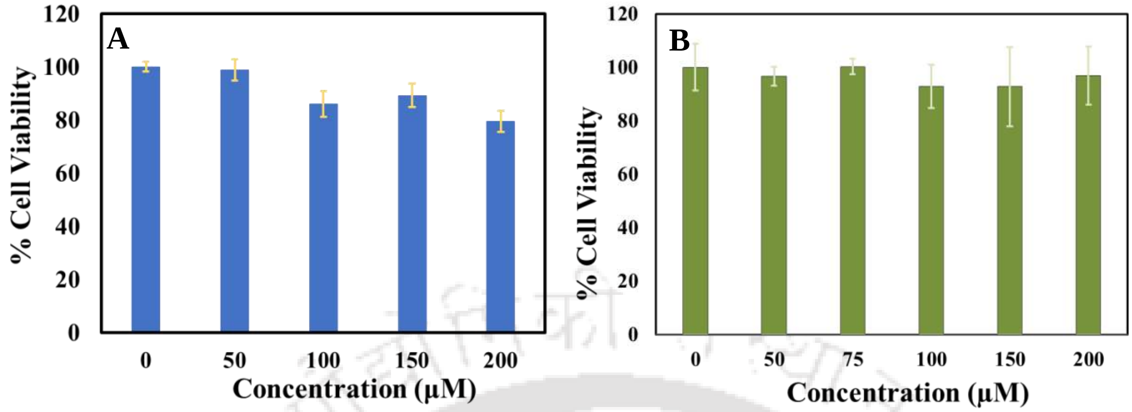

Figure 6.9. Cell viability of (**A**) HEK 293 cells and (**B**) HeLa cells treated with varying concentration of Au-NC- $Zn_3(PO_4)_2$ for 24 h.

The results revealed no such cytotoxicity up to 150 µM and 200 µM of the composite (with respect to the zinc ion) on HEK 293 (**Figure 6.9.A**) and HeLa (**Figure 6.9.B**), respectively as 90% of the cells were viable. Similar results were also observed in case of as-synthesized BSA-Au-NCs. (**Figure A6.10**) Following incubation of HeLa cells with the mineralized nanocomposite for 4 h, internalization of the nanomaterials was confirmed by confocal laser scanning microscopy (CLSM), performed using a diode laser; λ_{ex} = 405 nm. (Refer Experimental **Section 6.3.9.b**) Interestingly, HeLa cells treated with Au-NC-$Zn_3(PO_4)_2$ nanocomposite (**Figure 6.10.H**) showed clear images with prominent luminescence intensity, similar to the as-synthesized BSA-Au-NC treated ones (**Figure 6.10.B**).

However, weak luminescence was observed in HeLa cells incubated with digested BSA-Au-NCs (**Figure 6.10.E**), which could be due to loss of luminescence of the Au NCs after proteolytic digestion. Moreover, **Figure A6.11.C** depicts the corresponding depth projection of a typical CLSM image of a HeLa cell (**Figure A6.11.(A-B)**) treated with nanocomposite, confirming the internalization by the HeLa cells. Interestingly, sodium azide-based inhibition studies revealed endocytosis as a major pathway for internalization of the nanocomposites by HeLa cells (Experimental **Section 6.3.9.b**, **Figure A6.12**). It may be mentioned here that further experiments demonstrated successful internalization of AuNC-$Zn_3(PO_4)_2$

nanocomposite by HEK 293 cells (**Figure A6.13**) suggesting their non-specific cellular uptake, which might be desirable for an effective bio-imaging probe. Further quantitative analysis of CLSM images using Image J software, indicated two-fold increase in luminescence in HeLa cells (**Figure 6.11**, Experimental **Section 6.3.9.c**) treated with the mineralized composite as compared to those treated with BSA-Au-NCs.[28]

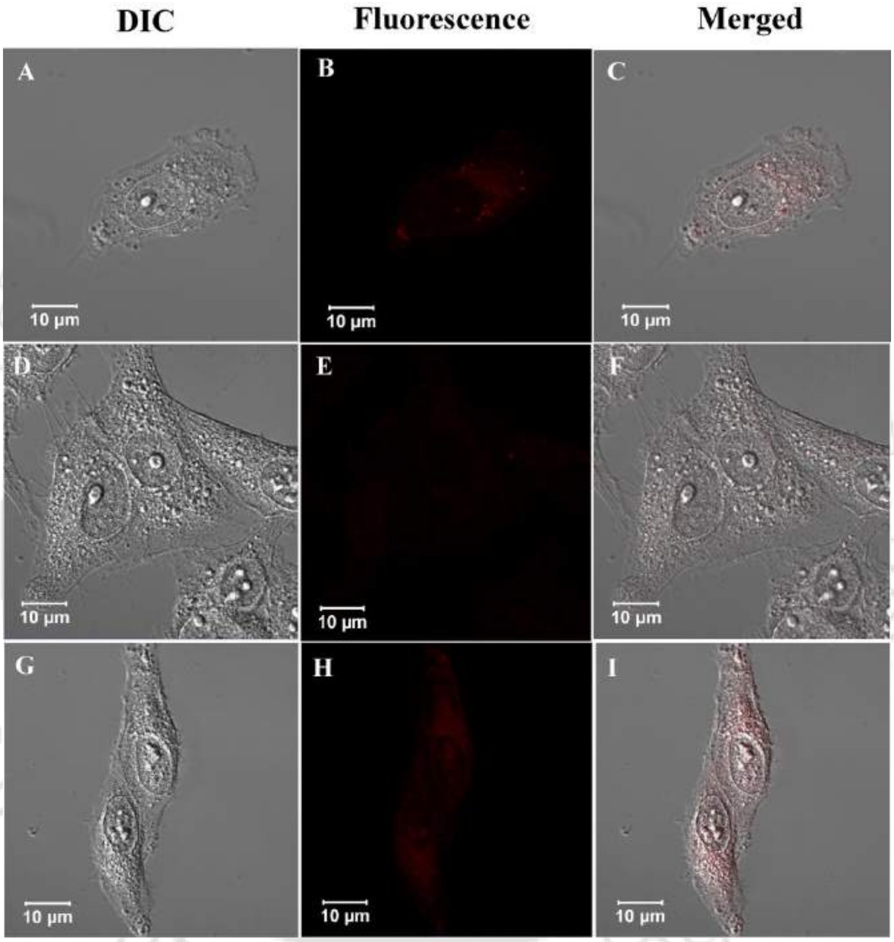

Figure 6.10. CLSM images of HeLa cells treated for 4 h at 37 °C with (**A-C**) BSA-Au-NCs, (**D-F**) digested BSA-Au-NC and (**G-I**) Au-NC-$Zn_3(PO_4)_2$. (Source: λ_{ex}= 405 nm; 63× oil immersion objective).

Herein, the presence of protein fragments and increased zeta potential of the mineralized composite (mentioned earlier) could be accounted for their better cellular uptake.[28] In addition, biomimetic formation of zinc phosphate nanocrystal in the present study offers a platform for effective accumulation of the nanoclusters, which could trigger their faster uptake due to size conformity and

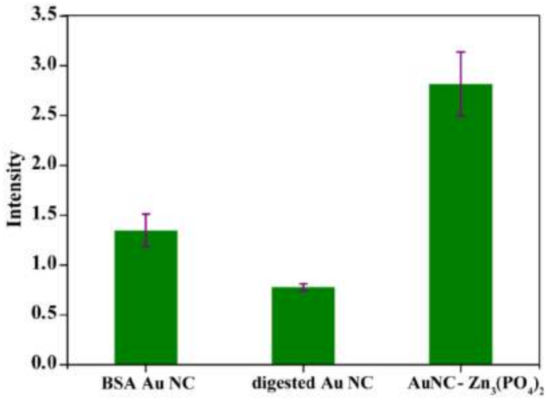

Figure 6.11. Mean luminescence intensity of HeLa cancer cells incubated with BSA-Au-NC, digested Au-NC and Au-NC-$Zn_3(PO_4)_2$ obtained from CLSM images using Image J software (5 different cell images). The data are represented as mean ± standard deviation.

hence the observed enhanced luminescence.[29] However, realizing true contribution of protein fragments, surface charge or clustering of Au NCs in uptake efficiency of the nanocomposite needs further studies. Serum stability and resistance to proteases, as already mentioned earlier are important parameters for potential application of the present composite as luminescent nanomaterials for in-vitro and in-vivo bio-imaging. Therefore, protease treatment did not lead to any considerable change in luminescence of the composite as depicted in Figure

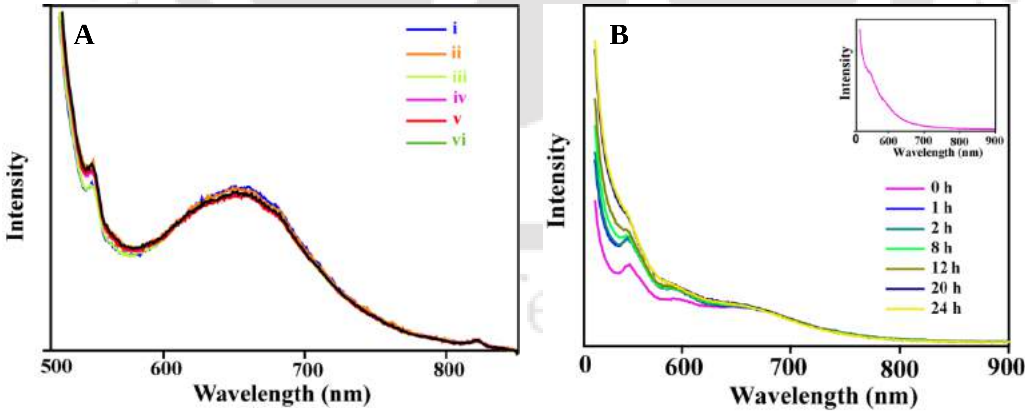

Figure 6.12. (**A**) Stability of Au-NC-$Zn_3(PO_4)_2$ against protease degradation. Emission spectra (λ_{ex} = 500 nm) recorded for (**i**) as synthesized Au-NC-$Zn_3(PO_4)_2$; proteinase K treated Au-NC-$Zn_3(PO_4)_2$ at (**ii**) 0, (**iii**) 10, (**iv**) 30, (**v**) 90, (**vi**) 120 min of incubation at 37 °C. (**B**) Stability of Au-NC-$Zn_3(PO_4)_2$ in human blood serum. Emission (λ_{ex} = 500 nm) spectra of Au-NC-$Zn_3(PO_4)_2$ in human blood serum at different intervals of time. Inset: emission spectra of human blood serum only (λ_{ex} = 500 nm).

6.12.A (Refer Experimental **Section 6.3.10**). In addition, the mineralized nanocomposites were also found to be stable in human blood serum till 24 h as shown in **Figure 6.12.B** (Refer Experimental **Section 6.3.11**).

6.6. Conclusion

Thus, a new probe is reported for efficient bio-imaging via biomimetic method of crystallization of zinc phosphate from zinc mediated assembly of digested BSA-Au-NCs. The presence of protein fragments obtained from enzymatic digestion of BSA-Au-NCs was critical in obtaining mineralized zinc phosphate with controlled shape and size. Interestingly the zinc phosphate formation led to the recovery of luminescence of Au NCs, which was lost following enzymatic degradation. The mineralized nanocomposite was mesoporous in nature and was realized to be non-toxic and thus bio-compatible. Enhanced internalization by HeLa cells, notable protease resistance and excellent stability in human blood serum make the present composite ideal for in vitro and possible in-vivo imaging agent in mammalian cells. Further, the biomimetic approach of zinc phosphate crystallization may possibly be achieved with different protein stabilised metal nanoclusters of choice depending upon the target to be accomplished, thus providing a new idea in theranostics.

6.7. References

1. Peer, D.; Karp, J. M.; Hong, S.; Farokhzad, O. C.; Margalit, R.; Langer, R. *Nature Nanotechnology* **2007**, *2*, 751.
2. (**a**) Bijuab, V. *Chem. Soc. Rev*. **2014**, *43*, 744; (**b**) Fan, Z.; Shelton, M.; Singh, A. K.; Senapati, D.; Khan, S. A.; Ray, P. C. *ACS Nano* **2012**, *6*, 1065.
3. Khandelia, R.; Jaiswal, A.; Ghosh, S. S.; Chattopadhyay, A. *J. Mater. Chem. B* **2014**, *2*, 6472.
4. (**a**) Zhao, T. X.; He, W.; Li, W. Y.; Zhangab, Y. K. *J. Mater. Chem. B* **2015**, *3*, 2388; (**b**) Wang, Y.; Chen, J.; Irudayaraj, J. *ACS Nano* **2011**, *5*, 9718; (**c**) Guo, X.; Li, D.; Yang, G.; Shi, C.; Tang, Z.; Wang, J.; Zhou, S. *ACS Appl. Mater. Interfaces* **2014**, *6*, 8549, (**d**) Chen, T.; Xu, S.; Zhao, T.; Zhu, L.; Wei, D.; Li, Y.; Zhang, H.; Zhao, C. *ACS Appl. Mater. Interfaces* **2012**, *4*, 5766.
5. (**a**) Retnakumari, A.; Setua, S.; Menon, D.; Ravindran, P.; Muhammed, H.; Pradeep, T.; Nair, S.; Koyakutty, M. *Nanotechnology* **2010**, *21*, 055103; (**b**) Li, Z.; David, E.; Lakshminarayanan, R.; Loh, X. J. *Small* **2016**, *12*, 4782.
6. (**a**) Wilcoxon, J. P.; Abrams, B. L. *Chem. Soc. Rev.* **2006**, *35*, 1162. (**b**) Chen, L. Y.; Wang, C. W.; Yuan, Z.; Chang, H. T. *Anal. Chem.* **2015**, *87*, 216.
7. Khandelia, R.; Bhandari, S.; Pan, U. N.; Ghosh, S. S.; Chattopadhyay, A. *Small* **2015**, *11*, 4075.
8. Luo, Z.; Zheng, K.; Xie, J. *Chem. Commun*. **2014**, *50*, 5143.
9. Dutta, D.; Chattopadhyay, A.; Ghosh, S. S. *ACS Biomater. Sci. Eng.* **2016**, *2*, 2090.
10. Hatakeyama, H.; Akita, H.; Harashima, H. *Adv. Drug Deliv. Rev.* **2011**, *63*,152.
11. Rica, R. de la.; Velders, A. H. *J. Am. Chem. Soc.* **2011**, *133*, 2875.
12. Xie, J.; Zheng, Y.; Ying, J. Y. *J. Am. Chem. Soc.* **2009**, *131*, 888.
13. Wang, Y.; Wang, Y.; Zhou, F.; Kim, P.; Xia, Y. *Small* **2012**, *8*, 3769.
14. Yang, L.; Shang, L.; Nienhaus, G. U. *Nanoscale* **2013**, *5*, 1537.
15. Wen, X.; Yu, P.; Toh, Y. R.; Hsu, A. C.; Lee, Y. C.; Tang, J. *J. Phys. Chem. C* **2012**, *116*, 19032.
16. Assefa, Z.; McBurnett, B. G.; Staples, R. J.; Fackler, J. P.; Assmann, Jr, B.; Angermaier, K.; Schmidbaur, H. *Inorg. Chem*. **1995**, *34*, 75.
17. Yoo, Q.; Luo, Z.; Yuan, X.; Yu, Y.; Zhang, C.; Xie, J.; Lee, J. Y. *Sci. Rep*. **2014**, *4*, 3848.
18. Lee, S. Y.; Gao, X.; Matsui, H. *J. Am. Chem. Soc.* **2007**, *129,* 2954.
19. Luo, Z.; Yuan, X.; Yu, Y.; Zhang, Q.; Leong, D. T.; Lee, J. Y.; Xie, J. *J. Am. Chem. Soc.* **2012**, *134*, 16662.
20. Min, Y.; Zheng, F.; Chen, Y.; Zhang, Y. *J. Mater. Sci.: Mater. Electron.* **2012**, *23*, 1116.

21. Ge, J.; Lei, J.; Zare, R. N. *Nat. Nanotechnol.* **2012**, *7*, 428.

22. (**a**) Bach, S.; Celinski, V. R.; Dietzsch, M.; Panthöfer, M.; Bienert, R.; Emmerling, F.; auf der Günne, J. S.; Tremel, W. *J. Am. Chem. Soc.* **2015**, *137*, 2285; (**b**) Chung, S.-Y.; Kim, Y.-M.; Kim, J.-G.; Kim, Y.-J. *Nat. Phys.* **2009**, *5*, 68.

23. Liu, P.; Zhu, B.; Yuan, X.; Tong, G.; Su, Y.; Zhu, X. *J. Mater. Chem. B*, **2015**, *3*, 1301.

24. Rathnayake, S.; Unrine, J. M.; Judy, J.; Miller, A. F.; Rao, W.; Bertsch, P.M. *Environ. Sci. Technol.* **2014**, *48*, 4757.

25. Herschke, L.; Enkelmann, V.; Lieberwirth, I.; Wegner, G. *Chem. Eur. J.* **2004**, *10*, 2795.

26. Mekhatria, D.; Rigolet, S.; Janiak, C.; Masseron, A. S.; Hasnaoui, M. A.; Bengueddach, A. *Crystal Growth & Design* **2011**, *11*, 396.

27. Yuan, X.; Zhu, B.; Ma, X.; Tong, G.; Su, Y.; Zhu, X. *Langmuir* **2013**, *29*, 12275.

28. Luan, L.; Meng, Q.; Xu, L.; Meng, Z.; Yan, H.; Liu, K. *J. Mater. Chem. B* **2015**, *3*, 1068.

29. Yang, L.; Shang, L.; Nienhaus, G. U. *Nanoscale* **2013**, *5*, 1537.

CHAPTER 7

Thesis Summary and Future Prospects

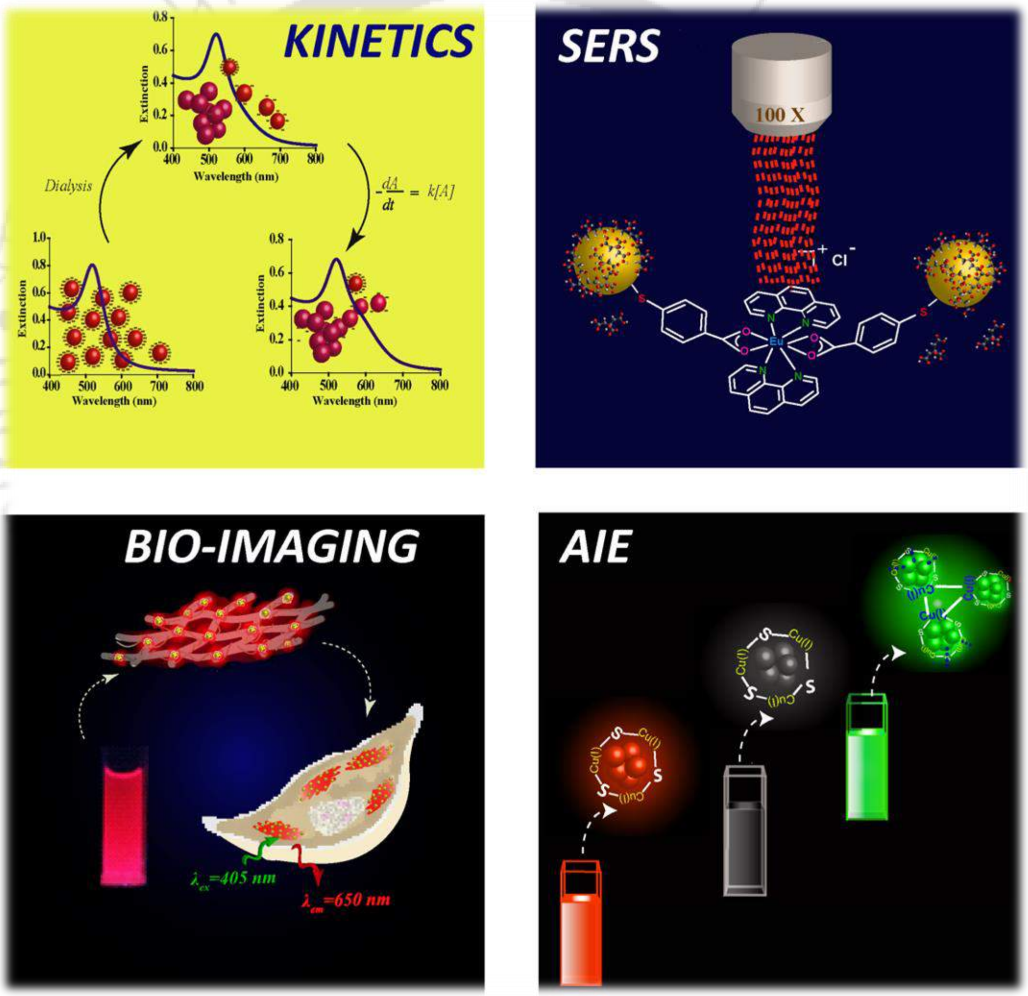

7.1. Summary of the Thesis

In summary, the present thesis demonstrates the different strategies to design higher ordered nanostructures of nanoscale metal particles and understanding their reaction mechanisms for their potential utility in SERS, superior bio-imaging and mammalian cell line detection.

In this regard, reaction kinetic study of Cit-Au NPs mediated by ligand desorption from the surface (via method of dialysis) showed the prevalence of first order kinetic pathway, which was further accounted for based on a proposed reaction model. Further, time-dependent kinetic study in the temperature range 20–60 °C exhibited a linear dependence showing increase of rate constant of the reaction with increase in temperature, akin to the general trend as observed in conventional kinetic study. Kinetic data revealed the existence of reaction limited colloidal aggregation with an activation energy of 36.2±3.0 kJ mol^{-1} for first order rate law in the temperature range 20–60 °C. Further, metal complex (Eu-complex) mediated reaction of Cit-AuNPs led to the formation of discrete dimers in liquid dispersion. The as-synthesized Au dimers exhibited exclusive SERS and TERS of the ligated Eu-complex at the hot-spot with an enhancement factor calculated to be on the order of 10^9 and 10^4, respectively. Additionally, the potential application of engineered fluorescent probes of Cu and Au NCs has also been explored. A pH responsive Cu NCs with orange-red emission at pH 4.5 upon internalisation into living cells exhibited striking green emission inside the cellular environment (pH ~ 7.4) *via* AIE. Interestingly, the rate constant value derived for AIE kinetics in MCF-7 cells was found 3-fold higher than that in HEK-293 cell lines paving a new way to study different cell lines based on intracellular AIE in living cells. Further, a luminescent probe developed *via* biomimetic crystallization of zinc phosphate in presence of peptide stabilised gold nanocluster assembly is reported. The engineered probe - with Au nanoclusters assembled on the crystal - was protease resistant, offered stability in human blood serum and therefore served as an efficient bio-imaging nanocrystal.

7.2. Future Prospects

The present idea to employ various physical and chemical means to design higher order nanostructures and further understanding of their reaction pathway would provide us with better future engineering options towards the development of advanced nanomaterials. The future therefore lies in studying the reaction kinetics of nanoparticles of Au with Ag, Pt, Pd and Cu to generate bimetallic or alloyed nanoparticulate system, which could serve as platform for enhanced catalysis, signal enhancing devices or as wider antibacterial and drug delivery vehicle with therapeutic property. The metal complex mediated dimerization or otherwise the availability of metal of choice in the hot-spot and hence affinity of the same for any probe molecule to be studied would allow us to carry further complex chemical reaction at the hot-spot. This would enhance the sensitivity of the system towards carrying out plasmon mediated catalysis, detection and also in plasmon assisted hot carrier devices such as FET, photodetectors etc. Next, the pH responsive AIE featured CuNCs may find its use as a sensitive probe for specific biomolecule and overexpressed proteins recognition, which could then be used as diagnostic tool for disease detection *in vitro* as well as *in vivo*. Moreover, the present biomimetically crystallized Au NCs embedded zinc phosphate nanostructures could further be utilised for uptake study and as fluorescence based targeted drug delivery vehicle, owing to its highly porous nature, biocompatibility and enhanced uptake efficiency.

APPENDIX

Chapter 2: A2

Calculation of concentration of monomeric Au NP during time-dependent study

Calculation of concentration of gold nanoparticle (NP) formed when 1mL of 1.72×10^{-2} M $HAuCl_4$ is reduced by citrate reduction method in a volume mixture of 100 mL.

Moles of $HAuCl_4$ in 1 mL $HAuCl_4$ stock

= moles of $HAuCl_4$ in 100 ml volume mixture = 1.72×10^{-5}

$[HAuCl_4]=[Au]$, since dissociation of a unit mole of $HAuCl_4$ produces a unit mole of Au-ion and assuming all Au^{3+} ions undergo complete reduction,

Moles of Au-atom in 100 mL volume mixture = 1.72×10^{-5} moles

Therefore, total number of Au atoms in 100 mL volume mixture (N) can be calculated by multiplying moles of Au-atom with Avogadro number = $1.72\times10^{-5} \times N_A$ atoms.

For a spherical gold nanoparticle,**[A1]**

$$V_{NP} = nV_{atom}$$

$$\Rightarrow \frac{4}{3}\pi R^3 = n\,\frac{4}{3}\pi r^3$$

where V_{NP} = volume of a nanoparticle,

V_{atom} = volume of a gold atom,

n = total number of Au atoms in a nanoparticle,

R= average radius of a gold NP as calculated from TEM measurement =8.5 nm,

R= radius of Au-atom =0.146 nm.

Therefore, $n = \left(\frac{R}{r}\right)^3 = 197332$

Number of gold atoms per nanoparticle = 197332

Number of Au atoms in the nanoparticle dispersion = n×N

where, n= number of Au-atoms in NP dispersion,

N=number of Au NPs in the volume mixture.

$$N = \frac{N_A \times 1.72 \times 10^{-5}}{197332} = \frac{6.023 \times 10^{23} \times 1.72 \times 10^{-5}}{197332} = 5.2498 \times 10^{13}$$

Hence, concentration of gold nanoparticle can be calculated by dividing the number of nanoparticle obtained in 100 mL volume mixture by N_A.

$$[AuNP] = \frac{N}{N_A} = \frac{5.2498 \times 10^{13}}{6.023 \times 10^{23}} = 0.8717 \times 10^{-10} moles$$

Therefore, final concentration of gold nanoparticle is = $\frac{0.8717 \times 10^{-10}}{100} \times 1000$ M

= 0.8717×10^{-9} M

= 0.8717 nM.

The area under the SPR band of as synthesized Cit-Au NPs is proportional to the initial concentration of as synthesised Au NPs, $[Au]_0$.[A2] The area under the SPR band was obtained using function set in Origin 7.0 software.

However, each time the as synthesized Cit-Au NPs were centrifuged at 4000 rpm for 10 min, and supernatant were used for carrying out experiment. Therefore, final concentration of Au NPs reported in the manuscript is based on the area under the SPR band of Au NPs obtained from the supernatant. The peak area for different sets of as-synthesized Cit-Au NPs was calculated after centrifugation and was found to be reproducible i.e 69.81 AU (arbitrary unit). Peak area to concentration conversion was 69.81 AU = 0.734 nM, which has been used as standard value to calculate the concentration of Cit-Au NPs dialysed at different dilution and monomer Au NP left at time ‘t’ during time-dependent study.

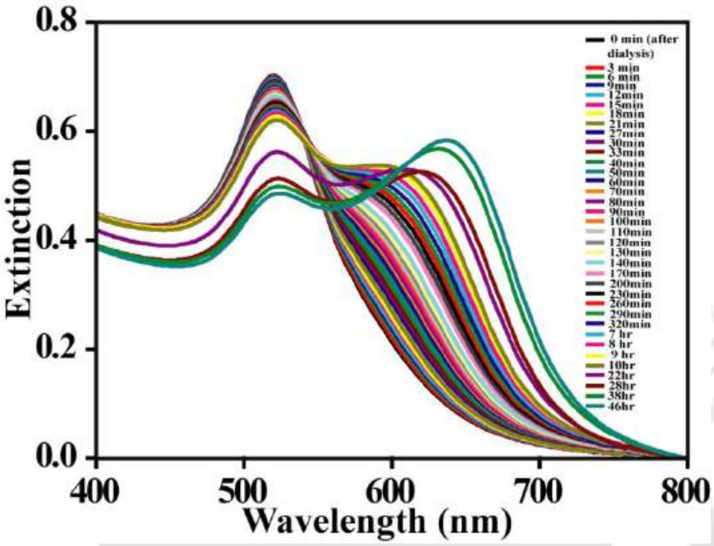

Figure A2.1. Time-dependent SPR extinction spectra of dialysed Cit-Au NPs, which was carried for longer time period in comparison to those reported in the chapter 2.

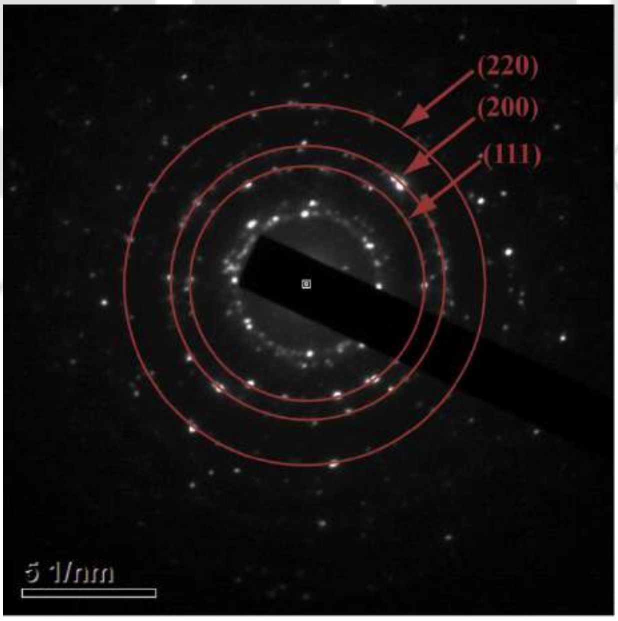

Figure A2.2. Selected area electron diffraction (SAED) pattern of Cit-Au NPs corresponding to TEM image shown in **Figure 2.3.D**. Diffractions corresponding to various planes (of fcc Au) are identified in the image.

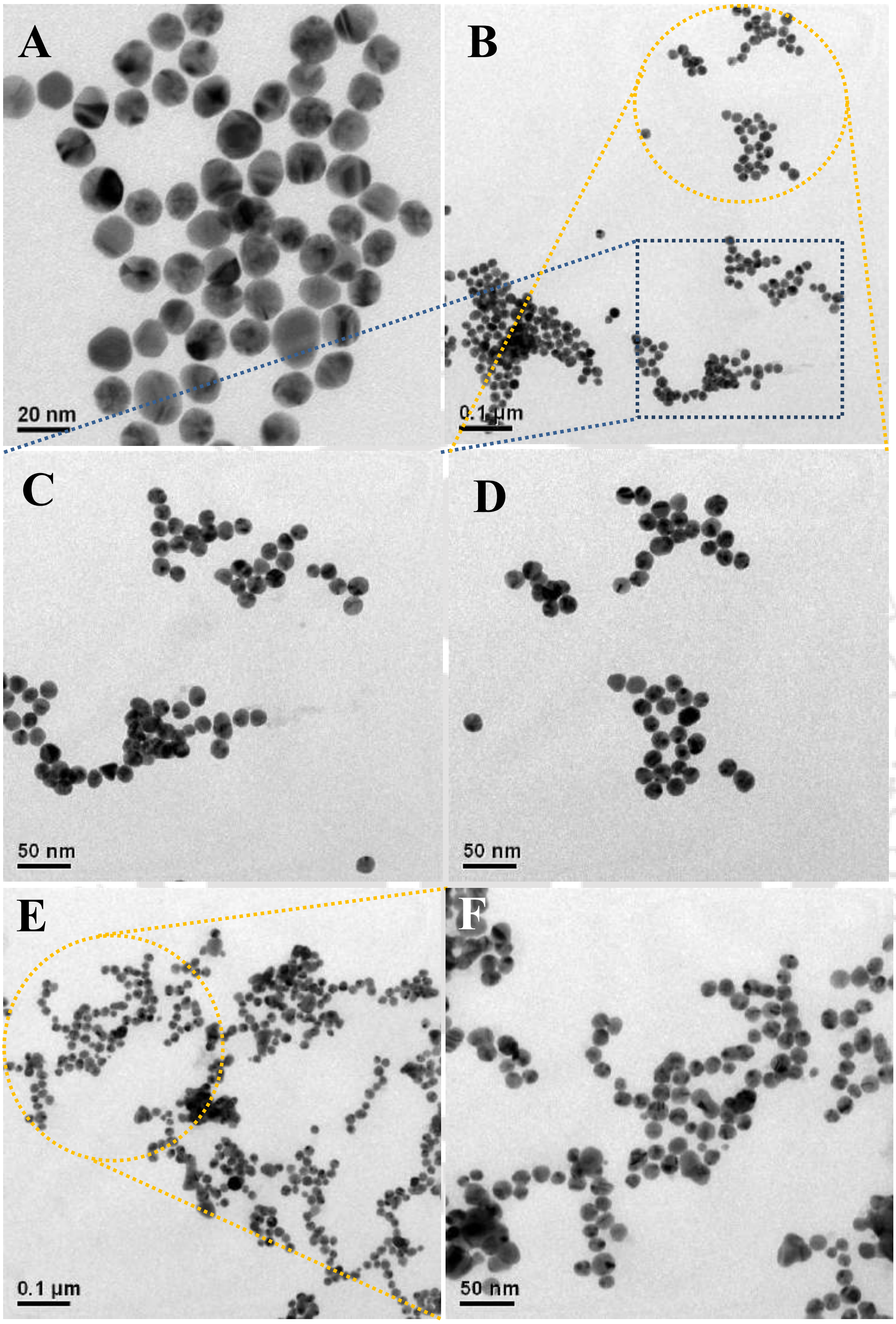

Figure A2.3. TEM images of 0.39 nM Cit-Au NPs recorded at different times on standing of the solution following dialysis for 270 min. (**A**) t = 0 min, (**B**) t = 15 min, (**C**) and (**D**) are the expanded views from selected region of image (**B**) i.e, blue dotted box and yellow dotted circle respectively, (**E**) TEM image of Cit-Au NPs at t=30 min, (**F**) Expanded view of the image in (**E**) from a selected region.

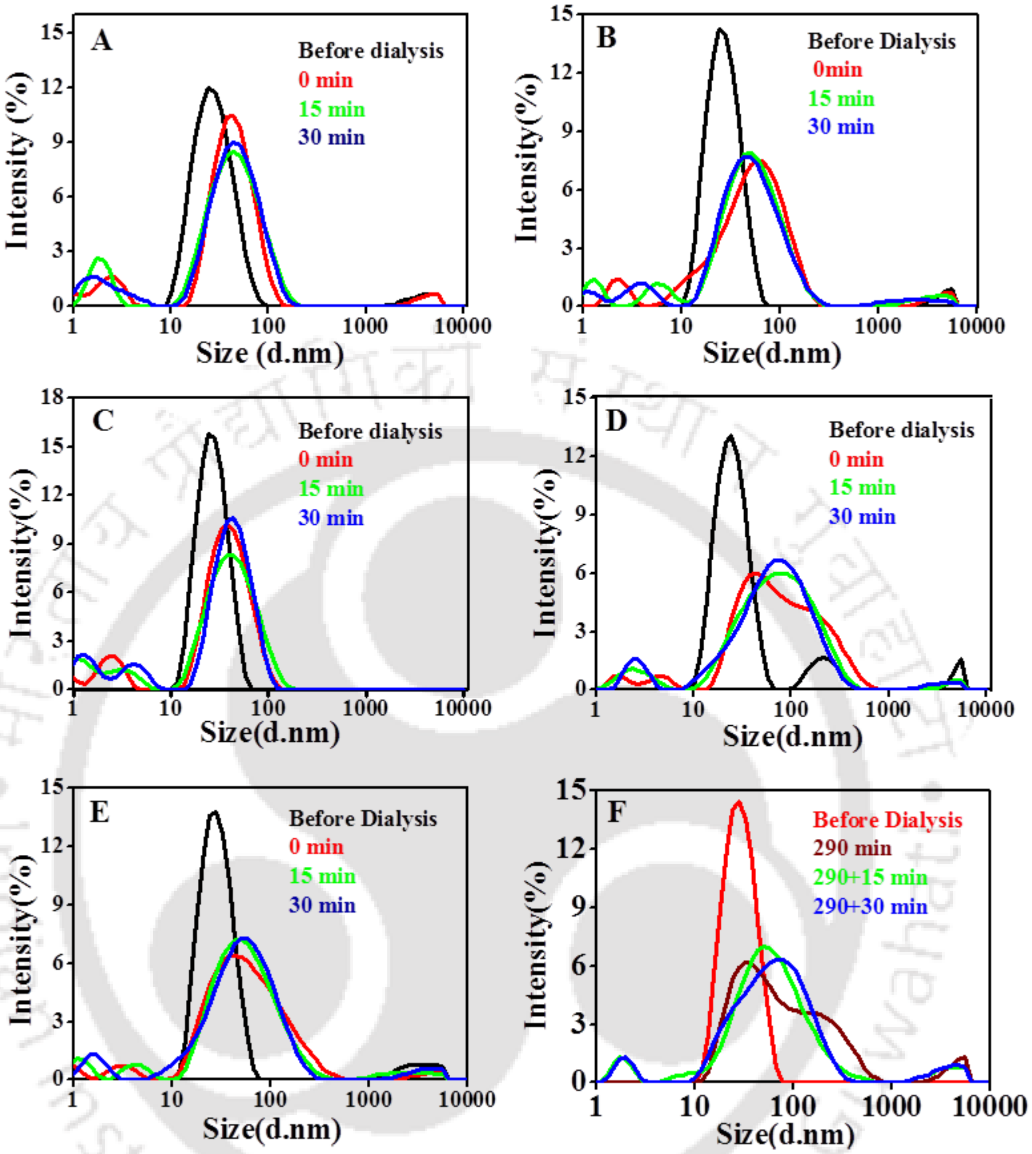

Figure A2.4. Dynamic light scattering (DLS) based particle size distribution of (**A**) 0.62 nM, (**B**) 0.49 nM, (**C**) 0.42 nM, (**D**) 0.39 nM (**E**) 0.32 nM and (**F**) 0.24 nM Cit-Au NP dispersion after dialysis. The samples were dialysed for 260-290 min.

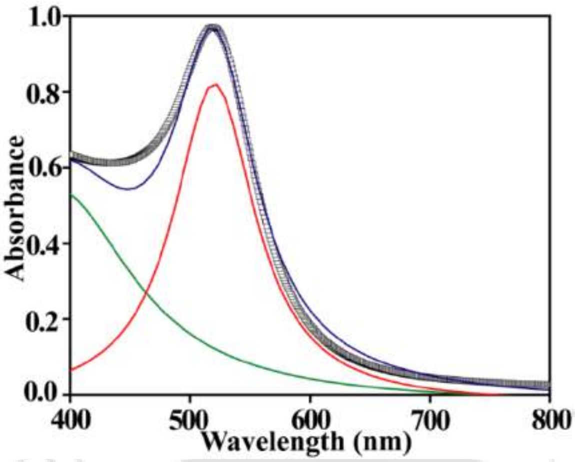

Figure A2.5. Deconvoluted spectral SPR peak of as synthesized Cit-Au NPs. The curve in grey is the experimental curve, one in blue is its Lorentzian fit, one in red represents the primary band and the green curve is the background spectrum.

Table A2.1. Mean rate constant value from experimental spectra and from deconvoluted primary band spectra following integrated rate law. The mean rate constant value is reported from the average of slopes obtained from the characteristic plot as mentioned in below.

From	Integrated rate law	Mean rate constant (min^{-1}) / 10^{-3}
Experimental Spectra	ln(Ext.) Vs t	**0.80 ± 0.56**
Deconvoluted Spectra	ln[*A*] Vs t	**1.58 ± 0.27**

Table A2.2. Mean rate constant value from experimental spectra and from deconvoluted primary band spectra following differential rate law. The mean rate constant value is reported from the average of slopes (from six different sets of data) obtained from the characteristic plot as mentioned below.

From	Differential rate law	Mean rate constant (min^{-1}) / 10^{-3}
Experimental Spectra	Initial Rate Vs Ext$_0$	**0.92 ± 0.35**

Deconvoluted Spectra	Initi	0.34

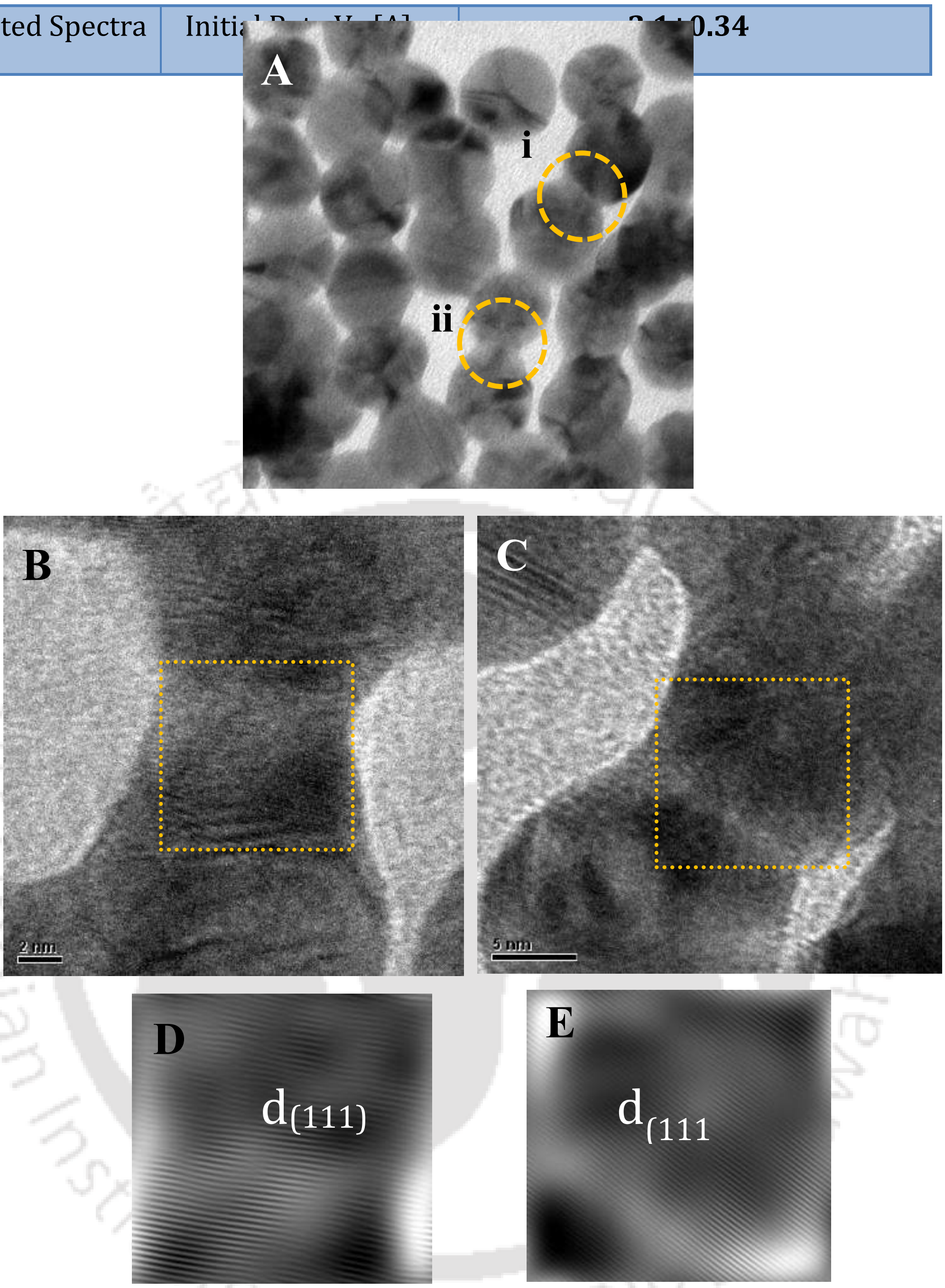

Figure A2.6. (**A**) TEM image of Au NPs recorded from sample collected during time-dependent study at time 30 min, following dialysis showing fused region **i** and **ii** (yellow dotted circle) and agglomeration, (**B**) and (**C**) shows the HRTEM image corresponding to region (**i**) and (**ii**) from figure (**A**), (**D**) and (**E**) are IFFT image from select region in (**B**) and (**C**) respectively.

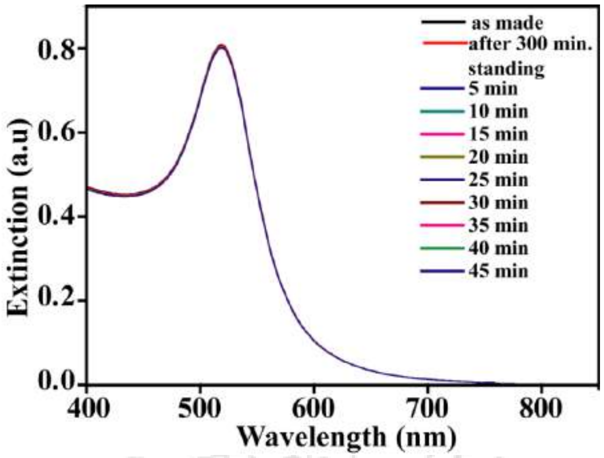

Figure A2.7. Time dependent UV-Vis spectra of Au NP (as made) after allowing it to stand for 300 min.

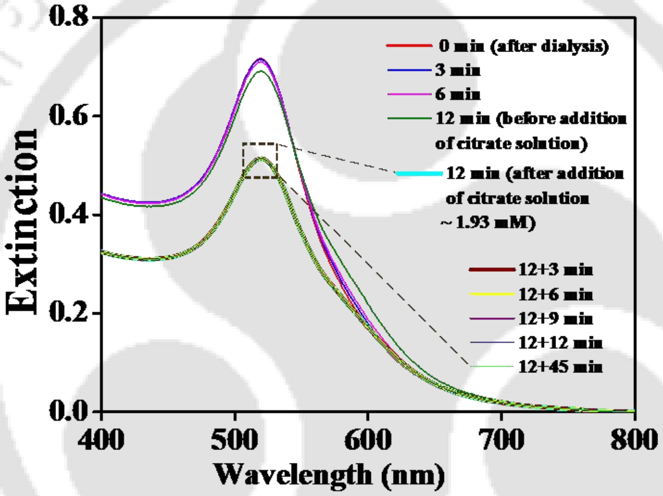

Figure A2.8. UV-Vis spectra recorded following dialysis and addition of tri-sodium citrate solution (~ 1.93 mM) during time dependent study.

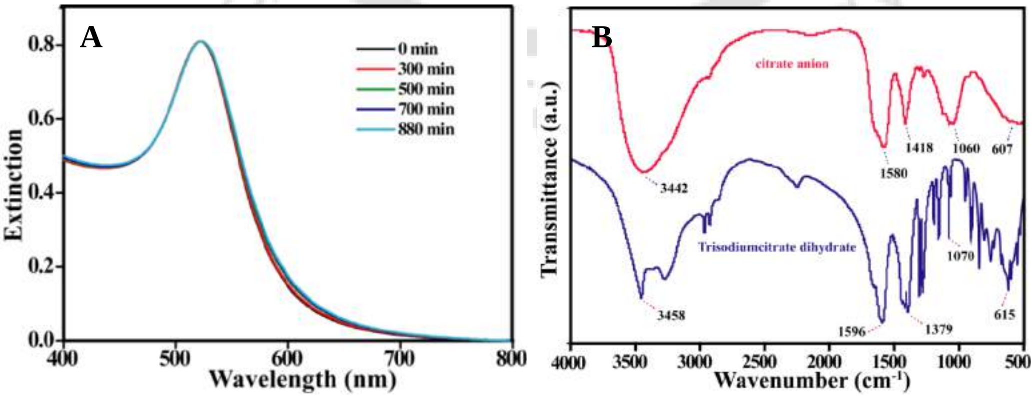

Figure A2.9. (**A**) Surface plasmon resonance (SPR) extinction spectra of as-synthesized Cit-Au NP (with [Au NP] ~0.62 nM) dispersion recorded at different time period during dialysis when dialysed against sodium citrate aqueous solution. (**B**) FTIR spectra of tri-sodium citrate (in dried form) recovered from the water in dialysis chamber after dialysis (red) and pure solid trisodiumcitrate dihydrate (blue).

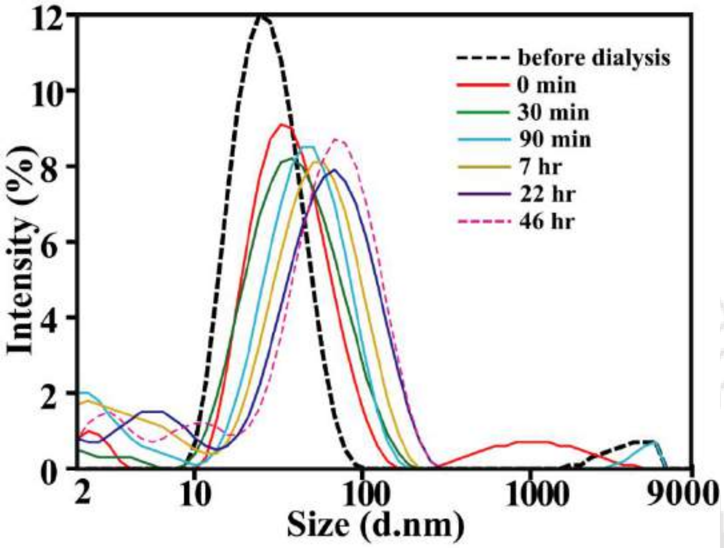

Figure A2.10. DLS based particle size distribution of dialysed Cit-Au NPs recorded during time dependent study and longer time period.

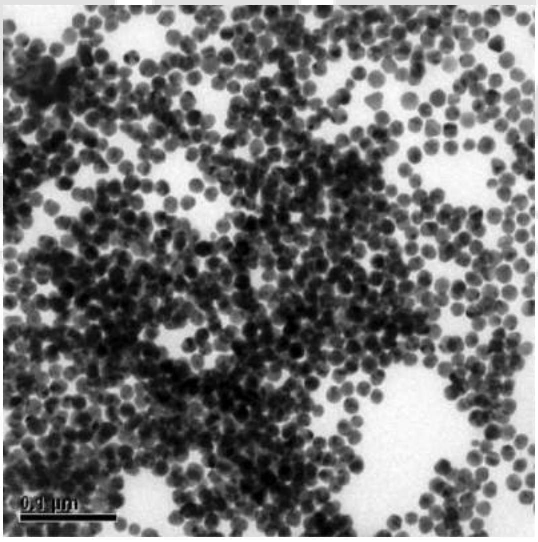

Figure A2.11. TEM image of Cit-Au NPs as taken after 46 h of time-dependent study following dialysis (corresponding UV-Vis spectrum and DLS size distribution shown in **Figure A2.1** and **Figure A2.9** respectively).

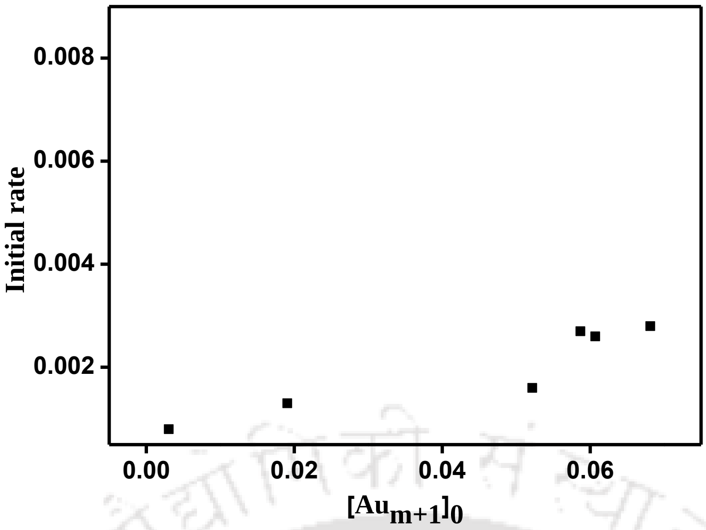

Figure A2.12. Plot of initial rate of agglomerate formation as a function of initial concentration of agglomerate. [Au$_{m+1}$]$_0$ corresponds to the initial concentration of agglomerate $\{Au_{m+1}(citrate)_{x+y}\}^{3(x+y)-}$ that absorbs at 600 nm.

Discussion A2.1

The essential mechanistic steps are as follows:

$$\{Au(citrate)_{x+q}\}^{3(x+q)-} \underset{k_{-cit}^{q}}{\overset{k_{cit}^{q}}{\rightleftharpoons}} \{Au(citrate)_{x}\}^{3x-} + q \times citrate^{3-} \quad K_{eq} = \frac{k_{cit}^{q}}{k_{-cit}^{q}} \qquad \textbf{(A1)}$$

In these reactions, citrate represents citrate^{3-}, q is average number of citrate ions removed from single gold nanoparticle to make it reactive. The above step represents equilibrium of the adsorption and desorption of citrate ions from the surface of the Au NP, which probably occurs during and after dialysis. The overall equilibrium constant will be product of the ratio of rate constants for each individual equilibrium reaction.

The following reaction is the first step towards formation of nucleation sites for formation of aggregated structures and which probably starts during the dialysis and may continue during the kinetic study period.

$$\{Au(citrate)_{x}\}^{3x-} + \{Au(citrate)_{x}\}^{3x-} \xrightarrow{k_1} \{Au_2(citrate)_{2x}\}^{3(2x)-} \qquad \textbf{(A2)}$$

Similar reactions may take place in a sequential manner, during the reaction, to give rise to products as below,

$$\{Au(citrate)_x\}^{3x-} + \{Au_{m-1}(citrate)_y\}^{3y-} \xrightarrow{k_{m-1}} \{Au_m(citrate)_{x+y}\}^{3(x+y)-} \quad \textbf{(A3)}$$

$$\{Au(citrate)_x\}^{3x-} + \{Au_m(citrate)_y\}^{3y-} \xrightarrow{k_m} \{Au_{m+1}(citrate)_{x+y}\}^{3(x+y)-} \quad \textbf{(A4)}$$

Here, m means the number of Au nanoparticles in the agglomerate with y meaning the number of citrate attached to the agglomerate. Also, $\{Au(citrate)_x\}^{3x-}$ represents the reactive species involved in reactions with the monomer and its concentration will be in steady state during the course of the reaction (at least in the initial period). The reactant $\{Au_m(citrate)_y\}^{3y-}$, in reaction (**A4**) is unstable and is formed through a sequence of reactions starting from reaction (**A2**) during and after dialysis. Reaction depicted in equation (**A4**) is predominant during the initial period of study. Species on right of reaction (**A4**) is the one that absorbs at 600 nm. All other aggregate species smaller than (m+1) are formed and subsequently consumed in steps preceding this step, and hence can be considered reactive intermediates forming this final state, $\{Au_{m+1}(citrate)_{x+y}\}^{3(x+y)-}$.

Further, bimolecular reaction of two agglomerated structures to give larger aggregated units (**A5**) can also be possible.

$$\{Au_m(citrate)_y\}^{3y-} + \{Au_{m+1}(citrate)_{x+y}\}^{3(x+y)-} \xrightarrow{k^b_{m+1}} \{Au_{(2m+1)}(citrate)_{(x+2y)}\}^{3(x+2y)-}$$

(**A5**)

This reaction will be in competition with reaction (**A2**) above and will predominate only at longer reaction times when [$\{Au(citrate)_x\}^{3x-}$] will be low and [$\{Au_m(citrate)_y\}^{3y-}$] large and will be accompanied by large red shift in the secondary SPR peak, as observed in our results and shown in **Figure A1**.

Following equilibrium equation (**A1**), we write

$$-\frac{d[\{Au(citrate)_{x+q}\}^{3(x+q)-}]}{dt} = k^q_{cit}[\{Au(citrate)_{x+q}\}^{3(x+q)-}] - k^q_{-cit}[\{Au(citrate)_x\}^{3x-}][citrate]^q$$

(**A6**)

Now, considering reactions (**A1**), (**A2**), (**A3**) and (**A4**), we can write,

$$\frac{d[\{Au(citrate)_x\}^{3(x)-}]}{dt} = k_{cit}^{q}[\{Au(citrate)_{x+q}\}^{3(x+q)-}] - [\{Au(citrate)_x\}^{3x-}]\{k_{-cit}^{q}[citrate]^{q} + k_1[\{Au(citrate)_x\}^{3x-}] .... + k_{m-1}[\{Au_{m-1}(citrate)_y\}^{3y-}] + .k_m[\{Au_m(citrate)_{x+y}\}^{-3(x+y)}] + ...\} = 0$$

(A7)

where k_{cit}^{q}, k_{-cit}^{q}, k_1, k_{m-1} and k_m are the rate constant for reactions (**A1**), (**A2**), (**A3**) and (**A4**).

Since the reaction can be considered to be a surface reaction, with the adsorption of the reactive Au NPs onto the surface of larger aggregated units we rewrite the above differential equation as below.

$$\frac{d[\{Au(citrate)_x\}^{3x-}]}{dt} = k_{cit}^{q}[\{Au(citrate)_{x+q}\}^{3(x+q)-}] - [\{Au(citrate)_x\}^{3x-}]\{k_{-cit}^{q}[citrate]^{q} + k_1 n_{Au_1} Area_{Au_1} + ... + k_{m-1} n_{Au_{m-1}} Area_{Au_{m-1}} + k_m n_{Au_m} Area_{Au_m} + ...\} = 0$$

(**A8**)

where n_{Au_m} is the number of $\{Au_m(citrate)_y\}^{3y-}$ agglomerates per unit volume of solution and $Area_{Au_m}$ is the area per unit of the agglomerate of $\{Au_m(citrate)_y\}^{3y-}$ and the rate constant k_j (with j varying from 1 to m), will depend on the reactivity of the surface of the agglomerate $\{Au_m(citrate)_y\}^{3y-}$. Now, the rate constant k_m will depend on the reactivity of aggregate which is expected to decrease with increasing m, since the surface free energy decreases with decreased surface area to volume ratio. On the other hand, the area per agglomerate unit, $Area_m$ will depend on the total surface sites available on the agglomerate structure for the individual $\{Au(citrate)_x\}^{3x-}$ to get attached. Thus $Area_m$ is expected to increase with increasing m. Hence the product of the rate constant and area, i.e. $k_m Area_m$, will have a maximum value for an optimum value of m. In other words, 'm' cannot be too small as then surface area will be too small and 'm' cannot be too large as reactivity will then be too small.

Therefore, steady state concentration of destabilized Au NP from the above expression (**A8**) is,

$$\left[\left\{Au(citrate)_x\right\}^{3x-}\right]_{ss} = \frac{k_{cit}^{q}\left[\left\{Au(citrate)_{x+q}\right\}^{3(x+q)-}\right]}{\left\{k_{-cit}^{q}\left[citrate\right]^{q} + \sum_{j=1}^{m} \mathrm{k}_{\mathrm{j}} n_{Au_j} Area_{Au_j}\right\}}$$

(**A9**)

Equation (**A1**) gives the net rate of consumption of $\left\{Au(citrate)_{x+q}\right\}^{3(x+q)-}$, which at steady state will be

$$\frac{-d\left[\left\{Au(citrate)_{x+q}\right\}^{3(x+q)-}\right]}{dt} = k_{cit}^{q}[\{Au(citrate)_{x+q}\}^{3(x+q)-}] - k_{-cit}^{q}[citrate]^{q}\left[\left\{Au(citrate)_x\right\}^{3x-}\right]_{ss}$$

(**A10**)

$$\frac{-d\left[\left\{Au(citrate)_{x+q}\right\}^{3(x+q)-}\right]}{dt} = \frac{k_{cit}^{q}\left\{\sum_{j} \mathrm{k}_{\mathrm{j}} n_{Au_j} Area_{Au_j}\right\}}{\left\{k_{-cit}^{q}\left[citrate\right]^{q} + \sum_{j=1}^{m} \mathrm{k}_{\mathrm{j}} n_{Au_j} Area_{Au_j}\right\}}\left[\left\{Au(citrate)_{x+q}\right\}^{3(x+q)-}\right]$$

(**A11**)

When [citrate^{3-}] is large, the denominator in equation (**A9**) is dominated by the first term in which case equation (**A10**) reduces to $\frac{-d\left[\left\{Au(citrate)_{x+q}\right\}^{3(x+q)-}\right]}{dt} = 0$, as observed experimentally by stable SPR peak at 520 nm at high citrate concentration (as prepared Au NPs).

On the other hand, as [citrate^{3-}] is lowered (by dialysis), however, the first term in the denominator of equation (**A9**) drops and when two denominator terms in equation (**A11**) become comparable, we may rewrite equation (**A11**) approximately as

$$\frac{-d\left[\left\{Au(citrate)_{x+q}\right\}^{3(x+q)-}\right]}{dt} = \frac{k_{cit}^{q}\left\{\sum_{m} \boldsymbol{k}_j n_{Au_j} Area_{Au_j}\right\}}{2\left\{\sum_{m} \boldsymbol{k}_j n_{Au_j} Area_{Au_j}\right\}}\left[\left\{Au(citrate)_{x+q}\right\}^{3(x+q)-}\right]$$

$$= \frac{k_{cit}^{q}}{2}\left[\left\{Au(citrate)_{x+q}\right\}^{3(x+q)-}\right]$$

(**A12**)

Equation (**A12**) is valid when the 520 nm peak starts diminishing and we find that equation (**A12**) gives a first order decay for $\left\{Au(citrate)_{x+q}\right\}^{3(x+q)-}$ just as we observed experimentally in **Figure 2.1.E** and **Figure 2.6.C**. Integration of (**A12**) gives,

$$\left[\left\{Au(citrate)_{x+q}\right\}^{3(x+q)-}\right]=\left[\left\{Au(citrate)_{x+q}\right\}^{3(x+q)-}\right]_o \exp\left(\frac{-k_{cit}^{q}}{2}t\right)$$

(**A13**)

From reactions (**A3**) and (**A4**) we can write under steady-state approximation,

$$\frac{d[\{Au_m(citrate)_y\}^{3y-}]}{dt}=k_{m-1}[\{Au(citrate)_x\}^{3x-}][\{Au_{m-1}(citrate)_y\}^{3y-}]-k_m[\{Au(citrate)_x\}^{3x-}][\{Au_m(citrate)_y\}^{3y-}]\approx 0$$

Or,

$$\frac{d[\{Au_m(citrate)_y\}^{3y-}]}{dt}=[\{Au(citrate)_x\}^{3x-}]_{ss}\left\{k_{m-1}n_{Au_{m-1}}Area_{Au_{m-1}}-k_m n_{Au_m}Area_{Au_m}\right\}\approx 0$$

(**A14**)

which is possible only if the term inside i.e. $\left\{k_{m-1}n_{Au_{m-1}}Area_{Au_{m-1}}-k_m n_{Au_m}Area_{Au_m}\right\}$ in equation (**A14**) is zero. Here $k_{m-1}Area_{Au_{m-1}}<k_m Area_{Au_m}$ (the product of rate constant and area will increase with increasing m, as discussed above), however $n_{Au_{m-1}}>n_{Au_m}$ (the number of smaller aggregates will be slightly larger than number of larger aggregates per unit volume, as the former require less number of steps (**Reaction A2**) to form than the latter). In other words $\{Au_m(citrate)_y\}^{3y-}$ is an intermediate the concentration of which does not build up but remains in the steady state during the course of reaction.

$\{Au_{m+1}(citrate)_{x+y}\}^{3(x+y)-}$ however, is stable and its concentration grows (i.e. 600 nm peak grows) and is due to the fact that now $k_m Area_{Au_m}>k_{m+1}Area_{Au_{m+1}}$ (as discussed above). Similarly, following equation (**A14**), the rate of formation of number of aggregate species considering surface reaction $\left\{Au_{m+1}(citrate)_{x+y}\right\}^{3(x+y)-}$ is

$$\frac{d[\{Au_{m+1}(citrate)_{x+y}\}^{3y-}]}{dt} = [\{Au(citrate)_{x}\}^{3x-}]_{ss}\left\{k_m n_{Au_m} Area_{Au_m} - k_{m+1} n_{Au_{m+1}} Area_{Au_{m+1}}\right\}$$
$$= +ve$$

.....(**A15**)

The rate of formation of aggregate species $\{Au_{m+1}(citrate)_{x+y}\}^{3(x+y)-}$ from reaction (**A4**) involves surface reactions. It is obvious as stated above that the value of k_m (reactivity) will decrease while $Area_m$ will increase with increasing m, (i.e. the size of the agglomerate). Hence the product $k_m Area_m$ in equation (**A15**) will have a maximum value at some optimum value of m, which will depend on the nature of the NPs, temperature and amount of stabilizer present in the system. This value of m will give the highest overall rate of reaction (**A4**), which in turn will produce $\{Au_{m+1}(citrate)_{x+y}\}^{3(x+y)-}$ with highest rate, and is possibly the species that corresponds to the rapid increase in absorbance at 600 nm. In other words $\{Au_{m+1}(citrate)_{x+y}\}^{3(x+y)-}$ corresponds to a stable agglomerated species, at least on a small time scale of reaction (i.e. before **reaction 5** in becomes dominant), as its reactivity is low compared to the smaller aggregates formed in the previous generation. Thus equation (**A15**) could be rewritten as,

$$\frac{d[\{Au_{m+1}(citrate)_{x+y}\}^{3y-}]}{dt} = \frac{k_{cit}^{q}\left[\{Au(citrate)_{x+q}\}^{3(x+q)-}\right]}{\left\{k_{-cit}^{q}[citrate]^{q} + \sum_{m} \mathrm{k}_{j} n_{Au_j} Area_{Au_j}\right\}} \times \left\{k_m n_{Au_m} Area_{Au_m} - k_{m+1} n_{Au_{m+1}} Area_{Au_{m+1}}\right\}$$

(**A16**)

Like before, we can argue here that the two terms in the denominator of equation (**A16**) are equal and further using results of (**A13**) we may rewrite equation (**A16**) as,

$$\frac{d[\{Au_{m+1}(citrate)_{x+y}\}^{3y-}]}{dt} = \frac{k_{cit}^{q}\left[\left\{Au(citrate)_{x+q}\right\}^{3(x+q)-}\right]_o \exp\left(-\frac{k_{cit}^{q}}{2}t\right)}{\left\{2k_{-cit}^{q}\left[citrate\right]^{q}\right\}} \times \left\{k_m n_{Au_m} Area_{Au_m} - k_{m+1} n_{Au_{m+1}} Area_{Au_{m+1}}\right\}$$

(**A17**)

All terms of right hand side of equation (**A17**), except for the exponent term and the term $\left\{k_m n_{Au_m} Area_{Au_m} - k_{m+1} n_{Au_{m+1}} Area_{Au_{m+1}}\right\}$ can be said to remain constant with time (at least just after dialysis when only 600 nm peak is growing). So we may write,

$$\frac{d[\{Au_{m+1}(citrate)_{x+y}\}^{3y-}]}{dt} = k_{eff} \exp\left(-\frac{k_{cit}^{q}}{2}t\right)\left\{k_m n_{Au_m} Area_{Au_m} - k_{m+1} n_{Au_{m+1}} Area_{Au_{m+1}}\right\}$$

(**A18**)

where

$$k_{eff} = \frac{k_{cit}^{q}\left[\left\{Au(citrate)_{x+q}\right\}^{3(x+q)-}\right]_o}{\left\{2k_{-cit}^{q}\left[citrate\right]^{q}\right\}}$$

(**A19**)

Equation (**A18**) indicates that the initial rate of formation of the aggregate (i.e. at t=0) may be independent of the concentration of the aggregate, and this is possible only if $\left\{k_m n_{Au_m} Area_{Au_m} - k_{m+1} n_{Au_{m+1}} Area_{Au_{m+1}}\right\} = const$. The latter is possible if the size distribution of aggregates remains more or less same at t=0 for different initial concentrations of aggregate (as measured by the initial absorbance at 600 nm, just after dialysis), which is likely in our case. Hence now the initial rate is given by,

$$\left(\frac{d[\{Au_{m+1}(citrate)_{x+y}\}^{3y-}]}{dt}\right)_o = k_{eff}\ const$$

(**A20**)

During the growth of 600 nm peak, the term inside the $\left\{k_m n_{Au_m} Area_{Au_m} - k_{m+1} n_{Au_{m+1}} Area_{Au_{m+1}}\right\}$ in equation (**A18**) can be roughly taken to be constant and then integrating equation (**A18**) within the limits of t=0 to t=t and

$\left[\{Au_{m+1}(citrate)_{x+y}\}^{3(x+y)-}\right]_o$ to $\left[\{Au_{m+1}(citrate)_{(x+y)}\}^{3(x+y)-}\right]_t$ gives

$$\left[\{Au_{m+1}(citrate)_{x+y}\}^{3(x+y)-}\right]_t - \left[\{Au_{m+1}(citrate)_{x+y}\}^{3(x+y)-}\right]_o = k_{eff}\frac{2\left\{k_m n_{Au_m} Area_{Au_m} - k_{m+1} n_{Au_{m+1}} Area_{Au_{m+1}}\right\}}{k_{cit}^q} \times \left\{1-\exp\left(-\frac{k_{cit}^q}{2}t\right)\right\}$$

$$\left[\{Au_{m+1}(citrate)_{x+y}\}^{3(x+y)-}\right]_t - \left[\{Au_{m+1}(citrate)_{x+y}\}^{3(x+y)-}\right]_o = Const\left\{1-\exp\left(-\frac{k_{cit}^q}{2}t\right)\right\}$$

(A21)

which shows that the aggregate (which absorbs at 600 nm) grows as an exponential function with time as observed experimentally.

Of course several gross, but reasonable approximations were made to arrive at equations (**A13**) and (**A21**). Further, 600 nm peak probably includes a set of $\{Au_{m+1}(citrate)_{x+y}\}^{3(x+y)-}$ species and so the experimental results will show a lot of scatter. However, the simple consecutive mechanistic steps proposed here are able to explain the general trend in our observation, which is that the aggregation kinetics is first order with respect to monomer concentration.

Chapter 3: A3

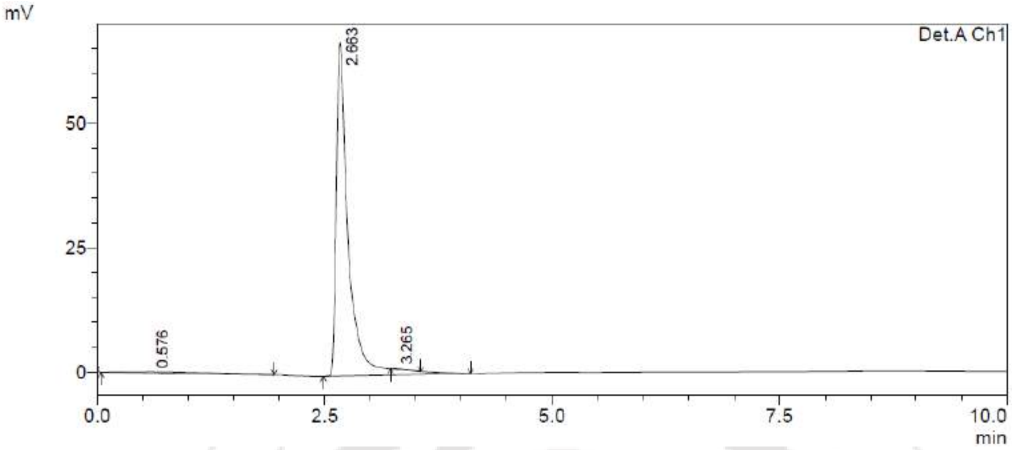

Figure A3.1. A typical standard high performance liquid chromatogram of sodium citrate solution.

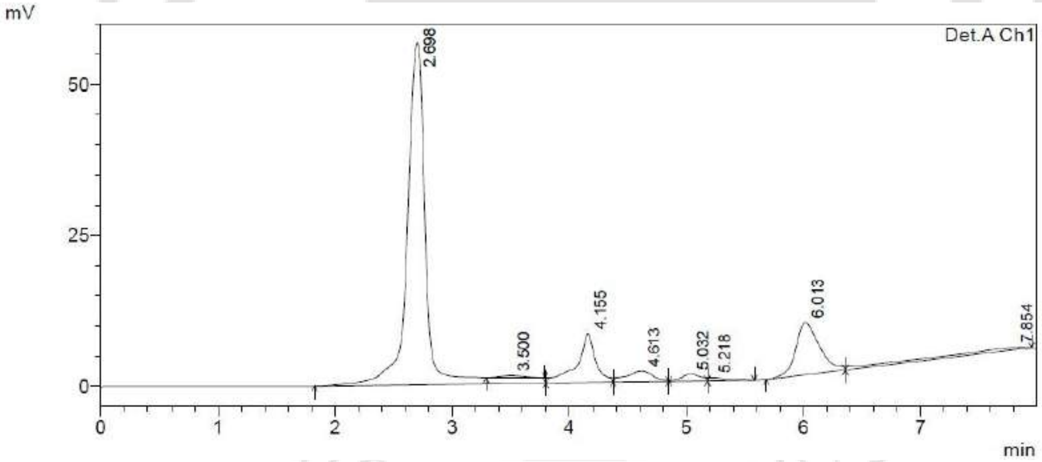

Figure A3.2. A typical high performance liquid chromatogram obtained for citrate corresponding to 1.59 nM Au NP dispersion following dialysis (i.e., in the liquid medium outside the dialysis bag).

Calculation A3.1

Calculation of concentration of as synthesized Cit-Au NP

Concentration of $HAuCl_4$ stock used = 1.72×10^{-2} M

Therefore, number of moles of $HAuCl_4$ in 1.0 mL $HAuCl_4$ stock solution

= Number of moles of $HAuCl_4$ in reaction mixture = 1.72×10^{-5}

Assuming complete reduction, we can write $[HAuCl_4] = [Au]$,

Total number of Au atoms in reaction mixture = $1.72\times10^{-5} \times N_A$ atoms.

For a spherical gold nanoparticle,

$0.74 \times V_{NP} = nV_{atom}$ (Considering packing density of 74.08 % in case of fcc structure)

$$\Rightarrow 0.74 \times \frac{4}{3}\pi R^3 = n\,\frac{4}{3}\pi r^3$$

where V_{NP} = volume of a nanoparticle,

V_{atom} = volume of a gold atom,

n = total number of Au atoms in a nanoparticle,

R= average radius of a gold NP as calculated from TEM measurement =7.5 nm,

r= radius of Au-atom = 0.144 nm.

Therefore, Total number of Au atoms in one NP, $n = 0.74 \times \left(\frac{R}{r}\right)^3$

Number of Au atoms in the nanoparticle dispersion = n×N

where, n= number of Au-atoms in one NP.

N= number of Au NPs in the reaction mixture.

Therefore,

$$N = \frac{N_A \times 1.72 \times 10^{-5}}{0.74 \times \left(\frac{R}{r}\right)^3} = 99086.22 \times 10^9$$

Therefore, concentration of as synthesized gold nanoparticle was obtained as follows:

$$[Au\,NP] = \frac{N}{N_A} = \frac{9.9086\times 10^{13}}{6.023\times 10^{23}} = 1.64\times 10^{-10}\ moles$$

Hence, final concentration of Cit-Au NP was = $\frac{1.64 \times 10^{-10}}{100} \times 1000$

= 1.64×10^{-9} M

= 1.64 nM

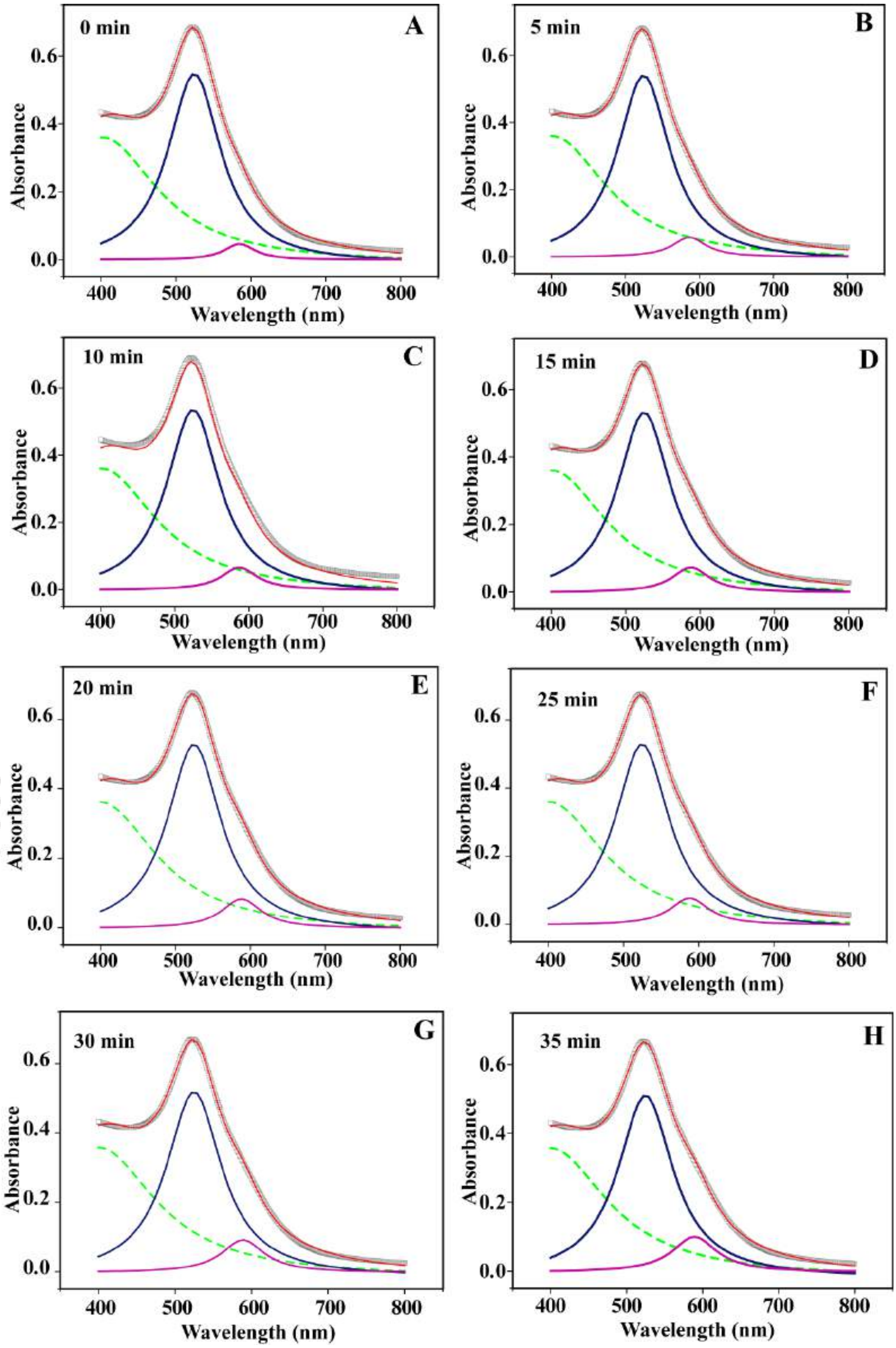

Figure A3.3. Representative deconvoluted spectral band obtained from time-dependent UV-Vis spectra of sample monitored at 40 °C following dialysis of 1.59 nM Cit-Au NPs for 270 min. The curve in grey is the experimentally obtained curve, the one in red is the Lorentzian fit; one in blue and pink are the primary and the secondary deconvoluted band whereas the green (dotted) curve represented the background spectra.

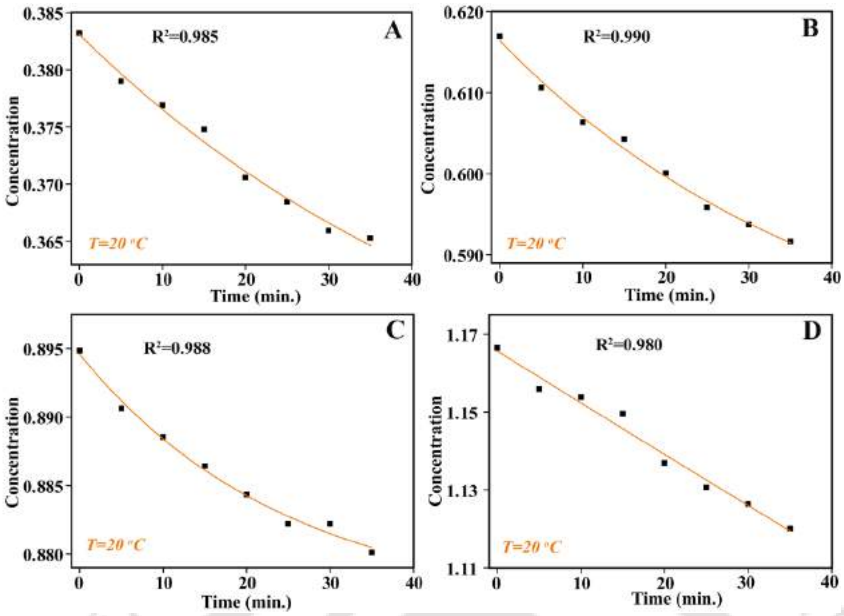

Figure A3.4. Plots of concentration of Au NP (as obtained from the area under the primary deconvoluted band) monitored with respect to time at T = 20 °C. The results were obtained from time-dependent study carried out for dialysed Au NPs with starting concentrations (**A**) 0.51 nM, (**B**) 0.78 nM, (**C**) 1.19 nM and (**D**) 1.59 nM. Data points were fitted to single exponential function for each concentration of Au NP dialysed. The initial rate was extracted from the slope of exponential fitting to the first four data points.

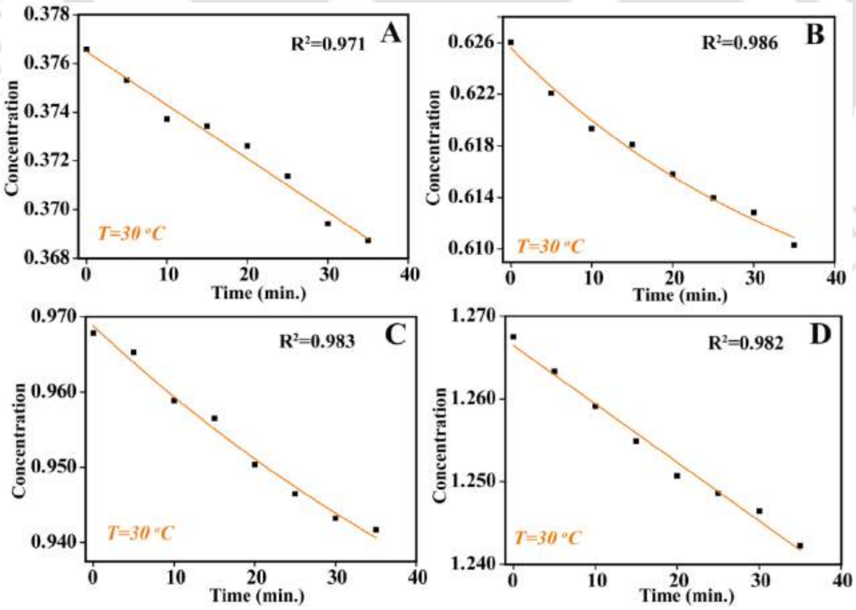

Figure A3.5. Plots of concentration of Au NP (as obtained from the area under the primary deconvoluted band) monitored with respect to time at T = 30 °C. The results were obtained from time-dependent study carried out for dialysed Au NPs with starting concentrations (**A**) 0.51 nM, (**B**) 0.78 nM (**C**) 1.19 nM and (**D**) 1.59 nM. Data points were fitted to single exponential function for each concentration of Au NP dialysed. The initial rate was extracted from the slope of exponential fitting to the first four data points.

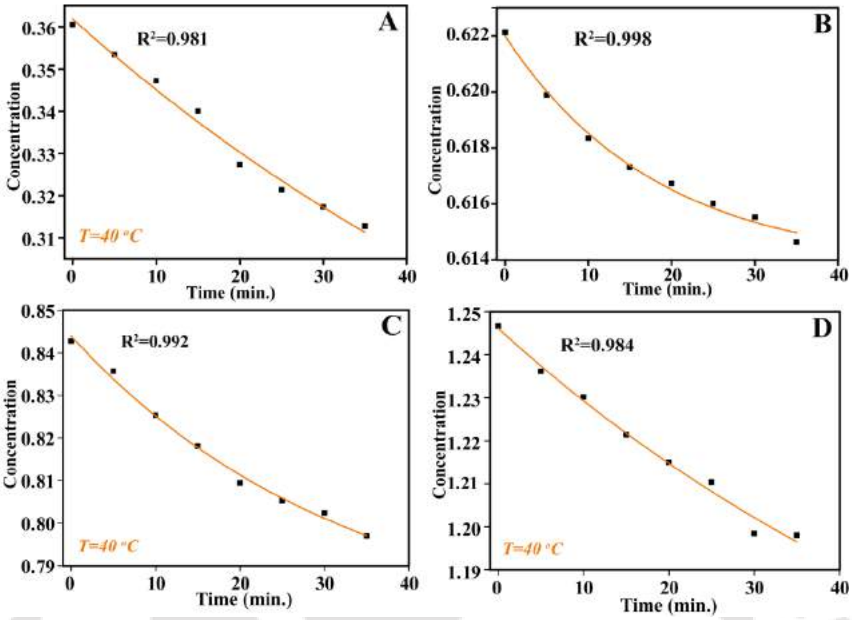

Figure A3.6. Plots of concentration of Au NP (as obtained from the area under the primary deconvoluted band) monitored with respect to time at T = 40 °C. The results were obtained from time-dependent study carried out for dialysed Au NPs with starting concentrations (**A**) 0.51 nM, (**B**) 0.78 nM, (**C**) 1.19 nM and (**D**) 1.59 nM. Data points were fitted to single exponential function for each concentration of Au NP dialysed. The initial rate was extracted from the slope of exponential fitting to the first four data points.

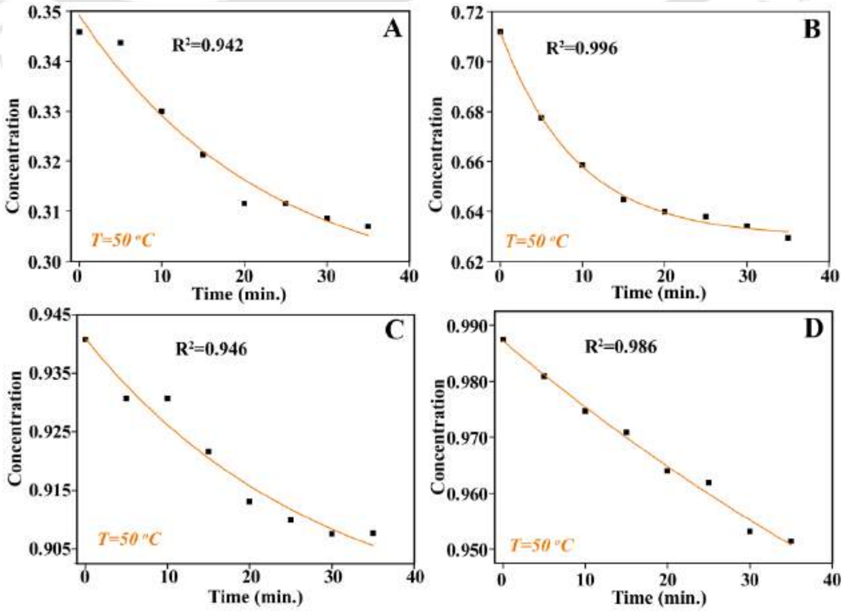

Figure A3.7. Plots of concentration of Au NP (as obtained from the area under the primary deconvoluted band) monitored with respect to time at T = 50 °C. The results were obtained from time-dependent study carried out for dialysed Au NPs with starting concentrations (**A**) 0.51 nM, (**B**) 0.78 nM, (**C**) 1.19 nM and (**D**) 1.59 nM. Data points were fitted to single exponential function for each concentration of Au NP dialysed. The initial rate was extracted from the slope of exponential fitting to the first four data points.

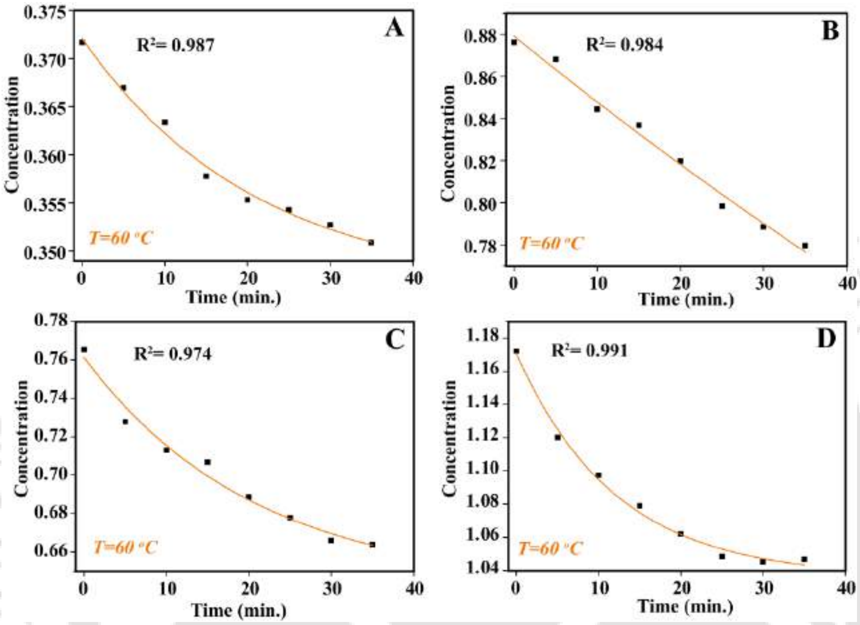

Figure A3.8. Plots of concentration of Au NP (as obtained from the area under the primary deconvoluted band) monitored with respect to time at T = 60 °C. The results were obtained from time-dependent study carried out for dialysed Au NPs with starting concentrations (**A**) 0.51 nM, (**B**) 0.78 nM, (**C**) 1.19 nM and (**D**) 1.59 nM. Data points were fitted to single exponential function for each concentration of Au NP dialysed. The initial rate was extracted from the slope of exponential fitting to the first four data points.

Table A3.1. Table summarizing the amount of citrate removed during dialysis, measured pH and ionic strength calculated for four different concentrations of Cit-Au NPs.

Concentration of Cit-Au NPs (nM)	pH of Cit-Au NP dispersion	Amount of citrate anion removed (mM) after 270 min. of dialysis (calculated with respect to Au NP dispersion inside the dialysis membrane)	% of citrate removed	Ionic Strength (mM), I
1.59	5.99	1.301	76.5	4.296
1.19	5.92	1.173	77.4	3.593
0.78	5.91	0.796	69.9	3.091
0.51	5.87	0.483	56.4	2.902

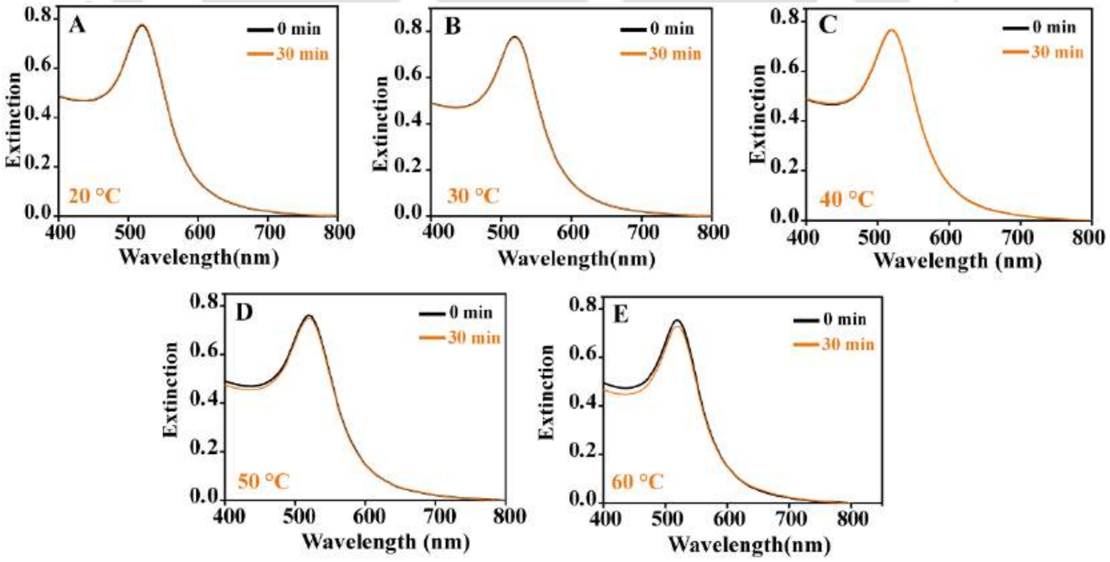

Figure A3.9. Surface plasmon resonance extinction spectra of as synthesized Cit-Au NPs recorded at 0 and 30 min of incubation and at five different temperatures viz. (**A**) 20 °C, (**B**) 30 °C, (**C**) 40 °C, (**D**) 50 °C and (**E**) 60 °C.

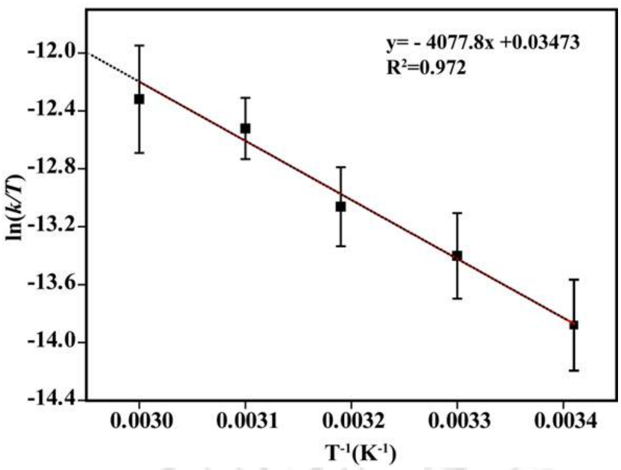

Figure A3.10. Eyring plot of *ln (k/T) versus* T^{-1} plot. Here, *k* refers to rate constant values extracted (following integrated rate method) from the time-dependent study carried out at five different temperature (20 °C, 30 °C, 40 °C, 50 °C and 60 °C) for dialysed 1.59 nM Au NP sample.

Chapter 4: A4

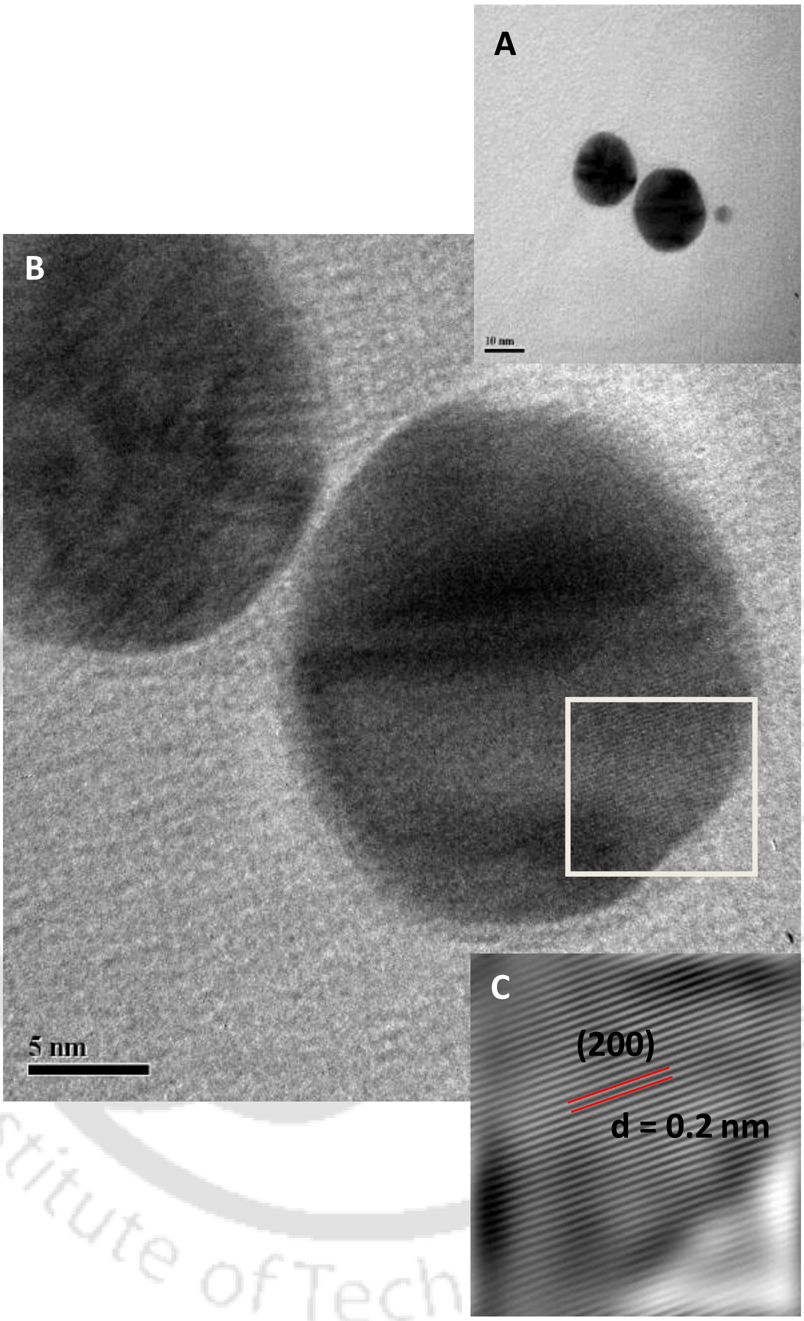

Figure A4.1. (**A**) A typical TEM image of gold nano dimer, (**B**) corresponding HR-TEM image of Au nano-dimer in **Figure A4.1.A**, (**C**) IFFT image obtained from HRTEM analysis of a select region (white box) from **Figure A4.1.A** reveals gold lattice fringes with d-value = 0.2 nm corresponding to (200) plane.

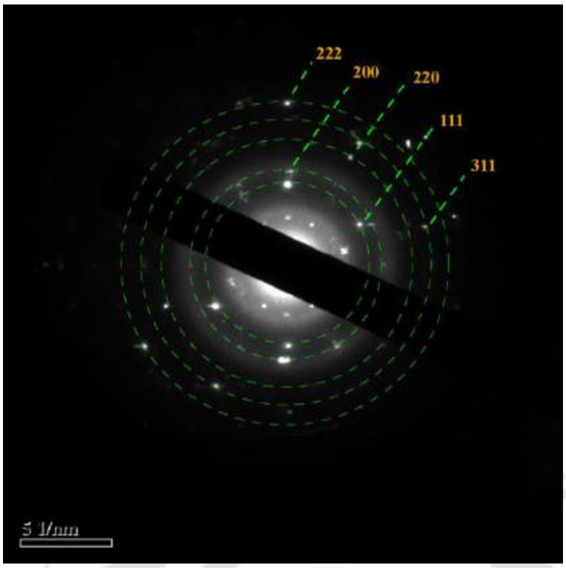

Figure A4.2. SAED pattern obtained from a representative Au nano-dimer showing diffraction corresponding to various planes of gold identified in the image by dotted circles.

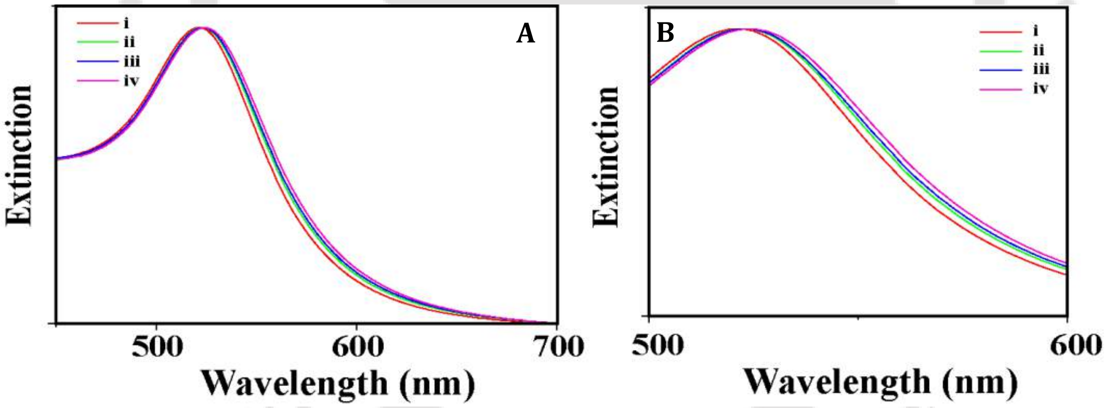

Figure A4.3. UV-vis spectra of (**A**) (**i**) as-synthesized cit-Au NP dispersion and cit-Au NP dispersions at different concentration of complex ($[Eu(phen)_2(MBA)_2]Cl$) - (**ii**) 15 µM; (**iii**) 30 µM and (**iv**) 90 µM respectively, (**B**) expanded view of the UV-vis spectra in the range 500-600 nm showing red-shift and broadening with increasing concentration of metal complex (**ii-iv**) in cit-Au NP dispersion.

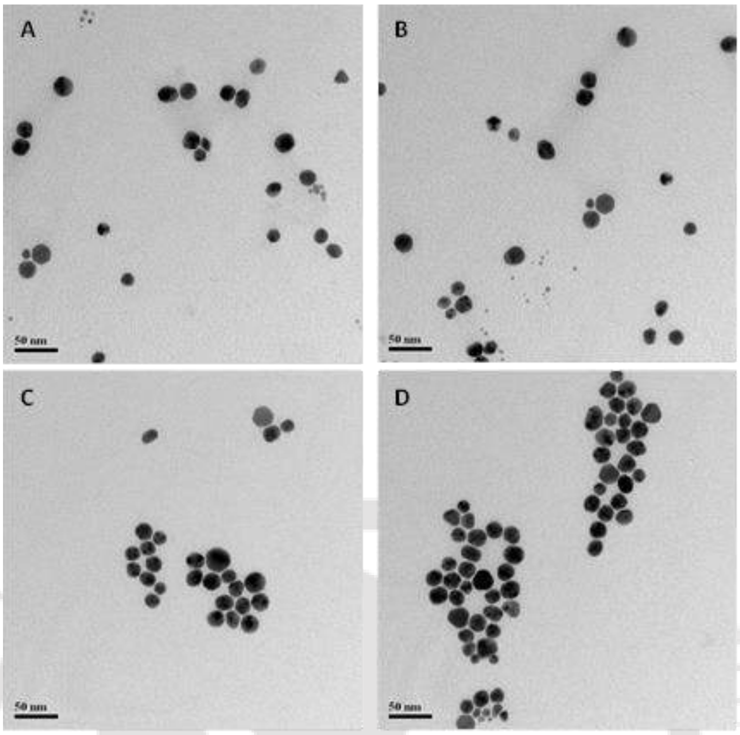

Figure A4.4. TEM images of as synthesised (**A**) and (**B**) Au nano-dimers, (**C**) and (**D**) Au NP discrete assemblies obtained at (**A**) and (**B**) 15 μM; (**C**) and (**D**) 90 μM of [Eu(phen)$_2$(MBA)$_2$]Cl respectively.

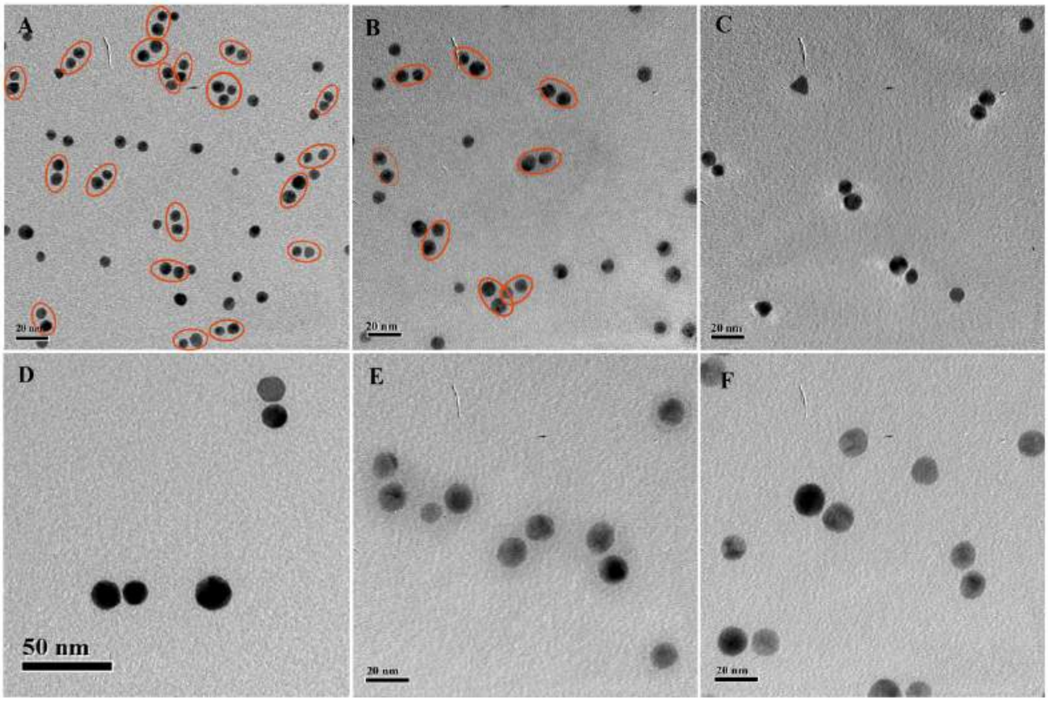

Figure A4.5. Representative TEM images of Au nano-dimer (**A-F**) obtained at complex concentration of 30 μM in cit-Au NP dispersion.

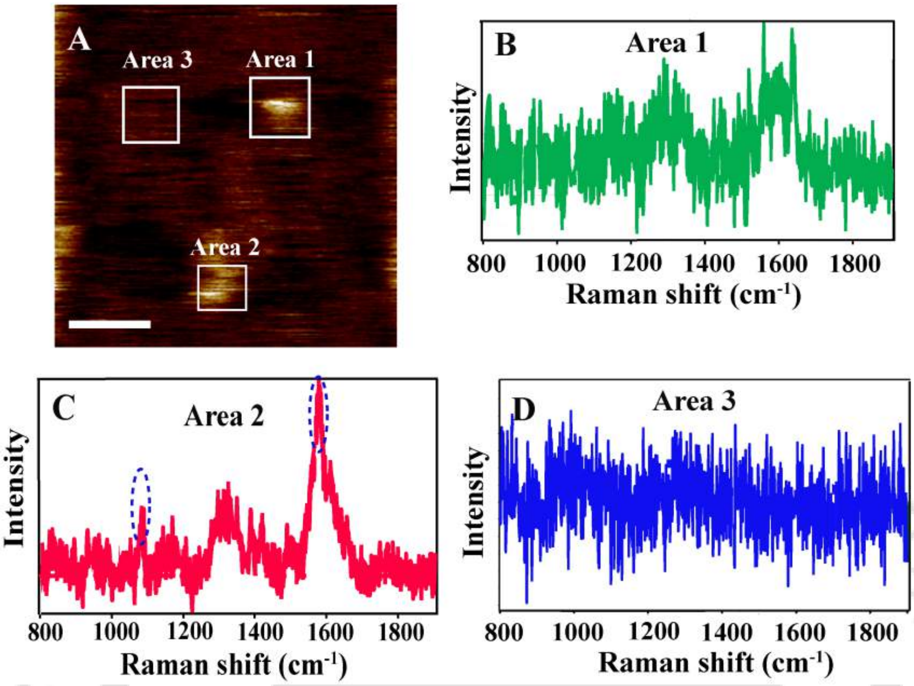

Figure A4.6. (**A**) TF amplitude feedback topograph (scale = 0.15μm) showing representative individual Au NP (area 1), dimeric Au NP (area 2) and corresponding TER spectra as in (**B**) and (**C**) respectively; (**D**) featureless Raman spectrum corresponding to area 3 in **Figure A4.6**.

Discussion A4.1.

In TERS, when a laser is focussed into the tip-apex, a large area encompassing the molecule of interest (positioned in the hot-site of the dimeric structure) is likely to be illuminated due to laser focus spot resulting in the generation of far-field in addition to near-field at the tip-apex. Therefore, far-field Raman signal (SERS) originating from all molecules within the laser spot will always contribute to the total TERS signal. Therefore, overall TERS signal (tip-in) is a cumulative effect of Raman scattering in the near vicinity of the tip (near-field) and from the rest of the laser illuminated area (far-field).

$$\text{TERS signal} = I_{\text{near-field}} + I_{\text{far-field}}$$

However, in case of monolayer or single molecule coverage, the far-field signal is barely noticeable. In that case, the noise level can be considered as an upper bound for the far-field intensity, which would lead to the underestimation of the EF. This clearly suggested that TERS signal enhancement would be more than SERS enhancement.

Now, let us consider various possible geometries for TERS measurements,

(i) An ideal TERS (-only) signal could be obtained when an appropriate laser, is focussed at the metal (preferably Au) tip aligned with the axis of the molecular bond. The enhanced electric field generated at the tip apex would then lead to the high enhancement of Raman scattering of the molecule placed underneath it, provided the field polarisation is aligned with the tip-molecular bond axis.

(ii) Now when the molecule of interest is placed in the junction between tip–metal substrate (molecule adsorbed on metal surface), within close proximity (~1−2 nm), the gap-mode effect between the tip and metal substrate would lead to the largest field enhancement,[A3] the Raman scattering intensity of which would be significant.

(iii) Now, let us consider a molecule positioned in the hot-spot between two plasmon active metal nanoparticles (Au) as is the case in our study, then tip-induced Raman enhancement would depend on the polarisation of vibrational bonds of the molecule with respect to the coupled particle surface and that of tip. If it is aligned such that the vibrational mode is polarized along the direction perpendicular to the axis joining the two nanoparticles and thus parallel to the tip then the enhancement can be expected (in an ideal scenario) to be maximum with little reduction in enhancement would be found for the tilted geometry of the same. Additionally, there can be redistribution of hot spots in the presence of the tip as interaction between fields generated by the tip and each nanoparticle may also become part of the system (**Figure A4.7**). Thus the enhancement at the hot-spot in the presence of the tip would be more complex than simple interaction between the field generated by the tip and the molecular bond. In a side illumination geometry, the direction of field polarization is found to be nearly parallel to the tip axis. Therefore, in addition to above mentioned factor, the enhancement due to the tip will depend upon the alignment of the metal complex positioned in the hot-spot of dimeric nanostructure with respect to the tip-axis. Thus, despite redistribution of the plasmon enhanced electric field generated at the tip sample junction one can still consider the overall enhancement as to have occurred in the presence of the tip.

However, the actual field enhancement depends upon many other factors, which include tip-size, tip material, tip radius, tip-sample distance, tip-sample alignment and dielectric properties of the probe molecule. In addition, laser focus aberration may also lead to a decrease in near field signal while leaving the spectral background maximum. Thus considering all the above factors, TERS enhancement factor of 10^4 can be considered as lower bound value.

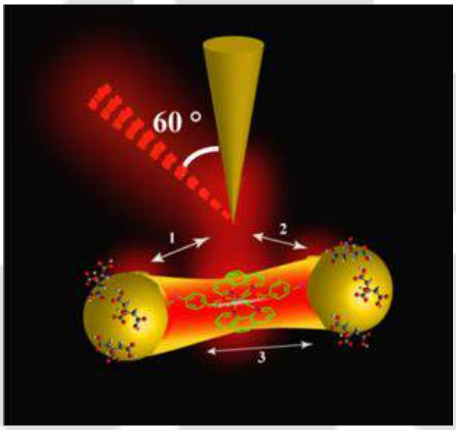

Figure A4.7. Plausible schematic showing the side illumination geometry in TERS set-up and the redistribution of hot-spot upon tip approach to the sample (metal complex ligated Au nano-dimer).

However, the actual field enhancement depends upon many other factors, which include tip-size, tip material, tip radius, tip-sample distance, tip-sample alignment and dielectric properties of the probe molecule. In addition, laser focus aberration may also lead to a decrease in near field signal while leaving the spectral background maximum. Thus considering all the above factors, TERS enhancement factor of 10^4 can be considered as lower bound value.

This is in contrast to SERS enhancement factor of 10^9 which is calculated from signals derived from an ensemble average of large number of molecules (metal complex positioned in a hot spot) for diffraction limited laser focus. SERS signal arises from enhanced electric field at the hot-spot due to the coupled plasmon arising out of dimeric Au nanostructures for incident light polarised along the dimer axis considering top illumination geometry. Additionally, polarization of the vibrational modes normal to the metal surface plane would also lead to the preferential enhancement.

Chapter 5: A5

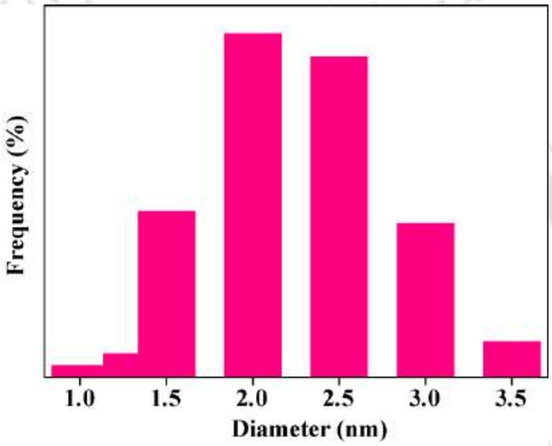

Figure A5.1. Particle size distribution of as synthesized CuNCs at pH 4.5.

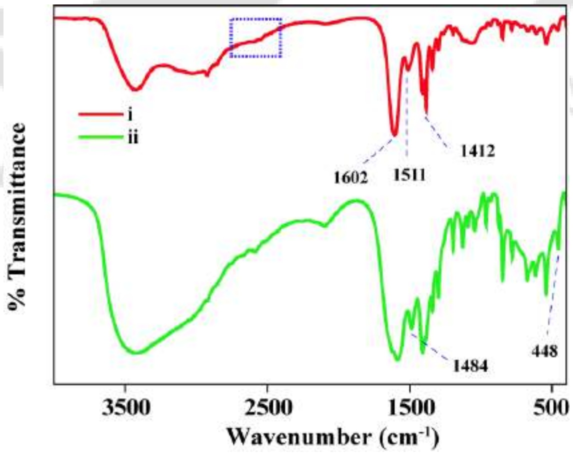

Figure A5.2. FTIR spectra of as synthesized CuNC at (**i**) pH 4.5 and that recorded after the dispersion was aged for 6 h at (**ii**) pH 7.4.

Discussion A5.1

The broad band in the range 3400 cm^{-1} (**Figure A5.2.**(**i**)) could be attributed to stretching vibration of –NH$_2$ and –OH group of the capping ligands along with the indication of intermolecular H-bond, which overlaps with each other.**[A4]** The sharp peak appearing at 1602 cm^{-1} corresponds to COO$^-$ asymmetric stretching vibrationwhich overlaps with amide II (N-H stretch) vibration whereas that at 1412 cm^{-1} represents the symmetric stretch of the –COO$^-$ group. Further vibrational band due to protonated amine group of chitosan that appears at ~ 1530 cm^{-1} showed a blue shift to 1511 cm^{-1}, which clearly evidenced its interaction with the carboxylate anion of the cysteine via H-bond.**[A5,A6]** Simultaneously, disappearance of –SH stretching band at 2548 cm^{-1} also gave evidence of the cysteine ligation with the copper centre through the thiol moiety at pH 4.5.**[A7]**

Further, FTIR spectra recorded for CuNC dispersion at pH 7.4 indicated peak broadening in the range 1630-1330 cm^{-1}. The peak broadening was accompanied by shift of amine bending vibration (δ_{NH2}) to lower frequency range – characterized by the vibrational band at 1484 cm^{-1}, which is indicative of secondary interaction of amine group at pH 7.4.**[A5]** This was validated from the appearance of a sharp absorption peak at 448 cm^{-1} assigned to Cu-N stretching vibration.**[A8]**

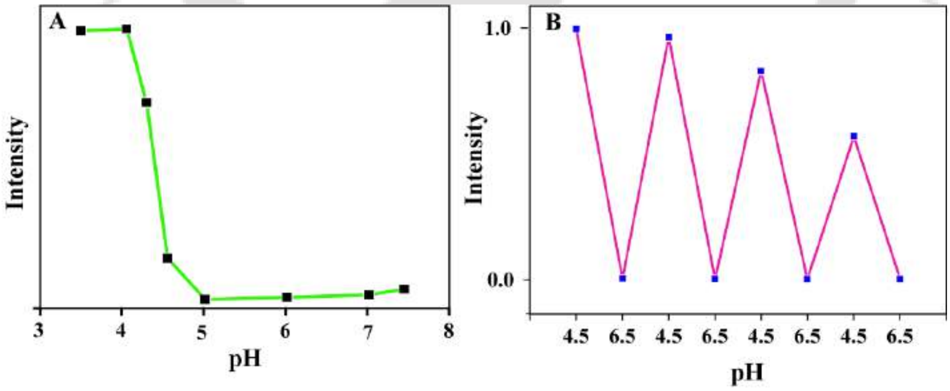

Figure A5.3. (**A**) Plot of change in luminescence intensity of CuNCs at 615 nm at different pH values, (**B**) reversible pH dependent emission of as synthesized CuNCs between pH 4.5 and 6.5 carried out for 4 consecutive cycles.

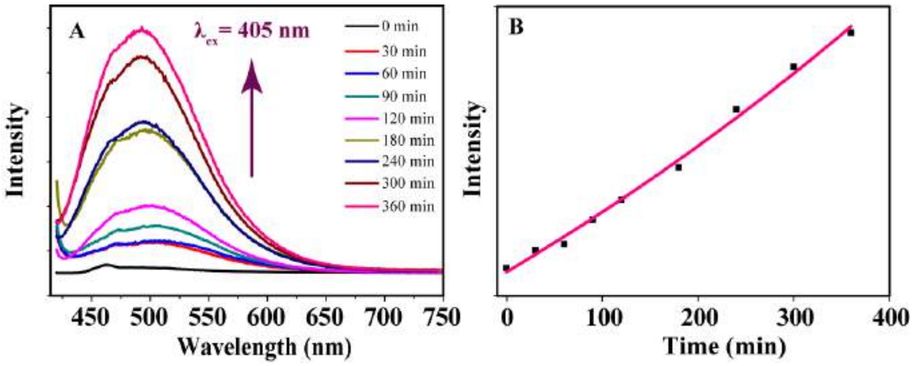

Figure A5.4. (**A**) Time-dependent change in PL spectra of as-synthesized CuNCs recorded at pH 7.4 showing AIE feature when monitored at excitation wavelength 405 nm, (**B**) Plot of change in emission intensity at 500 nm as recorded in **Figure A5.4** with respect to time.

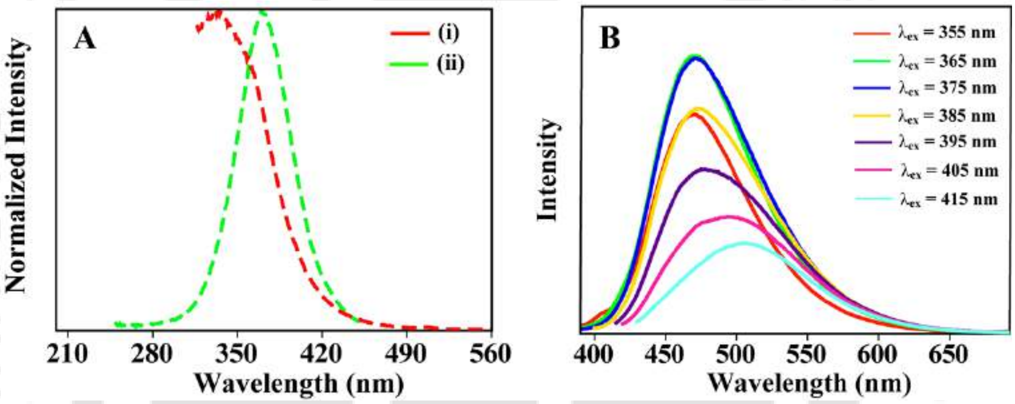

Figure A5.5. (**A**) PL excitation spectrum of as synthesized CuNCs at (**i**) pH 4.5 and that at (**ii**) pH 7.4, (**B**) Excitation tunable emission spectra of CuNCs obtained after aging at pH 7.4 for 6 h. Excitation wavelength values are represented in the legends.

Table A5.1. Time dependent change in hydrodynamic diameter (d_H) and zeta-potential of CuNC dispersion at pH 7.4.

Time (h)	d_H (d.nm) at pH 7.4	Zeta potential (mV) at pH 7.4
0	883.33±69.86	-9.01±0.34
3	593.33±130.40	-18.60±1.30
6	303.66±86.90	-23.50±1.05

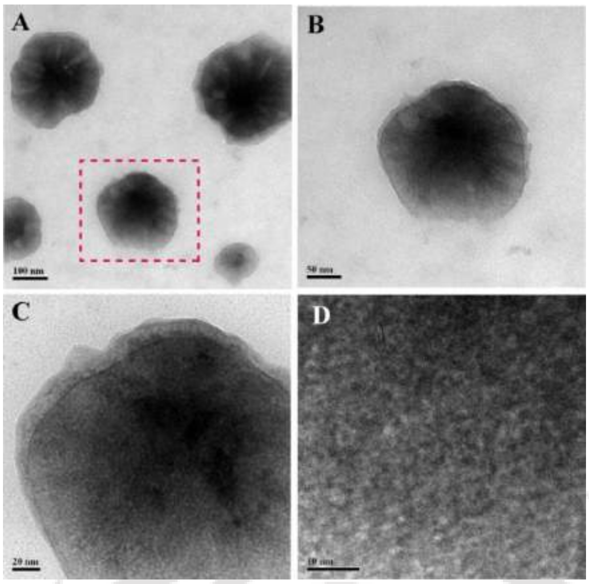

Figure A5.6. (**A**) Representative TEM image of CuNCs obtained after aging the dispersion at pH 7.4 for 4 h, (**B-D**) Differently magnified view of a selected aggregated structure from **Figure A5.6.A**. **Figure A5.6.C** and **D** clearly shows CuNCs clustered together.

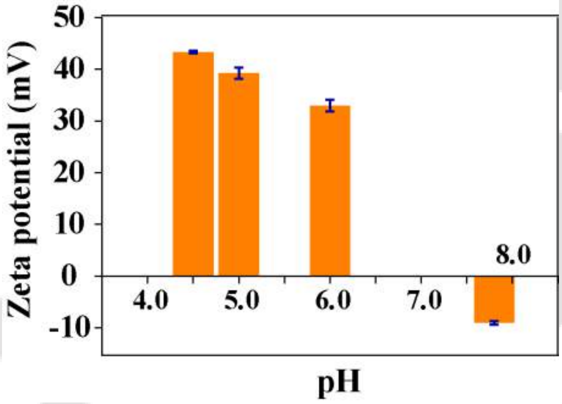

Figure A5.7. Plot of zeta-potential of as synthesized CuNC dispersion at different pH.

Table A5.2. Zeta potential of CuNC dispersion at various pH values.

Size	Zeta potential
4.5	43.3±0.26
5	39.2±1.10
6	32.9±1.13
7.4	-9.01±0.34

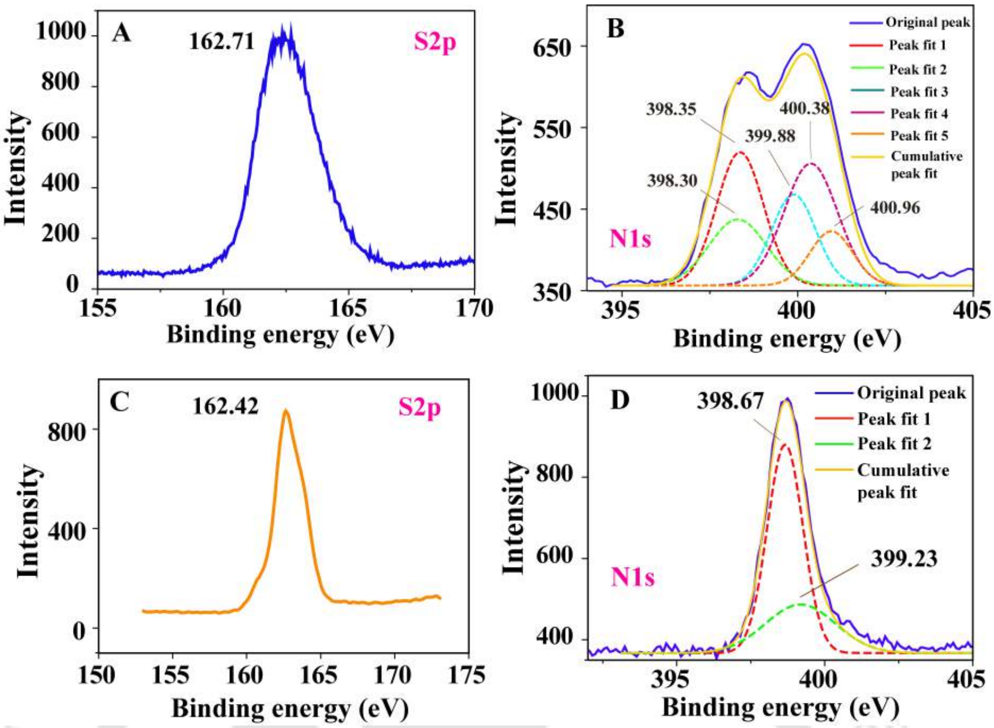

Figure A5.8. (**A**) S2p and (**B**) N1s XPS core spectra obtained at pH 4.5 whereas (**C**) and (**D**) represents S2p and N1s XPS core spectrum respectively obtained for CuNC dispersion after pH adjustment at 7.4.

Discussion A5.2

XPS analysis was carried out to determine the oxidation state of copper and gain further insight into chemical and surface properties of the as prepared CuNCs at pH 4.5 and then at pH 7.4. XPS analyses clearly revealed the presence of expected elements C, N, S, O and Cu in the sample at pH 4.5 as well as 7.4 (**Figure 5.5.B**). Further core level spectra of each of these elements present in the CuNCs at pH 4.5 and pH 7.8 were recorded, as shown in **Figure A5.8.**(**A-B**) and **Figure A5.8.** (**C-D**) respectively. Cu_{2p} XPS spectrum obtained in **Figure 5.5.C** and **D** at pH 4.5 and 7.4, respectively, showed two sharp peak appearing at 951.9 eV and 932.2 eV assigned to copper $2p_{1/2}$ and $2p_{3/2}$ levels thus clearly indicating the existence of copper in Cu(0) or Cu(+1) state. Further, the absence of any satellite peak at 942 eV in both indicated the absence of Cu(II) in the dispersion.[A9] A broad binding energy (B.E) peak appearing at 162.71 eV, corresponding to $S2p_{3/2}$ state at both the pH, indicated the existence of metal-thiolate bond (**Figure A5.8.A** and **C**).[A7] Further, deconvolution of N_{1s} core spectrum obtained for CuNCs at pH 4.5 showed multiple peaks as shown in **Figure A5.8.B**. The B.E. peak at 400.38 eV and 400.96

eV can be attributed to NH_3^+ (protonated amines) and H-bonded protonated amines, respectively.[A5,A10] On the other hand, peak at 399.88 eV and that at 398.30 eV and 398.35 eV were assigned to –N–C=O (amide) of chitosan and amine group involved in H-bond ($-NH_2\cdots O$).[A5,A11] Interestingly, B.E. peak at 400.96 eV, 400.38 eV and 398.35 eV observed in the deconvoluted spectrum corresponding to NC dispersion at pH 4.5 disappeared in the N_{1s} core spectrum obtained at pH 7.4. However, N_{1s} core spectrum at pH 7.4 (**Figure A5.8.D**) was dominated by a sharp narrow peak at 398.61 eV strongly indicating the presence dative co-ordination of amine group with the metal core along with a weak peak appearing at 399.23 eV corresponding to –N–C=O (amide) of chitosan.[A5,A12]

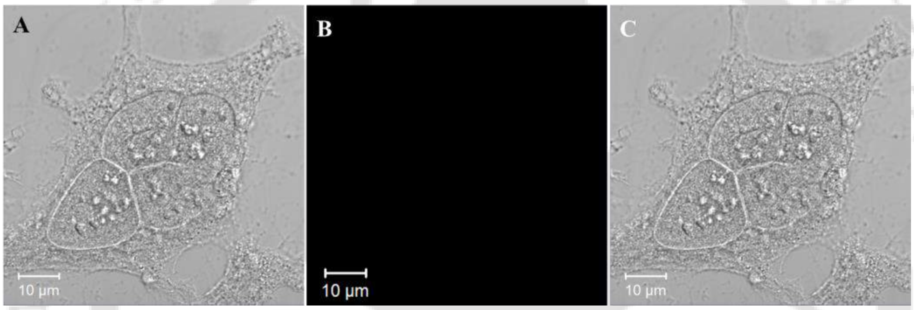

Figure A5.9. CLSM images of a typical MCF-7 cell treated with NC probe for 1 h. (**A**) Bright field image, (**B**) fluorescence image showing no signal under laser excitation of 488 nm in the green channel and (**C**) merged image of (**A**) and (**B**).

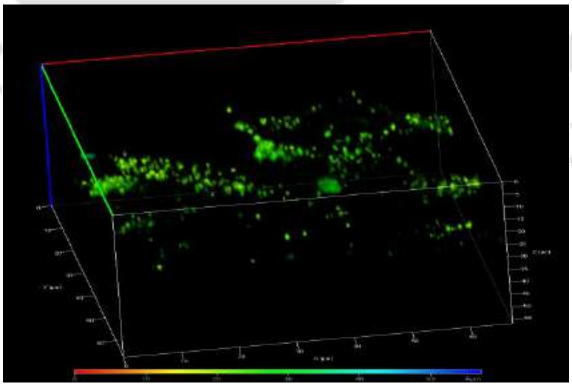

Figure A5.10. Depth projection of a typical CLSM image of MCF-7 cells obtained in **Figure 5.8.A** showing the cellular internalization

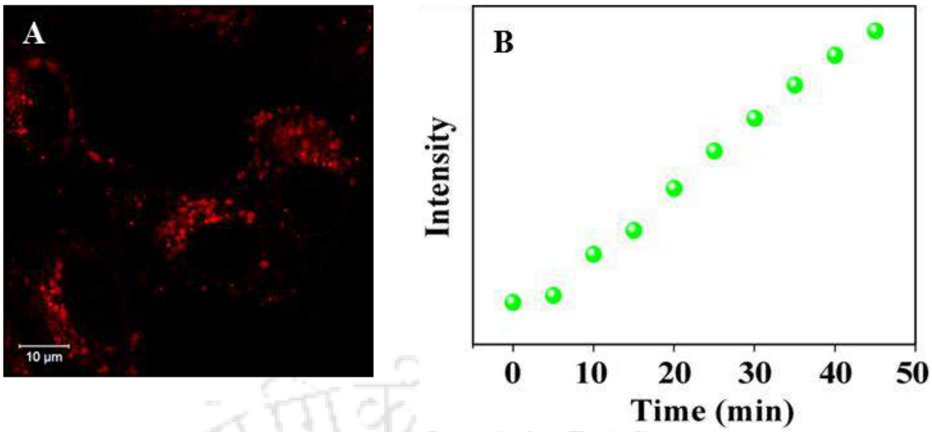

Figure A5.11. (**A**) CLSM image of MCF-7 cells recorded after 30 min incubation with CuNC probe (0.144 µg/mL) at pH=4.5 (culture medium) prior to time - dependent live cell imaging at pH 7.4. (**B**) Plot of intracellular fluorescence intensity obtained from selected region of interest (white solid box) shown in **Figure 5.9** with respect to time.

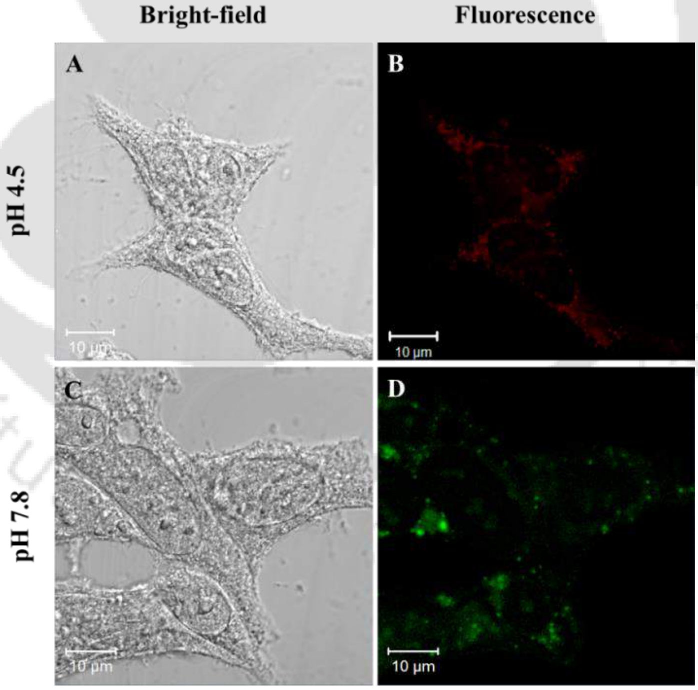

Figure A5.12. CLSM images of HEK-293 cells treated with NC probe for 1 h at pH 4.5 culture media. (**A**) Bright field image and (**B**) fluorescence image acquired in red channel; (**C**) Bright field image and (**D**) fluorescence image acquired in green channel of HEK 293 cells treated with NC probe for 1 h at pH 7.4 culture media. Excitation source: 405 nm laser; images were acquired using 63× oil immersion objective.)

Table A5.3. Rate constant value obtained from time dependent AIE kinetics carried out for as synthesized CuNC and that in presence of BSA and lysozyme. Kinetic constant values were obtained from the slope of integrated rate equation plot. The mean value calculated from the average of slope obtained from integrated rate equation plot is reported.

Sample	Rate constant (min^{-1})
CuNC	$(6.86 \pm 0.70)\times10^{-3}$
CuNC+ BSA	$(8.92 \pm 0.76)\times10^{-3}$
CuNC+Lyz	$(1.35 \pm 0.22)\times10^{-2}$

Chapter 6: A6

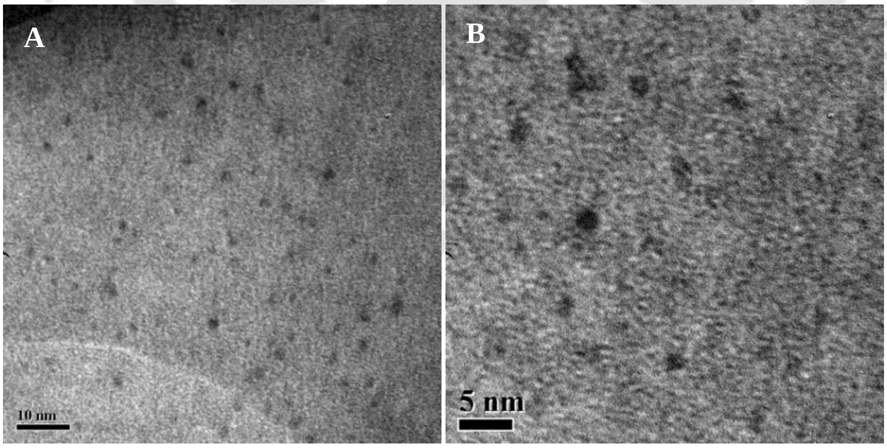

Figure A6.1. TEM image of as synthesized BSA stabilised Au NC at (**A**) low and (**B**) high magnification.

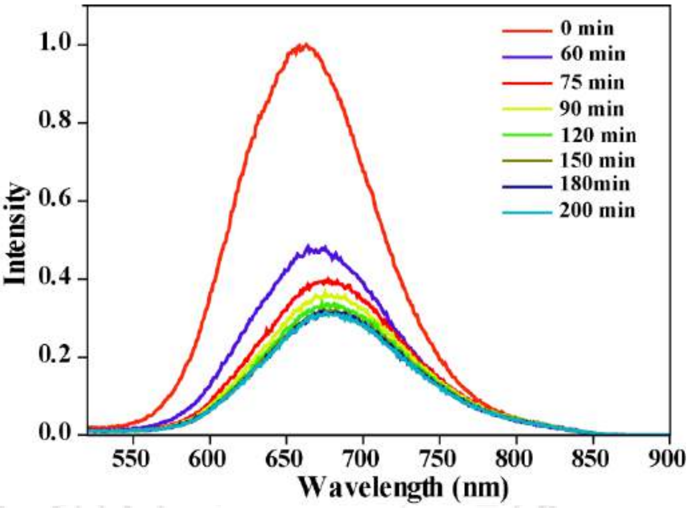

Figure A6.2. Time dependent PL spectra recorded for BSA-Au-NC dispersion incubated with Proteinase K at 37 °C in phosphate buffer at different time interval of incubation as mentioned in legend. Experimental results demonstrated very minute drop in PL intensity beyond 90 min of incubation, reaching a saturation at the end of 120 min. However, slight drop in PL intensity during longer time duration (120 min and beyond) could be due to aerial oxidative quenching in absence of BSA shell.

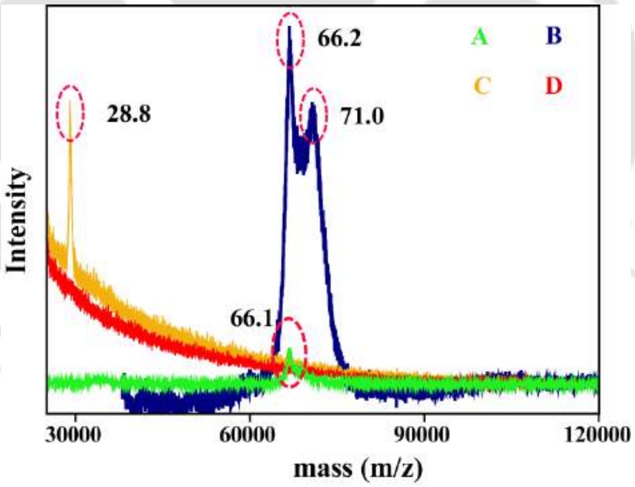

Figure A6.3. Matrix-assisted laser desorption ionization – time of flight (MALDI-TOF) mass spectra of (**A**) BSA only, (**B**) BSA-Au-NC only, (**C**) BSA-Au-NC after digestion with Proteinase K and (**D**) zinc acetate treated digested BSA-Au-NC (Au-NC-$Zn_3(PO_4)_2$).

Table A6.1. Decay parameters of BSA-Au-NC before digestion and following digestion, when excited with laser at 375 nm.

Decay parameters of the BSA-Au-NC, digested NC and Au-NC-$Zn_3(PO_4)_2$ (liquid dispersion and solid powder) are tabulated in **Table A6.1**. Decay curves were fitted using tri-exponential fit function achieving χ2 ~ 1. We then report the intensity-averaged lifetime (τ_{av}) as tabulated in **Table A6.1** using the equation as below,

$$\tau_{\text{av}} = \frac{\sum_i \alpha_i \tau_i^2}{\sum_i \alpha_i \tau_i}$$

where, α_i and τ_i are the pre-exponential factors and excited-state luminescence decay time of the *i*-th species, respectively.

Sample	**A_1 (%)**	**τ (ns)**	**A_2(%)**	**τ (ns)**	**A_3(%)**	**τ(ns)**	**τ_{av}(μs)**
BSA-Au-NC	0.93	5.71	5.93	205.59	93.14	1512.4	1.50
Digested BSA-Au-NC	1.61	2.88	9.65	135.47	88.73	1004.3	0.99
Au-NC-$Zn_3(PO_4)_2$(liquid)	1.56	4.68	15.07	226.45	83.36	1229.5	1.19
Au-NC-$Zn_3(PO_4)_2$(solid)	4.89	25	37.65	250.68	57.46	1343	1.22

Discussion A6.1

Formation mechanism of Au-NC-$Zn_3(PO_4)_2$ by TEM study

The first stage of biomimetic crystallization involves the complexation of peptide fragments stabilising the gold NCs with the zinc ions, generating a biological matrix, which serves as a nucleation centre for primary zinc phosphate growth.[A13] Although the exact amino acid residues taking part in the complexation is not known presently, it is speculated that amino acid residues with high zinc binding affinity (e.g, imidazole nitrogen of histidine, carboxylic group from cysteine, arginine, asparatic acid and asparagine residues) might be selectively responsible for primary complexation. The synthesis of Au-NC-$Zn_3(PO_4)_2$ was carried out by sequential addition of zinc acetate solution (300 µL, 68.3 mM) to digested Au-NC dispersion as previously discussed. The growth was monitored by extracting aliquots at different time of [Zn^{2+}] addition and probing them through transmission electron microscopy studies. Initial addition of [Zn^{2+}], (100 µL, 68.3 mM) to the digested Au-NC in phosphate buffer induced a metal mediated irregular crosslinking via electrostatic and coordinative interaction with the protein fragments stabilising the Au-NC cores. This is evident from the TEM image **Figure 6.4.B** recorded after initial addition of 100 µL (68 mM) zinc acetate solution at 4 min of reaction time. This led to partial emission recovery as depicted from **Figure 6.1.B**. Further, successive addition of zinc acetate i.e, 200 µL (68.3 mM) led to additional increase in emission intensity indicative of further reaction of zinc ion with the peptide fragments stabilising the Au-NC cores. TEM image obtained at this stage (8 min) of reaction represented an intermediate metastable phase (no characteristic SAED pattern seen, **Figure A6.4**) with the same surface morphology (**Figure 6.4.D**) as that seen in the initial stage. It was further observed that the size of the structures increased with time and concentration of the zinc salt. This stage marked the first step towards the transformation from amorphous into the thermodynamically stable crystalline phase. This is in accordance with the Ostwald's rule**A14** where a least stable (amorphous) state transformed through an intermediate metastable state by small loss of free energy, before reaching the thermodynamically stable state. At this stage, appearance of white cloudy suspension was observed due to increasing zinc ion concentration in the medium. Hence, final addition of 300 µL of [Zn^{2+}]=68.3 mM lead to a supersaturated state during which thermodynamically stable zinc phosphate decorated with Au-NCs was formed that precipitated out within 20 min of reaction time. TEM image in **Figure 6.4.E** clearly depicted the final morphology of as synthesized Au-NC embedded zinc phosphate taken at 20 min of reaction time. The degree of supersaturation is governed by the metal induced nucleation rate which leads to precipitation. Thus overall process represents a fast transition from amorphous to crystalline state in solution within 20 minutes of reaction time at 27 °C.**A15**

Figure A6.4. Featureless SAED image obtained at 8 min of reaction time after addition of 200 μL, 68.3 mM [Zn^{2+}] to digested Au-NC dispersion.

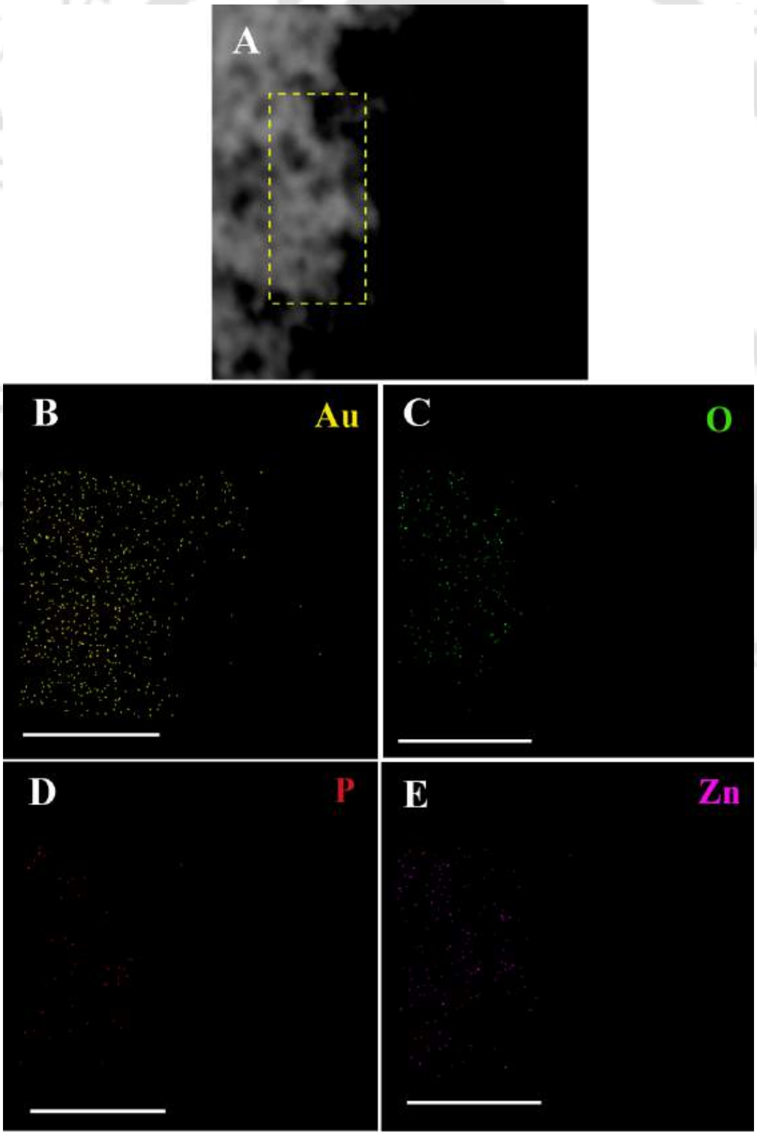

Figure A6.5. (**A**) Dark field scanning transmission electron microscopy (STEM) image of as synthesized Au-NC-$Zn(PO_4)_3$, EDX elemental mapping images (**B**) Au as yellow dots, (**C**) O as green dots, (**D**) P as red dots and (**E**) Zn as purple dots as obtained from STEM image (yellow dotted box) in **Figure A6.5.A**.

Discussion A6.2

Thermogravimetric and Differential Scanning Calorimetric Analysis

The first endothermic region from 79 – 120 °C, can be attributed to loss of physisorbed water at an early stage from 79 – 100 °C followed by first dehydration step forming unstable trihydrate intermediate (due to loss of first crystal water molecule) confirming the existence of β-hopeite phase (**Figure A6.6**). Although no clear gradation was seen for the water loss in TGA curve, a slight drop down at 230 °C marked the complete loss of second water molecule reaching the dihydrate state followed by loss of the rest crystal water.[A16] A weak transition at 375 °C in the TGA curve marked the start of decomposition of peptide fragments from BSA moiety and phosphate groups followed by sharp transition in the temperature range 520-579 °C indicating complete decomposition due to carbonization of organic-inorganic moieties at that temperature range.[A17,A18] Further, DSC thermogram of $Zn_3(PO_4)_2.4H_2O$ polycrystal, clearly distinguished the four step water loss which matched with the characteristic thermogram of β-hopeite. The onset temperature of thermal decomposition appeared at 121 °C (**Figure A6.7**) as evident from DSC thermogram with a broad endothermic peak appearing at 162 °C due to loss of one water molecule, corresponding to an unstable trihydrate structure. This was followed by a sharp peak at 184 °C, corresponding to loss of second molecule of water. Finally the dihydrate to anhydrous state transition was confirmed by appearance of two peak at 223°C and 265°C (**Figure A6.7**) featuring the β-hopeite phase, which is mostly favoured at lower reaction temperature (< 30 °C).[A16]

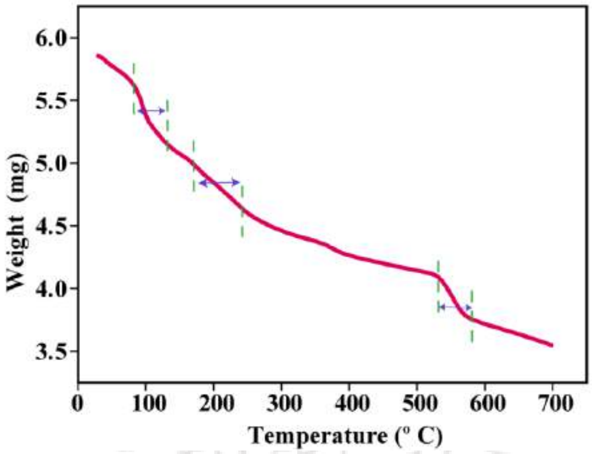

Figure A6.6. Thermogravimetric analysis of Au-NC-$Zn_3(PO_4)_2$.

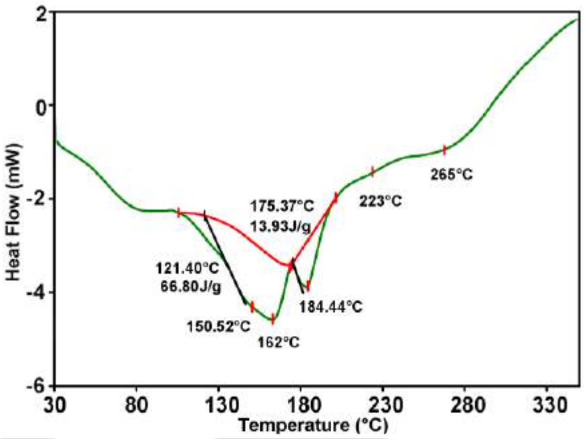

Figure A6.7. Differential scanning calorimetry thermogram of Au-NC-$Zn_3(PO_4)_2$.

Discussion A6.3

FTIR analysis

BSA-Au-NC shows characteristic band at 1632 cm^{-1} (amide I), arising due to $C = O$ stretching vibration along with out of plane $C - N$ stretching vibration. (**Figure A6.8.A**) Band at 1545 cm^{-1} (amide II) corresponds to out- of-phase combination of $N - H$ in plane bend combined with $C - N$ stretching vibration. The peak in the range 1200-1400 cm^{-1} (amide III) is attributed to in-phase combination of $N - H$ bend and $C - N$ stretching vibration (1259.7 cm^{-1}) with minor contribution from $C-O$ in-plane bending.[A19] The band appearing at 1744 cm^{-1} corresponds to $C=O$ stretch of COOH group of amino acids. The band at 1405 cm^{-1} and 1607 cm^{-1} can be assigned to the symmetric stretching mode ν_{str} in COO^- group and aromatic ($C=C$) bond respectively[A20,A21] whereas band at 1450 cm^{-1} can be ascribed to CH_2 bending mode of the alkyl chain in amino acid. (See enlarged view - from a select region in pink dotted box of **Figure A6.8.A**(**i**)) While the peak appearing at 1169 cm^{-1} is assigned to $C-O$ stretch due to tyrosine residues,[A21] a broad band seen in the range 500-850 cm^{-1} and 1000-1120 cm^{-1} is due to N-H bending modes of primary amide. A broad band appearing at 3424 cm^{-1} is ascribed to O-H and N-H stretching vibrations along with peaks in the range 2850-2966 cm^{-1} attributed to C-H stretching vibration.[A22] The IR spectral band obtained after digestion of BSA Au NC showed slight shift in the peak position however, bands remained unaltered with appearance of new peaks in the spectra (**Figure A6.8.A**(**ii**)). The amide (I), (II) and (II) bands are still preserved in the digested Au NC due to restricted cleavage site present in BSA. Interestingly, new peak appeared at 519 cm^{-1}, 935 and 2408 cm^{-1} respectively. The peak arising at 519 cm^{-1} as in **Figure A6.8.A**(**ii**) is due to the disulphide (S-S) bond from cysteine residues present in BSA, stabilising the Au NC core.[A23] The shift in peak position and appearance of new peak can be understood, due to the disruption of protein conformation upon proteolytic digestion altering the α-helix and β-sheet content in BSA moiety. Interestingly, FTIR spectra so obtained for as synthesized AuNC-$Zn_3(PO_4)_2$ appears albeit complex, however band assignment was carried out as follows: **Figure A6.8.B** displayed band at 1648 cm^{-1}, 1553 cm^{-1} and in the range 1200-1400 cm^{-1}which are assigned to amide (I), amide (II) and amide (III) band respectively, that are still preserved in the composite. Also, C-H stretching (symmetric and asymmetric) vibration peak appeared in the range 2800-3100 cm^{-1} as already mentioned. While the sharp peak appearing at 1634.4 cm^{-1} corresponds to the internal bending vibration (ν_3) of crystal water, peaks appearing at 3743 cm^{-1}, 3342 cm^{-1}, 3385 cm^{-1} and 3133 cm^{-1} corresponds to (O-H) stretching vibrational modes from the crystal water (two molecule of water), supporting the hydrated nature of the as made Au-NC-$Zn_3(PO_4)_2$. The four corresponding O-H peak obtained along with red-shift in stretching frequencies indicated the presence of β-hopeite phase and internal hydrogen bonding in the crystal respectively, as also mentioned in literature.[A16] The peak appearing in the range 500-1200 cm^{-1} are all ascribed to PO_4^{3-} stretching modes. While, three peak observed at 996, 1071 and 1129 cm^{-1} refers to ν_3 vibrational mode of PO_4^{3-} group corresponding to ν_{as}(P-O) vibration, peak appearing at 538, 557 and 619 cm^{-1} represents the triple degenerate ν_4 vibrational mode corresponding to δ_{as}(O-P-O) bending vibration. Additionaly, peak at 957 cm^{-1} represents the $P-O$ vibration arising in P—O—Zn with $(P-O-P)$ symmetric and antisymmetric stretch occurring at 761.1 and 863.7 cm^{-1} respectively.[A16,A22] Lastly, that the zinc ion in the system underwent complexation through the hydrolysed carboxylate anion (obtained following digestion) at pH=7.4 was further justified by appearance of peak at 478.3 cm^{-1}corresponding to $Zn-O$ stretching vibration.[A24]

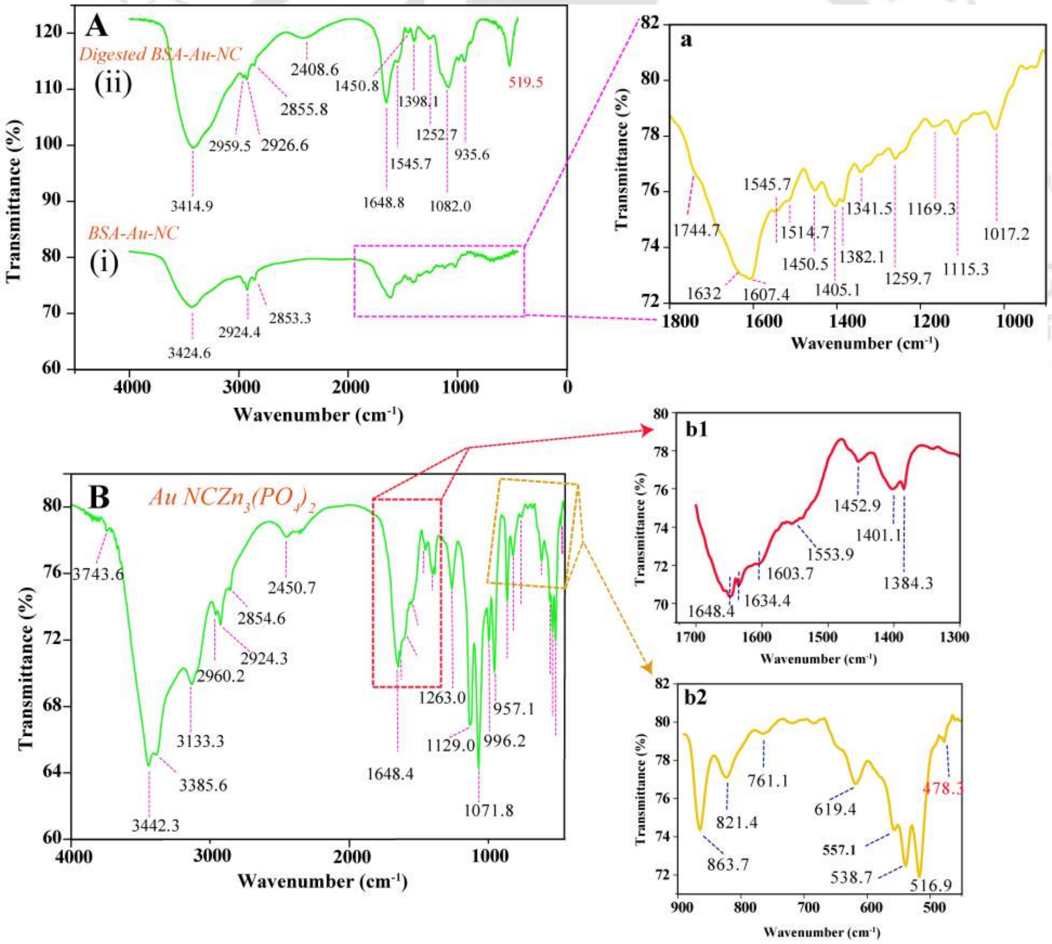

Figure A6.8. FTIR spectra of (**A**) – **(i)** BSA-Au-NCs; (**a**) shows the expanded view of BSA-Au-NC spectra in the range 1000 – 1800 cm^{-1} and (**ii**) digested BSA-Au-NCs, (**B**) as synthesized Au-NC-$Zn_3(PO_4)_2$; expanded spectral view of Au-NC-$Zn_3(PO_4)_2$ in the range (**b1**) 1300-1700 cm^{-1} and (**b2**) 500-900 cm^{-1}.

Table A6.2. Particle size (hydrodynamic diameter) distribution and the corresponding zeta-potential of BSA-Au-NC, digested BSA-Au-NC and Au-NC- $Zn_3(PO_4)_2$.

Sample	Hydrodynamic diameter (d.nm)	Zeta potential (mV)
BSA-Au-NC	10.7±1.5	- 40.7±1.4
Digested Au-NC	6.6±0.8	–
Au-NC- $Zn_3(PO_4)_2$	503.75±54	- 19.6±1.4

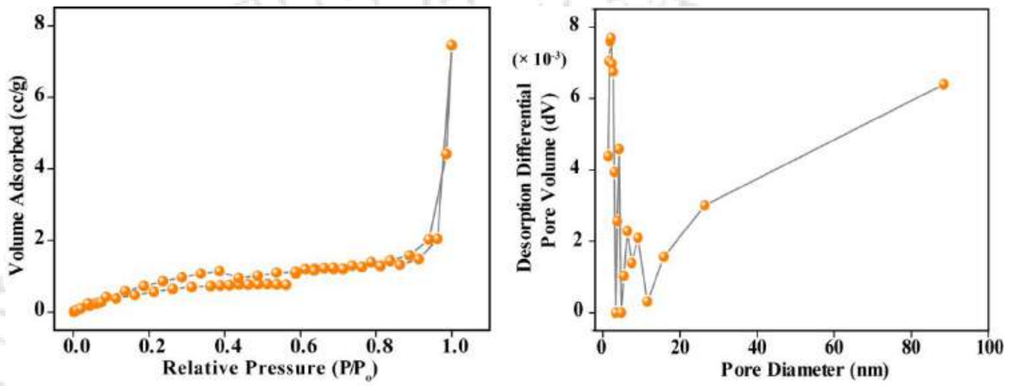

Figure A6.9. (**A**) N_2 adsorption and desorption isotherms and (**B**) differential pore volume against pore diameter plot obtained from N_2 gas desorption isotherm of as synthesized Au-NC- $Zn_3(PO_4)_2$.

Table A6.3. Specific surface area, specific pore volume and pore size distribution of Au-NC- $Zn_3(PO_4)_2$.

Sample	Surface Area (m^2/g)	Pore size distribution (nm)	Pore volume (cc/g)
Au-NC-$Zn_3(PO_4)_2$	6.394	2-17	0.015

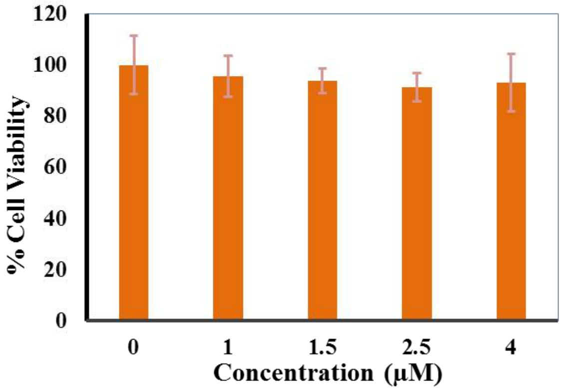

Figure A6.10. Cell viability of HeLa cells treated with varying concentration of BSA-Au-NC for 24 h.

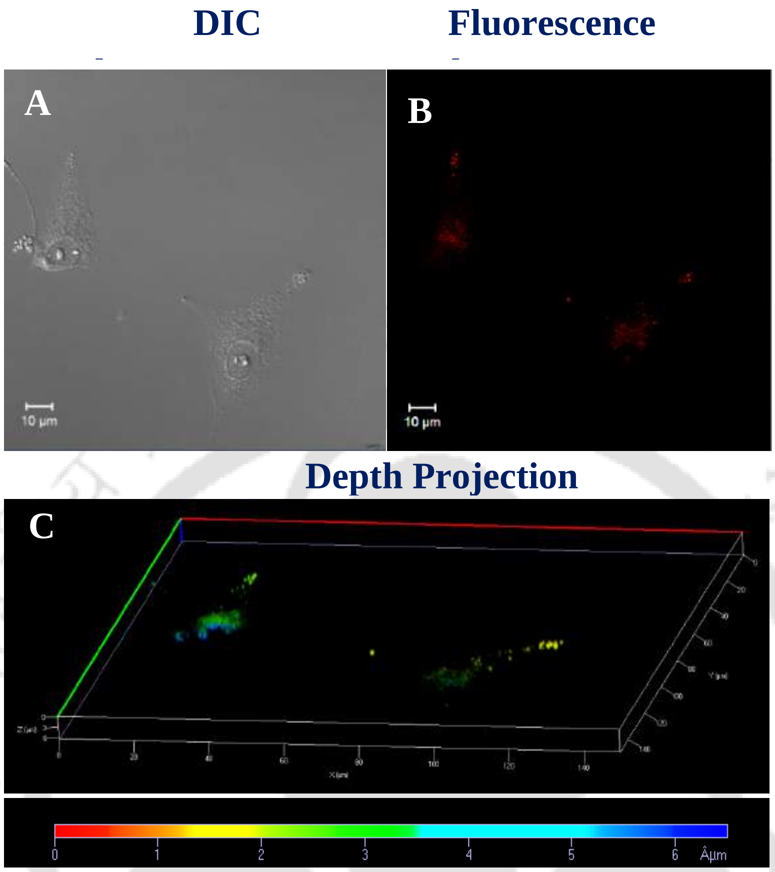

Figure A6.11. A typical CLSM image of Au-NC-$Zn_3(PO_4)_2$ treated HeLa cells (**A**) DIC, (**B**) fluorescence with corresponding (**C**) depth projection showing the internalization of Au-NC-$Zn_3(PO_4)_2$ by HeLa cells. (Excitation source: 405 nm laser; Magnification – 63x). Moreover, the results exclude the possibility of any Au-NC-$Zn_3(PO_4)_2$ nanocomposite being present on the surface of the treated cells.

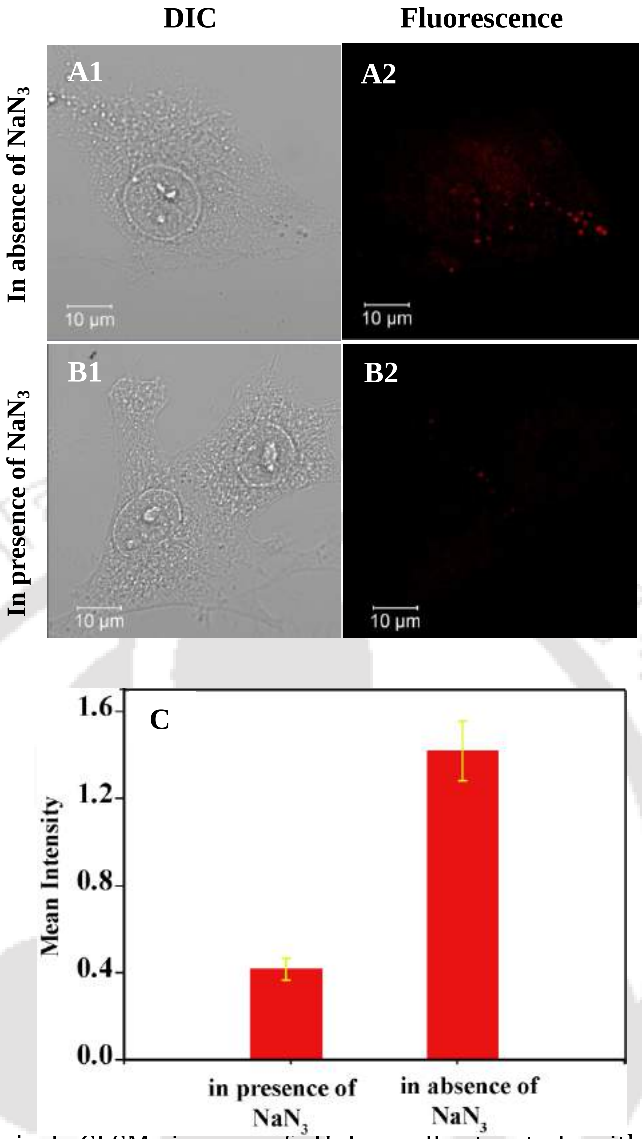

Figure A6.12. Typical CLSM image of HeLa cells treated with Au-NC-$Zn_3(PO_4)_2$ nanocomposite for 4 h in (**A1-2**) absence and (**B1-2**) presence of 0.1% sodium azide (NaN_3). (Excitation source: 405 nm laser; magnification – 63x). (**C**) Cellular uptake of Au-NC-$Zn_3(PO_4)_2$ expressed by the mean luminescence intensity (calculated from quantitative image analysis of CLSM images (3 different cell images) using Image J software) of HeLa cancer cells incubated with Au-NC-$Zn_3(PO_4)_2$ in absence and presence of 0.1 % sodium azide (NaN_3). Quantitative analysis of confocal images obtained for HeLa cells showed a decrease in cellular uptake of Au-NC-$Zn_3(PO_4)_2$ composite by 70 % in presence of NaN_3 as compared to its absence. The data are represented as mean ± standard deviation.

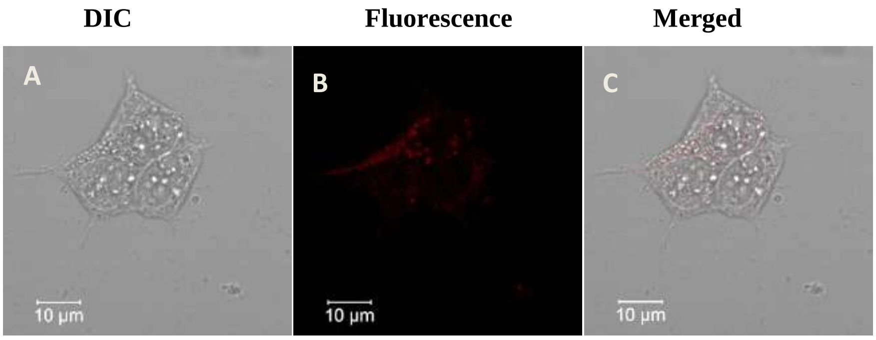

Depth projection

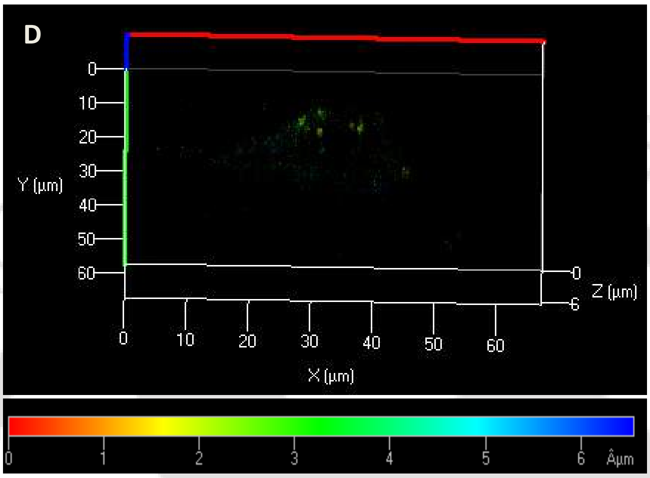

Figure A6.13. A typical CLSM image of HEK 293 cell treated with Au-NC-$Zn_3(PO_4)_2$ for 4 h (**A**) DIC, (**B**) fluorescence, (**C**) merged image with corresponding (**D**) depth projection showing the internalization of Au-NC-$Zn_3(PO_4)_2$ by HEK 293 cells. (Excitation source: 405 nm laser; Magnification – 63x).

APPENDIX REFERENCES

A1. Lewis, D. J.; Day, T. M.; MacPhersonb, J. V.; Pikramenou, Z. *Chem Commun.* **2006**, 1433.

A2. Espinoza, M. G.; Hinks, M. L.; Mendoza, A. M.; Pullman, D. P.; Peterson, K. I. *J Phys Chem C* **2012**, *116*, 8305.

A3. Yang, Z.; Aizpurua, J.; Xu, H. *J. Raman Spectrosc*. **2009**, *40*, 1343.

A4. Lawrie, G.; Keen, I.; Drew, B.; Chandler-Temple, A.; Rintoul, L.; Fredericks, P.; Grøndahl, L. *Biomacromolecules* **2007**, *8*, 2533.

A5. Dong, C.; Chen, W.; Liu, C.; Liu, Y.; Liu, H. *Colloids and Surfaces A: Physicochem. Eng. Aspects* **2014**, *446*, 179.

A6. Kumar, H.; Srivastava, R.; Dutta, P. K. *Carbohydrate Polymers* **2013**, *97*, 327.

A7. Wang, C.; Cheng, H.; Sun, Y.; Lin, Q.; Zhang, C. *ChemNanoMat* **2015**, *1*, 27.

A8. Selvam, S.; Balamuralitharan, B.; Jegatheeswaran, S.; Kim, M.-Y.; Karthick, S. N.; Raj, J. A.; Boomi, P.; Sundrarajan, M.; Prabakar, K.; Kim, H.-J. *J. Mater. Chem. A* **2017**, *5*, 1380.

A9. Su, X.; Liu, J. *ACS Appl. Mater. Interfaces* **2017**, *9*, 3902.

A10. Kannan, B.; Higgins, D. A.; Collinson, M. M. *Langmuir* **2014**, *30*, 10019.

A11. Zhou, Y.; Fan, M.; Luo, X.; Huang, L.; Chen, L. *Carbohydrate Polymers* **2014**, *113*, 108.

A12. Kerber, S. J.; Bruckner, J. J.; Wozniak, K.; Seal, S.; Hardcastle, S.; Barr, T. L. *J. Vac. Sci. Technol. A* **1996**, *14*, 1314.

A13. de la Rica, R.; Velders, A. H. *J. Am. Chem. Soc.* **2011**, *133*, 2875.

A14. Chung, S. Y.; Kim, Y. M.; Kim, J. G.; Kim, Y. J. *Nat. Phys.* **2009**, *5*, 68.

A15. Bach, S.; Celinski, V. R.; Dietzsch, M.; Panthöfer, M.; Bienert, R.; Emmerling, F.; auf der Günne, J. S.; Tremel, W. *J. Am. Chem. Soc.* **2015**, *137*, 2285.

A16. Herschke, L.; Enkelmann, V.; Lieberwirth, I.; Wegner, G. *Chem. Eur. J.* **2004**, *10*, 2795.

A17. Csach, K.; Jurikova, A.; Miskuf, J.; Koneracka, M.; Zavisova, V.; Kubovcikova, M.; Kopcansky, P. *Acta Physica Polonica A* **2012**, *121*, 1293.

A18. Gebregeorgi, A.; Bhan, C.; Wilson, O.; Raghavan, D. *J Colloid Interface Sci.*, **2013**, *389*, 31.

A19. Barth, A. *Biochim. Biophys. Acta, Bioenerg.* **2007**, *1767*, 1073.

A20. Grdadolnik, J.; Marechal, Y. *Biopolymers* **2001**, *62*, 40.

A21. Mehta, R.; Kumari, R.; Dasa, P.; Bhowmick, A. K. *J. Mater. Chem. B* **2014**, *2*, 6236.

A22. Buso, D.; Hill, A. J.; Colson, T.; Whitfield, H. J.; Patelli, A.; Scopece, P.; Doherty, C. M.; Falcaro, P. *Cryst. Growth Des.* **2011**, *11*, 5268.

A23. Navarra, G.; Tinti, A.; Leone, M.; Militello, V.; Torreggiani, A. *J. Inorg. Biochem.* **2009**, *103*, 1729.

A24. Babu, K. S.; Reddy, A. R.; Sujatha, C.; Reddy, V. K.; Mallika, A. N. *J Adv Ceram*. **2013**, *3*, 260.

PUBLICATIONS

1. **Dutta, A.**; Das, S.; Paul, A.; Chattopadhyay, A. Kinetics of reaction of gold nanoparticles following partial removal of stabilizers. *J Nanopart Res.* **2015**, *17*, 260.

2. **Dutta, A.**; Paul, A.; Chattopadhyay, A. The effect of temperature on the aggregation kinetics of partially bare gold nanoparticles. *RSC Adv.* **2016**, *6,* 82138.

3. **Dutta, A.**; Chattopadhyay, A. Surface and Tip-Enhanced Raman Spectroscopy at the Plasmonic Hot Spot of Coordination Complex-Conjugated Gold Nanoparticle Dimer. *J. Phys. Chem. C* **2017**, *121*, 18854.

4. **Dutta, A.**; Goswami, U.; Chattopadhyay, A. Probing Cancer Cells through Intracellular Aggregation Induced Emission Kinetic Rate of Copper Nanoclusters (**2017**) ***Communicated.***

5. **Dutta, A.**; Dutta, D.; Sanpui, Pallab.; Chattopadhyay, A. Biomimetically Crystallized Zinc Phosphate decorated with Gold Atomic Clusters for Protease-Resistant Imaging. *Chem. Commun.* **2017**, *53*, 1277.

6. Goswami, U.; **Dutta, A.**; Raza, A.; Kandimalla, R.; Kalita, S.; Ghosh, S. S.; Chattopadhyay, A. Transferrin-Copper Nanocluster-Doxorubicin Nanoparticles as Targeted Theranostic Cancer Nanodrug.(**2017**) ***Communicated***.

Conferences Attended

1. Presented a poster in DAE-BRNS 5th Interdisciplinary Symposium on Materials Chemistry, **ISMC 2014** held at Bhabha Atomic Research Centre, (**BARC**) Mumbai, India.

2. Participated in a national conference on New Advanced and Horizons in Nanoscience and Nanotechnology, **Nano Sci 2014** held at Institute of Advanced Study in Science and Technology (**IASST**), Guwahati, India.

3. Presented a poster in 4th International Conferences on Advanced Nanomaterials and Nanotechnology, **ICANN 2015** held at Indian Institute of Technology Guwahati (**IITG**), Guwahati, India.

4. Presented a poster in International Conference on Nanoscience and Technology, **ICONSAT 2016** held at Indian Institute of Science Education and Research (**IISER**), Pune, India.

5. Presented a poster in Young Scientists' Colloquium, **YSC-2017** organized by Materials Research of India (**MRSI**), Kolkata at Indian Institute of Engineering Science and Technology (**IIEST**) Shibpur, Howrah, India.

PERMISSIONS

Home Account Info Help

Title:	Surface plasmon subwavelength optics
Author:	William L. Barnes, Alain Dereux, Thomas W. Ebbesen
Publication:	Nature
Publisher:	Nature Publishing Group
Date:	Aug 14, 2003

Logged in as:
ANUSHREE DUTTA
Account #:
3001193266
LOGOUT

Order Completed

Thank you for your order.

This Agreement between ANUSHREE DUTTA ("You") and Nature Publishing Group ("Nature Publishing Group") consists of your license details and the terms and conditions provided by Nature Publishing Group and Copyright Clearance Center.

Your confirmation email will contain your order number for future reference.

printable details

License Number	4223061384624
License date	Nov 06, 2017
Licensed Content Publisher	Nature Publishing Group
Licensed Content Publication	Nature
Licensed Content Title	Surface plasmon subwavelength optics
Licensed Content Author	William L. Barnes, Alain Dereux, Thomas W. Ebbesen
Licensed Content Date	Aug 14, 2003
Licensed Content Volume	424
Licensed Content Issue	6950
Type of Use	reuse in a dissertation / thesis
Requestor type	academic/educational
Format	print and electronic
Portion	figures/tables/illustrations
Number of figures/tables /illustrations	1
High-res required	no
Figures	Box 1a
Author of this NPG article	no
Your reference number	
Title of your thesis / dissertation	Designing Nanoscale Metal Particles for Higher Order Assembly
Expected completion date	Dec 2017
Estimated size (number of pages)	200
Requestor Location	ANUSHREE DUTTA IIT GUWAHATI, NORTH GUWAHATI GUWAHATI, ASSAM 781039 India Attn: ANUSHREE DUTTA
Billing Type	Invoice
Billing address	ANUSHREE DUTTA IIT GUWAHATI, NORTH GUWAHATI GUWAHATI, India 781039 Attn: ANUSHREE DUTTA
Total	0.00 USD

ORDER MORE CLOSE WINDOW

Copyright Clearance Center RightsLink®

Home Account Info Help

npg nature publishing group

Title: Assembly of Nanoions via Electrostatic Interactions: Ion-Like Behavior of Charged Noble Metal Nanoclusters

Author: Qiaofeng Yao, Zhentao Luo, Xun Yuan, Yue Yu, Chao Zhang et al.

Publication: Scientific Reports

Publisher: Nature Publishing Group

Date: Jan 24, 2014

Logged in as:
ANUSHREE DUTTA
Account #:
3001193266

LOGOUT

Creative Commons

The article for which you have requested permission has been distributed under a Creative Commons CC-BY license (please see the article itself for the license version number). You may reuse this material without obtaining permission from Nature Publishing Group, providing that the author and the original source of publication are fully acknowledged, as per the terms of the license.
For license terms, please see http://creativecommons.org/

CLOSE WINDOW

Are you the author of this NPG article?

To order reprints of this content, please contact Springer Healthcare by e-mail: reprintswarehouse@springer.com, and you will be contacted very shortly with a quote.

Copyright Clearance Center RightsLink®

Home | Account Info | Help

Title: Kinetics of reaction of gold nanoparticles following partial removal of stabilizers

Author: Anushree Dutta, Subhojit Das, Anumita Paul et al

Publication: Journal of Nanoparticle Research

Publisher: Springer

Date: Jan 1, 2015

Logged in as:
ANUSHREE DUTTA
Account #:
3001193266

LOGOUT

Order Completed

Thank you for your order.

This Agreement between ANUSHREE DUTTA ("You") and Springer ("Springer") consists of your license details and the terms and conditions provided by Springer and Copyright Clearance Center.

Your confirmation email will contain your order number for future reference.

printable details

License Number	4234460137310
License date	Nov 22, 2017
Licensed Content Publisher	Springer
Licensed Content Publication	Journal of Nanoparticle Research
Licensed Content Title	Kinetics of reaction of gold nanoparticles following partial removal of stabilizers
Licensed Content Author	Anushree Dutta, Subhojit Das, Anumita Paul et al
Licensed Content Date	Jan 1, 2015
Licensed Content Volume	17
Licensed Content Issue	6
Type of Use	Thesis/Dissertation
Portion	Full text
Number of copies	1
Author of this Springer article	Yes and you are the sole author of the new work
Order reference number	
Title of your thesis / dissertation	Designing Nanoscale Metal Particles for Higher Order Assembly
Expected completion date	Dec 2017
Estimated size(pages)	200
Requestor Location	ANUSHREE DUTTA IIT GUWAHATI, NORTH GUWAHATI GUWAHATI, ASSAM 781039 India Attn: ANUSHREE DUTTA
Billing Type	Invoice
Billing address	ANUSHREE DUTTA IIT GUWAHATI, NORTH GUWAHATI GUWAHATI, India 781039 Attn: ANUSHREE DUTTA
Total	0.00 USD

ORDER MORE CLOSE WINDOW

RSC | Advancing the Chemical Sciences

Royal Society of Chemistry
Thomas Graham House
Science Park
Milton Road
Cambridge
CB4 0WF

Tel: +44 (0)1223 420 066
Fax: +44 (0)1223 423 623
Email: contracts-copyright@rsc.org

www.rsc.org

Acknowledgements to be used by RSC authors

Authors of RSC books and journal articles can reproduce material (for example a figure) from the RSC publication in a non-RSC publication, including theses, without formally requesting permission providing that the correct acknowledgement is given to the RSC publication. This permission extends to reproduction of large portions of text or the whole article or book chapter when being reproduced in a thesis.

The acknowledgement to be used depends on the RSC publication in which the material was published and the form of the acknowledgements is as follows:

- For material being reproduced from an article in *New Journal of Chemistry* the acknowledgement should be in the form:
    - [Original citation] - Reproduced by permission of The Royal Society of Chemistry (RSC) on behalf of the Centre National de la Recherche Scientifique (CNRS) and the RSC
- For material being reproduced from an article *Photochemical & Photobiological Sciences* the acknowledgement should be in the form:
    - [Original citation] - Reproduced by permission of The Royal Society of Chemistry (RSC) on behalf of the European Society for Photobiology, the European Photochemistry Association, and RSC
- For material being reproduced from an article in *Physical Chemistry Chemical Physics* the acknowledgement should be in the form:
    - [Original citation] - Reproduced by permission of the PCCP Owner Societies
- For material reproduced from books and any other journal the acknowledgement should be in the form:
    - [Original citation] - Reproduced by permission of The Royal Society of Chemistry

The acknowledgement should also include a hyperlink to the article on the RSC website.

The form of the acknowledgement is also specified in the RSC agreement/licence signed by the corresponding author.

Except in cases of republication in a thesis, this express permission does not cover the reproduction of large portions of text from the RSC publication or reproduction of the whole article or book chapter.

A publisher of a non-RSC publication can use this document as proof that permission is granted to use the material in the non-RSC publication.

Copyright Clearance Center RightsLink®

Home Account Info Help

ACS Publications
Most Trusted. Most Cited. Most Read.

Title: Surface and Tip-Enhanced Raman Spectroscopy at the Plasmonic Hot Spot of a Coordination Complex-Conjugated Gold Nanoparticle Dimer

Author: Anushree Dutta, Arun Chattopadhyay

Publication: The Journal of Physical Chemistry C

Publisher: American Chemical Society

Date: Aug 1, 2017

Logged in as:
ANUSHREE DUTTA
Account #:
3001193266

LOGOUT

PERMISSION/LICENSE IS GRANTED FOR YOUR ORDER AT NO CHARGE

This type of permission/license, instead of the standard Terms & Conditions, is sent to you because no fee is being charged for your order. Please note the following:

- Permission is granted for your request in both print and electronic formats, and translations.
- If figures and/or tables were requested, they may be adapted or used in part.
- Please print this page for your records and send a copy of it to your publisher/graduate school.
- Appropriate credit for the requested material should be given as follows: "Reprinted (adapted) with permission from (COMPLETE REFERENCE CITATION). Copyright (YEAR) American Chemical Society." Insert appropriate information in place of the capitalized words.
- One-time permission is granted only for the use specified in your request. No additional uses are granted (such as derivative works or other editions). For any other uses, please submit a new request.

BACK CLOSE WINDOW